Photofragmentation Studies of Metal Ion-Molecule Complexes and Metal Oxides

Andreas Iskra

Wadham College

A thesis submitted for the degree of

Doctor of Philosophy

Physical & Theoretical Chemistry Laboratory

University of Oxford

Trinity Term 2017

Photofragmentation Studies of Metal Ion-Molecule Complexes and Metal Oxides

Andreas Iskra, Wadham College

A thesis submitted for the degree of *Doctor of Philosophy*

Trinity Term 2017

Abstract

Gas phase metal-containing complexes provide suitable systems in which to study fundamental binding motifs between a metal ion and molecules in the absence of any solvent, support or competing charge effects. In this thesis, metal-containing species are explored experimentally using infrared-resonance enhanced photodissociation (IR-REPD) spectroscopy and velocity map imaging (VMI). The experimental results are further interpreted with the aid of spectral simulations based on density functional theory (DFT). These are the first studies reported using a newly built IR-REPD spectrometer equipped with a purpose-built laser ablation source to allow for the study of single metal ion–molecule complexes. The laser ablation source is shown to efficiently produce various complexes including $Rh^+(CO_2)_n$, $VO_2^+(N_2O)_n$ and $Au^+(CH_4)_n$ and the IR-REPD spectrometer has been characterised against a well-studied system of $V^+(CO_2)_n$ complexes. In order to record the IR-REPD spectra for small metal ion-molecule complexes, an argon atom is employed as the inert messenger.

A combined IR-REPD spectroscopy and DFT investigation of $M^+(CO_2)_n$ complexes (where M = Co^+, Rh^+ and Ir^+) reveals a common $[M^+(CO_2)_2]$ core structure for all three considered metal ions. Additional ligands, which are not directly bound to the central metal ion, experience lower perturbation as evident in the reduced blue-shift for the ligand in the outer coordination shells. A further IR-REPD/DFT study involving CO_2 complexation around NbO_2^+ and TaO_2^+ ions reveals a strongly-bound core of four CO_2 ligands around the MO_2^+ ion (M = Nb, Ta). A significant increase in the intermolecular bond distances for the second coordination sphere ligands coincides with a decrease in the calculated binding energies.

Velocity map imaging is employed to explore the rich photodissociation dynamics of VO in the vicinity of $C^4\Sigma^-$ - $X^4\Sigma^-$(v',0) vibronic transitions in VO. The final quantum state distribution was observed to be strongly dependent on the intermediate vibronic state of VO *via* which the dissociation threshold is reached. This work provides a refined value for the VO dissociation energy of $D_0(\mathrm{VO}) = 53190 \pm 261$ cm^{-1} in excellent agreement with available literature.

Acknowledgements

Writing is always a solitary endeavour, however, during the past four years, I have received valuable support from my friends and colleagues. First and foremost, I wish to thank my supervisor Professor Stuart Mackenzie for his guidance and wisdom during these four years. I am forever grateful for the trust he bestowed upon me and for the opportunity to work on exciting projects.

I am grateful to Dr Alexander Gentleman for his continuous help with the experiments and computations. I wish to extend my gratitude to the members of the Mackenzie group I had pleasure to work with: Dr Imogen Parry, Dr Graham Cooper, Dr Dean Sheppard, Ethan Cunningham, Hansjochen Köckert, Alice Green, Tilo Zollitsch, Katherine Buckton, Dr Aras Kartouzian, Dr Lauren Jarocha, Robert van Wijk, Michael Kent, Alastair Sharp, Edward Barnard, Rhiannon Main, Benjamin Atkinson, Malcolm Kittle, Daniel Price, Peter Beardsmore, Jack Pickering, Ashley Redman and Jessica Walton. After all, often it is not so much about the destination but also about the journey.

I am also grateful to Professor John McGrady for valuable discussions on the topics concerning the density functional theory. I am thankful to the Advanced Research Computing (ARC) facility for providing access to their supercomputer facilities. I wish to thank the PTCL Lab Services, and Electrical and Mechanical Workshops for their professionalism and help in building and maintaining various lab instruments. I am grateful to Dr Martin Galpin, Keble College and Hertford College for entrusting me to tutor their students. I tend to think I have learned as much as a tutor as they did as students. I wish to thank my favourite astrophysicist, Kristine Lam, for valuable discussions regarding the astrophysical significance of VO.

My friends from Wadham College and other Oxford colleges made this last four years truly enjoyable. I wish to extend my gratitude to the members of

the Oxford University Volleyball Club. I am particularly grateful to everyone I have shared the volleyball court with on the path to three consecutive Varsity wins: Fabio Anza, Rory Kelly, Krzysztof Bar, Gregorio Dias, Steinar Halldorsson, Manuel Hepfer, Gytis Jankevicius, Sanders Lazier, Eric Chih-Chao Liang, Peter Marinov, Adam McBride, Yale Michaels, Stefan Nekovar, David Novotny, Krzysztof Palucki, Sven Sabas, Alexander Stockenhuber, Nicolas Stone-Villani, Jonas Pollex, Jakub Redlicki, and Linus Ubl. They were my Cape of Good Hope. Thank you!

I am grateful to everyone who has supported me in my journey prior to pursuing a doctorate. Particularly to Professor Helen Fielding who first introduced me to laser spectroscopy and to Mrs Keuc who inspired, then an exuberant youngster to study Chemistry.

My family and my parents have been a continuous source of encouragement. I would not be writing these words without their support.

Lastly, I am grateful to Wadham College and EPSRC for their generous financial support.

List of Publications

[1] Iskra, A; Gentleman, A. S.; Kartouzian, A.; Kent, M. J., Sharp, A. P.; Mackenzie, S. R. Infrared Spectroscopy of Gas-Phase $M^+(CO_2)_n$ (M = Co, Rh, Ir) Ion-Molecule Complexes, *J. Phys. Chem. A*, 2017, 121, 133–140

Publications based on the work presented in Chapter 5 and Chapter 6 are currently in preparation.

Other publications:

[2] Cooper, G. A.; Kartouzian, A.; Gentleman, A. S., Iskra, A.; van Wijk, R.; Mackenzie, S. R. Dissociation Energies of Ag–RG (RG = Ar, Kr, Xe) and AgO Molecules From Velocity Map Imaging Studies, *J. Chem. Phys.*, 2015, 143, 1243021–1243026

[3] Cooper, G. A.; Gentleman, A. S., Iskra, A.; Mackenzie, S. R. Photofragmentation Dynamics and Dissociation Energies of MoO and CrO, *J. Chem. Phys.*, 2017, 147, 0139211–0139218

[4] Cunningham, E. M.; Gentleman, A. S.; Beardsmore, P.; Iskra, A.; Mackenzie, S. R. Infrared Signature of Structural Isomers of Gas–Phase $M^+(N_2O)_n$ (M = Cu, Ag, Au) Ion—Molecule Complexes, *J. Phys. Chem.*, *J. Phys. Chem. A*, 2017, 121, 7565–7571

[5] Gentleman, A. S.; Green, A. E.; Price, D. R.; Cunningham, E. M.; Iskra, A. Mackenzie, S. R. Infrared Spectroscopy of $Au^+(CH_4)_n$ Complexes and Vibrationally-Enhanced C–H Activation Reactions, *Top. Catal.*, accepted

Contents

Chapter 1

Introduction

1.1 Interest in the Study of Isolated Metal-Containing Complexes

Experiments with isolated metal-containing complexes can provide insights into processes occurring at a molecular level unperturbed by the influence of solvent, aggregation or counter ion effects. Metal ion-molecule interactions are of fundamental importance in understanding many processes that occur across chemistry, biochemistry, planetary sciences, and astrophysics. Metal ions often play a crucial role in the active sites of enzymes, which greatly influences their function and determines their chemical reactivity.[1–4] Similarly, ions such as Na^+, Mg^+, Fe^+ and Co^+, resulting from meteor ablation constitute integral parts of aerosol particles in the Earth's atmosphere.[5,6] Numerous metal ions have further been detected in the atmospheres of Mars, Jupiter and Neptune.[7–9]

Interactions between metals and molecules are also crucial in understanding the role of an active centre in heterogenous catalysis.[10] With a countable number of atoms/ions, isolated complexes and clusters can serve as suitable model systems for heterogeneous catalysis susceptible for rigorous computa-

tional treatment.[11] Quantum chemical computations in conjunction with the experimental data can thus provide further insights into fundamental forces that govern interactions between ions and molecules.[12–14]

Many industrial catalysts are heavily dependant on their metal oxide components. The performance of the iron-based catalyst in the Haber-Bosch process is vastly enhanced by the Al_2O_3, CaO and K_2O promoters, which can also provide the support.[15,16] Furthermore, metal oxides, and particularly the dioxide complexes, are of paramount importance as oxygen carriers in biochemistry, where exposed metal ions in the enzyme active sites can form metal (ion) - O_2 adducts.[17–19]

1.2 Generation of Gas-Phase Metal-Containing Complexes

One of the crucial experimental challenges in the study of gas-phase metal-containing complexes is a reliable generation of thereof in adequate abundances. The early sources consisted of thermally-heated ovens – also known as Knudsen cells – where the vaporised metal is seeded in a background gas that supersonically expands over the oven.[20,21] The collisions with the background gas stabilise the newly-formed cluster against evaporation by removing any excess energy. Unfortunately, the oven source suffers from a high consumption rate of the sample and was initially limited to metals with low boiling points *e.g.* alkali metals,[22] although clusters of other metals including Al, Cr, Ni, Cu and Ag clusters produced by oven sources have since been reported.[23,24]

Moreover, metal clusters can be formed using the pulsed-arc cluster source (PACIS).[25,26] Here, an electric discharge produces plasma from the background gas which then flows towards the sample vaporising the metal surface. PACIS can operate at high repetition rates and produce high-intensity

cluster beams. However, the plasma requires additional cooling and like the oven sources, PACIS instruments consume a significant amount of the sample. Similar to a PACIS source is the inductively coupled plasma (ICP) source as used by the Bohme group.[27] In the case of an ICP source, typically an argon plasma is produced by electromagnetic induction and the metal salt solution is sprayed into the plasma. Collisions between electrons and charged particles in the argon plasma then generate individual metal ions.

In the case of sputtering sources, an ion gun generates rare-gas ions (typically Xe, Kr or Ar) which are accelerated towards the metal target.[28,29] If the kinetic energy of the incoming rare-gas ion is sufficient, metal atoms (or ions if a voltage is applied to the target cathode) will be ejected. Sputtering sources can produce clusters in all three charge states. For instance, Lineberger *et al.* studied coinage metal cluster anions (Cu_n^-, Ag_n^- and Au_n^-) up to $n = 10$.[30] An extension of the traditional sputtering source is the magnetron sputtering source, which initially confines the argon plasma in a magnetic field prior to acceleration towards the target.[31–33]

The laser vaporisation (ablation) source (Figure 1.1) developed independently by groups of Smalley[34] and Bondybey[35] in 1981 has become the most widely-used source for the generation of gas-phase metal-containing species. Local heating of a metal target is achieved by a focused beam of a pulsed laser (typically the 2^{nd} (532 nm) or 3^{rd} (355 nm) harmonic of a Nd:YAG laser). Upon heating of the metal surface, the neutral and ionised metal atoms are emitted from the surface; ablation also produces free electrons that can attach to newly-ablated atoms. The metal plasma produced by the ablation is then typically entrained in a gas pulse confined to a growth channel. This promotes the three-body collisions necessary for the formation of larger clusters.[36] Collisions with the background gas disperse any excess energy that results from the newly formed metal-metal bonds. Following the cluster channel, the background gas containing the clusters expands freely into vacuum before being skimmed as it enters the next region of the experi-

mental apparatus. Metal targets are generally rods or discs, and the target is continuously rotated to ensure the ablation of a fresh surface. Non-metallic clusters have also been successfully prepared by laser vaporisation, including C_{60} by Kroto, Curl and Smalley *et al.*[37]

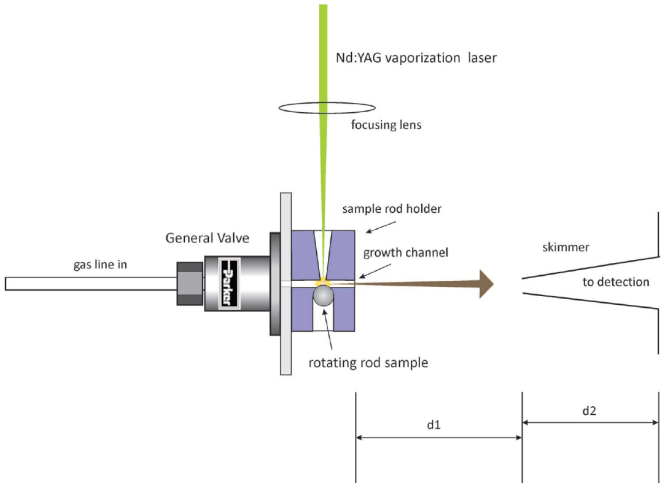

Figure 1.1: A traditional Smalley/Bondybey laser vaporisation source used by the Duncan group. Reprinted from Duncan, M. A. *Rev. Sci. Instrum.*, 2012, 83, 041101-01–041101-19 with permission from American Institute of Physics.[36]

The Duncan group has observed that a "cutaway" modification of the Smalley / Bondybey-type ablation block with no growth channel is particularly suitable for the production of weakly-bound atomic ion–ligand complexes.[36] Duncan *et al.* have produced complexes with several ligands including H_2O, CO_2 and benzene using this ablation block design.[38–40]

Laser vaporisation sources with a cryogenically cooled cluster channel have been reported in the literature. Knickelbein *et al.* used liquid nitrogen to cool the growth channel to 77 K in order to enhance the cooling process and the production of large metal clusters.[41] Knickelbein *et al.* were thus able to form neutral nickel clusters (Ni_n of up to $n = 90$). Similarly, Fielicke *et al.* used an additional cryogenically cooled block (following the growth channel) with a liquid nitrogen reservoir to produce vanadium clusters with

weakly-bound argon atoms ($V_nAr_m^+$).[42] Often a cryogenically cooled cluster channel is required to bind weakly-bound rare-gas tags to metal clusters (as discussed in Section 2.4.2 and 2.6).

Kaya and co-workers designed a dual-rod ablation source for the production of mixed-metal binary clusters.[43] In this design, two metal rods positioned in the source are ablated with two counter-propagating lasers. Mixed-metal complexes formed by Kaya *et al.* using the dual-rod ablation source include Co_nV_m, Si_nNa_m, $Co_nAl_m^-$ and Au_nPd^-.[43–46]

Originally developed for the mass-spectrometric studies of biological macromolecules by Fenn *et al.*, electrospray ionisation (ESI) is becoming a viable alternative to laser ablation.[47,48] A liquid sample is passed through a small capillary placed at a potential difference of a few thousand volts. The capillary emits a jet of small charged liquid droplets which are inherently unstable and undergo further evaporation of solvent until only isolated ions remain. ESI serves as a particularly reliable source of the generation of large metal-ligand complexes. Niedner-Schatteburg and co-workers used ESI to produce large coordination complexes of iron $[Fe_3O(OAc)_6(N_2)_n]^+$ (with n = 1 – 3, OAc = $CH_3CO_2^-$) and complexes of Ag^+ with 1-methylamine.[49,50] Similarly, Johnson and co-workers formed complexes such as $[MgSO_4(H_2O)_{n=4-11}]^{2+}$ and $M^{2+}RCO_2^-$ (where M = Mg, Ca; R = CD_3, CD_2CD_3).[51,52]

1.3 Catalysis at a Single Metal Atom / Ion Centre

Several atomic ions were found to exhibit a propensity for catalytic activity. In their ion cyclotron resonance (ICR) mass spectrometry experiments, Kappes and Stanley were first to observe Fe^+ mediated oxidation of CO by N_2O:[53]

$$Fe^+ + N_2O \rightarrow FeO^+ + N_2. \tag{1.1}$$

$$FeO^+ + CO \rightarrow Fe^+ + CO_2. \tag{1.2}$$

Even though this reaction is strongly exothermic ($\Delta_r H = 3.79$ eV), the oxidation of CO by N_2O does not occur in the absence of a catalyst due to large energy barrier of 2.05 eV as calculated at the B3LYP/6-311+G(d)triple-ζ basis set augmented level of theory by the Bohme group.[54] Other metals, which have shown an ability to mediate this process are Pt^+, Os^+ and Ir^+.

One of the most intriguing reactions again involves FeO^+. Fe^+ is inert towards H_2, however FeO^+ was observed to mediate catalytic conversion of H_2 into H_2O:[55–58]

$$FeO^+ + H_2 \rightarrow Fe^+ + H_2O. \tag{1.3}$$

FeO^+ can be simply formed in reaction 1.1, which then yields a full catalytic cycle. The reaction efficiency of 1% is surprisingly low, which several early computational studies attributed to spin crossings between different potential energy surfaces.

As shown in Figure 1.2, the transition energy barrier for a sextet potential energy surface is significantly higher than for the quartet equivalent. The reaction is thought to proceed through (two) spin-inversion junction(s) between the two surfaces, which was initally thought to reduce the reaction efficiency.[55,59] Nevertheless, recent transition state theory calculations and surface hopping dynamics simulations by Harvey *et al.* suggest that the reaction bottleneck lies in the insertion of FeO^+ into the H–H bond on the quartet surface.[60,61] Experimentally, however, the exact product quantum state distribution is still unknown. This example illustrates the crucial interplay

between experiment and theory required to fully understand the complexity of metal mediated catalysis even at a single atomic ion centre.

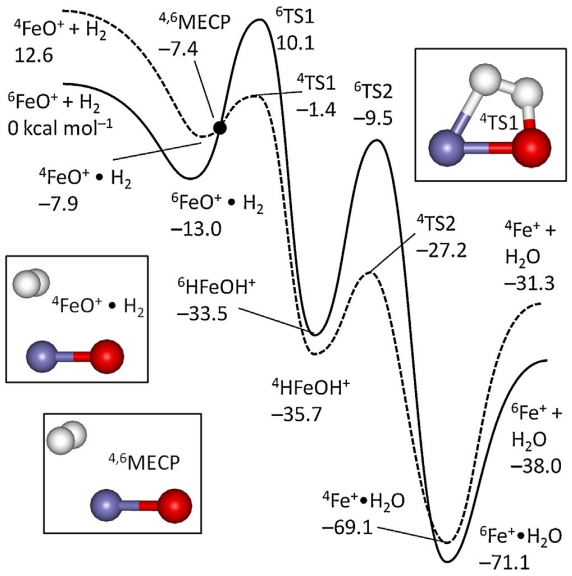

Figure 1.2: Potential energy surfaces for $FeO^+ + H_2 \rightarrow Fe^+ + H_2O$ reaction, calculated at CCSD(T)/aug-cc-pVXZ(X=T,Q) level of theory. MECP indicates the minimum energy crossing point and TS refers to transition states. Reprinted from Harvey, J. N.; Tew, D. P. *Inter. J. Mass. Spectros.*, 2013, 354–355, 263–270 with permission from Elsevier B.V.[60]

Several other interesting catalytic systems have been reported in the literature. On this topic, extensive reviews were written by Bohme and Schwarz, Schwarz, and Roithová and Schröder.[62–64]

1.4 Metal Clusters as Tractable Models for Heterogeneous Catalysis

Small metal clusters can also serve as tractable models for heterogeneous catalysis. Various extensive accounts of the field that extend the focus of this thesis can be found in the literature.[11,14,65] Here, only a short and selective description of some recent developments is presented.

Countable number of atoms renders small metal clusters particularly suitable for theoretical treatment to both gain additional insight into catalytic processes, and to benchmark different computational methods. Shi and Ervin observed that small anionic platinum clusters Pt^{-}_{n} (where $n = 3 - 7$) can act as an effective catalyst in converting CO into CO_2 in a reaction with either N_2O or O_2.[66] The oxidation cycle involving CO and N_2O on gas-phase platinum clusters was also observed in a FT-ICR mass spectrometry study by Beyer, Bondybey *et al.*[67] In a reaction involving Pt_7^+ and 1:6 mixture of CO and N_2O, the authors observed a formation of a steady-state between Pt_7^+, Pt_7O^+ and $Pt_7O_2^+$ after 3 second residence time in an ICR cell.

Bernhardt, Landman, Heiz and co-workers later studied the conversion of CO to CO_2 by Au_2^- dimer by measuring the kinetics of the reaction in conjunction with computational modeling.[68,69] The authors observed the following catalytic cycle:

$$Au_2^- + O_2 + 2CO \rightarrow Au_2^- + 2CO_2. \tag{1.4}$$

As shown in Figure 1.3, the first step in the catalytic cycle is the barrierless formation of a superoxo-like $Au_2O_2^-$ complex. Partial charge transfer to the antibonding π-orbital of O_2 increases the propensity for CO molecule insertion, forming either a peroxyformate $Au_2(CO)O_2^-$ complex, or the more stable carbonate isomer $Au_2CO_3^-$. The co-adsorption of CO to form the carbonate isomer requires surmounting a barrier of 0.3 eV, whereas the formation of the peroxyformate isomer is barrierless. The structure with the stoichiometry of this intermediate step has also been detected experimentally by the authors. Formation of CO_2 from the peroxyformate isomer involves a metastable $Au_2CO_2^-$ intermediate. However, the heat of reaction from desorption of the first CO_2 is sufficient to offset the binding energy of the remaining CO_2; the second CO_2 is thus also easily desorbed. Production of CO_2 from the reaction of the carbonate isomer with CO involves an activation barrier of 0.5 eV. Desorption of the first CO_2 molecule produces an unstable

Au_2OCO^-, which readily decays releasing the second molecule of CO_2 and the remaining Au_2^- dimer. Both of these catalytic cycles are expected to be contributing to the Au_2^- catalysed oxidation of CO.

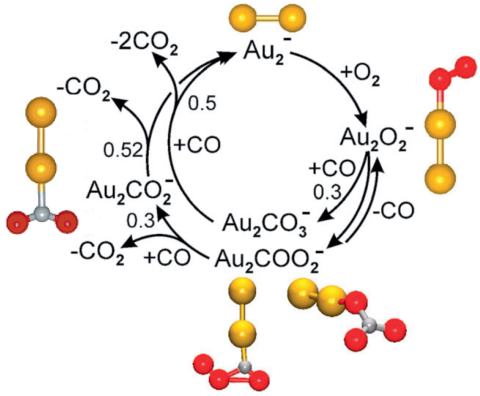

Figure 1.3: Catalytic cycle for the gas-phase oxidation of CO to CO_2 *via* O_2 co-adsorption on Au_2^-. The numbers in the catalytic cycle refer to the calculated reaction barriers (in eV). Colour scheme: Au – yellow, C – grey, and O – red. Adopted from Lang, M. S; Bernhardt, T. M. *Phys. Chem. Chem Phys.*, 2012, 14, 9255–9269 with permission from the Owner Societies.[68]

1.5 Reactivity Studies of Atomic Metal Ions

Of particular relevance to the work in this thesis, Bohme and co-workers have studied extensively reactions of CO_2 with main-group and transition-metal atomic cations.[70] The kinetics measurements were performed using the selected-ion flow (SIFT) tandem mass spectrometer.[71] Atomic metal ions were produced in a ICP source and cooled to *ca.* 295 K *via* collisions with helium background gas in the flow tube, and mass-selected using a quadruple mass analyser. Pure CO_2 reagent was then injected into the flow tube while monitoring the ion signal at different CO_2 flow rates. This allowed the authors to measure the reaction kinetics for 46 atomic-metal cations, as displayed in Figure 1.4. CO_2 was found to cluster with the majority of the metal ions. The initial step in complexation is thought to be a termolecular

process where collisions with the helium background gas remove any excess energy arising from metal-ligand binding.

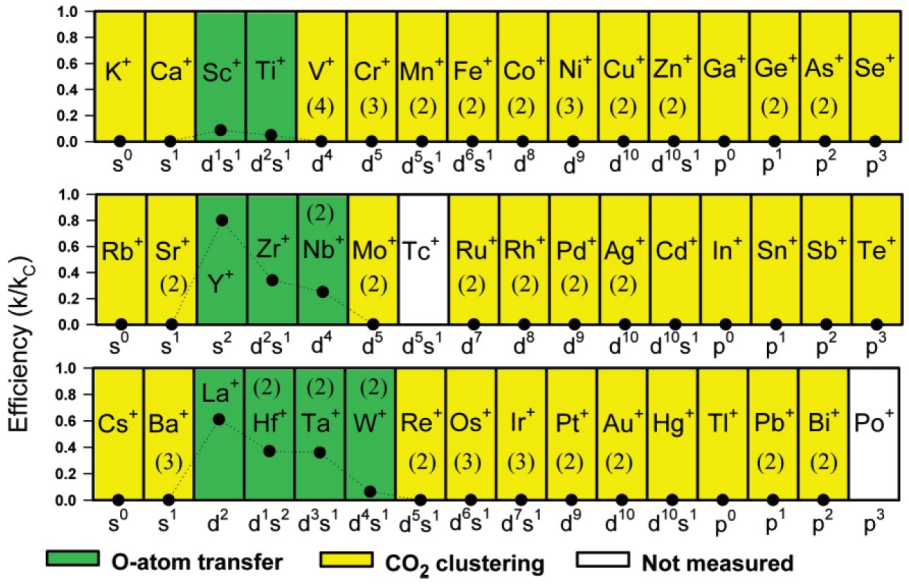

Figure 1.4: Reactions of metal ions with CO_2 studied by Bohme *et al.* Efficiency refers to the ratio between the reaction rate constant and the calculated collision rate. For Sc^+, Ti^+, Y^+, Zr^+, Nb^+, La^+, Hf^+, Ta^+ and W^+ O-atom transfer is the dominant reaction pathway. Reproduced from Koyanagi, G. K.; Bohme, D. K. *J. Phys. Chem. A*, 2006, 110, 1232–1241 with permission of American Chemical Society.[70]

Bohme *et al.* also measured equilibrium constants for the clustering process. This allowed the Gibbs free energy of CO_2 complexation to each metal ion to be determined. All processes are found to be exothermic and the extent of exothermicity depends on the strength of the attraction between the metal ion and CO_2 (for the instances where $D_0(M^+–CO_2)$ are known[72]). Nine early transition-metal ions are found to abstract an O atom from a CO_2 molecule as the dominant reaction pathway: Sc^+, Ti^+, Y^+, Zr^+, Nb^+, La^+, Hf^+, Ta^+ and W^+. In all nine instances, the O-atom abstraction is thermodynamically driven; all nine cations have oxygen affinities larger than CO. Hence, the O-atom transfer is an exothermic process for all observed reactions. Of these reactions, only O-abstraction by Hf^+ is spin-allowed. However, the crossings

between potential energy surfaces remain unknown and continue to present an experimental and theoretical challenge.

The Bohme group extended their survey to lanthanide ions, where they observed O-atom abstraction when reacting CO_2 with La^+, Ce^+, Pr^+, Nd^+, Gd^+, Tb^+ and Lu^+.[73] Futhermore, Bohme *et al.* also studied reactions of atomic metal cations with various other ligands including N_2O, CS_2, NH_3, O_3 and CH_4.[74–77] In the case of N_2O, both O-atom and N-atom transfer reactions were observed for Ti^+, Zr^+, Nb^+, Ta^+, Os^+ and Ce^+. For most metals O-transfer from N_2O occurs much more readily than from CO_2, which is consistent with the relatively lower oxygen affinity of N_2O. Again, O-atom abstraction is thermodynamically driven. Similarly, in reactions with CH_4, As^+, Nb^+, Ta^+, W^+, Os^+, Ir^+ and Pt^+ showed propensity for H_2 abstraction.[77]

1.6 Collision-Induced Dissociation

Armentrout and co-workers have extensively investigated the properties, particularly the binding energies, of not only naked metal clusters but also various metal-ligand complexes *via* collision-induced dissociation (CID).[78] In their guided ion beam (GIB) experimental setup,[79,80] Armentrout *et al.* form metal ions in a sputtering source before introducing the ligand of interest seeded within the carrier gas. The complexes are subsequently extracted from the source region, mass selected in a magnetic sector momentum analyser and decelerated to the required translational energy. An octopole ion guide transports the ions through a gas cell containing the collision gas (typically Ar or Xe). If the kinetic energy of the ions is sufficient, the collision with a rare gas atom will cause dissociation of the complex. The reactants and products are finally detected with a quadrupole mass analyser. In their study of water-solvated first row transition metal ions ($M^+(H_2O)_n$, $n = 1$ – 4 with M = Ti to Cu), Armentrout *et al.* observed a step change in disso-

ciations energies between $n = 2$ and $n = 3$ for all ions except Mn^+.[81] The dissociation energies for $M^+(H_2O)_{1-2}$ are considerably larger than the energies for the $n = 3$ and $n = 4$ counterparts. This can be interpreted as the first two ligands occupying the inner solvation sphere to which other water molecules bind more weakly.

Armentrout *et al.* also studied CID of various Mg^+ complexes with CO, CO_2, ammonia, methane, methanol and benzene.[82] For Mg^+CO_2 a binding energy of 0.60 eV was measured. In the case of using Xe as the collision gas, ligand exchange reactions for $Mg^+(CO_2)$ and $Mg^+(CO_2)_2$ were observed with the Xe atom replacing the CO_2 ligand. However, the exchange reaction is endothermic, which signifies that CO_2 is bound more strongly than Xe.

1.7 Rotational Spectroscopy of Metal Species

The recent development of the chirped-pulse Fourier transform microwave (CP-FTMW) spectrometer[83] presents a major advancement in performing high-resolution broadband rotational spectroscopy. CP-FTMW allows a measurement of broadband rotational spectra across a large (typically 12 GHz) bandwidth within a single experiment. Cooke and co-workers equipped the CP-FTMW spectrometer with a laser ablation source, which enabled them to record rotational spectra of metal-containing complexes such as AgCl, AuCl and SnO.[84,85]

The ablation of a metal rod in the presence of an expansion gas (typically argon) seeded with a low percentage of the ligand of interest allowed the Walker group to produce various weakly-interacting metal-ligand complexes.[86] Using CP-FTMW spectroscopy, Walker *et al.* were able to determine the geometry of the $C_2H_2 \cdots AgCCH$ complex.[87] The authors observed transitions in the rotational spectrum of $C_2H_2 \cdots AgCCH$ consistent with a planar T-shaped C_{2v} asymmetric top geometry, where the C_2H_2 ligand lies perpendicular to the axis defined by AgCCH. A minor deviation from a linear C_2H_2 is ob-

served upon coordination to AgCCH. The CCH angle in the ethyne ligand is increased to 186° from 180° upon complexation to AgCCH. This geometry is also confirmed by high-level coupled cluster singles and doubles (triples) (CCSD(T)) *ab initio* calculations. CP-FTMW spectrometry can thus serve as an effective tool for structure determination of small metal-containing complexes. Other systems studied by the Walker group include the carbenes of platinum and palladium PtC_3 and PdC_3, H_2S complexation with MI (for M = Cu, Ag, Au,) and $NH_3 \cdots CuCl$.[88–90] In CP-FTMW experiments involving metal containing species produced *via* laser ablation, the identity of the parent species can often only be identified in the post-analysis stage. A similar experimental challenge is encountered with the velocity map imaging studies involving metal containing species as discussed in Chapter 7.

1.8 Motivation to Study CO_2

Today less than 1% of global CO_2 emissions are reused.[91] The scientific community has been extensively investigating potential pathways for CO_2 activation and its eventual re-use in industrial processes.[92–94] CO_2 can serve as a suitable one-carbon (C1) feedstock material in synthetic chemistry. Alas, the activation of CO_2 is particularly challenging due to its thermodynamic stability and chemical inertness, and it ostensibly requires highly reactive reagents in extreme reaction environments.[95,96] Nevertheless, viable synthetic routes exist for the industrial use of CO_2 as a building block in the production of urea, salicylic acid and various polymers.[91] In most catalytic transformations a metal-based catalyst is employed,[96] thus it is of paramount importance to understand the nature of the interaction between CO_2 and the metal (ion).

Of a particular interest is recycling CO_2 into a useful fuel source using the Sabatier reaction:[97]

$$CO_2 + 4H_2 \rightarrow CH_4 + 2H_2O. \tag{1.5}$$

A nickel based catalyst was originally used in a Sabatier reactor, although other metals have been explored also, with a Ru-based catalyst being most-widely used nowadays.[97–100] A Sabatier reactor is currently used on board the International Space Station (ISS).[101] CO_2 produced by astronauts and H_2 formed *via* water hydrolysis (together with O_2) are then recycled in a Sabatier reactor to form water in a near-closed loop (methane as a by-product is discarded). Additionally, the Sabatier reaction is currently being considered to be used for fuel (CH_4) production needed for Mars exploration - CO_2 could be harvested from Mars' atmosphere.[102]

Another key catalytic hydrogenation of CO_2 involves the reverse-gas shift reaction:[91]

$$CO_2 + 2H_2 \rightleftharpoons CO + 2H_2O. \tag{1.6}$$

CO can then react further in a Fisher-Tropsch reactor to form various alkanes:[103]

$$nCO + (2n + 1)H_2 \rightarrow C_nH_{2n+2} + nH_2O. \tag{1.7}$$

1.9 Thesis Overview

This thesis is laid out in the following manner: Chapter 1 already introduced techniques that can be applied to the study of gas-phase metal containing species. Chapter 2 provides a description of both experimental and theoretical methods used in this work. Applications of these methods in recent literature are further discussed and briefly reviewed. In Chapter 3 characterisation of a purpose built laser ablation source and IR-REPD spectrometer designed for the study of metal ion-molecule complexes is presented. Chapter 4 presents the first substantive study involving the new IR-REPD spectrometer described in Chapter 3. Experimental data in conjunction with

quantum chemistry calculations allows for the structures and binding motifs in $M^+(CO_2)_n$ (where M = Co, Rh, Ir) to be explored. Chapter 5 extends the domain to transition metal oxides with the study of $TaO_2^+(CO_2)_n$ and $NbO_2^+(CO_2)_n$ complexes. In Chapter 6 a VMI study of VO is presented. This study is performed using a modified Oxford VMI spectrometer equipped with a laser ablation cluster source. A refined value for the dissociation energy of VO is obtained. The thesis concludes with Chapter 7 (Summary and Outlook) to highlight the main outcomes of this work and to present a scope for future studies.

Chapter 2

Methods

2.1 Molecular Vibrations

A quantum mechanical interpretation of vibrational motion in a molecule can be approximated by a simple harmonic oscillator (SHO), which obeys the classical Hooke's law given by:

$$F = -kx, \tag{2.1}$$

where F is the force, k is the force constant and x is the displacement from the equilibrium position. The potential energy, V, of such oscillator is then expressed as:

$$V = \frac{1}{2}kx^2. \tag{2.2}$$

Here x can be written as $r - r_e$ by defining r_e as the equilibrium distance:

$$V = \frac{1}{2}k\Big(r - r_e\Big)^2. \tag{2.3}$$

Thus the quantum mechanical Hamiltonian for a SHO is:

$$H = -\frac{\hbar^2}{2\mu}\Big(\frac{d^2}{dx^2}\Big) + \frac{1}{2}kx^2, \tag{2.4}$$

where μ is the reduced mass of the atoms, and $\hbar$ is the Planck's constant (h) divided by 2π.

This gives the following expression for the Schrödinger equation for a SHO:

$$\Big[-\frac{\hbar^2}{2\mu}\Big(\frac{d^2}{dx^2}\Big) + \frac{1}{2}kx^2\Big]\psi_v = E_v\psi_v, \tag{2.5}$$

where ψ_v is the vibrational wavefunction. Within the simple harmonic approximation, the solutions to the Schrödinger equation and the vibrational energy levels in a diatomic molecule, E_v, are given by:

$$E_v = h\nu\Big(v + \frac{1}{2}\Big), \tag{2.6}$$

in which v is the vibrational quantum number which can take any positive integer value, or zero.[104] The classical vibration frequency, ν, is equal to

$$\nu = \frac{1}{2\pi}\sqrt{\frac{k}{\mu}}. \tag{2.7}$$

By convention, the energy eigenvalues of a SHO are often expressed as vibrational term values, G_v:

$$G_v = w_e\Big(v + \frac{1}{2}\Big) \tag{2.8}$$

where w_e is the classical vibration wavenumber that can be related to the classical vibration frequency *via* $w_e = \frac{\nu}{\widetilde{c}}$ (by convention, w_e is expressed in cm^{-1} thus, $\widetilde{c}$, the speed of light expressed in cm/s). A plot of SHO with quantised energy levels is depicted in Figure 2.1 a). Allowed vibrational transitions for a SHO follow the selection rule $\Delta v = \pm 1$ (which follows from

the perfect parabolic nature of the potential), and the separation between vibrational energy levels is simply w_e. The SHO is a reasonable approximation of molecular systems only at the bottom of the potential well where deviations from the equilibrium geometry are negligible.

Real molecules, however, do not behave like a harmonic oscillator. Even at large internuclear separations, the SHO permits no dissociation. This is at odds with real molecules that dissociate at large internuclear separation with a finite dissociation energy, D_e. Real systems also show anharmonic behaviour as the restoring force of a bond is reduced as the bond is being stretched.

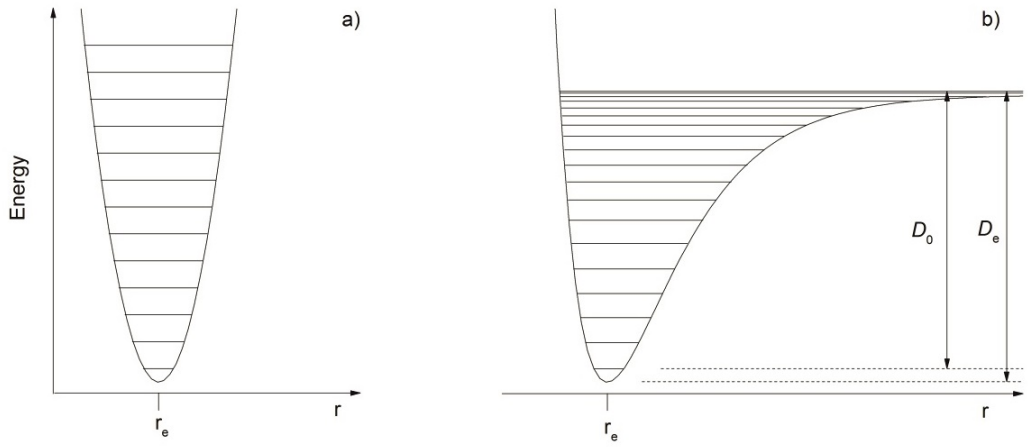

Figure 2.1: a) Simple harmonic oscillator with illustrated equally spaced energy levels; b) Morse potential with energy levels converging towards the dissociation continuum.

A better representation of molecular vibrations would thus be an anharmonic potential such as Morse potential:[105]

$$V(r) = D_e[1 - \exp(-ax)]^2 \tag{2.9}$$

where a is:

$$a = \sqrt{\frac{2\pi^2 c\mu}{D_e h}} w_e. \tag{2.10}$$

In order to account for the anharmonicity, the vibrational term values, G_v, are adapted to a power series in $(v + \frac{1}{2})$:

$$G_v = w_e\Big(v + \frac{1}{2}\Big) - w_e x_e\Big(v + \frac{1}{2}\Big)^2 + w_e y_e\Big(v + \frac{1}{2}\Big)^3 + ... \tag{2.11}$$

where w_e, is the classical vibrational wavenumber, x_e and y_e are first and second order anharmonic constants, respectively. The form of the Morse potential is shown in Figure 2.1 b). The vibrational energy levels are no longer equally spaced but gradually converge towards the dissociation limit with only a finite number of vibrational levels supported by an individual potential. At large internuclear distances the potential flattens out, *i.e.*, the force constant becomes zero, which allows for dissociation of a molecule. At small r (*i.e.*, the inner turning point), internuclear repulsion causes the potential energy to increase at a faster rate than for a SHO. The reduced symmetry of the anharmonic potential relaxes the vibrational selection rules which become $\Delta v = \pm 1, \pm 2, \pm 3...$ However, the intensities of the overtones are typically weaker than the intensity of the fundamental transition.

In polyatomic molecules, oscillations of individual nuclei need to be considered. The potential energy of a polyatomic molecule is a function of displacements of the atoms from their respective equilibrium positions. Therefore, the potential energy of a polyatomic molecule can be expanded as a Taylor series:[106]

$$V = V_0 + \sum_i \Big(\frac{\partial V}{\partial x_i}\Big)_0 x_i + \frac{1}{2}\sum_{i,j} \Big(\frac{\partial^2 V}{\partial x_i x_j}\Big)_0 x_i x_j + ... \tag{2.12}$$

Given that the potential energy at the equilibrium position must be a minimum, the first derivatives $\sum_i \left(\frac{\partial V}{\partial x_i}\right)_0$ are all zero. For small displacements the

higher order derivatives (> 2) can be neglected. Considering only changes relative to the ground state potential energy, we can set $V_0 = 0$. The expression for the potential energy can thus be simplified to:

$$V = \frac{1}{2} \sum_{i,j} k_{ij} x_i x_j \tag{2.13}$$

where $k_{ij} = \left(\frac{\partial^2 V}{\partial x_i x_j} \right)_0$, also known as the generalised force constant.

A polyatomic molecule of N atoms has $3N$ - 6 normal vibrational modes ($3N$ - 5 for a linear molecule). In addition to the selection rules identified above for a diatomic, for a transition between vibrational states to be infrared-active (allowed) it also needs to lead to a change in the dipole moment.[107]

The electric dipole transition moment, R, involving a transition between a lower vibrational state described by the wavefunction, ψ''_v, and upper vibration state given by ψ'_v, is expressed as:

$$R^{v'v''} = \int \psi'^*_v \mu \psi''_v d\tau_v \tag{2.14}$$

where μ is the electric dipole moment operator.

For a transition between non-degenerate states the transition moment, $R^{v'v''}$, is non-zero when:

$$\Gamma(\psi'_v) \otimes \Gamma(\mu) \otimes \Gamma(\psi''_v) = A \tag{2.15}$$

where Γ indicates an irreducible representation and A marks a totally symmetric irreducible representation of any point group.

It can be shown that the electric dipole moment operator, μ, is further divided along the three cartesian axes into μ_x, μ_y and μ_z.[104] Hence:

$$\Gamma(\psi'_v) \otimes \Gamma(\mu_x) \otimes \Gamma(\psi''_v) = A \tag{2.16}$$

$$\Gamma(\psi'_v) \otimes \Gamma(\mu_y) \otimes \Gamma(\psi''_v) = A \tag{2.17}$$

$$\Gamma(\psi'_v) \otimes \Gamma(\mu_z) \otimes \Gamma(\psi''_v) = A \tag{2.18}$$

At least one of the above operations must be true for the $R^{v'v''}$ to be non-zero and for a vibrational transition to be IR-allowed.

2.2 Experimental Measurements of Absorption

Absorption spectra are traditionally measured directly through use of direct absorption spectroscopy. These methods generally rely upon measurement of the extinction coefficient (ε) for a particular species. According to the Beer-Lambert law, the change in the initial intensity of light (I_0) due to absorption is given by:

$$I = I_0 e^{-\varepsilon c l}, \tag{2.19}$$

where I is the light intensity after a passage through the sample, c is the concentration of the sample, and l is the path travelled by the light through the sample. For gas-phase species the extinction coefficient and the sample concentration can be thought of as the absorption cross-section and the number density, respectively.

Direct absorption techniques suffer from two experimental challenges when applied to the study of gas-phase clusters. Firstly, laser ablation sources typically produce a wide distribution of cluster species entrained in a molecular beam. It is, therefore, not possible to record an absorption spectrum

for a particular cluster size as any change in the light intensity would be a convolution of the signals from a myriad of different species.

Secondly, the number densities of clusters produced by means of laser ablation are, in general, too low to be probed by direct absorption. A standard Smalley/Bondybey cluster source might produce *ca.* 10^6 of a particular cluster per laser shot, which is an equivalent of around 2×10^{-18} mole. Assuming that the clusters are confined to a cube with a side length of 1 cm, this would amount to a concentration of 2×10^{-15} mole/L. Typical molar extinction coefficients found for small gold nanoparticles are on the order of 4×10^6 L mol^{-1} cm^{-1}.[108] So a 1 cm pathlength of clusters will yield an absorbance of only *ca.* 8×10^{-9}, well beyond typical sensitivities using pulsed sources.

Cavity ring-down spectroscopy, which dramatically increased the absorption path length, has been successfully applied in the visible region to strongly absorbing systems such as AuSi and WO.[109,110] Other, non-Beer-Lambert type spectroscopic techniques such as laser-induced fluorescence (LIF) experiments have been performed on few systems, including Cu_2 or Ag–Ar.[111,112]

Both of these two techniques, however, fall short when applied to larger gas-phase complexes. By contrast, mass spectrometric detection offers the very highest sensitivity possible, with single ion detection efficiencies close to 1. Hence, the most successful gas-phase spectroscopic methods involve the use of "action spectroscopy", which can overcome the problems associated with traditional spectroscopic methods.

2.3 Time-of-Flight Mass Spectrometry

Mass spectrometry is a particularly advantageous tool for studying gas phase clusters as it allows detection of a single ion with essentially unit efficiency at high repetition rates. In a typical time-of-flight mass spectrometer electric (and/or magnetic) fields are applied to separate the ions by virtue of different

mass-to-charge ratios. In the simplest setup by Cameron and Eggers in 1948, ions were accelerated using a constant electric field and a field-free drift region.[113] Ions of different mass-to-charge ratios can thus be differentiated by their arrival time at the detector (also known as the ion time-of-flight).

This design suffers from a particular experimental problem. Namely, ions reach the acceleration region in a finite volume rather than as a point-in-space. The ions will thus have a variety different initial positions and consequently a range of velocities in the drift regions. This leads to different arrival times at the detector and consequently a reduction in the mass resolution.

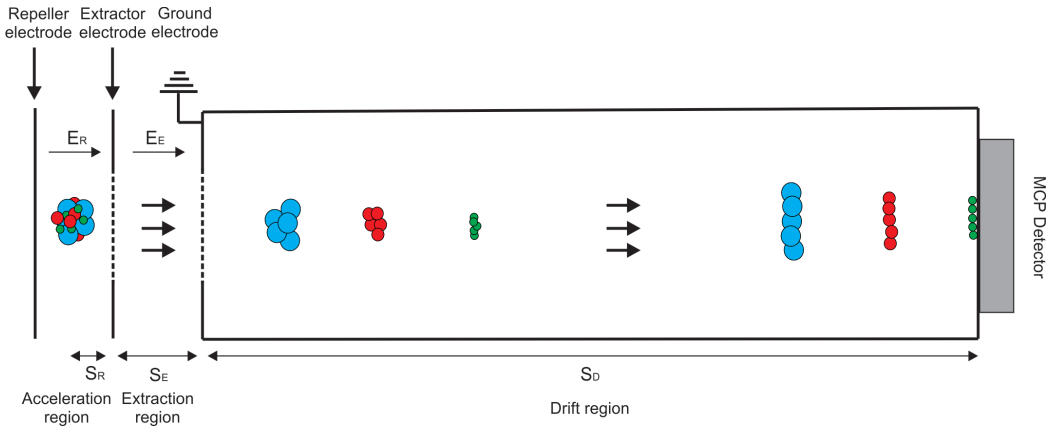

Figure 2.2: Schematic of the classical Wiley-McLaren time-of-flight mass spectrometer used to detect cluster ions. Three ions of different masses are shown to be temporally separated in the drift region by mass (assuming the same electric charge) E_R and E_E represent electric fields in the acceleration and extraction region, respectively. Likewise, s_R, s_E and s_D represent the path travelled by ions in the acceleration, extraction and drift region, respectively.

To address this issue, a mass-spectrometer with two electric fields followed by a field-free drift region was developed by Wiley and McLaren in 1955.[114] Separate electric fields provided by repeller and extractor electrodes (Figure 2.2) compensate for the initial spread in the ion spatial distribution and yield a narrow space focus at the detector.

In a Wiley-Mclaren time-of-flight mass spectrometer, ions with a given charge

q are accelerated within the electric field (E) and traverse the distance s. As the ions are accelerated through a potential difference, their potential energy (U) is converted into kinetic energy (KE):

$$U = qEs \iff KE. \tag{2.20}$$

Hence the kinetic energy after the extraction region equals to:

$$KE = \frac{1}{2}mv^2 = q(E_R s_R + E_E s_E). \tag{2.21}$$

From here, the velocity can be expressed as:

$$v = \sqrt{\frac{2q(E_R s_R + E_E s_E)}{m}} \tag{2.22}$$

Species with lower mass will thus achieve higher velocities and will traverse the drift region faster. The ion time-of-flight will be dependant on their m/q ratio. Wiley and McLaren have shown that the total time-of-flight is proportional to the square root of the mass-to-charge ratio for particular ion.[114] The lighter ions (of the same charge) will reach the detector faster than heavier counterparts. In practice, a "time zero" term, t_0 needs to be introduced to account for any inaccuracies in experimental time-of-flight measurements. The mass can be calculated by performing a fit to the follow expression:

$$t = k\sqrt{\frac{m}{q}} + t_0 \tag{2.23}$$

where k and t_0 are constants. This can be now used to convert time-of-flight scale into mass-to-charge scale. All mass spectra displayed in this thesis have been converted from their time-of-flight to the mass-to-charge scale using equation 2.23. Mass spectrometry is an essential detection technique for the complexes studied in this work.

2.4 IR-REPD Spectroscopy

2.4.1 Overview of IR-REPD Spectroscopy

Number densities of gas-phase metal-ion complexes produced using the laser ablation source described in Section 1.2 are generally too low to be probed by traditional direct absorption spectroscopic techniques. Instead, experiments are performed using infrared resonance-enhanced photodissociation (IR-REPD) spectroscopy – a variant of action spectroscopy – which utilises the sensitivity of mass spectrometric detection for spectroscopic measurements. Successful IR-REPD experiments were first demonstrated in 1985 by Y.T. Lee and co-workers who studied the protonated hydrogen clusters H_5^+, H_7^+ and H_9^+.[115]

The principles of IR-REPD are the following: a molecule is irradiated with tunable IR light while the ion signal is monitored as a function of wavelength. An IR photon can only be absorbed if the energy of the incident photon matches an allowed transition of an IR-active mode of the molecule. The absorption of a photon induces vibrational motion within the molecule the energy of which can then be internally redistributed around the complex *via* Intramolecular Vibrational Redistribution (IVR) eventually causing fragmentation of the M^+–Ligand bond and ejection of the ligand:

$$M^+(L)_n(v=0) + h\nu \rightarrow M^+(L)_n(v^*) \xrightarrow{IVR} M^+(L)_{n-1} + L. \tag{2.24}$$

2.4.2 Inert Messenger Techniques

Binding energies of metal-ion ligand complexes are often greater than photon energies in the infrared region. For instance, typical binding energies of a CO_2 molecule to transition metal cations are on the order of *ca.* 0.5 – 1 eV.[72] Hence, absorption of multiple photons would be required to photodissociate

such a strongly-bound system. As illustrated in Figure 2.3, absorption of multiple resonant photons is particularly challenging as a consequence of anharmonic throttling.

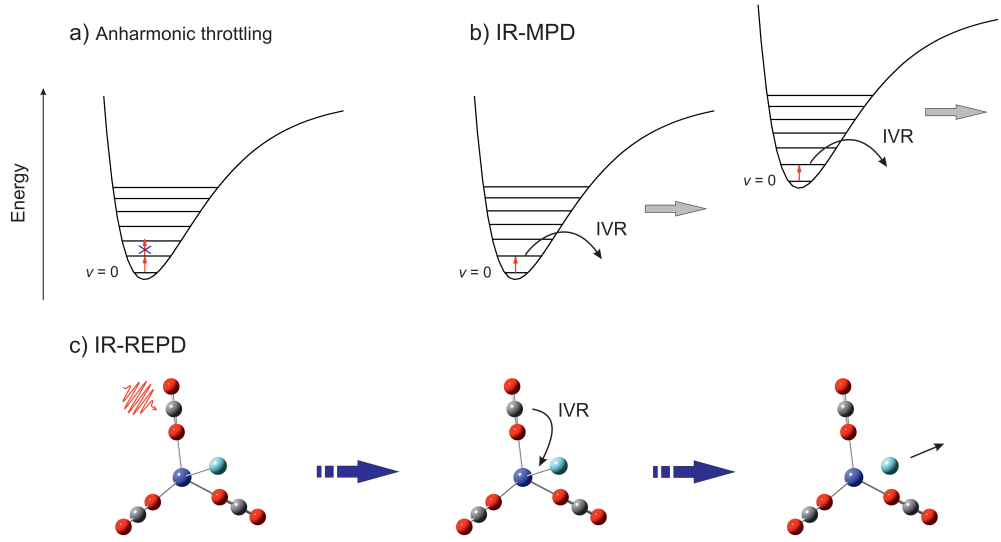

Figure 2.3: Schematics illustrating: a) Anharmonic throttling of multiple resonant photon absorption presented on a Morse potential; b) The IR-MPD process. The IVR, which rapidly redistributes the energy over available vibrational degrees of freedom in the molecule, is completed before absorption of subsequent photons. This ensures that the molecule is always in the ground vibrational state and multiple-photons can thus be absorbed, while the total energy of the complex is increased; c) The inert messenger technique demonstrated on hypothetical $M^+(CO_2)_3$–RG, where an absorption of a photon leads to the fission of the weak M^+–RG bond.

One method to circumvent this problem involves a co-adsorption of a weakly-bound rare gas (RG) atom onto the complex, also known as "rare gas tagging".[116–120] Also referred to as the inert messenger technique, this method has gained importance in recent years in elucidating the structures of strongly-bound ionic cluster complexes.[121–123] Following the absorption of a photon, the complex undergoes rapid IVR which leads to the fragmentation of the M^+–RG bond. The loss of the rare-gas atom then serves as a signature of photon absorption and IR-REPD spectra can be recorded by monitoring the depletion in the intensity of rare gas tagged cluster (Figure 2.4).

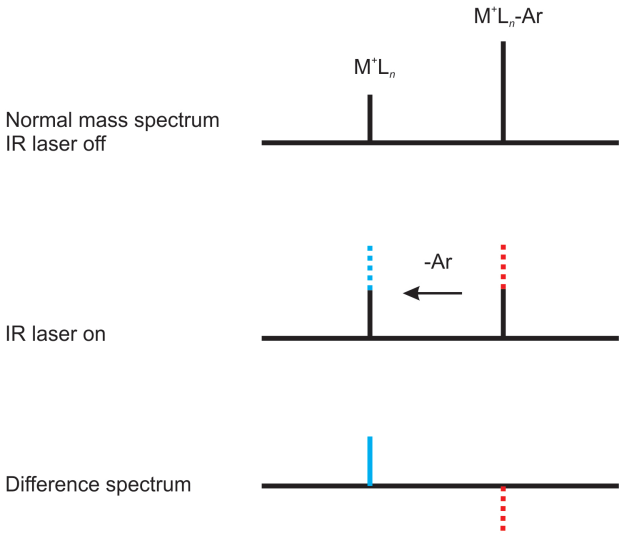

Figure 2.4: Schematic illustrating the IR-REPD process on a hypothetical M^+L_n–Ar complex. Following the absorption of an infrared photon, the M^+L_n–Ar complex dissociates by a loss of an argon atom, which leads to a decrease in the intensity of the parent M^+L_n–Ar ion and an increase in the M^+L_n daughter channel.

Co-adsorption of rare gas atoms, such as argon, is sufficiently weak as to cause little perturbation to the structure of the target complex. The addition of an inert messenger tag also results in a higher density of states, which facilitates the IVR and in-turn increases the fragmentation yield. Argon is a commonly used IR tag although recent years have seen successful demonstration of experiments involved using He-tagged complexes, which however

require cryogenic cooling.[124–126] Use of other rare gas atoms, such as Kr and Xe, has been reported in the literature particularly in the studies of larger metal clusters.[127,128] In some instances, H_2 molecule was also employed as the inert tag.[129,130]

Efficient photofragmentation of larger metal clusters can also be achieved with infrared multiple photon dissociation (IR-MPD), as illustrated in Figure 2.3 and further elaborated in Section 2.6.

2.5 Previous IR-REPD Experiments

The first IR-REPD experiments on metal-ion containing complexes were performed by Lisy and co-workers, who focused on several alkali metal-ion complexes with numerous ligands, including H_2O and CH_3OH.[131–134] Subsequently, Duncan *et al.* have performed extensive studies of metal-ion containing complexes involving H_2O, CO, CO_2, C_2H_2, acetone, benzene and N_2 ligands.[135–149] The Ohashi group focused on the study of NH_3 complexation with Mg^+, Al^+, V^+, Cu^+ and Ag^+[150–154] and NO coordination to Fe^+, Cu^+, Ag^+, Au^+ has been studied by Zhou *et al.*[155–157]

The next two subsections present a short overview of recent experiments involving CO, H_2 and CH_4 ligands. A more detailed discussion regarding CO_2 can be found in Chapter 3 and Chapter 4. Several excellent and extensive reviews by Walker, Walters and Duncan, Duncan, Lisy, Bieske *et al.* on the topic of IR-REPD provide a detailed discussion of complexes involving various ligands.[158–163]

2.5.1 $M^+(CO)_n$ Complexes

Metal-carbonyl complexes are known to form particularly stable complexes in the condensed phase with a total of 18 valence electrons.[164,165] Tradition-

ally, bonding in metal carbonyls is described by the Dewar-Chatt-Duncanson model involving electrostatic effects, σ-donation and π-backdonation into the antibonding π orbitals of CO which consequently weakens, or activates, the C–O bond (and lowers its stretching frequency).[166–168]

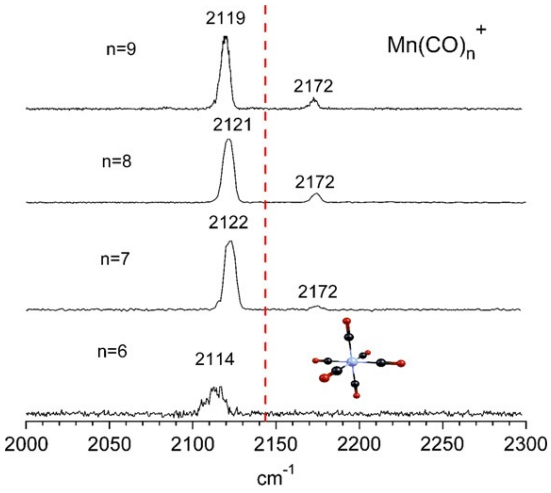

Figure 2.5: IR-REPD spectra for $Mn^+(CO)_n$ complexes. The strong feature at *ca.* 2120 cm^{-1} corresponds to stable $n = 6$ core of octahedral geometry (inset). The weaker feature at *ca.* 2170 cm^{-1} is due to CO ligands that are not directly attached to the Mn^+ ion. The dashed line marks the frequency of isolated CO at 2143 cm^{-1}. Reprinted from Ricks, A. M.; Reed, Z. E.; Duncan, M. A. *J. Mol. Spectrosc.*, 2011, 266, 63-74 with permission from Elsevier Inc.[142]

In their study of $Mn^+(CO)_n$ complexes Duncan and co-workers observed the formation of stable $Mn^+(CO)_6$ octahedral core (Figure 2.5),[142,169] isolectronic with a well-characterised neutral $Cr(CO)_6$ complex.[170] A noticeable decrease in the fragmentation yield for $n = 6$ was observed and an onset of the feature corresponding to CO ligands in the outer coordination shell is observed for $n \geq 7$ (Figure 2.5). CO ligands in the outer coordination sphere, in the absence of any covalent interaction, experience a modest blue-shift from the free CO frequency. $Mn^+(CO)_6$ also represents a common termination point in the fragmentation of larger complexes. Similarly, $Co^+(CO)_5$ forms a stable trigonal bipyramidal 18 electron complex isoelectronic to neutral $Fe(CO)_5$.[171]

CO coordination with other metals studied by the Duncan group include the following ions: Si^+, Sc^+, Y^+, V^+, Ti^+, Zr^+, Hf^+, Pt^+, Rh^+, Cu^+ and Au^+.[172–179] The red-shift of the comparable carbonyls is greater in neutral complexes as the positive charge on the metal contracts the electrons and thus limits their scope for potential π backdonation.[142]

Zhou and co-workers have studied CO coordination with metal dimers such as Ti_2^+, Ni_2^+, Fe_2^+ and Fe_2^-[180–183] and this has recently been extended to bimetallic dimers $CuFe^-$, $FeZn^+$ and $CoZn^+$.[184,185]

2.5.2 M^+H_2 Complexes

The Bieske group has dedicated considerable attention to the study of M^+H_2 complexes. These complexes are particularly interesting from the perspective of developing suitable hydrogen storage materials (zeolites, metal–organic frameworks) in which molecular hydrogen is attached to oxidised metal atoms /ions.[186–188] Bieske *et al.* recorded high-resolution rovibrational spectra by exciting the H–H stretch (using a narrow bandwidth IR-OPO/OPA laser), which leads to redistribution of energy along the weak M^+–H_2 bond and its rupture. A change in the M^+ intensity is then monitored as a function of wavelength. The authors thus managed to determine experimentally rotational constants, vibrational frequencies and bond distances for several M^+H_2 complexes including Li^+, Na^+, Mg^+, Al^+, Cr^+, Mn^+, Zn^+ and Ag^+ as the central ion.[189–196] Due to unfavourable mass resonances, complexes of Cr^+ and Zn^+ were studied with D_2 instead.

While an isolated H_2 molecule is IR-inactive, electric dipole vector in M^+H_2 complexes lies along the intermolecular bond, allowing M^+H_2 complexes to be probed by IR spectroscopy.[163] Bonding between metal cations and H_2 is dominated by the charge quadrupole and charge induced dipole induction interactions, which together favour a T-shaped configuration of C_{2v} symmetry with an intact H_2. At shorter intermolecular distances Pauli repulsion also

comes into play. Repulsive interactions of the metal with the σ_g orbital of H_2 pushes electron density away from the H–H bond reducing its vibrational frequency.[162] A modest red-shift in the H–H stretching frequency is observed for the systems studied by Bieske *et al.*, ranging from *ca.* 67 cm^{-1} for Na^+ to 406 cm^{-1} for Ag^+ (*cf.* H_2 binding energies of 860 and 3395 cm^{-1} to Na^+ and Ag^+, respectively).[190,196]

The studies by the Bieske group are, however, limited to the cases in which the vibrational frequency of the H_2 (*ca.* 4161 cm^{-1})[197] exceeds the binding energy of molecular hydrogen to a metal ion. Accurate measurements of binding energies of H_2 to M^+ thus still present an experimental challenge.

2.5.3 $M^+(CH_4)_n$ Complexes

$M^+(CH_4)_n$ complexes were first explored by the Bieske group who investigated the complexes of $Al^+(CH_4)_n$ and $Mn^+(CH_4)_n$.[198,199] Later, Lisy *et al.* studied $Li^+(CH_4)_n$ complexes.[200] Recently, Metz and co-workers have explored extensively methane complexation with Fe^+_{1-4}, Co^+, Ni^+, Cu^+ and Ag^+.[201–205] The IR-REPD spectra were typically recorded in the vicinity of the symmetric (ν_1 (a_1) = 2917 cm^{-1}) and asymmetric (ν_3 (t_2) = 3019 cm^{-1}) stretches of methane. The η^2 coordination of methane to a metal ion is preferred, as predicted by the calculations of Maitre and Bauschlicher using second order Møller-Plesset perturbation theory (MP2).[206] The complexes of methane with metallic cations are expected to exhibit some degree of covalency, which favours the η^2 coordination. Donation of σ electrons occurs from the valance d_{z^2} orbitals of the metal cation to the empty antibonding orbitals of methane.[205] Additionally, backdonation of electrons occurs from the t_2 bonding orbitals of methane ligand to the empty valence s orbitals of the metal ions (if the valance s orbital is unoccupied). Thus, the C–H bond can be considerably weakened, resulting in a large red–shift in the vibrational frequency of ligated CH_4.

For $Cu^+(CH_4)$ and $Ag^+(CH_4)$, redshifts of *ca.* 328 and 179 cm^{-1} from the symmetric stretch in free CH_4 are observed, respectively. The smaller redshift for the Ag^+ based complex is attributed to an increase in the ionic radius, which favours larger metal cation – ligand distances and hence leads to weaker interaction. IR-REPD spectra typically exhibit several vibrational bands with frequencies of C–H bonds closest to the metal ion being the most perturbed. For Cu^+ and Ag^+, with d^{10} configurations, the complexes tend to form symmetric complexes. For $n = 2$ complexes, both metal ions form a staggered configuration of CH_4 ligands attached on opposite sides as identified by DFT calculations. Likewise, the $n = 3$ complexes are all of trigonal planar structure. For $n = 4$ complexes, both trigonal pyramidal and tetrahedral structures are believed to contribute to the IR-REPD spectrum for $Cu^+(CH_4)_4$, whereas only tetrahedral structure is for $Ag^+(CH_4)_4$. However, the structures begin to differ from $n = 5$. The Metz group observed the formation of larger Cu^+ complexes by adding additional ligands to $Cu^+(CH_4)_4$, as inferred from larger bond distances in the case the fifth and sixth ligand. Conversely, ligands around Ag^+ are further apart, which reduces the ligand–ligand repulsion and leads to trigonal bipyramidal and octahedral structures for $Ag^+(CH_4)_5$ and $Ag^+(CH_4)_6$, respectively.

2.6 Infrared Multiple Photon Dissociation

As briefly mentioned in Section 2.4.2 and depicted in Figure 2.3, IR-MPD, involves fast absorption of multiple photons to drive the molecule above the dissociation limit. In an IR-MPD process, the cluster undergoes initial resonant absorption of a photon followed by efficient IVR process which redistributes the energy within the species. This allows the cluster to be in the ground vibrational state prior to the absorption of the subsequent photons. However, IR-MPD typically requires very high laser intensities such as that provided by *e.g.* free electron lasers, and efficient IVR into many available

vibrational degrees of freedom found in large metallic clusters. The "rare gas tagging" technique, in conjunction with IR-MPD, can also be used to elucidate structures of small metal clusters.[127,207] Here, the loss of rare gas atoms indicates photon absorption associated with metal-metal vibrations. IR-MPD experiments are not featured in this thesis, however, it is important to appreciate the scope of IR-MPD in the study of metal containing complexes.

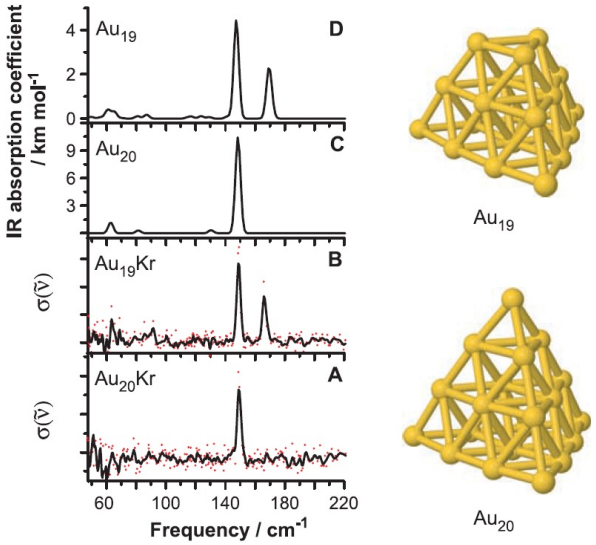

Figure 2.6: A and B are IR-MPD spectra of neutral $Au_{19}Kr$ and $Au_{20}Kr$, respectively, recorded in the channel corresponding to the loss of a Kr atom. C and D are the respectrive simulated spectra for the two structures calculated using the density functional theory. Reprinted from Gruene, P; Rayner, D. M.; Redlich, B.; van der Meer, A. F. G.; Lyon. J. T.; Meijer, G.; Fielicke, A. *Science*, 2008, 321, 674–676 with permission from AAAS.[127]

As showcased in Figure 2.6 displaying the work by Fielicke *et al.*[127] on structures of small gold clusters, IR-MPD spectroscopy, complemented by simulated vibrational spectra, is a powerful technique for discerning the geometries of small metal clusters. The highly-symmetric Au_{20} exhibits only a single strong feature in the IR-MPD spectrum corresponding to the triple degenerate t_2 vibration as also confirmed by theory. As a single atom is removed, Au_{19} forms a trigonal pyramidal structure with lower C_{3v} symmetry

with two bands observed in the spectrum; these features result from the e and a_1 vibrational modes. The IR-MPD spectra for both Au_{20} and Au_{19} were collected *via* the inert messenger technique, while scanning the free electron laser. The absorption of the photon only occurs if the photon energy is at resonance with the frequencies of the Au-Au bonds, which yields the strong IR bands in the IR-MPD spectrum.

Furthermore, IR-MPD experiments can also serve as an effective tool to characterise different ligand binding motifs. A study of CO adsorption on group 10 cationic clusters by Fielicke, Meijer and co-workers revealed dramatic differences in binding motifs across the group.[208] Nickel and platinum cationic cluster bind CO exclusively in the atop (μ_1) configuration, whereas palladium clusters show a propensity for binding in the atop (μ_1), bridge (μ_2) and hollow-site (μ_3) configuration. Three different binding configurations in the case of palladium clusters are attributed to the presence of isomers in the molecular beam. One can rationalise the preference for the atop configuration due to lack of free neighbouring atoms in small metal clusters.[209] Interestingly, the relativistic effects make Pt–CO bond relatively stronger than the Pd–CO bond and thus only the atop configuration is observed for platinum cluster.[208]

2.7 Resonance-Enhanced Multiphoton Ionisation

Resonance-enhanced multiphoton ionisation (REMPI) is now a well established laser-based technique for ionisation of isolated gas-phase molecules.[210] The technique relies on the fact that the likelihood of a multiphoton absorption is significantly increased in the event of resonant absorption to a real excited state of a neutral molecule at the energy of one or more absorbed photons. An outline of a typical one-color 2 + 1 REMPI scheme is depicted in Figure 2.7. As illustrated in Figure 2.7, the ionisation probability for

photons with frequency ν_2 is significantly larger than the likelihood for the non-resonant photons with the corresponding frequencies of ν_1 and ν_3. Here, the hypothetical excited electronic state is resonant at the 2 photon level for the photons with the frequency ν_2. The excited electronic state of a molecule is required to be sufficiently long-lived (tens of picoseconds) to allow for an absorption of an additional photon, which can push the molecule to the ionisation continuum. Any successful ionisation event can be detected by mass spectrometry and thus, the formation of ions serves as a signature of resonant absorption of photons.

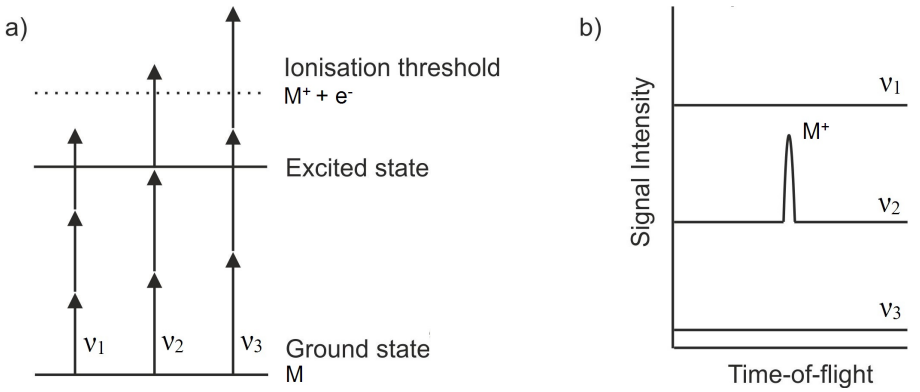

Figure 2.7: a) A typical one-colour 2 + 1 REMPI scheme for species M resonant at the frequency of ν_2. Two photons with frequency ν_2 will drive the species to an intermediate excited state from where it can ionised by an absorption of an additional photon. A mismatch in the energy between the excited state and the photons of frequency ν_1 and ν_3 leads to low ionisation likelihoods in these two instances. b) Mock time-of-flight spectra expected for REMPI scheme displayed in a). Only photons with frequency ν_2 will ionise the species and produce M^+ ions that can detected using mass spectrometry.

Often irradiation of a molecule leads to a fragmentation of the parent species. In this instance, techniques such as velocity map imaging (VMI) can be employed to study the photofragmentation dynamics. REMPI detection schemes are particularly suitable for the VMI experiments as they allow for quantum state-selective ionisation of products following photofragmentation.

2.8 Velocity Map Imaging

2.8.1 Overview of Ion Imaging Techniques

Following laser-induced photolysis, the resulting fragments will begin to expand as a series of concentric spheres, commonly referred to as Newton spheres. The radius of each sphere will be determined by the recoil velocity of the fragments. Chandler and Houston were first to demonstrate that the fragments resulting from a photolysis can be accelerated in a time-of-flight mass spectrometer and detected by a time and position sensitive detector.[211] In their study of the photodissociation of CH_3I at 266 nm, Chandler and Houston observed the cleavage of the C–I bond, and formation of a CH_3 radical and an I atom. The iodine atom can be formed in its ground electronic state ($^2P_{3/2}$) state or in the first excited state ($^2P_{1/2}$), which is 7603 cm^{-1} higher in energy. Single-colour 2 + 1 REMPI with the laser fixed at 330 nm is used to state selectively ionise the CH_3 fragment from the ground vibrational state ($v" = 0$). Chandler and Houston detected an image of CH_3^+ with two concentric rings corresponding to the production of iodine co-fragment in two different spin-orbit states.

The experimental set-up used by Chandler and Houston employed a repeller plate followed by a pair of grounded grid plates in the ion extraction region. Although the grids ensured a uniform field, their presence proved to be a major disadvantage: the grids disturb the ion trajectories and lower the ion transmission. The presence of the grids requires rather high ion densities that consequently lead to ion–ion repulsion (space charge) and image blurring.

A major advancement in achieving higher resolution arrived in 1997 with the development of Velocity Map Imaging (VMI) by Eppink and Parker.[212] By removing the grids, Eppink and Parker designed an “open” ion lens consisting of repeller, extractor and ground electrodes (Figure 2.8). The electric field in the extraction region is now inhomogeneous, however, as the curvature of

the field can be shaped by tweaking the voltage ratio between the repeller and extractor plates. By applying suitable voltage ratios, the ions can be space focused onto the position sensitive detector located at the end of the flight tube. Space focus ensures that all ions with different origin positions but the same velocity component in the plane of the detector are mapped to the same point on the 2D position-sensitive detector. Thus the Newton spheres corresponding to a particular pair of photodissociation fragments are superimposed on the 2D detector.

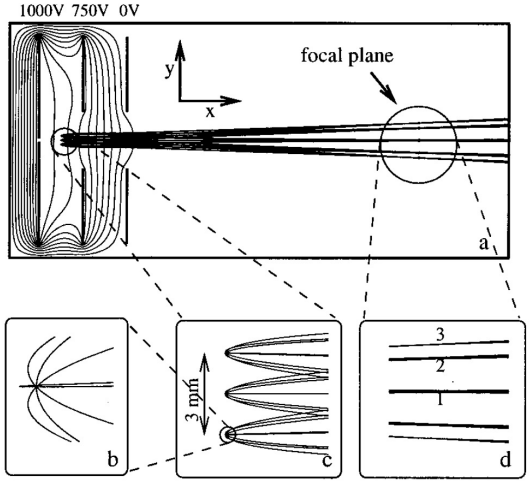

Figure 2.8: Schematic of the ion lens design used by Eppink and Parker in their original VMI experimental set-up, as shown in (a). In the zoomed in portion (c), ions are generated at three different source positions. These ions are ejected at eight different angles separated by 45° as shown in b). At the focal plane shown in d), the ions become space focused. Reprinted from Eppink, A. T. J. B.; Parker, D. H. *Rev. Sci. Instrum.* 1997, 68, 3477-3484, with permission of AIP Publishing.[212]

2.8.2 Inversion Techniques for Image Reconstruction

Multiple inversion techniques allow the recovery of the 3D Newton sphere from the crushed 2D image. For systems with cylindrical symmetry, an analytical reconstruction can be performed using the inverse Able transform. However, direct Able transform performs particularly poorly in low signal-to-

noise conditions. Several forward convolution methods have been developed that can invert the image at low computational costs. For instance, BASEX method involves fitting the observed image to a basis set expansion of well-behaved Gaussian functions.[213] Its polar extension, pBASEX, uses polar basis sets functions that include the Legendre polynomials used for fitting of the angular distributions of photofragments.[214] A widely applicable technique is also the onion-peeling method, which involves a subsequent removal of contributions from the outermost layers of the recorded image.[215] Its polar adaptation, polar onion-peeling (POP),[216] invokes the basis set functions of pBASEX. An alternative approach – which involves no image inversion – is incorporated in the recently developed maximum entropy velocity image reconstruction methods.[217] Here, the algorithm finds the forward Abel transform to generate a simulated ideal image and then with reliance on Bayesian statistics finds the representation, which would best represent the data set in the consideration. An example of a POP reconstructed image following the photodissociation of VO at 431.10 nm, with the corresponding kinetic energy release (KER) spectrum, is shown is Figure 2.9.

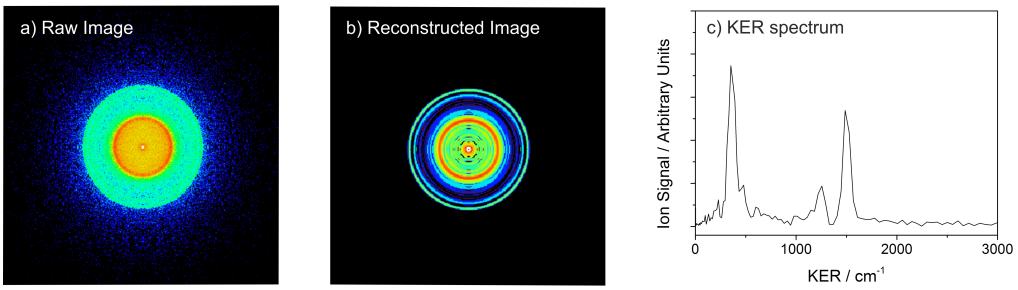

Figure 2.9: a) Raw image recorded in the V^+ channel following the photodissociation of VO (and subsequent ionisation of V) at 431.10 nm. The corresponding POP reconstructed image is presented in b) and the resulting KER spectrum of the vanadium is shown in c). Each ring in the image corresponds to a peak in the KER spectrum, with each peaks representing the formation of photofragments in different quantum states.

Although not a reconstruction method *per se*, the central slice of the image can be obtained through the use of "slicing" techniques. For instance, direct

current (DC) slicing involves an additional stepped series of electrodes in order to prolong the ion time-of-flight and also, stretching out the Newton sphere.[218,219] The central slice of the ion Newton sphere is then selectively detected with a narrow detector time-gate of sub 20 ns. Slicing discards a significant fraction of potential experimental data and as such, might not be suitable for species formed by laser ablation which are typically produced in low number densities.

2.8.3 Applications of Velocity Map Imaging

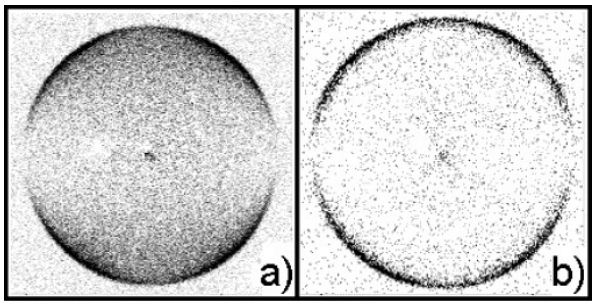

Figure 2.10: Velocity map images of O(^{1}D) following the photodissociation of O_2 at 157 nm. The crushed image of the Newton sphere is shown in a). The corresponding DC-sliced image is shown in b). Polarisation of the laser is parallel to the detector. Both images are highly anisotropic as anticipated from the $B^3\Sigma_u^-$ – $X^3\Sigma_g^-$ parallel transition. Adopted from Chestakov, D. A; Wu, S.-M.; We, G.; Parker, D. H; Eppink, A. T. J. B.; Kitsopoulos, T. N. *J. Phys. Chem. A*, 2004, *108*, 8100-8105 with permission from American Chemical Society.[220]

Since its inception, VMI has been applied to a variety of chemical systems. The Parker group has extensively studied laser photolysis of molecular oxygen.[221] Excitation of molecular oxygen at 157 nm from its ground vibronic state (X $^3\Sigma_g^-$, $v = 0$) to the B $^3\Sigma_u^-$ state yields oxygen atoms in the ground (^{3}P) and first excited (^{1}D) state. The O(^{1}D) fragment can then be state-selectively ionised using 2 + 1 REMPI scheme at 205.3 nm.[220] Both crushed

and DC sliced velocity map images recorded in the O(^{1}D) fragment channel display a significant degree of anisotropy, as observed in Figure 2.10. Highly anisotropic images are also consistent with the $B^3\Sigma_u^- - X^3\Sigma_g^-$ parallel transition at 157 nm.

In addition to photofragment imaging, VMI studies have also been extended to photoelectron imaging. Wang and co-workers have employed VMI in their study of mass-selected metal-containing anions.[222] They have obtained photodetachment spectra for various species including Au_2^-, AuC_2^-, Au_4^-, B_{11}^- and B_{12}^-.[223–226] Similarly, Neumark *et al.* recorded photodetachment spectra of metal oxides including Fe_3O^-, Co_3O^-, $Ti_2O_4^-$ and $Zr_2O_4^-$.[227,228] In their experimental approach, the Neumark group cryogenically-cools the anions in a radiofrequency trap prior to near-threshold photodetachment, which allows them to record high-resolution photoelectron velocity map images.[229] Groups of Fielding and Verlet applied photoelectron VMI to the study of chromophore anions encountered in biological systems such as the green fluorescence protein, and the photoactive yellow protein.[230–232] A time-dependent study of the green fluorescence protein chromophore also gave an insight into the excited state relaxation pathways following photon absorption.[233]

In a crossed-molecular beam set-up, VMI can also be used to study reactive collisions. Liu *et al.* have extensively studied the reactive scattering of the F atom with CD_4 forming both DF and the CD_3 radical.[234–236] The scattering at a centre-of-mass collision energy of 0.233 eV revealed several well resolved rings in the image of the detected CD_3 product in $v = 0$; these rings correspond to vibrational excitation of the DF co-product. Additionally, strong angular dependence is observed for different product channels. CD_3 produced with DF in $v' = 4$ shows a strong propensity for forward scattering, while the distribution with DF in $v' = 2$ is strongly shifted towards backwards scattering.

Similarly, Brouard *et al.* have extensively explored inelastic collisions of NO with various rare gas atoms.[237–244] NO is an open-shell molecule, which ren-

ders it available for full quantum state selection with a hexapole state-selector that exploits the Stark effect.[245] The inelastic scattering of a state selected NO($X^2\Pi_{1/2}$, $v = 0$, $j = 0.5$, f) with Ar produces rotationally excited NO.[237] Any increase in the rotational excitation of the NO collision partner (higher j' values) will result in lower fragment velocity of NO and consequently in smaller velocity map images. The authors observed a significant dependence of the differential cross section on the total NO parity conservation in the collisions, which reveals the presence of quantum mechanical interference as also confirmed by full quantum mechanical calculations. A static electric field further allows orientation of a state-selected NO molecule with either the 'N' or 'O' end directed towards the incoming Ar molecular beam.[243] Each of these two orientations leads to noticeable differences in the differential cross sections of these inelastic collisions. These experiments demonstrate a significant degree of initial quantum state control one can employ in conjunction with a crossed-molecular beam VMI setup.

Recent developments of fast sensors used for ion detection, such as PImMS, opened the potential for multi-mass detection.[246] Brouard, Stapelfeldt and co-workers used a PImMS sensor for covariance imaging to determine the structure of a pre-aligned molecule (3,5-dibromo-3,5-difluoro-4-cyanobiphenyl) that underwent a femtosecond laser-induced Coulomb explosion.[247]

2.9 Computational Methods

2.9.1 Overview of Density Functional Theory

Density functional theory (DFT) allows for accurate quantum chemical calculations to be performed at comparably low computational cost. Hohenberg and Kohn have shown that the properties of an n-electron system are completely determined by the ground state electron density, $\rho(\mathrm{r})$.[248] The breakthrough for DFT arrived with the formulation of Kohn and Sham,[249] which

allows the ground state electron density to be described as:

$$\rho(r) = \sum_{i=1}^{N} |\varphi_i(r)|^2 \tag{2.25}$$

where φ_i(r) is the electron wavefunction of the ith electron. The total energy of a system can thus be described as a sum of different energy contributions:

$$E[\rho(r)] = T[\rho(r)] + E_{ne}[\rho(r)] + J[\rho(r)] + E_{xc}[\rho(r)] \tag{2.26}$$

where $T[\rho(r)]$ is the kinetic energy of the non-interacting electrons, $E_{ne}[\rho(r)]$ is the Coulombic attraction between nuclei and electrons, $J[\rho(r)]$ is the Coulombic electron-electron term, and $E_{xc}[\rho(r)]$ is the exchange-correlation energy, which contains contributions from the non-classical repulsion between electrons, and the correction to the kinetic energy due to presence of other electrons.[250]

Equation 2.17 can be expressed in bra-ket notation as:[251]

$$\begin{aligned} E[\rho(r)] = & -\frac{1}{2}\sum_{i}^{N}\left\langle\varphi_i|\nabla_i^2|\varphi_i\right\rangle - \sum_{i}^{N}\left\langle\varphi_i|\sum_{k}^{m}\frac{Z_k}{|r_i - r_k|}|\varphi_i\right\rangle \\ & + \sum_{i}^{N}\left\langle\varphi_i|\frac{1}{2}\int\frac{\rho(r)\rho(r')}{|r-r'|}drdr'|\varphi_i\right\rangle + E_{XC}[\rho(r)] \end{aligned} \tag{2.27}$$

By applying the variational principle, Kohn and Sham showed that this yields the following Kohn-Sham equation:[249]

$$\left(-\frac{1}{2}\nabla_i^2 - \sum_{k}^{m}\frac{Z_k}{|r_i - r_k|} + \int\frac{\rho(r')}{|r-r'|}dr' + V_{XC}\right)\varphi_i = \varepsilon_i\varphi_i \tag{2.28}$$

By combining the potential terms, this can be written succinctly as:

$$\left(-\frac{1}{2}\nabla_i^2 + V_{KS}\right)\varphi_i = \varepsilon_i\varphi_i \tag{2.29}$$

where

$$V_{KS} = -\sum_{k}^{m} \frac{Z_k}{|r_i - r_k|} + \int \frac{\rho(r')}{|r - r'|} dr' + V_{XC} \tag{2.30}$$

with $V_{XC} = \delta E_{XC}/\delta\rho(r)$. Hence, the exchange-correlation potential, V_{XC}, is the functional derivative of E_{XC} with respect to the density. One can consider the electrons as independent particles moving in the effective potential, V_{KS}.[252] In principle, DFT is exact, the only part of the formulation with no explicit expression is the exchange-correlation energy, E_{XC}. Kohn and Sham initially proposed the local density approximation (LDA), which locally treats the density as a uniform electron gas. A more practical extension, local spin-density approximation (LSDA), allows for a separate treatment of different electron spins. Nevertheless, LSDA still significantly overestimates the electron correlation in molecules.

A significant improvement arrived with the generalised gradient approximation (GGA), which includes the (higher) derivatives of the electron density.[251,252] In real chemical systems, the electron density is not uniform, hence the correlation will not only depend on the local density, but also on the degree of the local variation of the electron density, which makes the gradient of the density particularly important. One of the first GGA exchange functionals was developed by Becke (B),[253] which was followed by another popular functional PBE of Perdew, Burke and Ernzerhof.[254] Commonly used examples of correlation functional include Perdew's P86[255] or Perdew and Wang's PW91.[256] Additionally, some correlation functionals such as LYP (Lee, Yang and Parr),[257] also include semi-empirical parameters.

Functionals can be further improved by combining the exchange part of the density functional with a proportion of Hartree-Fock exchange to produce what one is refered to as a hybrid functional. One of the most widely-used hybrid functionals B3LYP,[258] combines the LYP correlation functional with Becke's exchange functional, while also replacing a part of GGA ex-

change with 20% Hartree-Fock exchange. B3LYP is particularly popular with calculations involving organic molecules but the LYP correlation functional performs somewhat poorly with metals.[259] Computations performed in this work rely heavily on the B3P86 functional, which combined the correlation functional of Perdew (P86)[255] with the exchange functional of Becke (B)[253] coupled with 20% Hartree-Fock exchange. Buhl *et al.* benchmarked the performance of several functionals for the third-row transition-metal complexes against available experimental data and deduced the best performance for B3P86 (joint top with hybrid PBE).[260]

2.10 Summary

This chapter described experimental and computation techniques employed throughout this work: IR-REPD spectroscopy, DFT and VMI. IR-REPD spectroscopy and DFT methods are core techniques used in the study of metal ion-molecule complexes, as presented in Chapters 3, 4 and 5. Furthermore, a VMI study of VO is presented in Chapter 6. This chapter also provided an overview of applications of these techniques in the recent literature.

Chapter 3

Development and Characterisation of an IR-REPD Spectrometer

A new IR-REPD spectrometer equipped with a laser ablation source is specifically constructed for the study of metal ion-molecule complexes. Metal ion complexes are generated in a purpose-built laser ablation source and photdissociation events are induced using the infrared radiation from IR-OPO/OPA laser. The laser ablation source is principally designed to promote the production of single metal ion complexes with weakly-bound ligands. Successful operation of the new ablation source is demonstrated by the formation of $Rh^+(CO_2)_n$, $VO_2^+(N_2O)_n$ and $Au^+(CH_4)_n$ complexes. The performance of the IR-REPD spectrometer is characterised with a well-known system of $V^+(CO_2)_n$.

3.1 Overview of the IR-REPD Experiment

The new IR-REPD experiment comprises of two differentially pumped chambers: (i) a source chamber, housing a laser ablation source, and (ii) a detection chamber containing a commercially-built Wiley-McLaren time-of-flight mass spectrometer (R. M Jordan Co., Inc). The two chambers are maintained at a background pressure of *ca.* 10^{-7} mbar using two turbomolecular pumps, which are in turn backed by two individual rotary pumps. A schematic of the experiment is depicted in Figure 2.1. During experimental runs, the pressures in the source chamber and detection chamber rise to *ca.* 1×10^{-4} mbar and 8×10^{-6} mbar, respectively.

Metal-containing species are generated in a laser ablation cluster source (*vide infra* - Section 3.3) and entrained in a pulse of buffer gas (typically Helium or Argon) seeded with a low percentage of the ligand of interest. Following the jet expansion, the molecular beam is skimmed (Beam Dynamics, 2 mm diameter) upon entering the detection chamber. In the detection region, ions are pulse-extracted orthogonally using a Wiley-McLaren stage into the drift region of a time-of-flight mass spectrometer operated in linear mode. The metal-containing ions are detected at the end of the drift region using a dual microchannel plate (MCP) detector. Charged clusters are formed nascently in the ablation process and can be probed directly with no need for an ionisation step. The repeller and extractor electrodes in the Wiley-McLaren stage are initially held at zero potential. When charged clusters reach the extraction region, a pulsed voltage is applied to the electrodes which consequently accelerates the ions towards the detector.

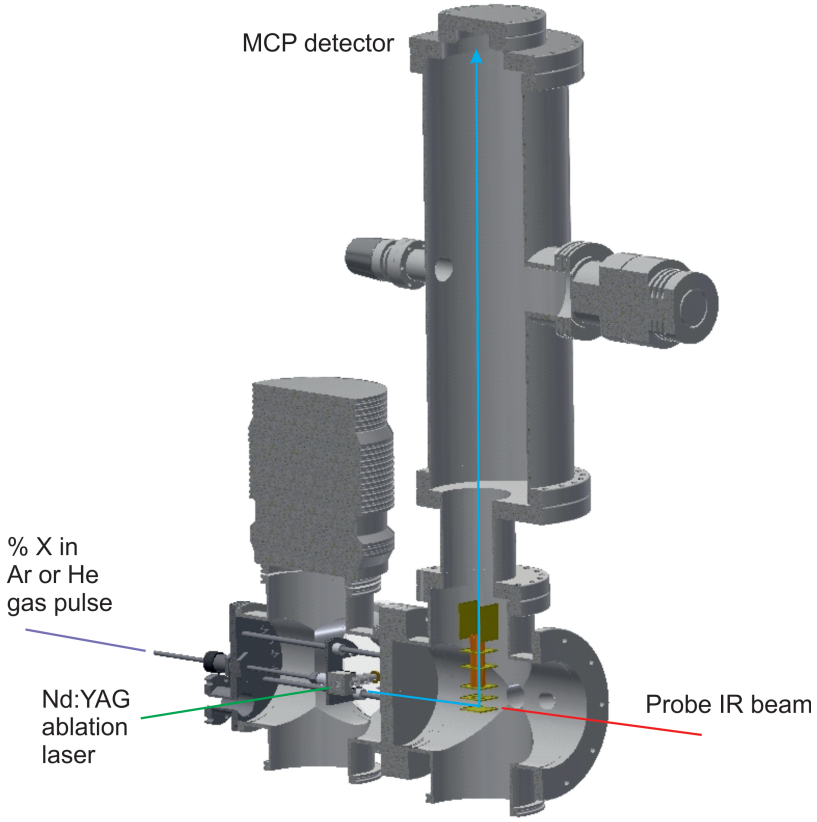

Figure 3.1: Schematic of the overall experimental setup used in the IR-REPD experiments.

The orthogonal extraction ensures that the velocity spread does not diminish the time-of-flight resolution as the velocity distributions of particles in a molecular beam are narrower perpendicular to the beam than along the axis of travel.[261] The ion beam can be enhanced by two deflector plates, which help to direct the ions towards the centre of the detector without changing their time-of-flight. The signal from the MCP detector is then displayed on an oscilloscope (LeCroy Wavesurfer 64X), which is connected to a personal computer (PC) through an ethernet cable.

IR photodissociation is induced using tunable IR light generated from an optical parametric oscillator/optical parametric amplifier (OPO/OPA) system (LaserVision). The OPO/OPA itself is pumped by *ca.* 700 mJ of the funda-

mental harmonic (1064 nm) of pulsed Nd:YAG laser (Continuum Powerlite II, 5–9 ns pulse width) laser operated at 10 Hz. The OPO stage comprises of two non-linear KTP ($KTiOPO_4$) crystals and the OPA stage comprises of four non-linear KTA ($KTiOAsO_4$) crystals.

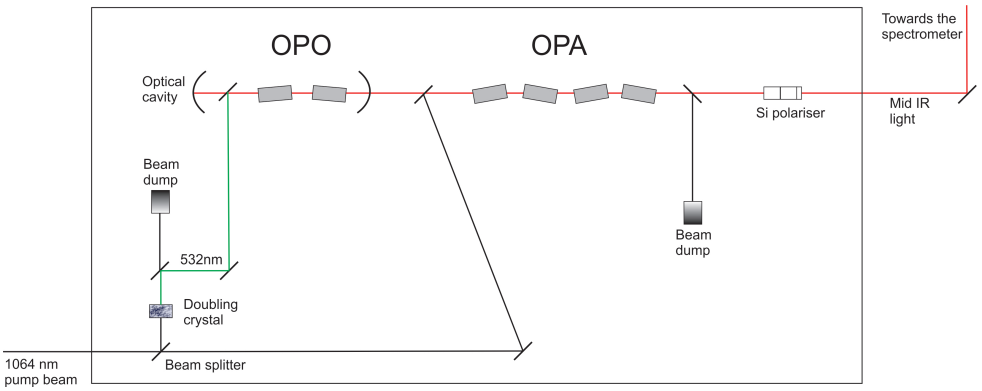

Figure 3.2: A simplified schematic depicting crucial elements of the IR-OPO/OPA system used for generation of tunable IR light.

In order to generate tunable IR light, the OPO stage is pumped with 532 nm light, which is generated by frequency doubling the first harmonic of the Nd:YAG pump laser using a BBO ($Ba(BO_2)_2$) crystal as illustrated in Figure 3.2. Thus generated light is then amplified by mixing the idler of the OPO stage and the 1064 nm fundamental *via* difference-frequency mixing. Following the OPA stage the silicon Brewster stack polariser isolate the idler from the combined idler/signal output. The IR-OPO/OPA system can reliably produce IR light between 710–885 nm (14085–11299 cm^{-1}) and 1.35–5 μm (7407–2000 cm^{-1}) with a bandwidth of *ca.* 3.7 cm^{-1}. IR light below 2000 cm^{-1} can be produced by externally adding $AgGaSe_2$ non-linear crystal, which can extend the tuning range of the IR-OPO/OPA to as low as 1000 cm^{-1}. The beam path between IR-OPO/OPA and the spectrometer is continuously purged with N_2 to prevent any atmospheric absorptions and depreciation in the IR light intensity.

Photodissociation of cluster ions is performed by overlapping loosely-focused

IR light and the cluster beam in a counterpropagating manner. IR-REPD spectra are recorded by capturing time-of-flight mass spectra alternately with and without IR light for few hundred laser shots at each laser wavelength. A new LabVIEW program, which oversees all data acquisition and scanning, has been written by the author of this thesis for the purpose of the IR-REPD experiment.

3.2 IR-OPO/OPA Calibration by Means of Photoacoustic Spectroscopy

Rough calibration of the IR-OPO/OPA can be achieved by manually translating each KTP crystal of the OPO stage to normal incidence, which will give a signal wavelength at 802.942 nm (12454.2 cm^{-1}) and idler wavelength at 1576.659 nm (6342.526 cm^{-1}). However, this method relies on visually observing reflections from the KTP crystal and can thus be rather imprecise. Instead, a photoacoustic spectrum of a molecule with a known IR absorption profile is recorded and used to ensure that IR-OPO/OPA laser is calibrated.

3.2.1 Principles of Photoacoustic Spectroscopy

The photoacoustic effect was discovered by Alexander Graham Bell in 1880.[262] The first photoacoustic spectra using laser radiation were recorded in the 1960s.[263] Following the absorption of an IR photon, a molecule can relax to the ground state either by the emission of light, or through a third-body collision. Loss of vibrational energy *via* collisions is typically the dominant pathway following infrared excitation since lifetimes of vibrationally excited levels are generally relatively long, around few milliseconds. Following a collision, the vibrational energy is converted into translation energy of the third-body. This increase in the translational energy then propagates through the gas medium as a sound wave.[104] The resulting sound wave can then be

recorded by a microphone. The sound wave will only be produced if the laser wavelength is at resonance with a (ro)vibrational transition of the molecule of interest. The observed sound wave then serves as an indicator of photon absorption.

3.2.2 Experimental Setup

The experimental setup for recording a photoacoustic spectra is shown in Figure 3.3.

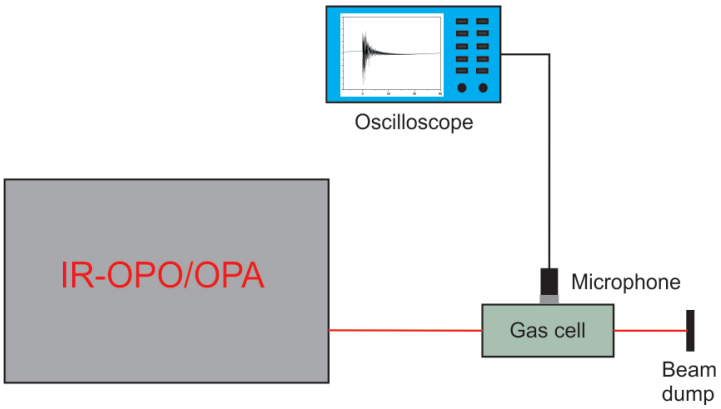

Figure 3.3: Schematic depicting experimental setup used to perform photoacoustic spectroscopy.

Photoacoustic spectra are recorded for CH_4 and CO as they both strongly absorb infrared radiation in the region of interest and their rovibrational spectra are well-characterised. The gas of interest is placed in the gas cell at a pressure of 1 bar. The gas cell is equipped with CaF windows to permit transmittance of IR light through the cell. A microphone, which records any sound waves resulting from IR resonance is mounted inside the gas cell (Figure 3.3). Photoacoustic spectra are recorded by scanning the wavelength of the IR-OPO/OPA laser and monitoring the sound wave intensity as a function of IR photon energy.

3.2.3 Photoacoustic Spectra of CH_4 and CO

Integrating over the intensity of the sound wave at different laser energies produces the photoacoustic spectrum of CH_4 shown in Figure 3.4. The centre of Q-branch is at 3019.36 cm^{-1}, which is in a good agreement with literature value of 3019 cm^{-1}.[264] The deviation from the literature value is also smaller than the laser linewidth of the IR-OPO/OPA laser, which is *ca.* 3.7 cm^{-1}. Additionally, P and R branches around this band are also observed, indicating that rovibrational resolution of this particular is achievable with the IR-OPO/OPA laser.

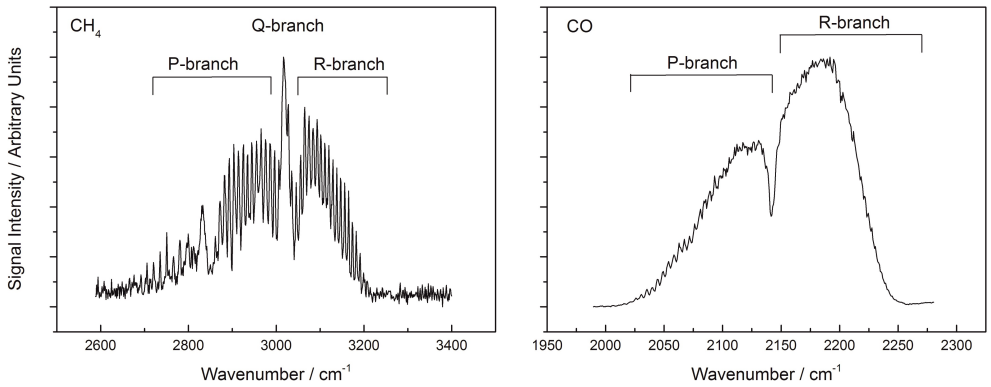

Figure 3.4: Left: Photoacoustic spectrum of CH_4 recorded in the range of asymmetric ν_3 stretch. Right: Photoacoustic spectrum of CO recorded in the range of C–O stretch.

The photoacoustic spectrum of CO monitored in the range of the C–O vibrational stretch is also shown in Figure 3.4 (right). The "dip" between the P and R branches occurs at *ca.* 2142 cm^{-1}, which is in good agreement with the literature value of 2143 cm^{-1}.[265] The recording of the photoacoustic spectra for CO and CH_4 gives confidence that IR-OPO/OPA laser is suitably calibrated.

3.3 Design of a New Laser Ablation Source

A Smalley/Bondybey-type ablation source[34,35] is employed to generate gas-phase metal ions. In a traditional Smalley/Bondybey source the cluster channel confines the metal vapour and backing gas, and consequently promotes three-body collisions needed for growth of larger metal clusters. However, the cluster channel is not necessary for producing complexes with single metal atoms/ions. Thus, a new laser ablation source (Figure 3.5) has been constructed with the aim of producing strong atomic ion signal. The development of the new source has been inspired by a metal rod-based source design by Duncan and co-workers.[36] The absence of a cluster channel minimises the generation of metal-metal clusters. The new source seeks to maximise the formation of metal complexes with weakly-bound ligands that require cold, free jet supersonic expansion. Cold expansion also facilitates the formation of argon tagged complexes necessary for the study of small metal ion – ligand complexes (see Section 3.5.4).

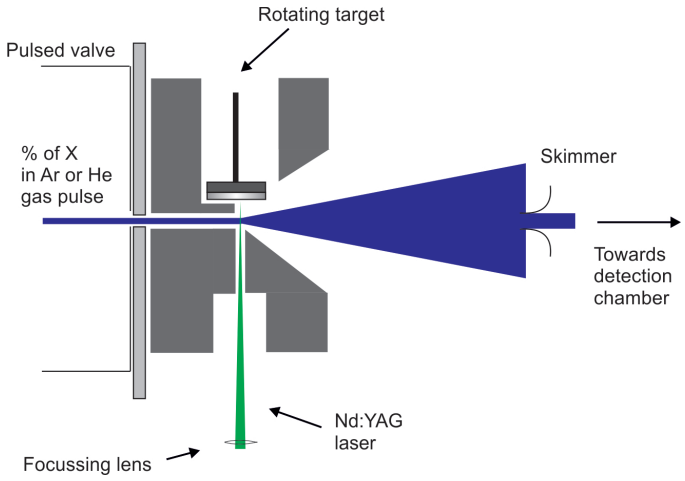

Figure 3.5: Schematic of the new cutaway laser ablation source.

A schematic of the new laser ablation source is shown in Figure 3.5. In our particular design, a rotating metal disc target is ablated by the focused 2nd harmonic (532 nm) output of a pulsed Nd:YAG laser (Continuum Minilite)

operated at 10 Hz with a typical pulse width of 5–7 ns and pulse energy of 5–10 mJ/pulse. The metal target is rotated and translated to ensure continuous ablation of a fresh surface. The metal vapour generated by the laser ablation is entrained in a pulse of an inert gas (predominantly helium or argon) seeded with a low fraction of the ligand of interest. A pulsed solenoid valve (Parker-Hannifin General valve, series 9) delivers the gas pulse from a typical backing pressure of 6–8 bar and a pulse duration of 500 μs. The molecular beam containing the metal-ligand complexes then passes through the skimmer as it enters the detection region housing a Wiley-McLaren time-of-flight mass spectrometer.

3.4 Laser Ablation Source Characterisation

3.4.1 Formation of $Rh^+(CO_2)_n$ Complexes

Figure 3.6 shows time-of-flight mass spectrum obtained by ablating rhodium target in the presence of a gas mix consisting of 7.5% of CO_2 in argon at a backing pressure of 6 bar. Expansions using different backing pressures were also investigated, however changes in backing pressures in the range 5–8 bar did not have a significant effect on production of clusters. A minimum pressure of 5 bar is normally required to achieve a stable cluster signal. As depicted in Figure 3.6, some very large CO_2-solvated species can be produced.

As observed in Figure 3.6, $Rh^+(CO_2)_n$ complexes are the dominant species produced. $RhO^+(CO_2)_n$ and $RhCO^+(CO_2)_n$ complexes are produced as well, albeit at lower intensities relatively to the $Rh^+(CO_2)_n$ ions. Nevertheless, clusters up to *ca.* $n = 15$ can be produced for $RhO^+(CO_2)_n$, and up to $n = 13$ for $RhCO^+(CO_2)_n$.

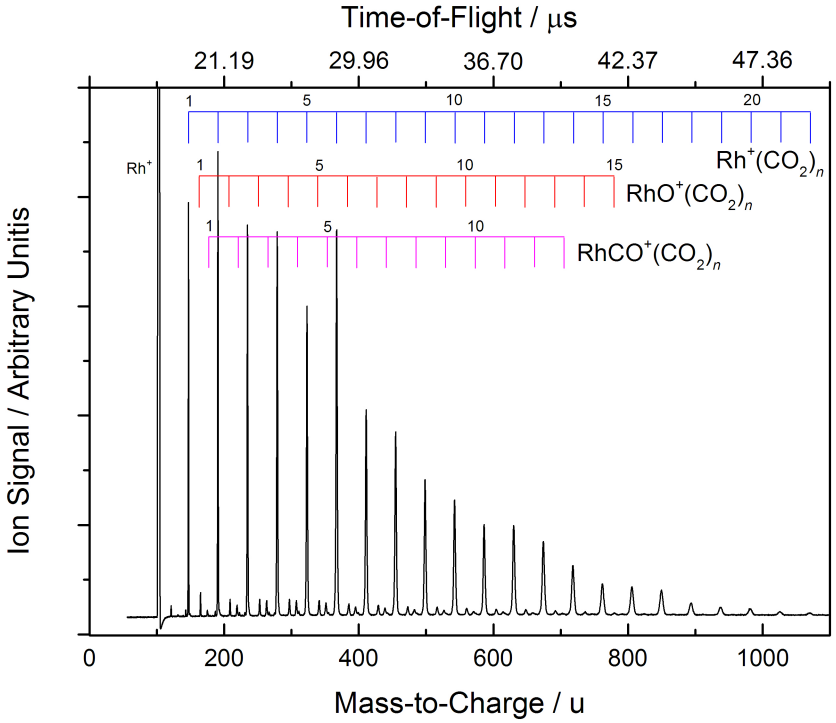

Figure 3.6: Typical time-of-flight mass spectrum formed upon ablation of rhodium target in the presence of an expansion of 7.5% CO_2 in argon at a backing pressure of 6 bar. In addition to $Rh^+(CO_2)_n$ complexes, $RhO^+(CO_2)_n$ and $RhCO^+(CO_2)_n$ complexes are also formed, albeit in lower abundances.

Both time-of-flight and mass-to-charge (m/z) scales are included in Figure 3.6. Raw experimental data is collected by measuring the arrival time of a particular ion. Conversion to the mass-to-charge scale can be made by assuming a square root relation between mass-to-charge and time-of-flight ($ToF \quad \alpha \quad \sqrt{m/z}$). Figure 3.7 shows the calibration plot for the mass spectrum presented in Figure 3.6. Using linear regression analysis, a linear fit can be obtained between time-of-flight and m/z. The R^2 value of 1.00 for the fit in Figure 3.7 gives strong confidence that the mass calibration is correct.

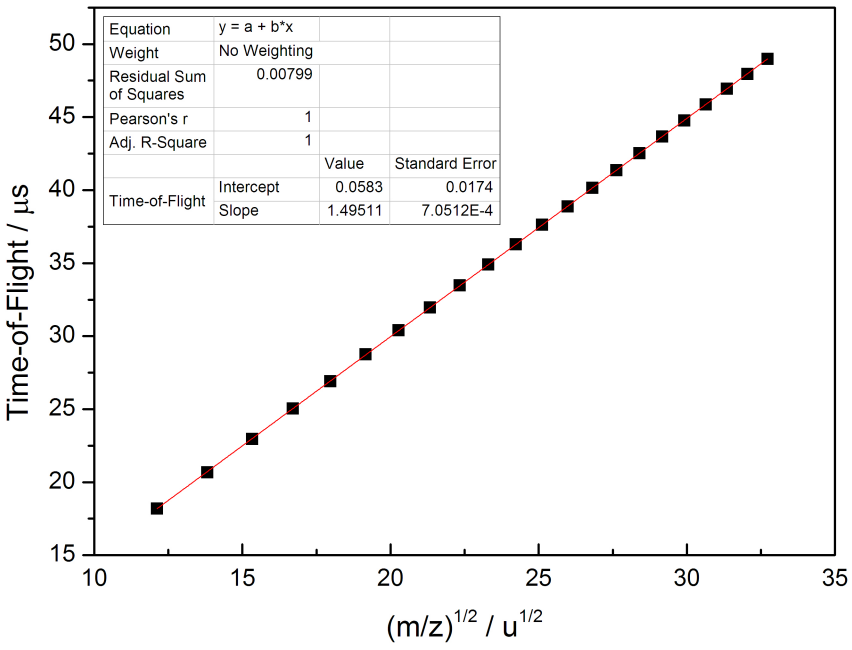

Figure 3.7: Conversion of time-of-flight scale to mass-to-charge (m/z) based on the assumption that time-of-flight is linearly proportional to the square root of mass-to-charge for a particular ion. In the calibration fit presented above, the linear regression gives an R^2 value of 1.

Effects of different percentages of CO_2 seeded in argon used for the expansion are illustrated in Figure 3.8. Higher concentrations of CO_2 lead to larger $Rh^+(CO_2)_n$ being produced. In the case of a 15% CO_2/Ar mix, complexes up to $n = 22$ can be produced. In contrast, 1% CO_2/Ar gas mix yields complexes of only up to $n = 11$. By reducing the amount of CO_2 in the gas mix, the distribution of complexes shifts towards forming smaller solvation spheres. For 15% expansion, $n = 6$ is the most abundant complex whereas $n = 2$ and $n = 1$ become the predominant species in the beam for the 7.5% and $\leq$ 2.5% expansions, respectively. For 15% and 7.5% expansions, significant amounts of $RhO^+(CO_2)_n$ and $RhCO^+(CO_2)_n$ complexes are produced, also.

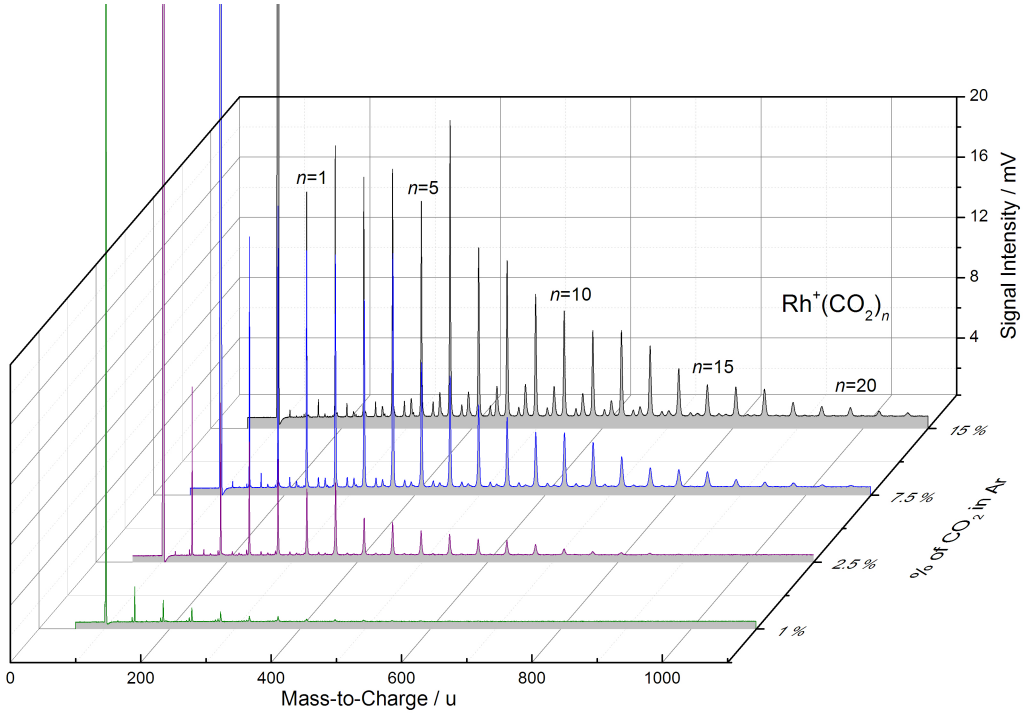

Figure 3.8: Time-of-flight mass spectra recorded at different concentrations of CO_2 seeded in argon at 6 bar backing pressure. For clarity, only $Rh^+(CO_2)_n$ are labelled, RhO^+- and $RhCO^+$-based complexes are also produced. Increasing the percentage of CO_2 in the backing gas mix increases the propensity for formation of larger $Rh^+(CO_2)_n$ complexes.

3.4.2 Formation of $VO_2^+(N_2O)_n$ Complexes

The new ablation source was designed to be flexible and adaptable, and can thus produce gas-phase complexes using a variety of different ligands. In the current setup, the ligand of interest needs to be efficiently seeded in argon or helium backing gas. Figure 3.9 depicts mass spectrum obtained by ablating vanadium target in the presence of a gas mix consisting of 2% N_2O in argon at a backing pressure of 6 bar. [i] As observed, the $VO_2^+(N_2O)_n$ complexes are

[i]This time-of-flight mass spectrum was collected together with M. J. Kent and some preliminary analysis appears in his part II thesis.[266]

the dominant species produced. At first sight, this is unexpected. However, upon measuring rate coefficients for reactions of atomic cations with N_2O Bohme and co-workers determined that the O-atom abstraction from N_2O is the dominant process over N_2O clustering.[267] In addition, Bohme *et al.* also observed formation of $VO_2^+(N_2O)_n$ complexes with VO_2^+ as the nucleation centre. This is in a stark contrast to using a gas mix of CO_2 in argon (*vide infra* - Section 3.5), where $V^+(CO_2)_n$ are the dominant clusters.

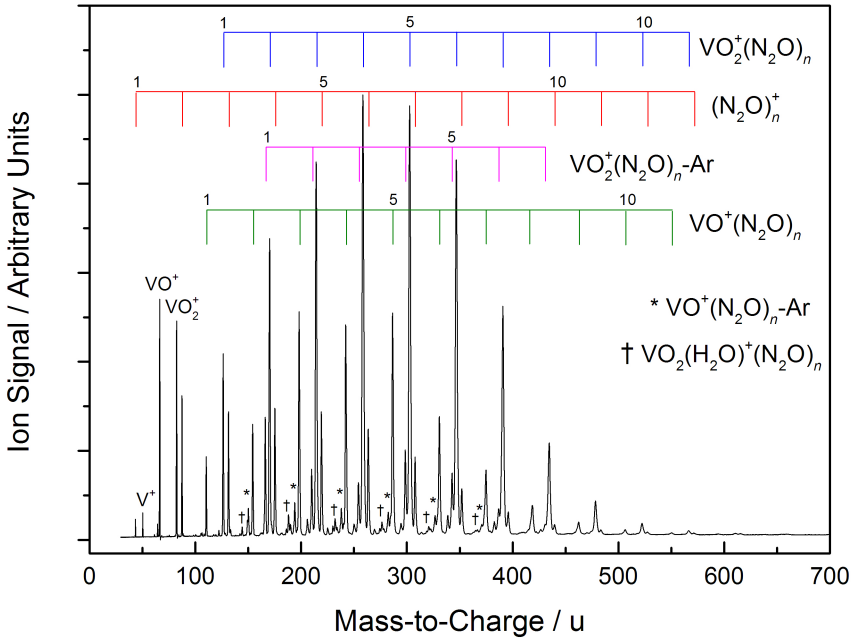

Figure 3.9: The rich time-of-flight spectra depicting clusters formed by ablating a vanadium target in the presence of a gas mix containing 2% of N_2O in argon. $VO_2^+(N_2O)_n$ complexes are the dominant species produced. Smaller amounts of Ar-tagged $VO_2^+(N_2O)_n$–Ar complexes are also observed. In addition, significant amounts of neat $(N_2O)_n^+$ complexes are also produced.

Interestingly, significant number densities of neat $(N_2O)_n^+$ complexes are also produced in the ablation process (as also observed in Figure 3.9). We further observed the formation of gaseous $(N_2O)_n^+$ complexes while ablating other

metals such as copper, silver and gold in presence of N_2O in argon.[268] One might envisage that upon formation of metal ions, the ablation process produces free electrons which can then act as ionisation agents for a molecule of N_2O. As soon as a single N_2O molecule is ionised, it can act as the nucleation site that leads towards forming larger clusters. In the mass spectrum presented in Figure 3.9, $(N_2O)_n^+$ complexes up to $n = 13$ are produced. A similar approach is employed by Beyer and co-workers, who form charged gaseous clusters by ablating a metal with a low workfunction such as zinc.[269] In addition to the species discussed above, non-trivial amounts of $VO_2^+(N_2O)_n$–Ar, $VO^+(N_2O)_n$, $VO^+(N_2O)_n$–Ar and $VO_2^+(H_2O)(N_2O)_n$ were also observed.

3.4.3 Formation of $Au^+(CH_4)_n$ Complexes

Time-of-flight spectra presented in Figure 3.10 display $Au^+(CH_4)_n$ complexes formed upon the ablation of gold target and by using the helium buffer gas with a low percentage of methane. [ii] In the time-of-flight mass spectrum presented in Figure 3.10 a), 10% CH_4 in helium buffer gas at 6 bar is used for expansion. As observed, $Au^+(CH_4)_n$ complexes are the dominant series formed, with cationic gold dimer and even trimer clusters formed in lower abundances. This is unexpected as the new ablation source was specifically designed to maximise the production of the atomic metal ion. In this case, it appears that the metal vapour undergoes a sufficient number of three-body collisions between gold ions/atoms to form larger metal clusters. In the example presented in Figure 3.10 a), gold dimer ion-based clusters $Au_2^+(CH_4)_n$ can be identified as well. Reducing the amount of CH_4 to 2% and adding 18% Ar as the total percentage of the helium buffer gas produces argon-tagged $Au^+(CH_4)_n$–Ar complexes as presented in Figure 3.10 b).

[ii] This time-of-flight mass spectrum is a result of joint work with D. Price and some preliminary analysis appears in his Part II thesis.[270]

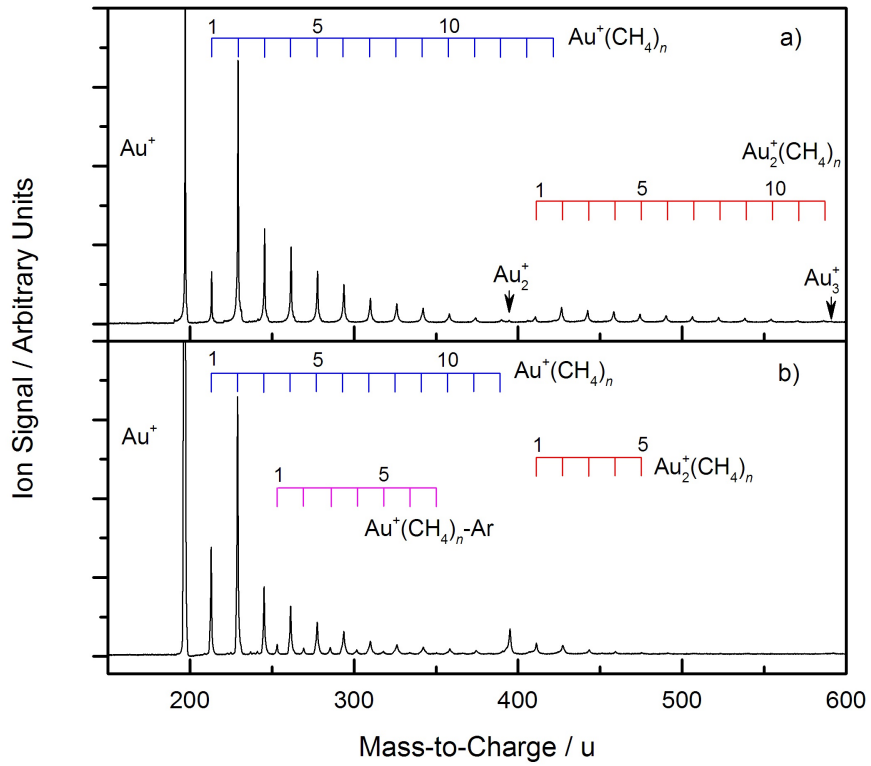

Figure 3.10: a) Complexes formed using 10% CH_4 in helium at 6 bar.
b) Complexes formed using 2% CH_4 and 18% Ar in helium at 7 bar. In both cases, a gold target is used for ablation. By introducing argon in the expansion gas mix, argon-tagged $Au^+(CH_4)_n$–Ar complexes are also produced.

3.5 Model System: $V^+(CO_2)_n$

3.5.1 Previous Work on $V^+(CO_2)_n$ Complexes

In order to characterise the new IR-REPD experiment, a well-studied system was chosen. The choice of CO_2 as the ligand was based on its large IR cross section (665 km/mol at 2349 cm^{-1}).[271] IR-REPD spectroscopic and theoretical studies of gas-phase $V^+(CO_2)_n$ complexes were first performed by the Duncan group.[272,273] The dissociation energy of 0.75 ± 0.04 eV for $V^+(CO_2)_n$

monomer was measured by Armentrout *et al.* using collision-induced dissociation.[274] This is similar to the theoretical value of 0.79 eV determined by Bauschlicher *et al.* at the CCSD(T) level of theory.[72] The binding energy of CO_2 to the vanadium cation is not insignificant, therefore one needs to rely on argon tagging to record IR-REPD spectra of small $V^+(CO_2)_n$ complexes. The subsequent subsections present the result obtained for neat and argon-tagged $V^+(CO_2)_n$ clusters. [iii]

3.5.2 IR-REPD Spectra for Neat $V^+(CO_2)_n$ Complexes

The vibrational modes of carbon dioxide are well characterised. The isolated CO_2 molecule has three normal vibrational modes ν_1, ν_2 and ν_3 with fundamental transitions at 1333, 667 and 2349 cm^{-1}, respectively.[276] The modes are visualised in Figure 3.11. The experiments presented here focus in the region around the asymmetric stretch of CO_2, ν_3, at 2349 cm^{-1} as it is the only infrared-active vibration mode within the tuning range of the IR-OPO/OPA system described in Section 3.1 (without the use of $AgGaSe_2$ crystal).

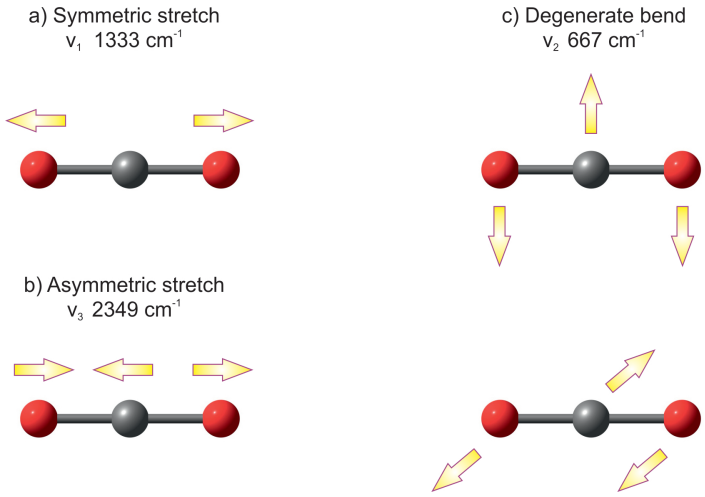

Figure 3.11: Visualisations of the normal vibrational modes of CO_2.

[iii] IR-REPD spectra for neat $V^+(CO_2)_n$ complexes was collected together with A. P. Sharp and some preliminary analysis appears in his part II thesis.[275]

A typical mass spectrum of the distribution of $V^+(CO_2)_n$ complexes formed in our ablation source with the IR laser "off" and "on" at 2349 cm^{-1} is presented in Figure 3.12. All mass spectra are recorded using 5% CO_2 in argon at a backing pressure of 6 bar.

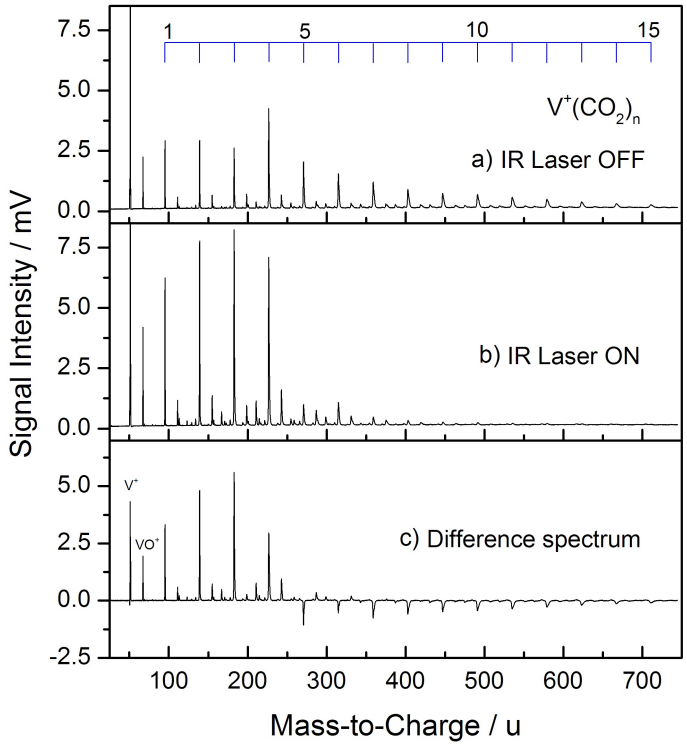

Figure 3.12: a) Mass spectrum recorded with the IR laser "off". The $V^+(CO_2)_n$ complexes are formed by ablation of vanadium target with 5% CO_2 in argon at 6 bar; b) a mass spectrum recorded with IR laser on-resonance with the asymmetric stretch of CO_2 at 2349 cm^{-1}; c) The difference spectrum obtained by subtracting the spectrum with IR laser on from the spectrum with the IR laser "off". The $VO^+(CO_2)_n$ and $VCO^+(CO_2)_n$ complexes are also observed but for clarity, only $V^+(CO_2)_n$ complexes are labelled.

In addition, Figure 3.12 c) shows the difference spectrum obtained by subtracting the mass spectrum with the IR laser "on" from the mass spectrum with the IR laser "off". A positive signal in Figure 3.12 c) indicates an increase in the signal for a particular cluster, whereas a negative signal indicates

a depletion. The IR-REPD spectra for a particular cluster size are recorded by monitoring the signal intensity of the difference spectra as a function of IR laser wavelength.

The difference spectrum in Figure 3.12 c) shows an enhancement for $n = 1 - 4$ and depletion for complexes where $n \geq 5$. This is in excellent agreement with the results of Duncan *et al.* who observed a common termination point for fragmentation at $V^+(CO_2)_4$. This also supports the conclusion that four CO_2 molecules constitute the first coordination sphere of ligands directly-bound to V^+. Any additional CO_2 is bound in the second coordination sphere. These particular ligands are thought to be bound significantly more weakly and, in larger complexes (n $\geq$ 5), can be photodissociated by a single IR photon with an energy around the CO_2 asymmetric stretch. Ligands in the second coordination sphere interact (to a great extent) only with other CO_2 molecules. Thus, it is expected for the binding energies of a second coordination sphere ligand to be close to that of a CO_2 dimer - several intermolecular potential models place this value at *ca.* 484 to 589 cm^{-1}.[277–279]

The IR-REPD spectra presented in Figure 3.13 confirms the premise presented above. The absorption spectrum for $V^+(CO_2)_5$ shows three bands centred at 2352, 2376 and 2397 cm^{-1}. The band at 2352 cm^{-1} is observed virtually at the vibrational frequency of the asymmetric stretch in a free CO_2 molecule. This feature arises from the ligands in the second coordination sphere, which are not directly bound to the vanadium cation. These ligands only experience interactions with other CO_2 molecules that are present in the second coordination sphere and as such their vibrational frequencies lie very close to that of a free CO_2. The blue-shifted band at 2376 cm^{-1} corresponds to ligands which are directly attached to CO_2. This feature arises as a result of the perturbation caused by the metal ion on the potential well of CO_2 (detailed discussion of bonding in $M^+(CO_2)_n$ complexes is provided in Chapter 4). The band at 2397 cm^{-1} is interpreted by Duncan *et al.* to arise from CO_2 ligands attached to an $(OVCO)^+$ "oxide-carbonyl" rearranged core. Lig-

ands attached to $(OVCO)^+$ core experience greater perturbation and hence a larger blue-shift from the free CO_2 vibrational frequency.

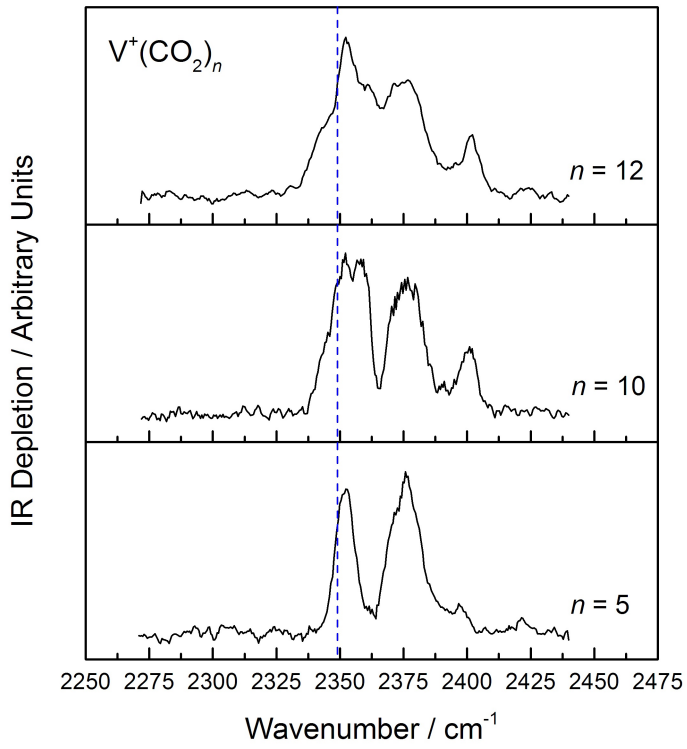

Figure 3.13: IR-REPD spectra of $V^+(CO_2)_n$ complexes for n=5, 10 and 12. The spectra are recorded by monitoring the depletion of the parent ion channel. The vertical dashed line indicates the energy of the asymmetric stretch in the free CO_2 at 2349 cm^{-1}.

The IR-REPD spectrum for $V^+(CO_2)_{10}$ shows four bands at 2352, 2358, 2376 and 2401 cm^{-1}. The new band that arises at 2358 cm^{-1} is assigned to CO_2 molecules in the intermediate coordination sphere between the first and second coordination sphere. As a result of these rigid coordination spheres, the vibrations of molecules in the intermediate layer are constrained and consequently, the ligands experience a moderate blueshift from 2349 cm^{-1}. Relative to $n = 5$, the most blueshifted band at 2401 cm^{-1} has become more pronounced, which signifies an increased number of ligands perturbed by the $(OVCO)^+$ rearranged core. These features are also repeated in the

IR-REPD spectrum for $n = 12$. In the case of $V^+(CO_2)_{12}$, these absorption bands appear at 2352, 2361, 2375 and 2401 cm^{-1}. The IR-REPD spectra for the collated complexes presented here compare very favourably with previous work of Duncan and co-workers.[272]

3.5.3 Effect of IR Laser Energy on Spectral Linewidth

In order to characterise the effect of laser energy upon the IR-REPD spectra, a polariser (Thor Labs Nanoparticle linear film polariser; range 1.5 – 5 μm) is installed in the path of IR light. As shown in Figure 3.14, higher infrared laser pulse energies lead to more pronounced depletion signals. Absorption spectra recorded at 2.2 mJ/pulse yield approximately 50% depletion, whereas spectra at 0.6 mJ/pulse yield less than 20% depletion. Moreover, higher laser energies promote multiple photon absorption, leading to the loss of several ligands. This is observed at higher laser energies as shown in Figure 3.14 a) and b). Negative signal observed here corresponds to an enhancement of $V^+(CO_2)_5$ due to larger complexes ($n > 5$) depleting into this channel. The interpretation of spectra at high laser energies is thus considerably more difficult.

Furthermore, higher IR laser energies also cause power broadening, which leads to diminishing resolution of spectral features. Two features at *ca.* 2350 and 2375 cm^{-1} are overlapped in Figure 3.14 a). The two spectral features are better resolved at pulse energies in Figure 3.14 c), d) and e).

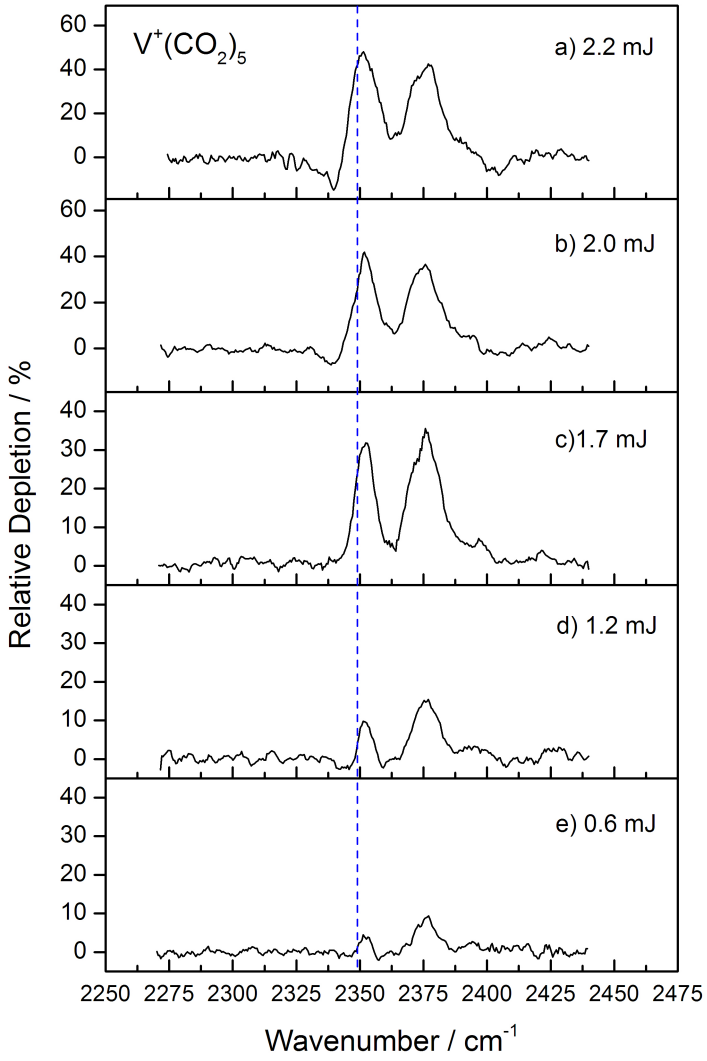

Figure 3.14: IR-REPD spectra for $V^+(CO_2)_5$ recorded at IR laser energies of a) 2.2, b) 2.0, c) 1.7, d) 1.2 and e) 0.6 mJ/pulse. These values correspond to different orientations of polariser angle used to attenuate the IR light. The polariser angles are 90°, 75°, 60°, 45° and 30°, respectively. Here, the spectra are shown as relative percentage change in the signal intensity of the parent ion. The ordinate is here labelled in terms of relative depletion of the parent ion. The vertical dashed line indicates the energy of the asymmetric stretch in the free CO_2 at 2349 cm^{-1}.

A quantitative comparison of laser energy on spectral linewidth is made in Figure 3.15, where FWHM of each of the two dominant peaks is plotted at

different energy. It can be deduced that the spectral linewidth is considerably larger at higher laser energy. The spectral linewidth increases approximately exponentially with the energy. However, lower laser energy also leads to reduced signal-to-noise resolution, as it can be seen in Figure 3.14 e) recorded at 0.6 mJ/pulse. Therefore, a correct balance needs to be reached between spectral linewidth and signal-to-noise resolution. If one continued to increase the laser energy, a full saturation of transitions would be achieved and it would result in a spectral linewidth reaching a plateau. Nevertheless, the spectral linewidth is still on the rise even at the highest available energy of 2.2 mJ/pulse, with full saturation not yet being achieved at this energy.

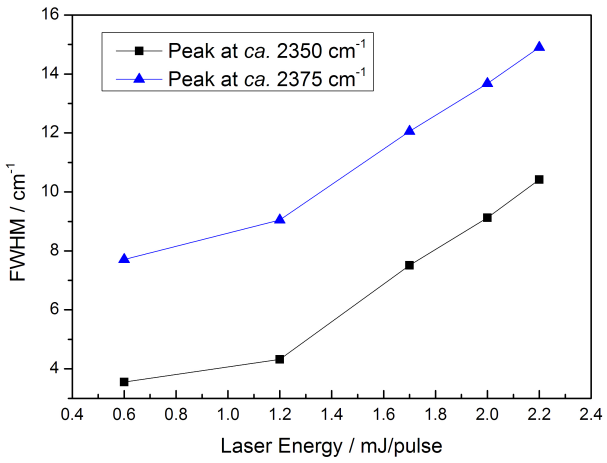

Figure 3.15: Comparison of FWHM linewidth of the two dominant peaks in the IR-REPD spectra of $V^+(CO_2)_5$ at different laser energies. Both spectral features become gradually broader upon increasing the energy of IR laser.

Overall, it can be concluded that high laser energies lead to power broadening and lowering resolution. Suitable laser pulse energies are found to be in the range of 1.7 – 0.6 mJ/pulse.

3.5.4 Argon-Tagged $V^+(CO_2)_n$-Ar Complexes

As mentioned in previous subsections, the binding energy of a CO_2 molecule to the vanadium cation at 0.75 ± 0.04 eV,[274] is not insignificant. A reliance on the inert messenger technique is thus necessary to record the IR-REPD spectra of smaller $V^+(CO_2)_n$ complexes. The argon-tagged complexes can be formed by reducing the percentage of CO_2 in the argon buffer gas. A mass spectrum produced with 0.5% of CO_2 in argon is shown in Figure 3.16.

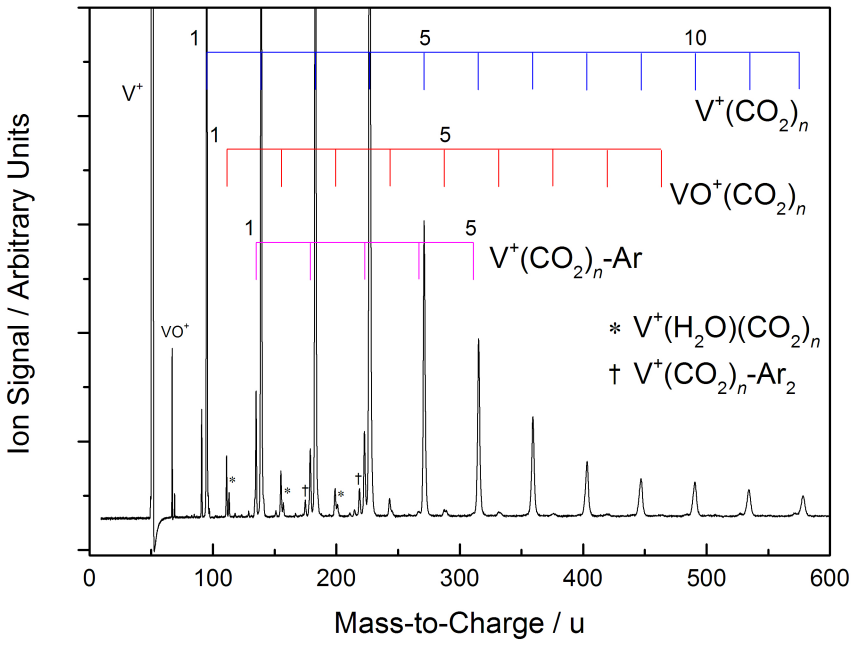

Figure 3.16: Time-of-flight mass spectrum produced by ablation of a vanadium target in the presence of 0.5% CO_2 in argon buffer gas at 6 bar. The argon-tagged $V^+(CO_2)_n$–Ar complexes are also produced in addition to neat $V^+(CO_2)_n$ complexes at this low percentage of CO_2 in argon.

As observed, only trace amounts of $V^+(CO_2)_n$-Ar complexes with $n > 3$ are produced. It appears that argon atoms behave here like any other ligand when occupying a binding site around V^+. This is consistent with the pre-

viously observed coordination number of four around a gas-phase vanadium cation.

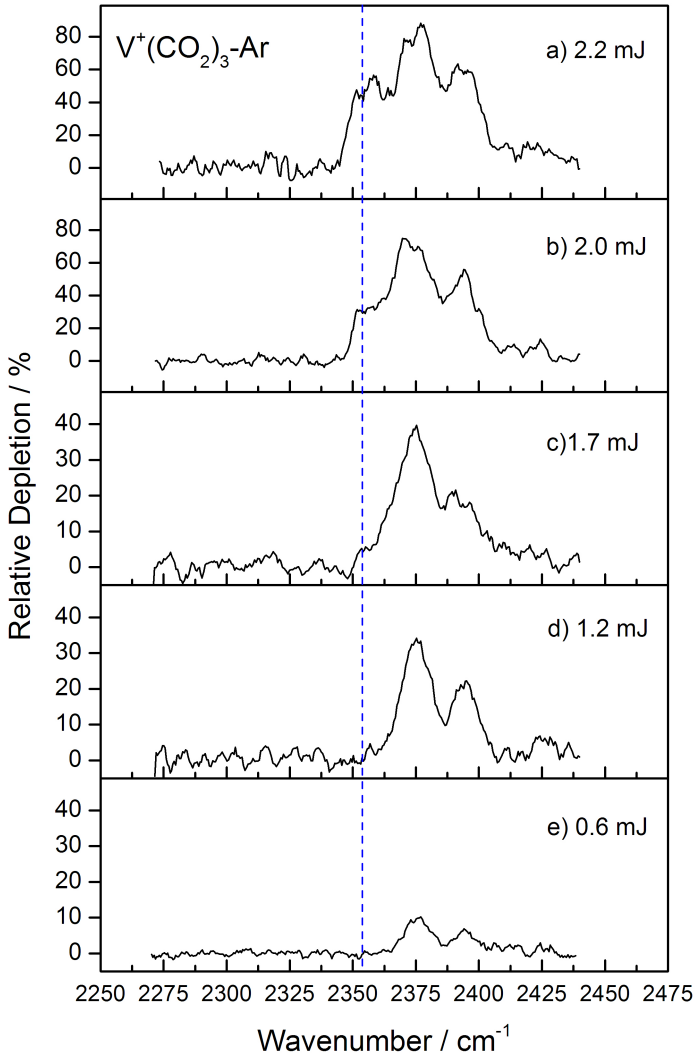

Figure 3.17: IR-REPD spectra for $V^+(CO_2)_3$–Ar recorded at a) 2.2, b) 2.0, c) 1.7, d) 1.2, and e) 0.6 mJ/pulse. The spectra are shown as the relative percentage change in the signal intensity of the parent ion.

Typical IR-REPD spectra for $V^+(CO_2)_3$–Ar recorded at different laser pulse energies from 2.2 – 0.6 mJ/pulse are presented in Figure 3.17. All spectra show two blue-shifted features at *ca.* 2375 and 2395 cm^{-1}. These peaks have

been interpreted by Duncan *et al.* to arise from low-symmetry structure or from a higher symmetry structure such as D_{3h} perturbed by argon atom. Spectra recorded at 2.0 and 2.2 mJ/pulse (Figure 3.17 a) and b)) also show an additional feature at around 2355 cm^{-1}. One can expect such a feature to arise from a higher-energy isomer that requires stronger laser fluences in order to photodissociate. Higher lying isomers may be formed in the source following ablation and in the case of inefficient cooling, they may survive long enough to reach the extraction region of the instrument. Additionally, argon atoms may further perturb the structure of underlying complex and "lock in" the higher lying isomer in the ablation process. Nevertheless, the IR-REPD spectrum for $V^+(CO_2)_3$–Ar recorded at 1.2 mJ/pulse as depicted in Figure 3.17 d) agrees well with previous work by Duncan and co-workers.

At the highest laser energy of 2.2 mJ/pulse, more than 80% depletion is achieved for $V^+(CO_2)_3$-Ar. This is is significantly more than *ca.* 50% depletion observed for $V^+(CO_2)_5$ at the same laser energy. This is not unexpected since loss of an argon atom from the complex is envisaged to be more facile than an equivalent loss of a CO_2 ligand. Moreover, argon atoms increase the density of states of the complex, which makes the IVR process even more efficient. This is then reflected in a high photofragmentation yield, as depicted in Figure 3.17.

3.6 Conclusions

A new IR-REPD experiment has been developed. A newly-designed laser ablation source can reliably produce a variety of metal ion-molecule complexes, including $Rh^+(CO_2)_n$, $V^+(CO_2)_n$, $VO_2^+(N_2O)_n$ and $Au^+(CH_4)_n$ complexes. The IR-REPD spectra for $V^+(CO_2)_n$ complexes agree very favourably with previously known literature. Further experiments using the experimental design described in this chapter are presented in Chapters 4 and 5.

Chapter 4

Infrared Spectroscopy of $M^+(CO_2)_n$ (M = Co, Rh, Ir) Complexes

Gas-phase $M^+(CO_2)_n$ (M = Co, Rh, Ir) ion-molecule complexes in the n = 2 – 15 size regime have been investigated both experimentally by IR-REPD spectroscopy and theoretically using DFT. This work aims to shed a light on fundamental metal cation – CO_2 interactions and lead towards a better understanding of metal ion solvation in CO_2. IR-REPD spectra for each cluster size are recorded in the region of the CO_2 asymmetric stretch. Data interpretation is supported by comparing the experimental IR-REPD spectra with simulated IR spectra at the DFT level of theory. A blue-shift in the vibrational frequency of the CO_2 asymmetric stretch relative to an isolated molecule is indicative of a direct attachment of CO_2 ligands to the metal ion. This is consistent with the binding of CO_2 to the metal centre being dominated by a charge-quadrupole interaction. For Co^+, Rh^+ and Ir^+, a core of $[M^+(CO_2)_2]$ is observed, to which successive ligands are bound less strongly and form outer coordination spheres.

The work discussed here involves the first substantive study with a new IR-

REPD spectrometer. Much of the results presented in this chapter has been published as an article by Iskra *et al.* in *The Journal of Physical Chemistry A*.[280]

4.1 Introduction

4.1.1 Previous Studies of Cationic $M^+(CO_2)_n$ Complexes

Theoretical studies by Bauschlicher *et al.* at CCSD(T) level of theory have indicated that the binding of CO_2 to the metal cation occurs nearly entirely *via* a charge-quadrupole interaction through the oxygen atom.[72] There is little evidence of charge transfer between the metal ion and CO_2 ligands.

IR-REPD experiments with cationic $M^+(CO_2)_n$ complexes were first performed by Duncan and co-workers who studied gas-phase CO_2 complexes with main group metals (Mg^+, Al^+ and Si^+)[281–283] and first row transition metals (Fe^+, V^+ and Ni^+).[272,273,284–287] These experiments, in conjunction with DFT calculations, allowed for accurate characterisation of geometries for a particular complex, while the Duncan group was also able to identify the specific number of ligands directly coordinated around the central ion. Zhou *et al.* later studied $Ti^+(CO_2)_n$ complexes[288] and Jiang *et al.* investigated the complexes of $Cu^+(CO_2)_n$ and $Ag^+(CO_2)_n$.[289]

All experimental studies report a systematic blue-shift of the fundamental transition associated with the asymmetric stretch of ligated CO_2 relative to that of free CO_2. With increasing number of CO_2 molecules, several vibrational bands are observed including some that appear at or very close to the vibrational frequency of isolated CO_2. These bands indicate the presence of ligands in secondary solvation sphere or ligands that are more weakly-bound to the central ion. Comparison of experimental IR-REPD spectra with DFT simulated IR spectra for low-lying isomers can identify characteristic CO_2 coordination numbers for a particular metal cation. Previous studies have

identified a coordination number of four CO_2 ligands around V^+ and Ni^+, and between 4 and 7 for Fe^+.[272,285–287] For Mg^+, Al^+ and Si^+ no definitive coordination numbers were observed, although a marked increase in the photodissociation yield is observed for $n \geq 3$ in $Al^+(CO_2)_n$ and $Si^+(CO_2)_n$ clusters.[282,283] Previously determined geometries of small $M^+(CO_2)_n$ complexes are collated in Table 4.1. For $Mg^+(CO_2)_n$ and $Al^+(CO_2)_n$ complexes, bent C_{2v} and trigonal pyramidal C_{3v} geometries were confirmed for $n = 2$ and 3 complexes, respectively, by density functional calculations (B3LYP and BP86 basis sets with augmented TZP basis set).[281,282]

Table 4.1: Comparison of geometries and coordination numbers for $M^+(CO_2)_n$ complexes.[272,273,281–287,289]

M^+	$n = 2$	$n = 3$	Coordination number
Mg	bent	trigonal pyramidal	unclear
Al	bent	trigonal pyramidal	$n \geq 3$
Si	bent	trigonal planar	$n \geq 3$
V	unclear	unclear	4
Fe	linear	distorted trigonal planar	4 - 7
Ni	linear	unclear	4
Cu	–	trigonal planar	unclear
Ag	–	trigonal planar	unclear

In addition to providing geometrical information, some IR-REPD investigations also revealed intracluster reactions such as oxide-carbonyl formation, as observed for $Si^+(CO_2)_n$, $Ti^+(CO_2)_n$ and $Ni^+(CO_2)_n$ complexes.[283,287,288273] In their investigation of $Ti^+(CO_2)_n$ complexes, Zhou *et al.* also identified $OTi^+CO(CO_2)_{n-1}$ to be present in the molecular beam, which was confirmed with absorption in the CO region in addition to the region of the CO_2 asymmetric stretch.[288] Moreover, an oxalate-type anion moiety was identified in large $V^+(CO_2)_n$ complexes.

Armentrout and co-workers have studied the thermochemistry of a variety

of metal cations, such as Mg^+, V^+ Cr^+, Mo^+, Fe^+ and Pt^+, with CO_2 using guided ion beam tandem mass spectrometry.[82,274,290–293] From collision-induced processes, Armentrout and co-workers were able to measure experimentally the binding energies of a CO_2 molecule to the aforementioned ions. The binding energies of CO_2 to the metal cations range from 0.51 ± 0.07 eV for Mo^+ to 0.77 ± 0.08 eV for Fe^+.[291,292]

Brucat *et al.* studied the photodissociation of $Co^+(CO_2)$ monomer in the visible region.[294] By probing the A'–X electronic transition in $Co^+(CO_2)$ and fitting the spectroscopy constants for the A' state, Brucat *et al.* were able to estimate the $D_0(Co^+(CO_2))$ to be 0.86 eV. Other systems studied by the Brucat group include $Ni^+(CO_2)$ and $V^+(CO_2)$ with a measured dissociation energy for $Ni^+(CO_2)$ of 1.08 eV.[295,296]

Of particular relevance to the present study, the Bohme group studied the kinetics of gas-phase reactions of CO_2 with atomic metal cations using tandem mass spectrometry. Bohme *et al.* observed a propensity for CO_2 clustering with Co^+, Rh^+ and Ir^+. Formation of M^+CO_2 is the dominant reaction, rather than the insertion reaction and formation of MO^+ + CO, for all three metal cations.[297]

A Walsh diagram depicting the molecular orbitals of CO_2 is shown in Figure 4.1. In a linear geometry, $1\pi_g$ is the highest occupied molecular orbital (HOMO). As seen in the Walsh diagram, addition of electrons into the $2\pi_u$ lowest unoccupied molecular orbital (LUMO) dramatically bends the angle to 90° (and additionaly splits the degeneracy of the π-orbitals). The bending of CO_2 is also observed upon complexation of the CO_2 ligand with metal anions as demonstrated by the Weber group.[298–305] A sufficient degree of covalency and electron donation into $2\pi_u$ is achieved in the case of $M^-(CO_2)_n$ complexes that consequently leads to the bending of the CO_2 ligand. In order to form CO_2 cation, electrons would have to be removed from the $1\pi_g$ orbital with no change from the linear geometry. Similarly, upon complexation of CO_2 with a metal cation the charge-quadrupole interaction is expected as the dominant

term[72] and hence $1\pi_g$ remains the HOMO. Hence the linear geometry of CO_2 ligands remains predominantly intact as they interact with a metal cation.

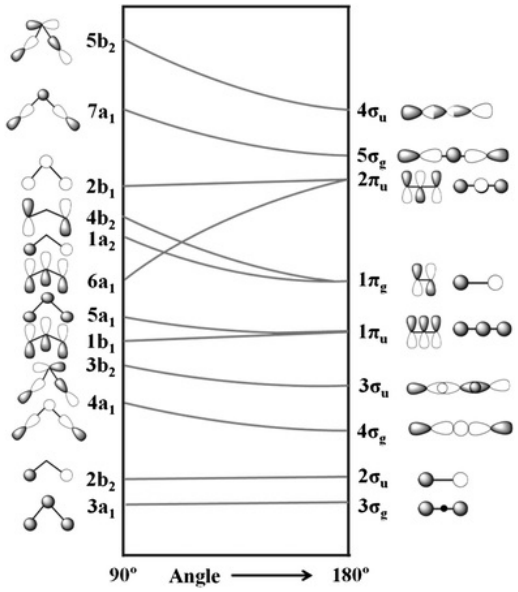

Figure 4.1: The Walsh digram of CO_2 molecular orbital energies in linear (180°) and bent (90°) geometries. A qulitative representation of the energy positions of the molecular orbitals is shown. $1\pi_g$ and $2\pi_u$ correspond to HOMO and LUMO orbitals, respectively. Reprinted from Ansari, M. B.; Park, S.-E. *Energy Environ. Sci.*, 2012, 5, 9419–9437 with permission from the Royal Society of Chemistry.[306]

4.1.2 Previous Studies of Anionic $M^-(CO_2)_n$ Complexes

The Weber group has studied anionic $M^-(CO_2)_n$ complexes extensively. In a sharp contrast to cationic counterparts, IR-REPD investigations of anionic $M^-(CO_2)_n$ clusters (for M = Co, Ni, Cu, Ag, Au, Bi) exhibit a significant degree of CO_2 activation consistent with the Walsh diagram.[298–305] Red-shifts in vibrational wavenumber on the order of several hundred cm^{-1} have been observed. For anionic $Co^-(CO_2)_n$ clusters, the frequency of the asymmetric stretch of the directly-bound CO_2 ligand experiences a red-shift to *ca.* 1750 cm^{-1}. In this particular complex, the CO_2 bond is significantly weakened, which increases the propensity for bond insertion reactions leading to the

inserted $OCo^-(CO)(CO_2)_n$ complexes.[298]

4.2 Experimental and Theoretical Methods

The laser ablation/time-of-flight instrument used to perform experiments presented here has been described in detail in Chapter 3 so only salient points related to the specific clusters studied are revisited here. Briefly, the ablation of a disk target (Co(1 mm thick) and Rh (0.5 mm thick, both Sigma-Aldrich 99.95%); Ir (0.125 mm thick, Goodfellow 99.9%)) produces the atomic metal cation of interest. Following the ablation, the metal vapour is entrained in a pulse of argon buffer gas seeded with a low percentage of CO_2. The gas pulse is delivered by a pulsed solenoid valve operated at 6 bar backing pressure. Photodissociation events are induced using a tunable IR-OPO/OPA (LaserVision) laser pumped by the 1064 nm fundamental of Nd:YAG laser (Continuum Powerlite II). IR-REPD spectra are recorded in the region between *ca.* 2275 – 2450 cm^{-1}. Initial scan would first survey an extended region from *ca* 2200 cm^{-1} up to 2500 cm^{-1} to ensure all spectral features are detected.

In the calculations, in addition to manually specifying starting geometries, a stochastic Kick algorithm by Addicoat and Mehta[307] is employed to generate a myriad of starting structures. The algorithm allows any number of arbitrary molecular fragments and atoms to be randomly placed in a virtual box of pre-specified dimensions. Batches of jobs are run until no new isomers are discerned. Initially, the geometry optimisations are run with no symmetry constraints – this allows for an unbiased and random search of the potential energy surface. A complementary script is then employed to identify all successfully terminated processes and to list their cartesian coordinates. The B3P86 density functional,[255] together with Def2TZVP basis set[308] on all atoms, is used for all calculations. Symmetry constrained geometry optimisations are performed following an initial unconstrained optimisation.

Harmonic vibrational frequencies are then calculated on all unique minima structures. Calculating vibrational frequencies also ensures that the optimised structures correspond to true minima with zero imaginary vibrational frequencies. In order to examine the effect of the inert messenger, additional calculations are performed on all structures of interest including the Ar atom. Simulated infrared spectra are produced by convoluting calculated infrared signals with a Lorentzian function with full-width half-maximum (FWHM) of 4 cm^{-1}. Simulated infrared spectra are scaled by a scaling factor of 0.962 determined by ensuring that the calculated value for the CO_2 asymmetric stretch (2442 cm^{-1}) matches the experimental value (2349 cm^{-1}). All calculations are performed using the Gaussian 09 software package.[309]

4.3 $Co^+(CO_2)_n$–Ar Infrared Spectra

As discussed above, the experimentally measured binding energy of CO_2 to Co^+ at 0.86 eV (6960 cm^{-1}) is rather high. Similarly, the CCSD(T) level computation of Bauschlicher and co-workers places this value at *ca.* 0.92 eV (7450 cm^{-1}).[72] $D_0(Co^+(CO_2))$ is thus considerably larger than the photon energy around the asymmetric stretch of CO_2 and therefore a multiple photon process is required to photodissociate $Co^+(CO_2)$. The high binding energy of CO_2 ligand to Co^+ ion hence commands the use of an inert messenger to record absorption spectra of small $Co^+(CO_2)_n$ complexes. Even the Ar binding energy to Co^+ is not insignificant. Brucat *et al.* measured the Co^+–Ar binding energy to be 0.51 eV (4111 cm^{-1}),[310] which is nevertheless lower than $D_0(Co^+(CO_2))$. Comparable argon binding energies have been encountered by Duncan *et al.* in their study of $Ni^+(CO_2)_n$ complexes.[287]

Figure 4.2 shows a time-of-flight mass spectrum generated by ablating a cobalt target in the presence of *ca.* 0.5% of CO_2 in argon buffer gas at 6 bar backing pressure. For clarity, only $Co^+(CO_2)_n$ complexes and their argon tagged counterparts are labelled.

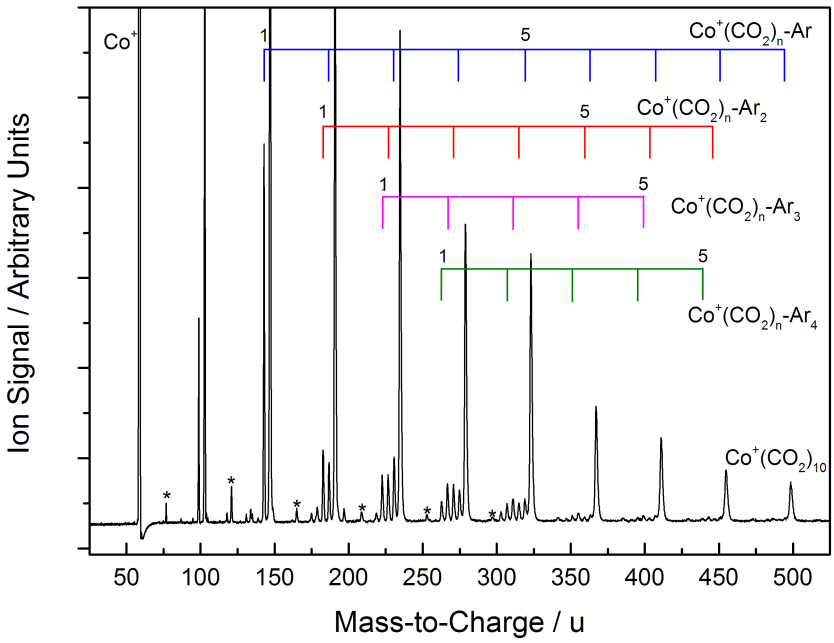

Figure 4.2: Time-of-flight mass spectrum obtained by ablation of a cobalt target while using approximately 0.5% of CO_2 in argon at 6 bar backing pressure as the expansion gas mix. $Co^+(CO_2)_n$ complexes are still observed as the dominant species in the beam. In addition to $Co^+(CO_2)_n$–Ar and neat $Co^+(CO_2)_n$ complexes, $Co^+(CO_2)$–Ar_2, $Co^+(CO_2)$–Ar_3, $Co^+(CO_2)_n$–Ar_4 and $CoO^+(CO_2)_n$ (*) are produced, albeit in lower intensities.

Figure 4.3 displays IR-REPD spectra for argon tagged $Co^+(CO_2)_n$–Ar (n = 2 – 5) complexes recorded in the region *ca.* 2275 – 2450 cm^{-1}. The IR-REPD spectrum for the smallest complexes studied here, $Co^+(CO_2)_2$–Ar, shows a single intense feature at 2385 cm^{-1}. The vibrational frequency of the ligands in this complex is blue-shifted by *ca.* 36 cm^{-1} from the free CO_2 asymmetric stretch frequency (2349 cm^{-1}).

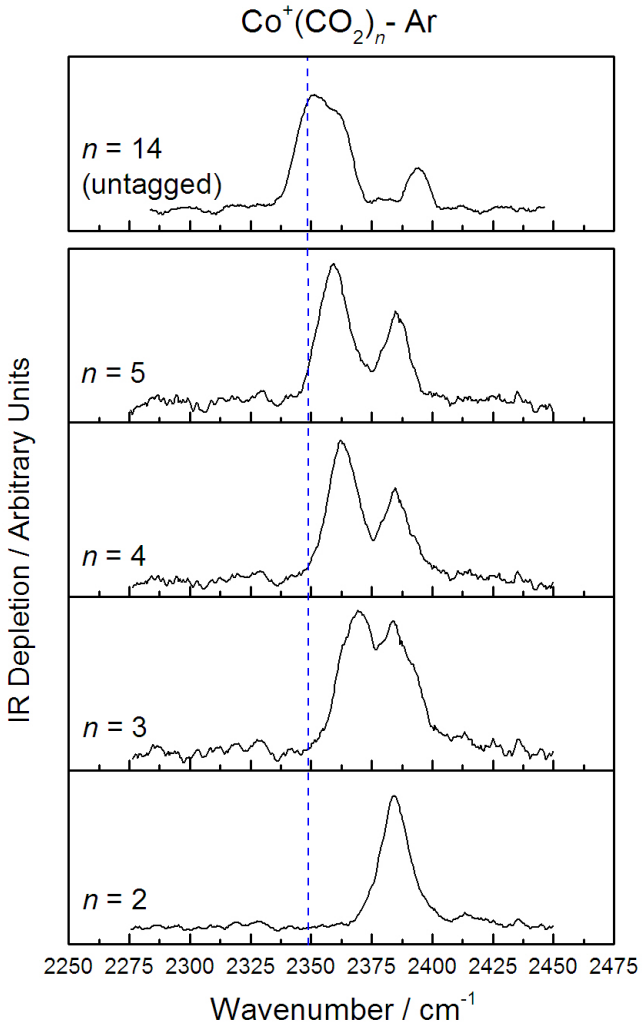

Figure 4.3: IR-REPD spectra for $Co^+(CO_2)_n$ (n = 2 – 5) complexes. The spectra are recorded in the channel corresponding to depletion of the parent ion signal. The vibrational frequency of the asymmetric stretch (ν_3) of free CO_2 at 2349 cm^{-1} is indicated by the vertical dashed line. IR-REPD spectrum for the neat $Co^+(CO_2)_{14}$ cluster is also shown for juxtaposition.

4.3.1 DFT Calculations for $Co^+(CO_2)_{2-3}$ Complexes

The interaction between the metal cation and CO_2 is dominated by the charge-quadrupole interaction.[72] For each CO_2 ligand, η^1 complexation through the O–end of the molecule is preferred. This is consistent with the negative quadrupole moment for CO_2 of -3.2 ea_0.[311] [i] Complexation *via* the O–end of CO_2 is favoured since a partial negative charge resides on each oxygen in an isolated molecule of CO_2. This is also reflected in the partial electric charges in the DFT calculated structure for $Co^+(CO_2)_n$ as presented in Figure 4.4.

A blue-shift in the vibrational frequency of the asymmetric stretch of the CO_2 results from the increased repulsion on the inner potential wall of the CO_2 due to the presence of the metal cation.[273] The IR-REPD spectra show little CO_2 activation owing to the lack of back–bonding from the electron deficient metal and a slightly negatively charged oxygen atom. Similar blue-shifts from 2349 cm^{-1} have hitherto been observed in other $M^+(CO_2)_n$ systems.[272,273,284–287]

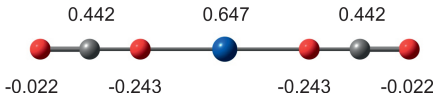

Figure 4.4: Partial electric charges derived from Mulliken population analysis for the optimised geometry of $Co^+(CO_2)_2$ calculated at B3P86/DefTZVP level of theory. Colour scheme: cobalt (dark blue), oxygen (red) and carbon (grey).

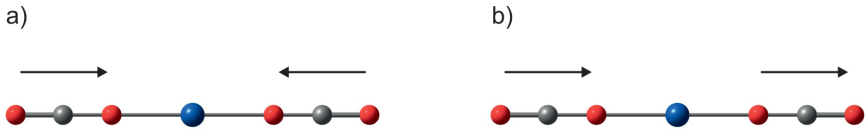

Figure 4.5: In-phase (a)) and out-of-phase (b)) combinations of normal modes shown as vectors for $Co^+(CO_2)_2$. Only out-of-phase combination is IR-active since in-phase leads to no change in the electric dipole moment.

For the $Co^+(CO_2)_2$ complex, a combination of isolated normal vibrational modes needs to be considered. Two CO_2 ligands can form either in-phase

[i] $e = 1.602 \times 10^{-19}$ C , $a_0 = 0.529 \times 10^{-10}$ m

or out-of-phase combinations. However, in the case of a linear $D_{\infty h}$ complex only the out-of-phase combination would be IR–active; an in-phase combination leads to no change in the electric dipole moment and is thus IR–inactive (Figure 4.5). The single band in the IR-REPD spectrum for $n = 2$ hence points towards a linear, $D_{\infty h}$ geometry. Such a conclusion is supported by the global minimum structure from the DFT calculations as depicted in Figure 4.6 (structure c1).

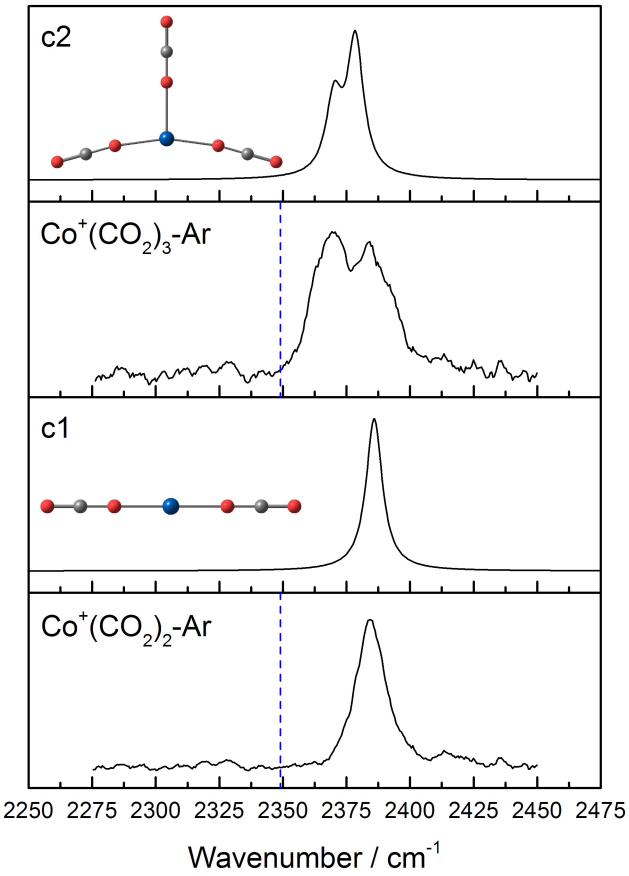

Figure 4.6: Experimental IR-REPD spectra for $Co^+(CO_2)_2$–Ar and $Co^+(CO_2)_3$–Ar together with the simulated IR spectra for each considered species (structure c1 and c2, respectively). All calculations are performed at the B3P86/Def2TZVP level of theory. The vertical dashed line marks the position of the asymmetric stretch ν_3 in an isolated CO_2.

Moreover, the linear geometry reflects a significant degree of s–d hybridisation which directs electron density away from the CO_2 ligands. This minimises ion-ligand repulsion and promotes binding of CO_2 molecules on the opposite ends of the metal cation. A similar argument provided an explanation for a linear structure of the $Sr^+(CO_2)_2$ complex predicted by theory.[312]

Structural parameters for the DFT optimised geometry for $Co^+(CO_2)_2$ and other structures are shown in Figure 4.7. The angle between the two CO_2 ligands is calculated to be 180°, as expected for a perfectly linear structure. The bond distance between Co^+ and each CO_2 ligand is 1.95 Å.

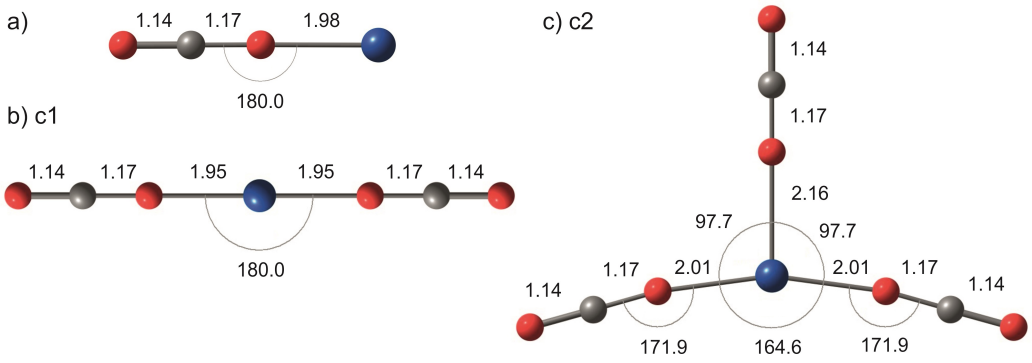

Figure 4.7: Structural parameters for a) $Co^+(CO_2)$, b) $Co^+(CO_2)_2$ (structure c1) and c) $Co^+(CO_2)_3$ (structure c2) calculated structures. Bond distances are in Ångstroms (Å) and bond angles are in degrees (°). All calculations are performed at the B3P86/Def2TZVP level of theory.

With an increasing number of CO_2 ligands, an additional vibrational feature arises in the IR spectra for complexes with $n \geq 3$ (see Figure 4.3). This new feature appears to the red of the original band in $n = 2$ and gradually red-shifts with increasing cluster size towards 2349 cm^{-1}. The IR spectrum for $Co^+(CO_2)_3$–Ar exhibits two bands at *ca.* 2385 and 2370 cm^{-1}. For the $Co^+(CO_2)_3$ complex, several vibrational modes need to be considered. A fully symmetric planar D_{3h} geometry would yield only one IR-active mode and would not explain the experimental data. The DFT calculated structure (Figure 4.7 c), structure c2) consists of a near-linear $[Co^+(CO_2)_2]$ core with a

third CO_2 ligand more weakly-bound in a planar fashion. The feature at 2370 cm^{-1} can thus be interpreted as the signature of a more weakly-bound CO_2. The feature is still blue-shifted from the free CO_2 vibrational frequency by approximately 20 cm^{-1}. The blue-shift is nevertheless less pronounced than for the "core" ligands whose vibrational frequency is observed at 2385 cm^{-1}.

Table 4.2 collates all theoretical energies for $Co^+(CO_2)_{1-3}$ and $Co^+(CO_2)_{2-3}$–Ar. Singlet, triplet and quintet multiplicities were considered. The triplet multiplicities are consistently the lowest in energy. This is to be expected as Co^+, with a $3d^8$ valance electronic configuration, is triplet itself in the electronic ground state and interacts with a closed shell CO_2 ligand.

Table 4.2: Theoretical energies (with included zero-point energy corrections) for $Co^+(CO_2)_{1-3}$ and $Co^+(CO_2)_{2-3}$-Ar calculated at the B3P86/Def2TZVP level of theory. The ΔE refers to the relative difference between a particular multiplicity and the global minimum structure. Global minimum structures have $\Delta E = 0$. Simulated IR spectra for Ar-tagged structures c1* and c2* are shown in Appendix A.

Species	Multiplicity	Energy / eV	ΔE / eV	Structure
$Co^+(CO_2)$	triplet	-42779.42673	0.0	–
	singlet	-42777.11093	2.32	–
	quintet	-42777.09900	2.33	–
$Co^+(CO_2)_2$	triplet	-47924.32409	0.0	c1
	quintet	-47922.79408	1.53	–
	singlet	-47922.28912	2.03	–
$Co^+(CO_2)_2$-Ar	triplet	-62289.26299	–	c1*
$Co^+(CO_2)_3$	triplet	-53068.74166	0.0	c2
	quintet	-53067.11920	1.62	–
	singlet	-53066.89897	1.84	–
$Co^+(CO_2)_3$-Ar	triplet	-67433.66192	–	c2*

The interpretation of a two-ligand core structure is also reinforced by DFT calculations. Considering the calculated Co^+–ligand bond distances (Figure

4.7 c), structure c2) reveals a Co^+–O bond length of 2.01 Å for core ligands and 2.16 Å for the third CO_2 molecule. Moreover, the relative binding energies reflect this trend with an approximate halving of the $Co^+(CO_2)_{n-1}$–CO_2 binding energy from *ca.* 0.91 to 0.43 eV between $n = 2$ and 3 (*vide infra* Section 4.6). It can be thought that two CO_2 ligands form the first coordination sphere and any additional ligand would then reside in the second coordination sphere. Such a low coordination number is not without precedence. Both $Al^+(CO_2)_n$ and $Si^+(CO_2)_3$ complexes show an increase in photodissociation yield for $n \geq 3$.[282,283] Other transition metal cations however show a tendency for larger coordination numbers, as in the case of V^+ and Ni^+ with $n = 4$ and Fe^+ with $n \geq 4$.[272,285,287]

4.3.2 IR-REPD Spectra for Multiply Argon-Tagged Complexes

The effect of multiple argon atoms has also been examined. Figure 4.8 shows IR-REPD spectra for singly and doubly argon tagged complexes of $Co^+(CO_2)_2$ and $Co^+(CO_2)_3$. No new major features are observed in complexes with an additional argon. In the case of $Co^+(CO_2)_3$–Ar_2 the two strong spectral features are even better resolved. The only noticeable difference is an additional small shoulder feature to the blue of the two main bands that could arise as a result of an additional argon. Overall, this comparison signifies that argon binds in a manner which does not significantly perturb the underlying parent complex nor change the positions of the bands.

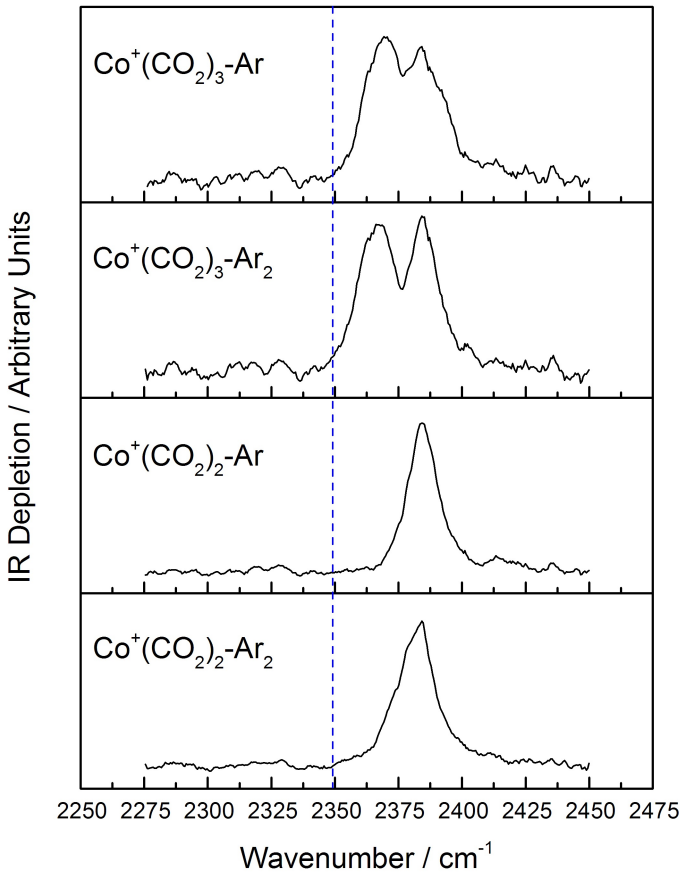

Figure 4.8: The IR-REPD spectra for $Co^+(CO_2)_2$–Ar_{1-2} and $Co^+(CO_2)_3$–Ar_{1-2} complexes. The vertical dashes line indicates the energy of the asymmetric stretch in an isolated molecule of CO_2.

4.3.3 Trends for Larger $Co^+(CO_2)_n$ Complexes

Figure 4.3 also shows the IR spectrum for the "untagged" $Co^+(CO_2)_{14}$ complex to illustrate a typical spectrum for the larger clusters. The spectrum shows a broad feature around the energy of the CO_2 asymmetric stretch and a strongly blue–shifted core band. The rather broad spectral feature around 2349 cm^{-1} might indicate a structure with unresolved multiple coordination shells. The core band is further blue-shifted than in any of the

smaller complexes - this may reflect further rigidity in larger coordination shells. Intermediate coordination shells have in the past been observed in the case of Fe^+, Ni^+ and V^+ complexes with CO_2.[272,285,287]

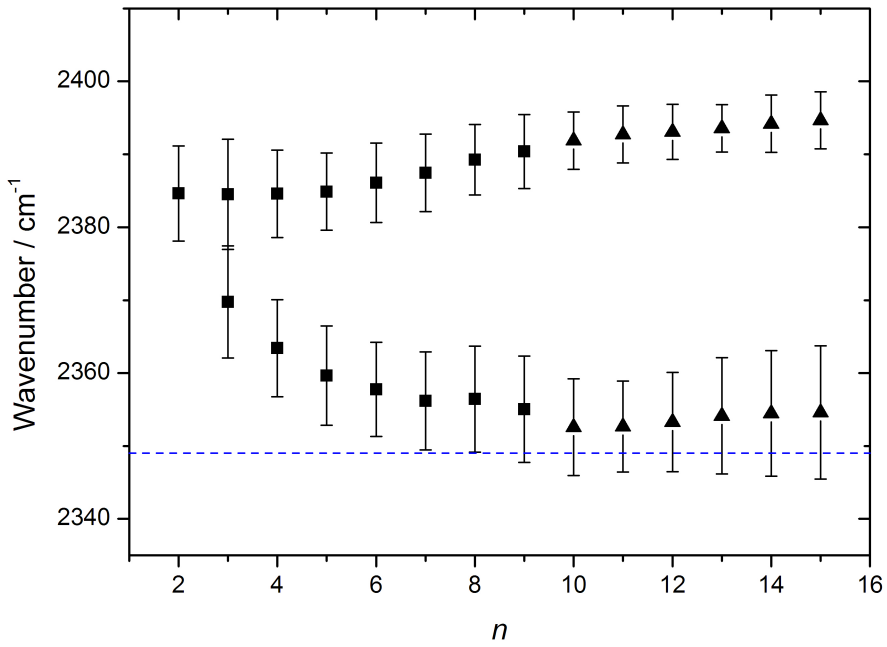

Figure 4.9: Experimentally recorded peak positions presented as a function of cluster size for $Co^+(CO_2)_n$ complexes between $n = 2 - 15$. The square markers correspond to argon-tagged complexes whereas triangles correspond to neat $Co^+(CO_2)_n$ complexes. The error bars correspond to the full-width-half-maximum of a fitted Gaussian used to identify the exact centre of each peak. The horizontal dashed line indicates the vibrational frequency of the asymmetric stretch of an isolated CO_2 at 2349 cm^{-1}.

Figure 4.9 shows a summary of vibrational bands observed for different cluster sizes (experimental spectra for the remaining complexes are displayed in Appendix A). The more blue-shifted feature corresponding to the $[Co^+(CO_2)_2]$ core continues to blue-shift with increasing cluster size. More ligands in outer coordination spheres, coinciding with an increase in rigidity, continue to exalt an additional perturbation on the core ligands and push core ligand vibra-

tional frequency further to the blue. For the largest complexes studied here, $n = 15$, the band appears to be close to reaching a plateau around 2395 cm^{-1}. The second band, conversely, depicts a continuous red-shift towards the wavenumber of free CO_2. This energy is finally reached around $n = 9$ or 10. For some other metals, such as V or Ni, the change between coordination spheres is more pronounced.[272,287] Here, however, the change is gradual. Although the $n = 3$ complex already sets the direction of change, the exact free CO_2 frequency is only reached at $n = 9$ or 10.

4.4 $Rh^+(CO_2)_n$–Ar Infrared Spectra

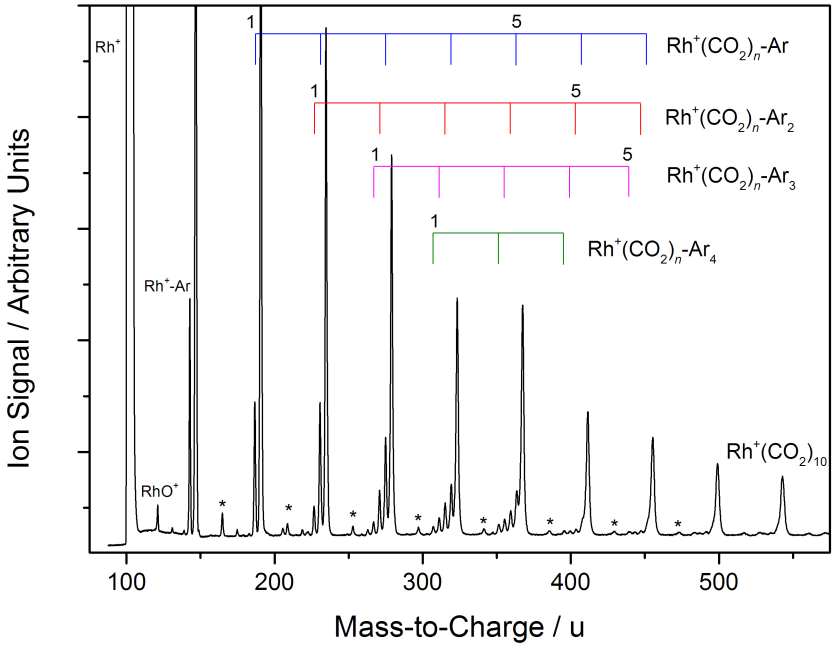

Figure 4.10: Time-of-flight mass spectrum generated by ablation of a rhodium target. 1% CO_2 in argon at 6 bar backing pressure is used as the buffer gas. $Rh^+(CO_2)_n$ and $Rh^+(CO_2)_n$–Ar complexes are the dominant complexes observed. Small amounts of $RhO^+(CO_2)_n$ (*) complexes are also observed.

Complexes produced upon the ablation of a rhodium target in the presence of 1% CO_2 in argon at 6 bar backing pressure are shown in Figure 4.10. Although $Rh^+(CO_2)_n$ complexes are the dominant species produced, a considerable amount of their argon tagged counterparts are formed also.

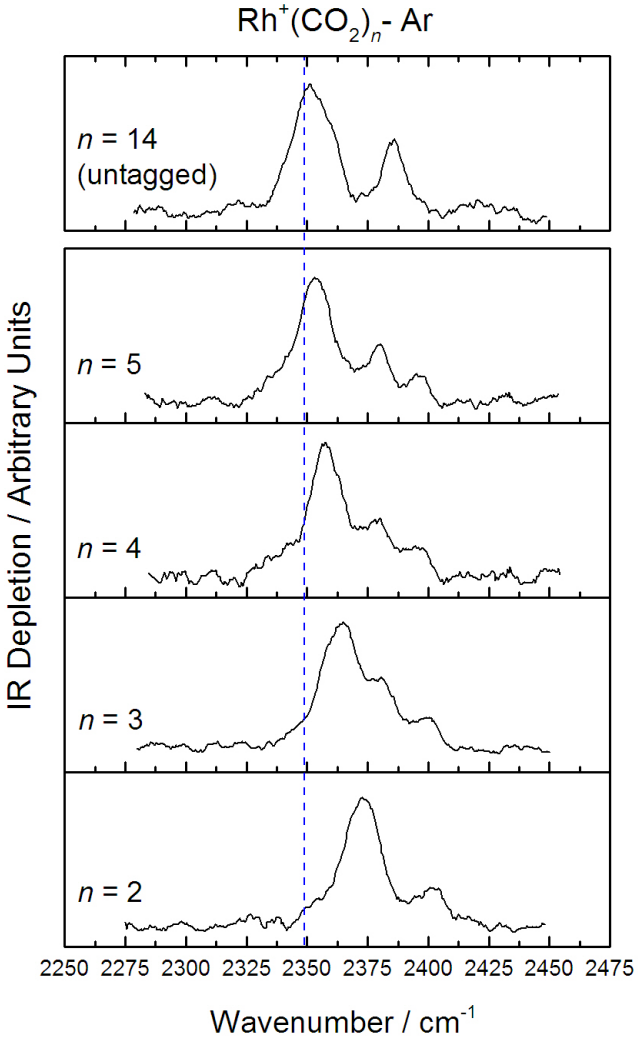

Figure 4.11: IR-REPD spectra for the $Rh^+(CO_2)_n$–Ar complexes (n = 2 - 5). The spectra are recorded in the channel corresponding to the depletion of the parent ion signal. A typical example of a large untagged complex, $Rh^+(CO_2)_{14}$, is shown. The vertical dashed line signifies the asymmetric stretch (ν_3) of isolated CO_2 at 2349 cm^{-1}.

Experimentally recorded IR-REPD for the $Rh^+(CO_2)_n$–Ar complexes are shown in Figure 4.11. Contrary to the $Co^+(CO_2)_2$–Ar IR spectrum, the smallest complexes considered here, $Rh^+(CO_2)_2$–Ar, shows a strong peak at 2373 cm^{-1} and an additional spectral feature at 2401 cm^{-1}. These features are blue-shifted by 24 and 52 cm^{-1}, respectively, from the isolated CO_2 asymmetric stretch (2349 cm^{-1}). These spectral features are consistent with a strongly bent non-linear structure, where both in-phase and out-of-phase combinations of the CO_2 normal modes are IR-active.

4.4.1 DFT Calculations for $Rh^+(CO_2)_{2-3}$ Complexes

However, DFT calculations predict a near-linear, C_{2v} structure as the putative global minimum (structure r1, Figure 4.12), which is inconsistent with the experimental observations since structure r1 predicts only a single IR band in the region examined. One would, therefore, expect at least one other higher lying isomer to be present that would give rise to the two features observed experimentally.

A low-lying isomer with C_{2v} symmetry was identified (structure r2). This strongly bent isomer, *ca.* 0.20 eV above the global minimum, has an O_2C–Rh^+–CO_2 bond angle of 109.3°. The simulated spectrum for structure r2 agrees reasonably well with the experimental data as shown in Figure 4.12. Including an argon atom in the calculations does not significantly affect the relative energies nor the simulated spectra of the two isomers. Singlet and quintet multiplicities were explored to find a suitable isomer that may explain the experimental observations but triplets are consistently the lowest in energy (*vide infra* - Table 4.3).

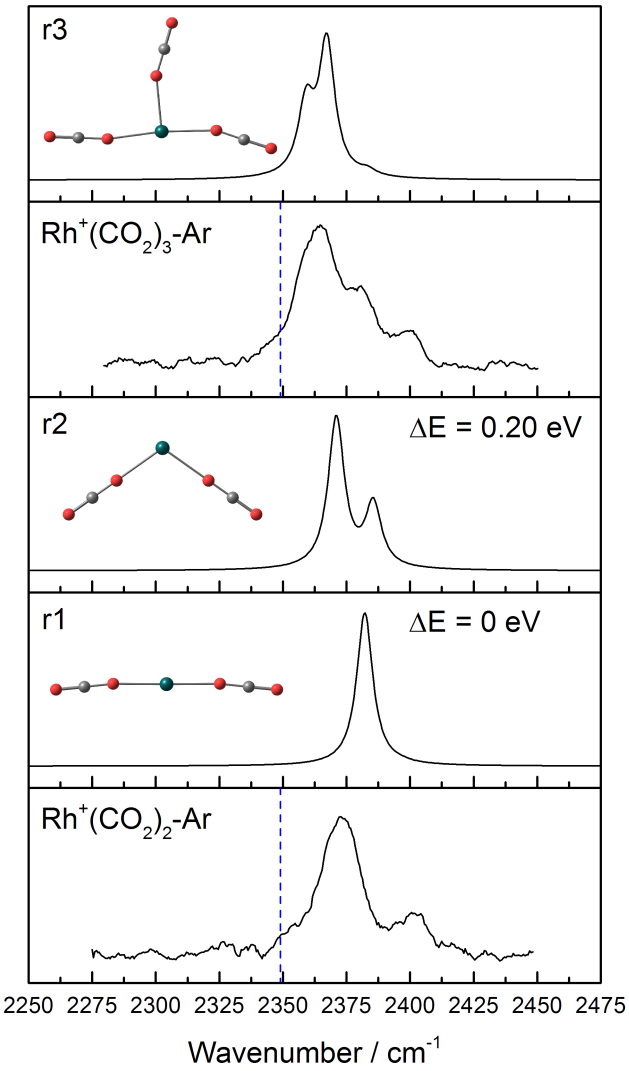

Figure 4.12: Experimental IR-REPD spectra for $Rh^+(CO_2)_2$–Ar and $Rh^+(CO_2)_3$–Ar together with the simulated IR spectra for each considered species (structures r1 and r2 for $n = 2$ and structure r3 for $n = 3$). All calculations are performed at the B3P86/Def2TZVP level of theory. Colour scheme: rhodium(blue-green), oxygen(red) and carbon(grey). The vertical dashed line marks the position of the asymmetric stretch ν_3 in an isolated CO_2.

The linear geometry is not a true minimum; constraining $Rh^+(CO_2)_2$ to a linear $D_{\infty h}$ geometry yields a structure with four imaginary frequencies. Similar bent geometries as structure r2 have been observed experimentally in the case of $Mg^+(CO_2)_2$ and $Al^+(CO_2)_2$[281,282] and rationalised for $Mg^+(CO_2)_2$ at

CASSCF level of theory.[312] The origins of non-linearity in metal – ligand dimers (ML_2) have been discussed extensively in the literature, particularly in the light of hybridisation of the metal ion and pseudo–Jahn–Teller distortion. Hybridisation can lead to prominent polarisation of the metal ion upon binding of the first ligand. This leads to a preference for off-axis binding of the second ligand.[312,313]

Examining the polarisabilities for the metal ions studied in this work reveals that Rh^+ at $\alpha = 34.4\ a_0^3$ is calculated to be rather more polarisable than Co^+ at $\alpha = 20.6\ a_0^3$.[314] The higher intrinsic polarisability of a rhodium cation would then support a bent geometry for $Rh^+(CO_2)_2$. Partial electric charges on each atom were explored yet they do not account for the non-linearity of $Rh^+(CO_2)_2$. A bent structure for $Rh^+(CO_2)_2$ yields both in-phase combinations and out-of-phase combinations of normal modes to be IR-active which rationalises the two features observed experimentally for $n = 2$. The main feature in the IR-REPD spectrum for $Rh^+(CO_2)_2$ corresponds to the out-of-phase combination, whereas the shoulder peak is due to the in-phase combination of normal modes.

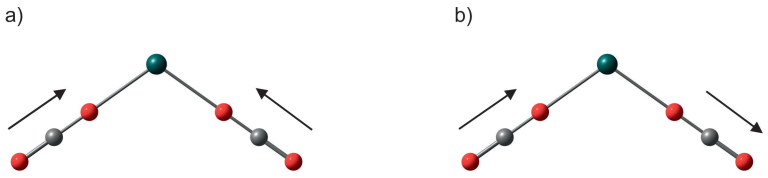

Figure 4.13: In-phase(a)) and out-of-phase(b)) combinations of normal modes shown for structure r2. Here both combinations of normal modes lead to a change in the electric dipole moment and are therefore both IR-active.

The IR-REPD spectrum for $Rh^+(CO_2)_3$–Ar shows three well resolved features. The two most blue-shifted features at *ca.* 2399 and 2378 cm^{-1} correspond to the same two features observed for the $n = 2$ complex. An additional feature, closer the asymmetric stretch of free CO_2, appears at 2364 cm^{-1}. Similarly to the $Co^+(CO_2)_3$ ion, the least blue-shifted feature is expected to arise from a weakly-bound CO_2 to the $[Rh^+(CO_2)_2]$ core. Such geometry is

further supported by the density functional calculations (structure r3, Figure 4.12). The simulated IR spectrum for r3 depicts three bands (at different relative intensities than the experimental data nonetheless). Comparing the Rh^+–OCO bond distances reveals a noticeably longer bond length for the more weakly-bound ligand at 2.35 Å relative to bond distances of *ca.* 2.20 Å for the core ligands. Structural parameters for all considered structures are shown in Figure 4.14.

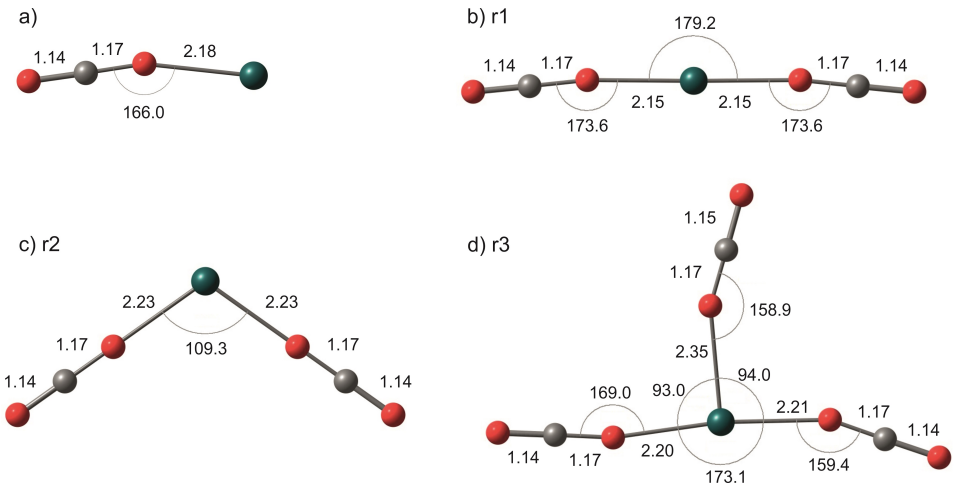

Figure 4.14: Structural parameters for a) $Rh^+(CO_2)$, b) $Rh^+(CO_2)_2$ (structure r1), c) $Rh^+(CO_2)_2$ (structure r2) and d) $Rh^+(CO_2)_3$ (structure r3) calculated structures. Bond distances are in Ångstroms (Å) and bond angles are in degrees (°). All calculations are performed at the B3P86/Def2TZVP level of theory.

Table 4.3 lists the energies of all considered structures. Structures for singlet, triplet and quintet multiplicities were calculated. Triplet multiplicities, just as for equivalent cobalt structures, are the lowest in energy.

Table 4.3: Theoretical energies (with included zero-point energy corrections) for $Rh^+(CO_2)_{1-3}$ and $Rh^+(CO_2)_{2-3}$–Ar calculated at the B3P86/Def2TZVP level of theory. The ΔE refers to the relative difference between a particular complex and the putative global minimum structure. Global minimum structures have ΔE = 0.

Species	Multiplicity	Energy / eV	ΔE / eV	Structure
$Rh^+(CO_2)$	triplet	-8154.550585	0	–
	singlet	-8153.007132	1.54	–
	quintet	-8152.19352	2.36	–
$Rh^+(CO_2)_2$	triplet	-13299.32945	0	r1
	triplet	-13299.12978	0.20	r2
	singlet	-13298.24992	1.08	–
	quintet	-13296.64062	2.69	–
$Rh^+(CO_2)_2$–Ar	triplet	-27664.20063	0	r1*
	triplet	-27664.0644	0.14	r2*
$Rh^+(CO_2)_3$	triplet	-18443.66879	0	r3
	singlet	-18442.66099	1.01	–
	quintet	-18440.92746	2.74	–
$Rh^+(CO_2)_3$–Ar	triplet	-32808.52121	–	r3*

4.4.2 IR-REPD Spectra for Multiply Argon-Tagged Complexes

Singly and doubly argon tagged complexes of $Rh^+(CO_2)_2$ and $Rh^+(CO_2)_3$ are presented in Figure 4.15. The additional argon atom leads to no additional spectral features. Addition of a second argon atom induces a modest red-shift relative to the singly Ar-tagged structures, which is most noticeable for $Rh^+(CO_2)_2$–Ar_2.

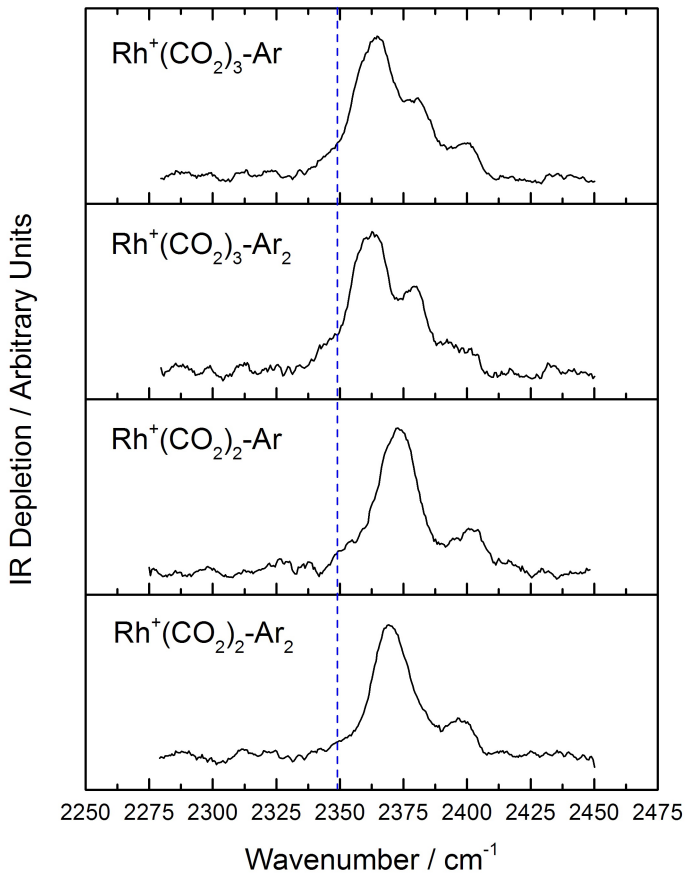

Figure 4.15: IR-REPD spectra for singly and doubly argon-tagged species of $Rh^+(CO_2)_2$ and $Rh^+(CO_2)_3$. The vertical dashed line indicates the position of the asymmetric stretch in free CO_2 at 2349 cm^{-1}.

4.4.3 Trends for Larger $Rh^+(CO_2)_n$ Complexes

As seen in Figure 4.16, with an increasing number of ligands the feature resulting from the more weakly–bound CO_2 molecules shifts further to the red towards 2349 cm^{-1}. For $n = 3$ this feature appears at 2364 cm^{-1}, for $n = 4$ at 2358 cm^{-1}, for $n = 5$ at 2353 cm^{-1} and for $n = 14$ at 2352 cm^{-1}. This signifies that each additional surface ligand experiences progressively weaker perturbation.

Figure 4.16 presents all peak positions for the complexes studied here. With an increasing number of ligands, the surface band becomes broader. A similar argument as for cobalt can be made. In very large complexes, the ligands will occupy different surface positions and thus the ligands would experience a range of perturbations.

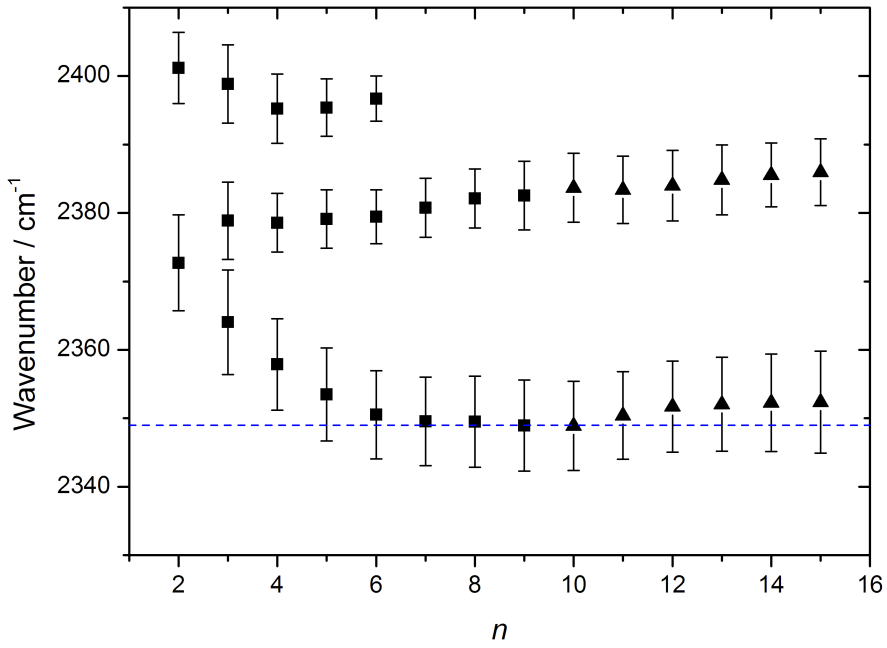

Figure 4.16: Experimentally recorded peak positions presented as a function of cluster size for $Rh^+(CO_2)_n$ complexes between $n = 2 - 15$. The square markers correspond to argon-tagged complexes whereas triangles mark neat $Rh^+(CO_2)_n$ complexes. The uncertainties are derived from the full-width-half-maximum of a fitted Gaussian used to identify the exact centre of each peak. The horizontal dashed line dashed line marks the energy of the asymmetric stretch (ν_3) of isolated CO_2 at 2349 cm^{-1}.

Beyond $n = 6$, the most blue-shifted feature corresponding to the in-phase combination of normal modes in $Rh^+(CO_2)_n$ complexes becomes too faint to be observed. The loss of intensity in this band might arise from the change in a geometry of the complex. The core may become increasingly linear in larger

complexes, which would make this particular mode IR-inactive. Overall, the spectra for larger clusters of $n \geq 7$ can be understood to consist of a single core vibrational (at *ca.* 2385 cm^{-1}) and a second more intense but largely unresolved band close to the energy of the free CO_2 asymmetric stretch. The latter broad feature reflects numerous ligands in the outer coordination sphere.

4.5 $Ir^+(CO_2)_n$–Ar Infrared Spectra

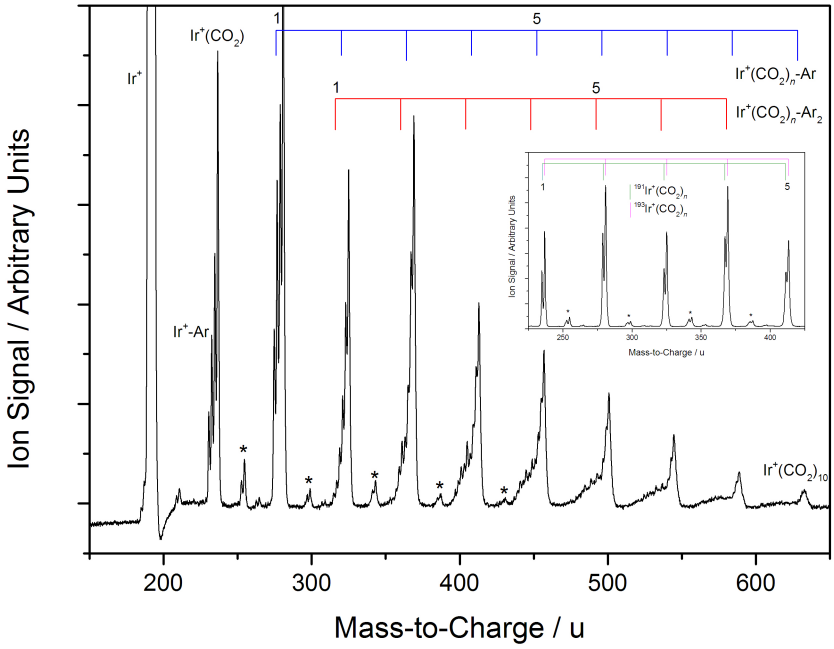

Figure 4.17: Time-of-flight mass spectrum produced by ablation of an iridium target in the presence of 1% CO_2 in argon at 6 bar stagnant pressure as the expansion gas. Inset: Complexes produced using 7.5% CO_2 in argon as the expansion gas. Complexes around the two iridium isotopologues (^{191}Ir and ^{193}Ir) are clearly resolved.

Figure 4.17 displays the Ar-tagged and neat $Ir^+(CO_2)_n$ complexes formed upon the ablation of an iridium target. 1% CO_2 and 7.5% CO_2 in argon at 6 bar backing pressure are used to form At-tagged and neat complexes, respectively.

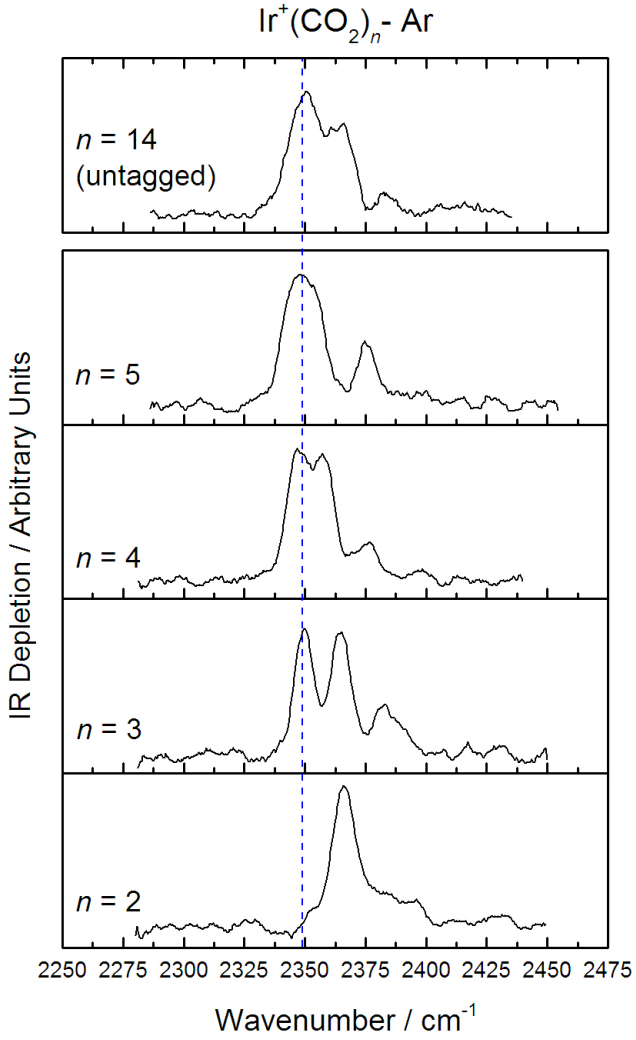

Figure 4.18: IR-REPD spectra for $Ir^+(CO_2)_{2-5}$–Ar recorded between *ca.* 2275 and 2450 cm^{-1}. For comparison, the spectrum for $Ir^+(CO_2)_{14}$ (untagged complex) is included. The spectra are recorded in the channel corresponding of the depletion of the parent ion. The vibrational frequency of the asymmetric stretch in free CO_2 at 2349 cm^{-1} is indicated by the vertical dashed line.

IR-REPD spectra for a particular complex are recorded by gating over complexes of both iridium isotopologues (^{191}Ir and ^{193}Ir). Experimental IR-REPD spectra for the $Ir^+(CO_2)_{2-5}$–Ar complexes are shown in Figure 4.18. Examination of the spectra for the smallest complex studied here, $n = 2$, reveals a strong feature at 2367 cm^{-1} and an additional broad shoulder that extends to *ca.* 2400 cm^{-1}. The spectrum for $n = 2$ exhibiting a strong main peak and a weaker shoulder peak to the blue, shows a considerable degree of similarity with the spectrum of $Rh^+(CO_2)_2$. Considering only experimental data one would anticipate a bent non-linear structure for $Ir^+(CO_2)_2$–Ar.

4.5.1 DFT Calculations for $Ir^+(CO_2)_{2-3}$ Complexes

Compellingly, DFT geometry optimisations predict a C_{2h} structure as the putative global minimum structure (Figure 4.19, structure i1) for $Ir^+(CO_2)_2$. On the other hand, a C_{2v} isomer (structure i2) some 0.78 eV above structure i1 has been identified. The higher-lying isomer provides a better agreement with the experimental data as seen in Figure 4.19. A linear structure is not a minimum – a $D_{\infty h}$ constrained optimisation yields a structure with four imaginary frequencies. The effect of an argon atom tag on the spectra gives further insight. Here argon does perturb the relative energetics of the complexes noticeably. Attaching an argon atom to the $Ir^+(CO_2)_2$ complex changes the relative energetic order of the identified geometries. The C_{2v} isomer of $Ir^+(CO_2)_2$–Ar is now calculated to be the global minimum (structure i2*).

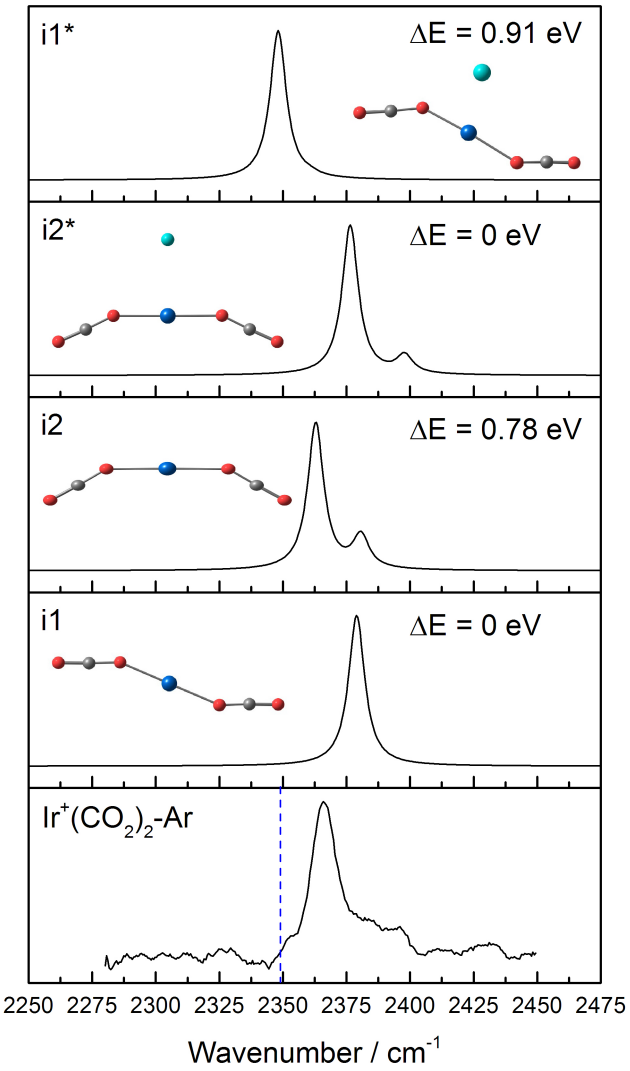

Figure 4.19: The not-so-inert messenger: Comparison of the IR-REPD spectra for $Ir^+(CO_2)_2$–Ar with DFT candidate structures (i1, i2, i1* and i2*) calculated at the B3P86/Def2TZVP level of theory. Both untagged and Ar-tagged calculated structures are considered. The relative energy differences are calculated with respect to the putative global minimum structures for both, the untagged and Ar-tagged complexes. Colour scheme: iridium (navy blue), oxygen (red) and carbon (grey). The vertical dashed line marks the position of the asymmetric stretch ν_3 in an isolated CO_2.

Examining polarisabilities for the three metal ions studied here reveals additional insight into structures of small complexes. The polarisability of the

Ir^+ ion at $\alpha = 27.9\ a_0^3$ lies between that of Co^+ and Rh^+.[314] A bent isomer, albeit not a global minimum structure, is identified for $Ir^+(CO_2)_2$, whereas $Co^+(CO_2)_2$ is linear.

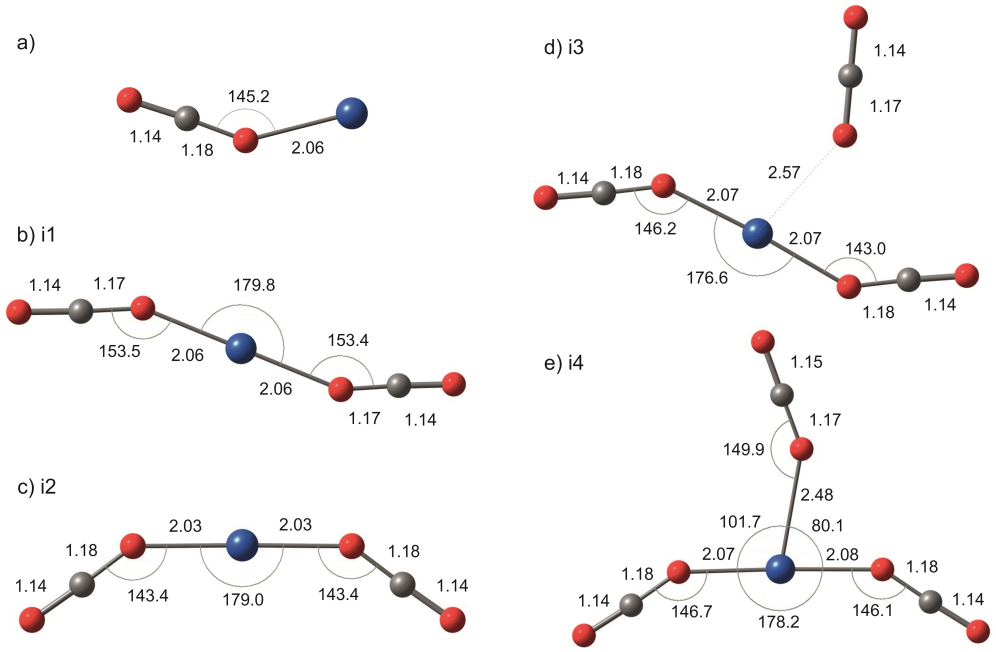

Figure 4.20: Structural parameters for all considered structures of a) $Ir^+(CO_2)$, b) $Ir^+(CO_2)_2$ (structure i1), c) $Ir^+(CO_2)_2$ (structure i2), d) $Ir^+(CO_2)_3$ (structure i3) and e) $Ir^+(CO_2)_3$ (structure i4). All calculations are performed at the B3P86/Def2TZVP level of theory.

Other multiplicities have also been considered in the quest to rationalise the experimental data, however triplet multiplicities have been found to be the lowest in energy for calculated structures as shown in Table 4.4. While this is not unsurprising for Co^+ and Rh^+, which both have d^8 ^{3}F ground terms, it is perhaps unexpected for Ir^+ given its $5d^76s^1$ ^{5}F ground term. Similar switching of the relative energetic ordering has been reported in the literature. Armentrout *et al.* observed switching of quartet and sextet states for Fe^+ upon complexation with CO_2 in their study of sequential binding energies in $Fe^+(CO_2)_n$ complexes.[292] For Ir^+, a d^8 lower spin configuration provides a more symmetric structure in which hybridisation of the metal ion

may be induced upon approach of CO_2 ligands.

Table 4.4: Theoretical energies (with included zero-point energy corrections) for $Ir^+(CO_2)_{1-3}$ and $Ir^+(CO_2)_{2-3}$–Ar calculated at the B3P86/Def2TZVP level of theory. The ΔE refers to the relative difference between a particular complex and the global minimum structure. Global minimum structures have ΔE = 0. In the case of triplet multiplicities for $n = 3$ complex (including the Ar-tagged structures), the energy difference between two isomers is 0 to two significant figures.

Species	Multiplicity	Energy / eV	ΔE / eV	Structure
$Ir^+(CO_2)$	triplet	-7983.563745	0	–
	quintet	-7983.080689	0.48	–
	singlet	-7981.831974	1.73	–
$Ir^+(CO_2)_2$	triplet	-13128.81827	0	i1
	triplet	-13128.04117	0.78	i2
	singlet	-13127.59865	1.22	–
	quintet	-13127.43988	1.38	–
$Ir^+(CO_2)_2$–Ar	triplet	-27492.71887	0.91	i1*
	triplet	-27493.63273	0	i2*
$Ir^+(CO_2)_3$	triplet	-18272.7958	0	i3
	triplet	-18272.79295	0.00	i4
	singlet	-18272.592686	0.20	–
	quintet	-18271.75867	1.04	–
$Ir^+(CO_2)_3$–Ar	triplet	-32637.83313	0	i4*
	triplet	-32637.83145	0.00	i3*

The IR-REPD spectrum for $Ir^+(CO_2)_3$–Ar in Figure 4.21 shows three well-resolved bands with one feature at 2350 cm^{-1}. This is virtually at the frequency of an asymmetric stretch in a free CO_2 molecule. Such vibrational frequency would point towards an extremely weakly-bound and thus rather unperturbed CO_2 ligand residing in the secondary coordination sphere. DFT calculations also point towards this interpretation. The putative global minimum geometry (structure i3) predicts a non-linear $Ir^+(CO_2)_2$ core with Ir^+–O

bond lengths of 2.07 Å and with the third ligand 2.57 Å away from the Ir^+.

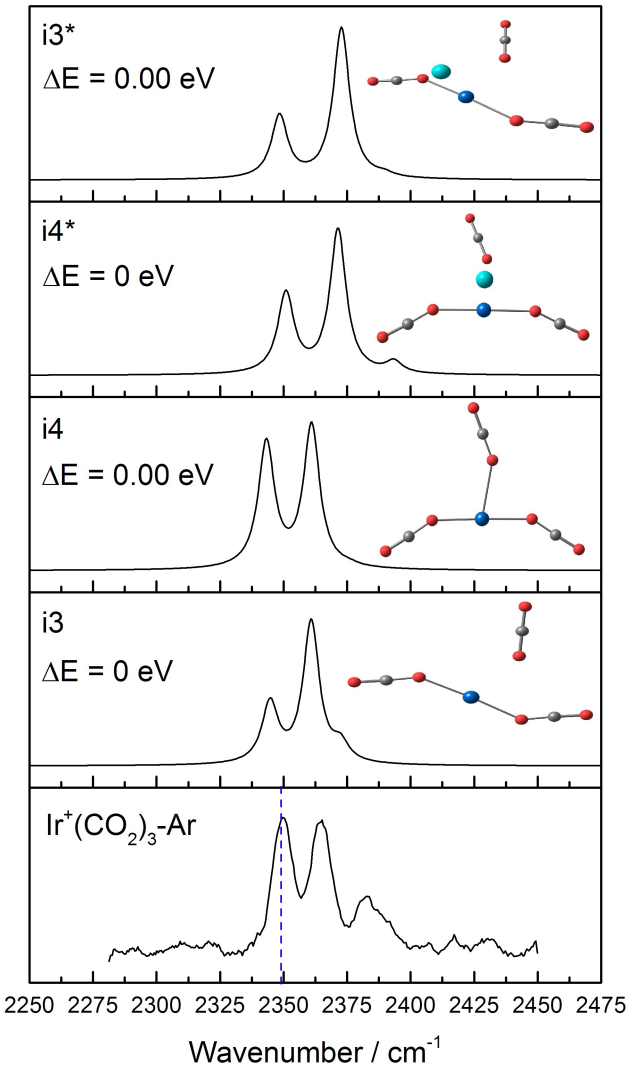

Figure 4.21: Comparison of the IR-REPD spectra for $Ir^+(CO_2)_3$–Ar with DFT candidate structures (i3, i4, i4* and i3*) calculated at the B3P86/Def2TZVP level of theory. Both neat and Ar-tagged calculated structures are considered. The relative energy differences are calculated with respect to the putative global minimum structures for both the untagged and Ar-tagged complexes. The two isomers are energetically indistinguishable (even after the addition of an argon atom). For both $Ir^+(CO_2)_3$–Ar DFT calculated isomeric structures, the three CO_2 molecules lie all virtually in the same plane with the argon atom perpendicular to that plane. The vertical dashed line marks the position of the asymmetric stretch ν_3 in an isolated CO_2.

A competing, almost isoenergetic structure (i4) shows a similar trend with significantly shorter bond distances for the two core molecules (*ca.* 2.07 Å versus 2.48 Å). Additionally, Ar-tagged counterparts for $n = 3$ geometries have been considered, which yielded structures i3* and i4*. These two structures are essentially isoenergetic. The Ar-tagged calculated structures predict no additional features in the IR spectrum. DFT simulated IR spectra for all identified structures compare well with the experimental data.

4.5.2 IR-REPD Spectra for Multiply Argon-Tagged Complexes

Figure 4.22 shows IR-REPD spectra for singly and doubly Ar-tagged complexes of $Ir^+(CO_2)_2$ and $Ir^+(CO_2)_3$. The binding of an additional argon atom does not appear to introduce any additional feature into the spectra recorded with only a single Ar-tag. Nor does an additional argon atom change the positions of the bands observed in the IR-REPD spectra.

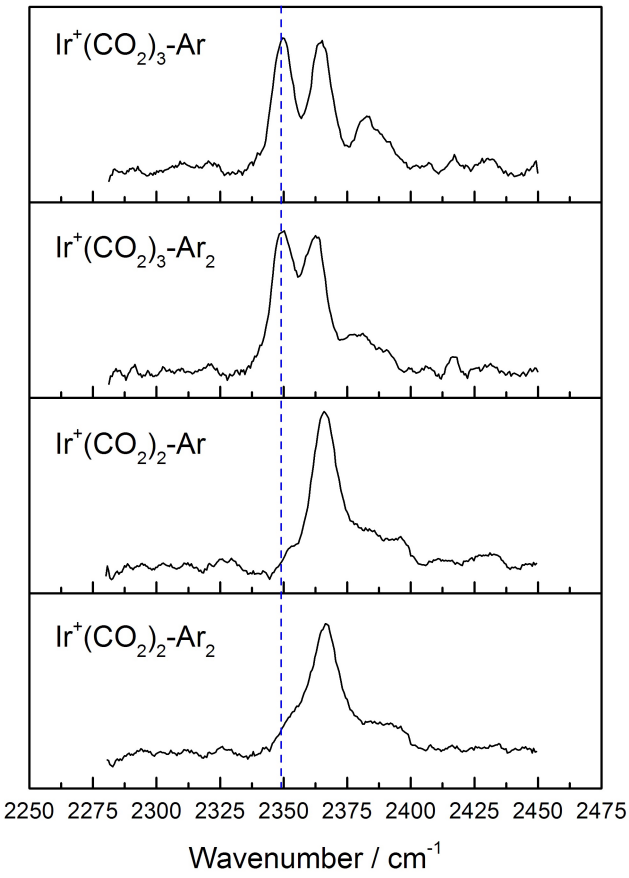

Figure 4.22: IR-REPD spectra for singly and doubly Ar-tagged complexes of $Ir^+(CO_2)_2$ and $Ir^+(CO_2)_3$. The dashed vertical line indicates the energy of the asymmetric stretch in free CO_2 at 2349 cm^{-1}.

4.5.3 Trends for Larger $Ir^+(CO_2)_n$ Complexes

Figure 4.23 shows peak positions plotted versus cluster size for $Ir^+(CO_2)_n$. Relative to $Co^+(CO_2)_n$ and $Rh^+(CO_2)_n$ complexes, the changes upon complexation with additional ligands are more noticeable for Ir^+. Contrary to the Co^+ and Rh^+ based complexes, the energy of the peak corresponding to the in-phase combination of the asymmetric stretch for core CO_2 ligands (at *ca* 2365 cm^{-1} for $n = 3$) initially red-shifts upon sequential addition of two CO_2 molecules. This feature appears at 2357 cm^{-1} for $n = 4$ and at 2353

cm^{-1} for $n = 5$. Tracing the movement of these features reveals a continuous blue-shift from $n = 6$ onwards and steadily plateaus with an increasing number of ligands. This feature can be found at approximately 2365 cm^{-1} for $n = 15$.

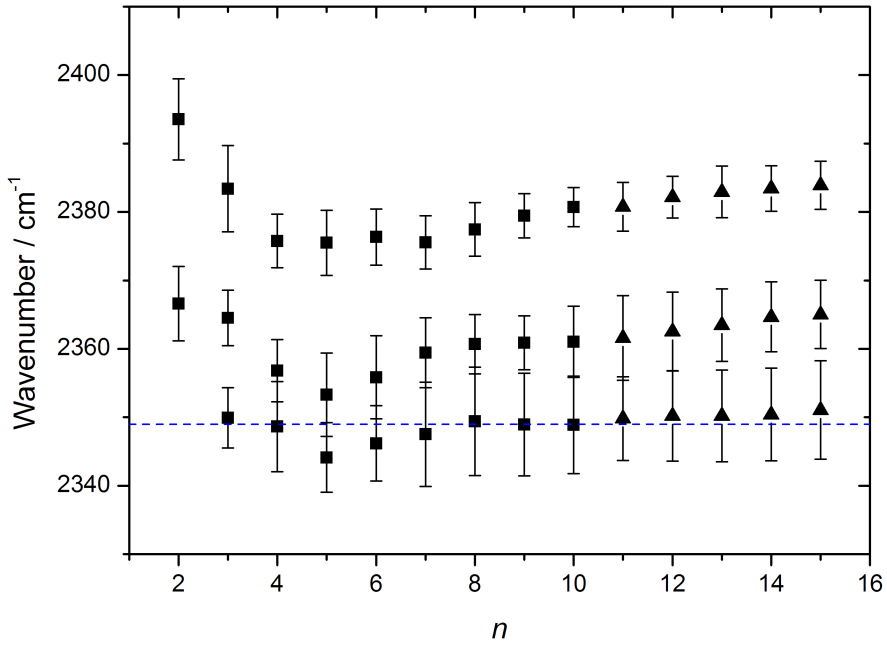

Figure 4.23: Peak positions plotted versus cluster size for $Ir^+(CO_2)_n$. The square markers correspond to argon-tagged complexes whereas triangles correspond to neat $Ir^+(CO_2)_n$ complexes. The error bars correspond to the full-width-half-maximum of a fitted Gaussian used to identify the exact centre of each peak. The horizontal dashed line indicates the vibrational frequency of the asymmetric stretch of an isolated CO_2 at 2349 cm^{-1}.

The feature corresponding to the out-of-phase combination of the asymmetric stretch of the two core ligands follows a similar trajectory reaching 2384 cm^{-1} for $n = 15$. It is worth noting that for $n = 5$, 6 and 7 the features due to out-of-phase combinations of core ligands and that of surface ligands overlap to the point where they become unresolved. Peak positions are then only found by fitting a Gaussian function, which is in itself a convolution of two

separate Gaussian functions. As anticipated, the features corresponding to the surface ligands experience minimal interaction with the central ion. These features remain around the energy of the asymmetric stretch of CO_2 even in the largest complexes studied here.

4.6 Trends and Comparisons for CO_2 Complexes of Group 9 Metal Cations

The spectra of $Co^+(CO_2)_2$ is anomalous in exhibiting only a single feature in its IR-REPD spectrum. This is, nevertheless, consistent with the high order $D_{\infty h}$ symmetry for the $Co^+(CO_2)_2$ complex. For Rh^+ and Ir^+ based complexes, an additional shoulder peak is observed in the case of $n = 2$ complexes. A bent structure for $Rh^+(CO_2)_2$ and $Ir^+(CO_2)_2$ renders the in-phase combination of CO_2 normal modes IR-active. On the other hand, in the case of a linear structure for $Co^+(CO_2)_2$, the in-phase combination remains IR-inactive.

An additional feature corresponding to the non-core ligands appears at $n = 3$ for complexes with all three group 9 metal cations. The surface bands for Co^+ and Rh^+ complexes exhibit a progressive red shift towards the energy of the asymmetric stretch in free CO_2 molecule (2349 cm^{-1}). Ligands with a frequency of free CO_2 vibrational frequency are identified at around $n = 9$ for Co^+ and at $n = 5$ for Rh^+. For Ir^+ complexes the change between the core and outer coordination sphere is, however, more striking – a band around 2349 cm^{-1} is already observed for the $n = 3$ complex. Comparing with complexes of the Co^+ and Rh^+ ion, $Ir^+(CO_2)_n$ complexes exhibit a more pronounced size-dependence. In the case of all three metal ions, the features corresponding to the core ligands continue to blue-shift without reaching a plateau even in the largest complexes studied here ($n = 15$).

Calculations performed at the DFT level of theory provide additional evi-

dence pointing towards the $[M^+(CO_2)_2]$ core structure to which additional CO_2 molecules bind more weakly. Trends in the binding energies for successive CO_2 ligands, displayed in Figure 4.24 as a function of cluster size, support this interpretation. The binding energies of a CO_2 ligand in a particular complex are calculated by considering the total energy of an optimised complex of size n versus the energy of an (n - 1) complex and an isolated CO_2 molecule (*i.e.* $M^+(CO_2)_n \rightarrow M^+(CO_2)_{n-1} + CO_2$).

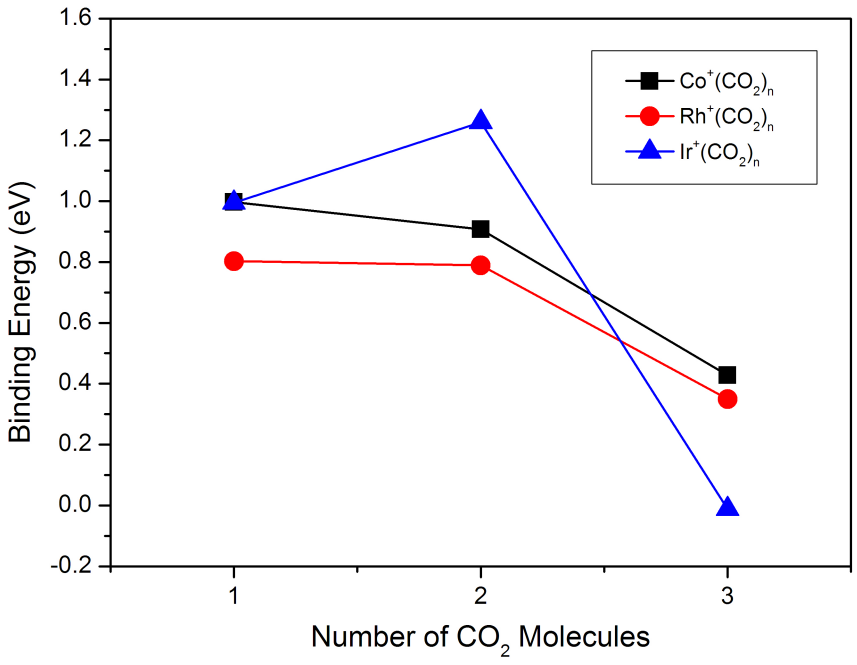

Figure 4.24: Binding energies of successive CO_2 ligands to $M^+(CO_2)_n$ complexes calculated at the B3P86/Def2TZVP level of theory. The energies include zero-point energy corrections. The binding energies for each complex are calculated by considering the energy difference between the putative global minimum structure of the parent cluster and the products resulting from a loss of a CO_2 ligand.

The binding of the third CO_2 molecule is significantly weaker than that for the first two ligands. The most pronounced change in binding energy is observed in the case of $Ir^+(CO_2)_3$ with a binding energy computed to be

close to zero. This is, nevertheless, consistent with a rather large Ir^+–O bond distance for the third CO_2 and the observation of a feature at virtually free CO_2 vibrational frequency in the IR-REPD spectrum for $Ir^+(CO_2)_3$.

4.7 Conclusions

IR-REPD spectra for the smaller complexes are acquired by employing an argon atom as the inert messenger. A combination of IR-REPD spectroscopy and DFT calculations reveals a common $[M^+(CO_2)_2]$ core for the complexes of Co^+, Rh^+ and Ir^+. Additional ligands experience less perturbation as evident in the reduced blue-shift for the surface ligands. Only in the case of $Ir^+(CO_2)_2$ does the addition of an Ar-tag perturb the system and significantly change the relative energetic order of the two lowest identified structures. For $Ir^+(CO_2)_n$ complexes the transition to second coordination sphere is the most pronounced, whereas the complexes of Co^+ and Rh^+ ions exhibit a more gradual transition. A linear structure is identified for $Co^+(CO_2)_2$, but propensity towards a non-linear structure is observed for $Rh^+(CO_2)_2$ and $Ir^+(CO_2)_2$. This is consistent with trends in polarisabilities for the group 9 metal cations.

Chapter 5

Transition Metal Oxides: Infrared Spectroscopy of $NbO_2^+(CO_2)_n$ and $TaO_2^+(CO_2)_n$ Complexes

$NbO_2^+(CO_2)_n$ and $TaO_2^+(CO_2)_n$ complexes are investigated in the region of the asymmetric stretch of CO_2, where the IR-REPD spectra for small complexes are recorded *via* the means of argon tagging. Ligands directly attached to the central ion experience a blue-shift from the vibrational frequency of free CO_2 consistent with O-end coordination of ligands. IR-REPD investigation of $NbO_2^+(CO_2)_n$ and $TaO_2^+(CO_2)_n$ complexes reveals, in both cases, a strongly bound core of four CO_2 ligands around NbO_2^+ and TaO_2^+ ions, as indicative from vibrational resonances observed at the energy close to that of free CO_2 at $n \geq 5$. Conclusions drawn from the experimental IR-REPD spectra are reinforced by the DFT calculations, which reveal a significant increase in the intermolecular bond distances and low binding energies for the ligands in the second coordination sphere. A remarkable similarity is observed among the equivalent complexes of the NbO_2^+ and TaO_2^+ ions in

stark contrast with well-studied $V^+(CO_2)_n$ complexes.

5.1 Introduction

As discussed in Section 1.3 of the Introduction, Bohme *et al.* studied the reactivity of various metal cations with CO_2.[70] For Nb^+ and Ta^+, O-atom transfer was observed as the dominant reaction pathway. This is explained on the grounds of large O-atom affinity of 7.13 ± 0.11 eV for Nb^+ and 8.15 ± 0.65 eV for Ta^+ that compensates for the cleavage of the O-CO bond.[315,316] Reaction efficiency for O-abstraction by Nb^+ and Ta^+ ions are 25% and 36%, respectively. For both ions, the O-atom abstraction is strongly exothermic. O-atom abstraction and formation of MO^+ is a spin-forbidden process for both Nb^+ and Ta^+. Alas, the exact potential energy surfaces and coupling between different states are not known and continue to represent a challenge for computational chemistry. Furthermore, Bohme *et al.* observed CO_2 clustering around NbO_2^+ and TaO_2^+ ions, which led to the formation of larger $NbO_2^+(CO_2)_{0-3}$ and $TaO_2^+(CO_2)_{0-4}$ complexes. Clustering around NbO_2^+ and TaO_2^+ is also an exothermic process for which Bohme and co-workers determined a negative standard energy of reaction ($\Delta G^\circ < 0$).

Reactions of Nb^+ and Ta^+ with O_2 in solid argon matrices were studied by Zhou and Andrews.[317] Laser ablated metal species were co-deposited with O_2 in a solid argon matrix at 10 K. Using FT-IR spectroscopy, the authors were able to identify the formation of NbO, NbO_2, TaO and TaO_2 in all three charge states. Both Nb^+ and Ta^+ ions are quintets in their electronic ground states. However, DFT calculations at the BP86/D95* level of theory by Zhou and Andrews identified the triplet as the ground states for NbO^+ and TaO^+. Ground states of NbO_2^+ and TaO_2^+ were both determined to be singlets.

Wesendrup and Schwarz studied the reaction of Ta^+ cation with CO_2 using the Fourier Transform Ion Cyclotron Resonance (FT-ICR) mass spectrom-

etry.[318] As shown in Figure 5.1, TaO_2^+ ions were formed in a reaction of laser ablated Ta^+ with CO_2 in FT-ICR cell. The dominant reaction product, TaO_2^+, is formed by sequential oxygen abstraction:

$$Ta^+ + CO_2 \rightarrow TaO^+ + CO, \tag{5.1}$$

$$TaO^+ + CO_2 \rightarrow TaO_2{}^+ + CO. \tag{5.2}$$

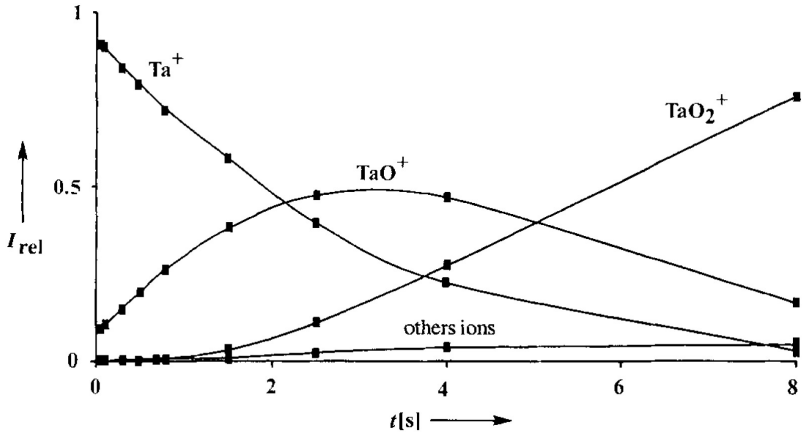

Figure 5.1: Plot of ion intensity versus resident time in the FT-ICR cell displays the temporal evolution of ions. Reaction of CO_2 with Ta^+ leads to the formation of TaO_2^+ as the dominant product. Figure reproduced from Wesendrup, R.; Schwarz, H. *Angew. Chem. Inter. Ed.*, 1995, 34, 2033–2035 with permission from Wiley & Sons Inc.[318]

Interestingly, Wesendrup and Schwarz also discovered that Ta^+ can assist in the coupling of CO_2 and CH_4 to form a ketene. Reaction of Ta^+ with CH_4 leads to direct dehydrogenation of methane. Thus formed TaH_2^+ sequentially abstracts oxygen atom from two CO_2 molecules while forming C_2H_2O. The following reaction scheme was proposed:

$$Ta^+ + CH_4 \rightarrow TaCH_2{}^+ + H_2, \tag{5.3}$$

$$TaCH_2^+ + CO_2 \rightarrow TaOCH_2^+ + CO, \tag{5.4}$$

$$TaOCH_2^+ + CO_2 \rightarrow TaO_2^+ + C_2H_2O. \tag{5.5}$$

The only known IR-REPD investigation of CO_2 solvation around a metal dioxide ion is the study of $NiO_2^+(CO_2)_n$ complexes by the Duncan group.[286] NiO_2^+ core was formed by seeding low percentage of O_2 to the buffer gas in addition to CO_2. The authors observed photodissociation of $NiO_2^+(CO_2)_n$ complexes only by loss of CO_2 ligands, which signified a strongly-bonded covalent dioxide for NiO_2^+. The photodissociation of $NiO_2^+(CO_2)_n$ complexes terminates at $n = 2$, which indicates a strongly-bound core of the $NiO_2^+(CO_2)_2$ ion. Furthermore, the complexes also display a notable increase in the photodissociation efficiency at $n = 3$. If oxygen occupies a ligand space then the coordination number in the inner sphere is in fact four. This is consistent with the work on $Ni^+(CO_2)_n$ complexes by the same authors, which revealed four CO_2 ligands in the first coordination sphere.[286,287] The spectrum for $NiO_2^+(CO_2)_3$ shows three strong features, including a feature close to 2349 cm^{-1} signifying a weakly-bound CO_2 ligand. The authors assigned the remaining two blue-shifted features to the in-phase and out-of-phase combinations of two CO_2 ligands directly attached to NiO_2^+ ion. Theory predicts a cyclic structure for NiO_2^+,[319] which could allow bonding of two CO_2 ligands either in the same plane or perpendicular to the plane defined by the NiO_2^+ ion (giving C_{2v} symmetry). Lastly, the larger blue-shift observed for NiO_2^+-based complexes also signifies a stronger interaction relative to the complexes containing only Ni^+.

5.2 Experimental Methods

The experimental setup used to study the infrared spectroscopy of $TaO_2^+(CO_2)_n$ and $NbO_2^+(CO_2)_n$ complexes has been extensively discussed in previous chapters so only a brief description will be provided here. Tantalum and niobium atomic cations are produced by laser ablation of tantalum (Sigma Aldrich, 1 mm thickness, 99.9% purity) and niobium (Sigma Aldrich, 0.25 mm thickness, 99.8% purity) disk targets, respectively. A focused second harmonic of a Nd:YAG laser (532 nm) is used for ablation. $TaO_2^+(CO_2)_n$ and $NbO_2^+(CO_2)_n$ complexes are formed by seeding a small percentage of CO_2 in argon backing gas. The complexes are photodissociated using tunable IR-OPO/OPA laser and detected in a time-of-flight mass spectrometer.

All DFT calculations are performed at the B3P86/Def2TZVP level of theory. Starting structures are generated both manually and using the Kick algorithm of Addicoat and Metha.[307] Simulated infrared spectra are produced by convoluting calculated infrared signals with a Lorentzian function with FWHM of 4 cm^{-1} and scaled by a scaling factor of 0.962 (see Section 4.2).

5.3 Time-of-Flight Mass Spectra

A time-of-flight mass spectrum produced upon ablation of a niobium target using 1% CO_2 in argon is shown in Figure 5.2. $NbO_2^+(CO_2)_n$ and their argon-tagged counterparts are the most abundant complexes.

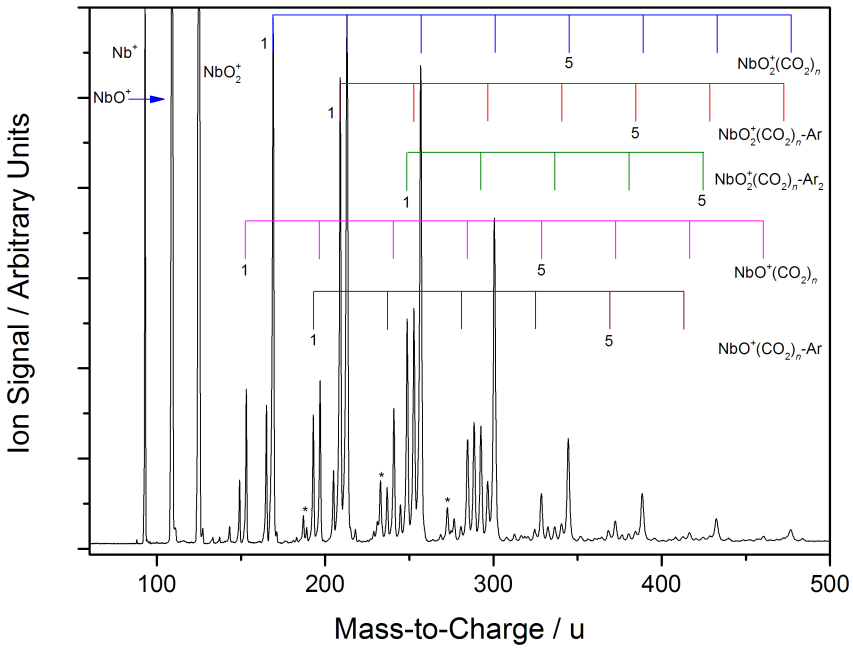

Figure 5.2: Time-of-flight mass spectrum generated by ablation of a niobium target in the presence of 1% CO_2 in argon at 6 bar backing pressure as the expansion gas. $NbO_2^+(CO_2)_n$ complexes and their argon-tagged counterparts dominate the mass spectrum. $NbO^+(CO_2)_n$ complexes are also detected. The asterisk * indicates a notable series that remains unassigned.

The time-of-flight mass spectrum generated upon ablation of tantalum disk in presence of 1% CO_2 in argon from 6 bar static pressure is shown in Figure 5.3. Similarly as for the ablation of a niobium target, the time-of-flight mass spectrum is dominated by $TaO_2^+(CO_2)_n$ complexes and its argon-tagged counterparts. Only trace amounts of $TaO^+(CO_2)_n$ complexes are produced. No $Ta^+(CO_2)_n$ complexes were observed, even at higher concentrations of CO_2 in the expansion gas.

Additionally, significant amounts of metal-free gaseous $(CO_2)_n^+$ are produced upon ablation of tantalum target. Conversely, no $(CO_2)_n^+$ complexes are formed when ablating niobium target. These gaseous-only complexes were

previously observed when ablating a vanadium target in the presence of N_2O in argon gas mix; $(N_2O)_n^+$ complexes, in this case, as discussed in Section 3.4.2. The ablation process also generates free electrons, which can in turn ionise CO_2. The formation of the $(CO_2)^+$ ion serves as a nucleation site to which other CO_2 can attach. This would not be a too dissimilar method for production of $(CO_2)_n^+$ complexes as that reported by Inokuchi *et al.*, who inject neat CO_2 gas into the source chamber where they cross the molecular beam with an electron beam.[320]

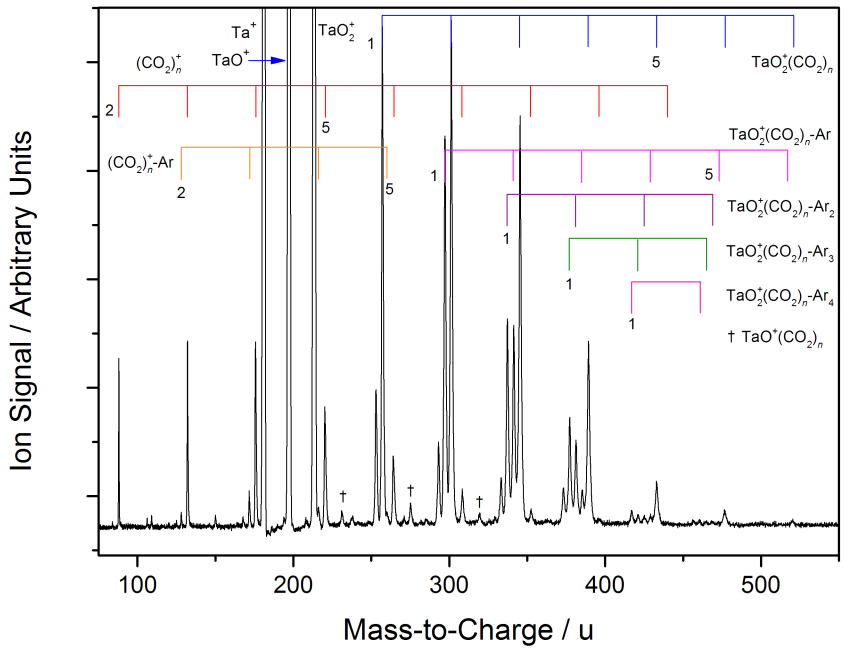

Figure 5.3: Time-of-flight mass spectrum produced by ablation of a tantalum target. 1% CO_2 in argon at 6 bar backing pressure is used as the expansion gas. $TaO_2^+(CO_2)_n$ complexes are the dominant species produced. Argon-tagged complexes with up to four argon atoms are produced.

The observed $MO_2^+(CO_2)_n$ complexes in the respective time-of-flight mass spectra for M = Nb and Ta are markedly different from the comparable distribution of species formed upon ablation of a vanadium target in presence of

CO_2/Ar expansion gas, as previous work by Duncan *et al.*[272] and experiments presented in Section 3.5 of this thesis demonstrate, where $V^+(CO_2)_n$ complexes dominate the mass spectrum. No $M^+(CO_2)_n$ complexes were observed for M = Nb and Ta. However, formation of $MO_2^+(CO_2)_n$ complexes is consistent with kinetics measurements by Bohme *et al.* and mass-spectroscopic work by Schwarz *et al.* (for Ta^+), who observed that Nb^+ and Ta^+ react with CO_2 molecules by O-atom transfer, forming NbO_2^+ and TaO_2^+, respectively.[297,318] Exothermic clustering of CO_2 around NbO_2^+ and TaO_2^+ was also observed by the Bohme group. While the reaction efficiencies for O-abstraction by Nb and Ta ions are 25% and 36%, respectively, the comparable value of 0.06% for V is markedly lower.

O-atom abstraction is exothermic for all group 5 cations: V^+, Nb^+ and Ta^+. [i] However, Bohme *et al.* attributed low reaction efficiency for the reaction involving V^+ to the absence of available surfaces to form ground state $VO^+(X^3\Sigma)$ from V^+ (X^5D) in a spin-forbidden process.[297] The Armentrout group nevetheless observed the formation of VO^+ *via* O-atom transfer to V^+ in their collision induced experiment even at centre-of-mass collision energies close to zero.[274] The authors assigned the formation of VO^+ from the V^+ ground state even though they leave open to speculation that VO^+ may result from excited state V^+ or by reaction with O_2 contaminant.

Upon ablation of a vanadium target in the presence of CO_2/Ar, we observed the formation of $VO^+(CO_2)_n$ complexes, albeit in lower abundances than the $V^+(CO_2)_n$ (*vide* Section 3.5.2). $VO^+(CO_2)_n$ complexes may result from the vanadium oxide layer formed on the top of the target (as exploited in the formation of neutral VO molecules, see Chapter 6). No VO_2^+ dominated complexes were ever observed in our experiment, nor by the Bohme group. However, Armentrout *et al.* observed the formation of VO_2^+ from the reaction of V^+ and CO_2 but only at high centre-of-mass collision energies of *ca.* 9

[i] Oxygen affinities are: 5.85 ± 0.15 eV, 7.13 ± 0.11 eV, 8.15 ± 0.65 eV for V^+, Nb^+ and Ta^+, respectively.[315,316,321] The corresponding oxygen affinity to CO (*i.e.* OA(CO)) is 5.52 eV.[316]

eV.[274] The measured oxygen atom affinity for OV–O of 3.6 ± 0.40 eV by Armentrout *et al.* makes the abstraction of second oxygen atom endothermic. Conversely, the abstraction of the second O-atom is exothermic for both Nb^+ and Ta^+, [ii] which governs the formation of NbO_2^+ and TaO_2^+ as exhibited in Figure 5.2 and Figure 5.3.

Lastly, comparison of the equivalent niobium and tantalum time-of-flight mass spectra also reveals that only trace amounts of $TaO^+(CO_2)_n$ complexes are produced, whereas $NbO^+(CO_2)_n$ are noticeably more abundant. This is consistent with comparatively higher O-affinity for Ta^+ and TaO^+ and with the formation of the MO_2^+ ion being the fastest for the Ta^+ ion as the kinetics experiments by Bohme *et al.* demonstrate.

5.4 DFT Calculations: NbO_2^+ and TaO_2^+ Ions

Nb^+ and Ta^+ ions themself are quintets in their ground electronic state.[323] Table 5.1 lists the calculated energy ordering for electronic states of NbO^+, NbO_2^+, TaO^+ and TaO_2^+. The calculations reveal a triplet ground state for MO^+ and singlet for MO_2^+ for M = Nb and Ta. For both metal ions, the triplet and quintet states for the MO_2^+ ion are significantly higher in energy (2.31 eV and 5.78 eV for NbO_2^+, and 1.60 eV and 5.27 eV for MO_2^+). Triplet and singlet ground states were previously reported by Zhou and Andrews for MO^+ and MO_2^+ where M = Nb and Ta, respectively.[317]

[ii] O–MO^+ oxygen affinities are 5.72 eV and 6.07 eV for NbO^+ and TaO^+, respectively.[322]

Table 5.1: Theoretical energies for NbO^+, NbO_2^+, TaO^+ and TaO_2^+ calculated at the B3P86/Def2TZVP level of theory. The electronic energies for Nb^+ and Ta^+ are quoted from the NIST Atomic Spectral Database.[323] Contrary to the metal ion, in their ground states, MO^+ and MO_2^+ are triplets and singlets for M = Nb and Ta, respectively.

Species	Multiplicity	ΔE / eV	Species	Multiplicity	ΔE / eV
Nb^+	quintet (^{5}D)	0.0	Ta^+	quintet (^{5}D)	0
	triplet (^{3}P)	0.72		triplet (^{3}P)	0.46
	singlet (^{1}D)	1.46		singlet (^{1}D)	1.33
NbO^+	triplet	0.0	TaO^+	triplet	0
	singlet	0.85		singlet	0.98
	quintet	15.32		quintet	3.48
NbO_2^+	singlet	0.0	TaO_2^+	singlet	0
	triplet	2.31		triplet	1.60
	quintet	5.78		quintet	5.27

Figure 5.4 displays structural parameters for NbO^+, NbO_2^+, TaO^+ and TaO_2^+ in their ground electronic states. NbO_2^+ and TaO_2^+ ions are of C_{2v} symmetry and all multiplicities give a structure with "dissociated" O_2. Ions with an intact oxygen molecule (M^+O–O) do not converge to a minimum.

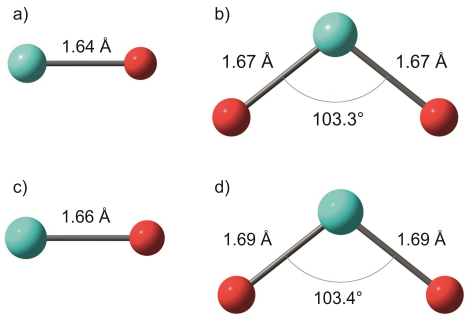

Figure 5.4: Structural parameters for optimised structures for the ground state multiplicities of a) NbO^+ (triplet), b) NbO_2^+ (singlet), c) TaO^+ (triplet) and d) TaO_2^+ (singlet). All calculations are performed at the B3P86/Def2TZVP level of theory and provide a basis for the calculation of complex structures to follow.

5.5 IR-REPD Spectra for $NbO_2^+(CO_2)_n$ and $TaO_2^+(CO_2)_n$

Figure 5.5 displays the experimental IR-REPD spectra for $MO_2^+(CO_2)_n$ complexes, where M = Nb and Ta. For the $n = 1$ complex, the IR-REPD spectrum is recorded by considering the doubly argon-tagged $NbO_2^+(CO_2)$–Ar_2 complex. Here we were unable to record an IR-REPD spectrum for a singly argon-tagged $NbO_2^+(CO_2)$–Ar. Instead, it was possible to record an IR-REPD spectrum for doubly argon tagged $NbO_2^+(CO_2)$–Ar_2 complex with an adequate signal-to-noise as shown in Figure 5.5. It appears that two argon atoms sufficiently increase the density of states for this particular complex and consequently an increased IVR rate allows the IR-REPD spectrum to be recorded experimentally. Additionally, the binding of the second argon atom might be significantly weaker.

Figure 5.5 also shows IR-REPD spectra for $TaO_2^+(CO_2)_{1-6}$–Ar and $TaO_2^+(CO_2)_7$ recorded in the channels corresponding to the depletion of the parent ion. Here we were able to obtain the experimental IR spectrum for the smallest cluster $n = 1$, albeit with a poorer signal-to-noise ratio than other comparable spectra. This is not unusual - $TaO_2^+(CO_2)_1$–Ar has a rather low fragmentation yield as it contains only one CO_2 available for IR absorption. Additionally, the IVR process is expected to be rather slow here - stemming from the low density of states available.[285]

As seen from Figure 5.5, there is a stark similarity between the complexes of the NbO_2^+ and TaO_2^+ ions. For all complexes, a blue-shift in the vibrational frequencies relative to that of a free CO_2 indicates an O-end binding of intact CO_2 ligands to the central ion. For both ions, a feature close to the frequency of free CO_2 becomes apparent from $n = 5$ onwards. This feature is indicative of a weakly-bound molecule not directly attached to the MO_2^+ ion for M = Nb and Ta.

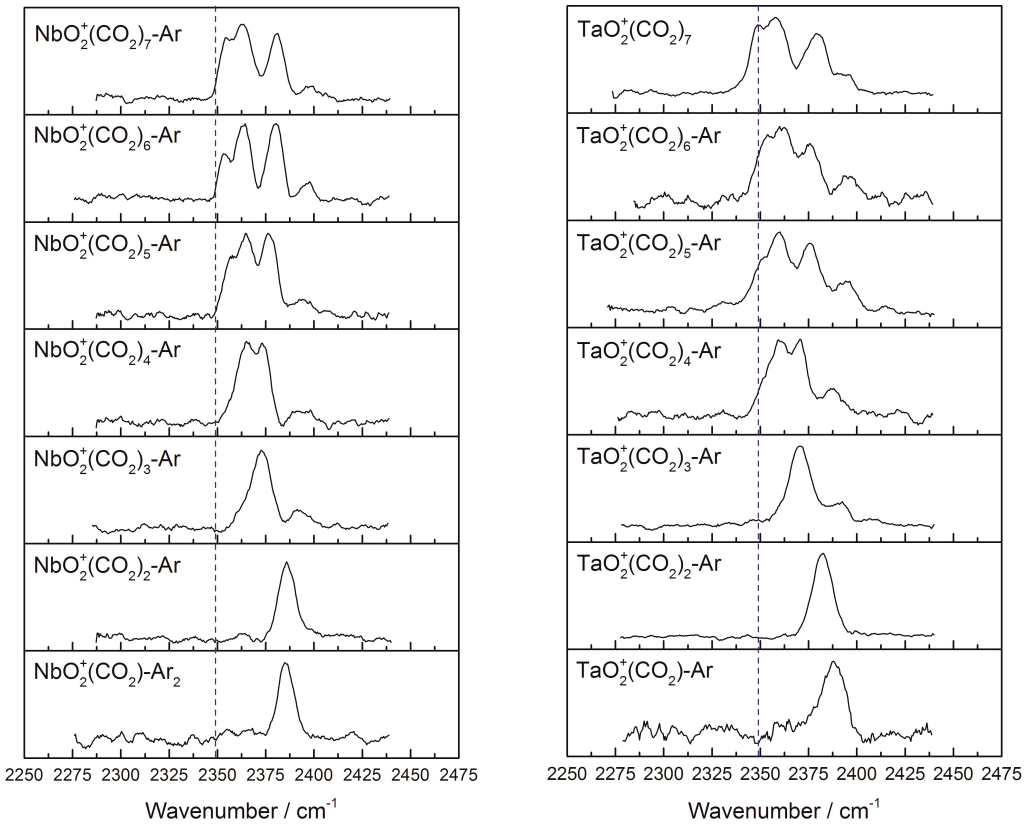

Figure 5.5: Left: IR-REPD spectra for argon-tagged $NbO_2^+(CO_2)_n$. Right: IR-REPD spectra for $TaO_2^+(CO_2)_{1-6}$–Ar and $TaO_2^+(CO_2)_7$ complexes. In all instances the IR-REPD spectra are recorded in the channel corresponding to the depletion of the parent ion. The vertical dashed line marks the position of the asymmetric stretch ν_3 in an isolated CO_2.

5.6 Simulated IR Spectra for $NbO_2^+(CO_2)_n$

5.6.1 Structural Parameters and Theoretical Energies

Table 5.2 lists the theoretical energies for all calculated structures. Singlet, triplet and quartet multiplicities were considered for $n = 1$, 2 and 3. Singlet multiplicities are consistently found to be the lowest in energy. Figure 5.6 displays structural parameters for all assigned structures.

Table 5.2: Theoretical energies for $NbO_2^+(CO_2)_n$ complexes calculated at the B3P86/Def2TZVP level of theory. The energies are inclusive of zero-point energy corrections. The ΔE refers to the relative energy difference to the global minimum structure for each complex size. For $NbO_2^+(CO_2)_{1-3}$, singlet, triplet and quintet multiplicities are considered. In all instances, the global minima structures are of singlet multiplicities.

Species	Multiplicity	Energy / eV	ΔE / eV	Structure
$NbO_2^+(CO_2)$	singlet	-10799.83011	0	n1
	triplet	-10797.39483	2.44	–
	quintet	-10793.97496	5.86	–
$NbO_2^+(CO_2)$–Ar	singlet	-25165.04869	–	n1*
$NbO_2^+(CO_2)$–Ar_2	singlet	-39529.93571	–	n1**
$NbO_2^+(CO_2)_2$	singlet	-15945.01979	0	n2
	triplet	-15942.2309	2.88	–
	quintet	-15938.31039	6.71	–
$NbO_2^+(CO_2)_2$Ar	singlet	-30309.86143	0	n2*
$NbO_2^+(CO_2)_3$	singlet	-21089.58285	0	n3
	singlet	-21088.89418	0.69	n4
	triplet	-21087.38134	2.20	–
	quintet	-21083.49917	6.08	–
$NbO_2^+(CO_2)_3$–Ar	singlet	-35454.33442	0	n3*
$NbO_2^+(CO_2)_3$–Ar	singlet	-35453.68869	0.65	n4*
$NbO_2^+(CO_2)_4$	singlet	-26233.90905	0	n5
	singlet	-26233.6949	0.21	n6
	singlet	-26233.47855	0.43	n7
	singlet	-26230.16875	3.74	n8
$NbO_2^+(CO_2)_5$	singlet	-31378.01330	0	n9
	singlet	-31378.01155	0.00	n10
	singlet	-31377.88365	0.13	n11
	singlet	-31373.29089	4.72	n12
$NbO_2^+(CO_2)_6$	singlet	-36522.11528	0	n13
	singlet	-36522.11321	0.00	n14
	singlet	-36521.991	0.12	n15
	singlet	-36517.03238	5.08	n16
$NbO_2^+(CO_2)_7$	singlet	-41666.20232	0	n17
	singlet	-41666.2014	0.00	n18
	singlet	-41661.13103	5.07	n19

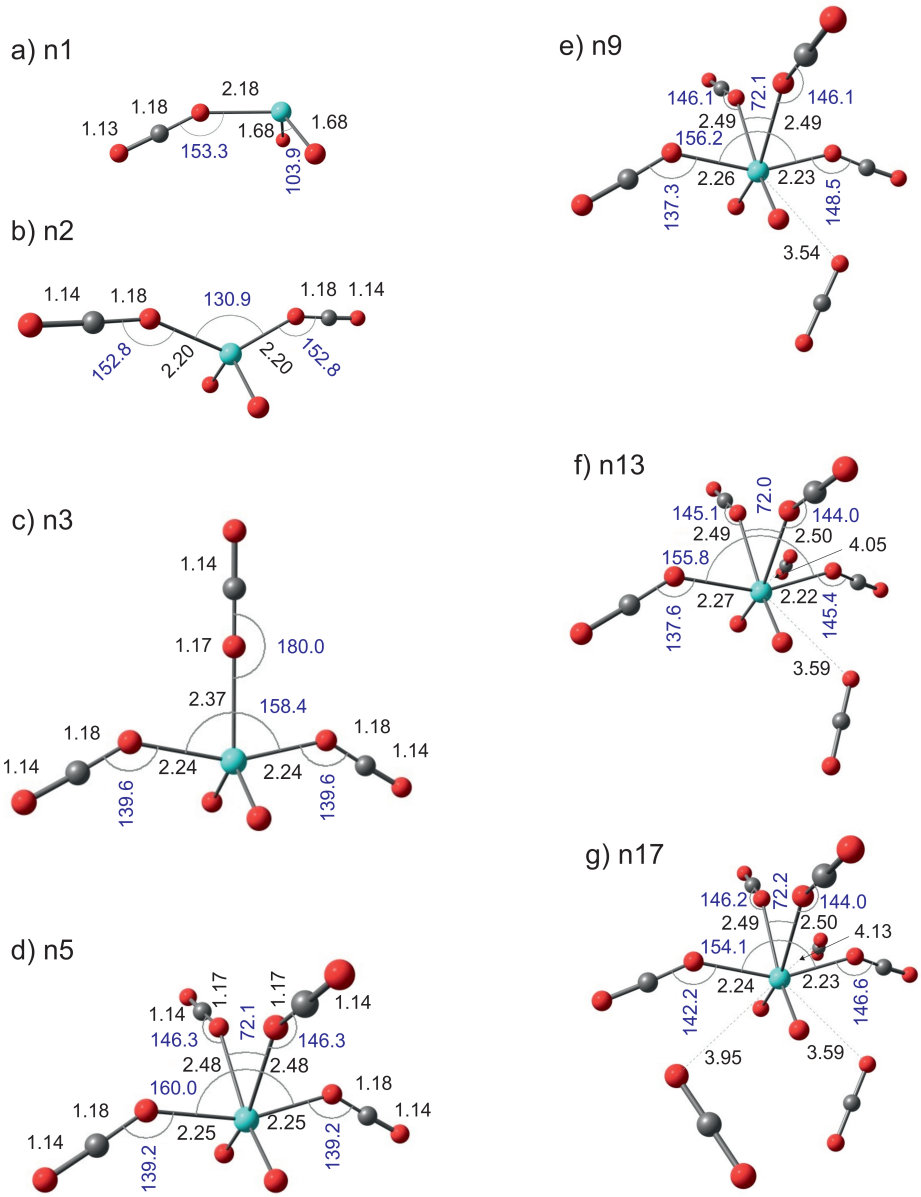

Figure 5.6: Structural parameters for the global minimum structures: a) $NbO_2^+(CO_2)$ (structure n1), b) $NbO_2^+(CO_2)_2$ (structure n2), c) $NbO_2^+(CO_2)_3$ (structure n3), d) $NbO_2^+(CO_2)_4$ (structure n5), e) $NbO_2^+(CO_2)_5$ (structure n9), f) $NbO_2^+(CO_2)_6$ (structure n13) and g) $NbO_2^+(CO_2)_7$ (structure n17). Bond distances (black) are in Ångstroms (Å) and bond angles (blue) are in degrees (°). All calculations are performed at the B3P86/Def2TZVP level of theory. Colour scheme: niobium (light green), oxygen (red) and carbon (grey).

5.6.2 $NbO_2^+(CO_2)$–Ar_2

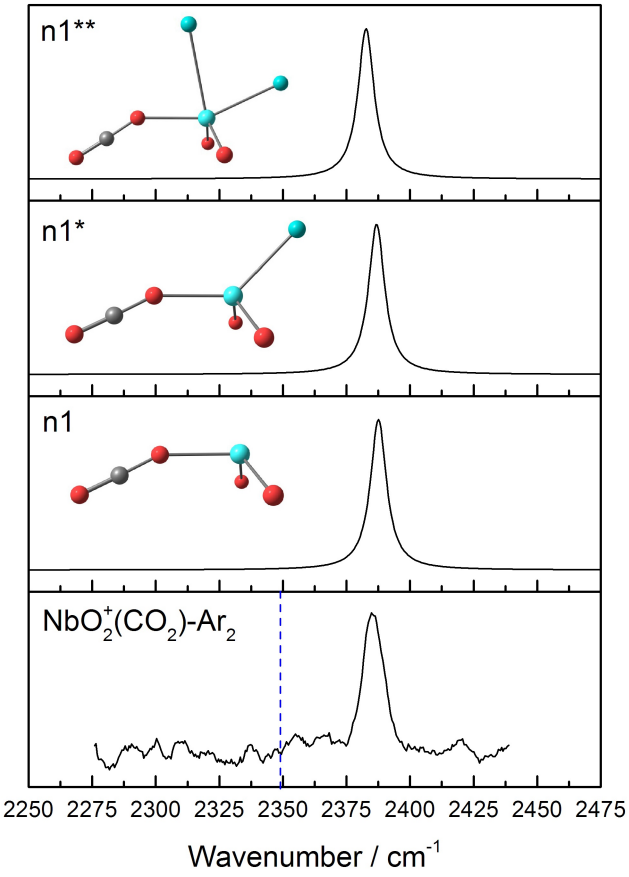

Figure 5.7: Experimental IR-REPD spectrum for $NbO_2^+(CO_2)$–Ar_2 together with the simulated IR spectra for neat (n1), singly and doubly argon-tagged structures (n1* and n1**, respectively). All calculations are performed at the B3P86/Def2TZVP level of theory. The vertical dashed line marks the position of the asymmetric stretch ν_3 in an isolated CO_2.

A comparison between the experimental and DFT simulated IR spectrum for $NbO_2^+(CO_2)$–Ar_2 is shown in Figure 5.7. A single strong feature centred at *ca.* 2386 cm^{-1} is observed. This feature is blue-shifted by 37 cm^{-1} from the asymmetric stretching frequency of free CO_2, which is consistent with an intact CO_2 bound to the NbO_2^+ ion as also confirmed by the DFT calculated structure, n1. The IR spectra for both singly and doubly argon-tagged calcu-

lated structures (n1* and n1**, respectively) show no discernible difference from the neat complex (n1). Only a modest relative red-shift is observed for the doubly argon-tagged structure, n1**. Examination of intermolecular bond distances (Figure 5.6, n1) reveals that the NbO_2^+ ion geometry remains virtually unperturbed upon complexation.

5.6.3 $NbO_2^+(CO_2)_2$–Ar

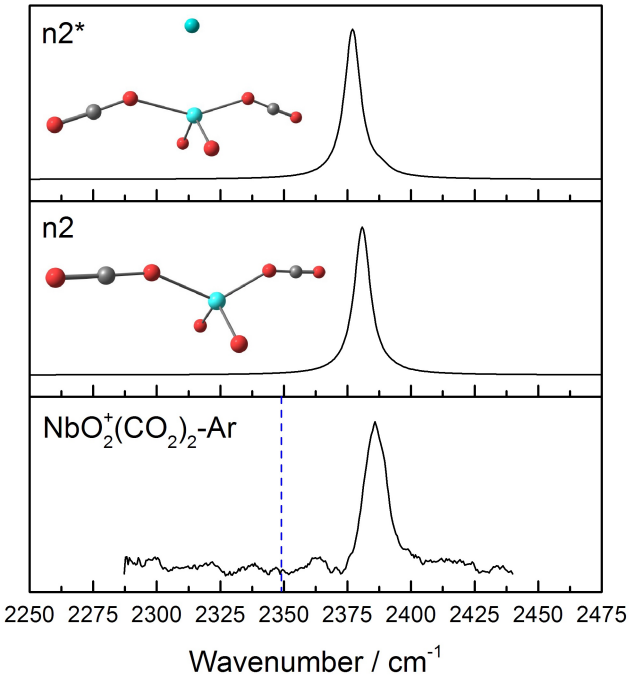

Figure 5.8: Experimental IR-REPD spectrum for $NbO_2^+(CO_2)_2$–Ar together with the simulated IR spectra for both the neat structure (n2) and its argon tagged counterpart (n2*). All calculations are performed at the B3P86/Def2TZVP level of theory. The vertical dashed line marks the position of the asymmetric stretch ν_3 in an isolated CO_2.

Similarly, the IR-REPD spectrum for $NbO_2^+(CO_2)_2$–Ar exhibits only a single blue-shifted feature centred at 2380 cm^{-1} (Figure 5.8). We previously observed a single feature for $Co^+(CO_2)_2$, which is of $D_{\infty h}$ symmetry. Here, DFT calculations predict a bent C_{2v} geometry with CO_2 molecules attached

on the opposite sides of the NbO_2^+ ion. As seen in Figure 5.6 (structure n2), the angle defined by C–O–Nb^+ is 152.8°, which is consistent with rather large polarisability of Nb^+ ($\alpha = 55.3\ a_0^3$).[314] Due to bending of each CO_2 ligand by 130.9° from the OCO–Nb^+–OCO axis, only the out-of-phase combination of the normal modes for the two CO_2 ligands leads to a change in the electric dipole moment. Even though the overall structure is bent, only a single feature is thus expected in the IR spectrum (as also observed experimentally). The geometry of structure n2 also indicates a non-covalently bound complex consistent with charge-quadrupole interaction between CO_2 and Nb^+, since steric repulsion would direct the ligands away from two oxygen atoms. Bent structures were similarly observed for $Rh^+(CO_2)_2$ and $Ir^+(CO_2)_2$ complexes as discussed in Chapter 4.

5.6.4 $NbO_2^+(CO_2)_3$–Ar

The IR-REPD spectrum for $NbO_2^+(CO_2)_3$–Ar shown in Figure 5.9 depicts a strong feature centred at *ca.* 2373 cm^{-1} and a blue-shifted shoulder peak at 2393 cm^{-1}. The DFT simulated IR spectrum agrees well with the experimental data. The "third" CO_2 is attached to the moiety identified for the $n = 2$ complex as revealed by comparing the intermolecular bond distances: 2.24 Å versus 2.37 Å for the third ligand (structure n3). The main spectral feature is a superposition of vibrations corresponding to: i) the asymmetric stretch centred on the third ligand, and ii) the out-of-phase combination of the asymmetric stretches of the two inner CO_2 molecules. The shoulder peak corresponds to the in-phase combination of the normal modes predominantly centred on the two inner CO_2 molecules. A higher lying isomer containing a "CO_3" moiety and *ca.* 0.69 eV above the global minimum structure is also identified (n4). This isomer is expected to absorb at *ca.* 1900 cm^{-1}. We looked in this spectral region but were unable to find any photofragmentation evidence that would support the presence of isomer n4 and its higher order derivatives in the molecular beam. Calculations involving an argon atom

reveal no additional features nor significant changes in the peak positions.

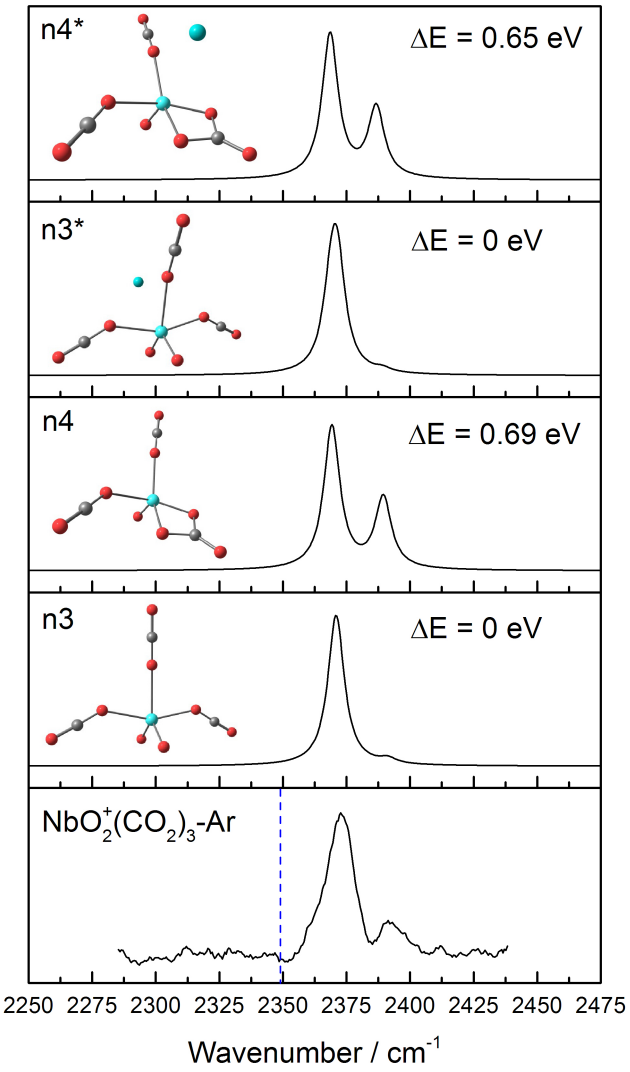

Figure 5.9: Experimental IR-REPD spectrum for $NbO_2^+(CO_2)_3$–Ar together with the simulated IR spectra for both, the neat structures (n3 and n4) and their argon-tagged counterparts (n3* and n4*). All calculations are performed at the B3P86/Def2TZVP level of theory. The vertical dashed line marks the position of the asymmetric stretch ν_3 in an isolated CO_2.

5.6.5 $NbO_2^+(CO_2)_4$–Ar

The calculated global minimum structure (n5) for $NbO_2^+(CO_2)_4$ consists of two "inner" CO_2 and two "outer" CO_2 ligands with the corresponding bond distances of 2.25 Å and 2.48 Å, respectively (see Figure 5.6 d)).

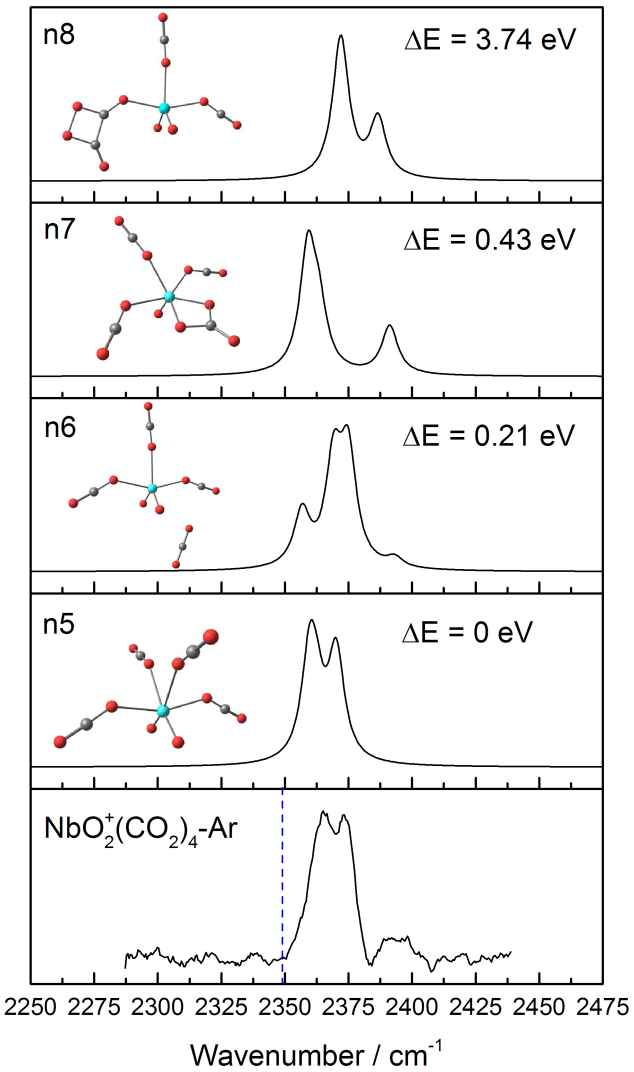

Figure 5.10: Experimental IR-REPD spectrum for $NbO_2^+(CO_2)_4$–Ar together with the simulated IR spectra for all candidate structures. All calculations are performed at the B3P86/Def2TZVP level of theory. The vertical dashed line marks the position of the asymmetric stretch ν_3 in an isolated CO_2.

The experimental IR-REPD spectrum for $NbO_2^+(CO_2)_4$ consists of three well-resolved features at 2366 cm^{-1}, 2373 cm^{-1} and 2394 cm^{-1}, as exhibited in Figure 5.10. This is reproduced well by the DFT simulated IR spectrum for structure n5, albeit with relatively weaker intensity for the most blue-shifted feature, which arises from in-phase combination of the asymmetric stretches of the two inner-most CO_2 molecules. The feature at *ca.* 2366 cm^{-1} is predicted to be a superposition of peaks due to both out-of-phase and in-phase combinations of the asymmetric stretches of the two outer CO_2 molecules. The remaining feature at 2373 cm^{-1} is due to the out-of-phase combination of the asymmetric stretching modes of the two inner-most CO_2 ligands. A higher-lying isomer (0.21 eV above global minimum) consisting of a $n = 3$ moiety and a more weakly-bound CO_2 was also identified (n6). This structure provides somewhat poorer agreement with the experimental data in terms of the relative band intensities. Nevertheless, its contribution to the overall IR spectrum cannot be completely disregarded. We see no evidence for isomer n7 being present in the molecular beam.

Interestingly, a structure with an oxalate C_2O_4 moiety laying 3.74 eV above the global minimum is also identified (structure n8). While this moiety has in the past been observed in large (n > 7) complexes of $V^+(CO_2)_n$ by Duncan *et al.*,[324] we see no evidence for this isomer in other spectral regions (*ca.* 1900 cm^{-1}) where the oxalate stretches are expected to occur. This isomer is also significantly higher in energy and as such, would be unlikely to form in the ablation source and be sufficiently long-lived to be probed experimentally.

5.6.6 $NbO_2^+(CO_2)_5$–Ar

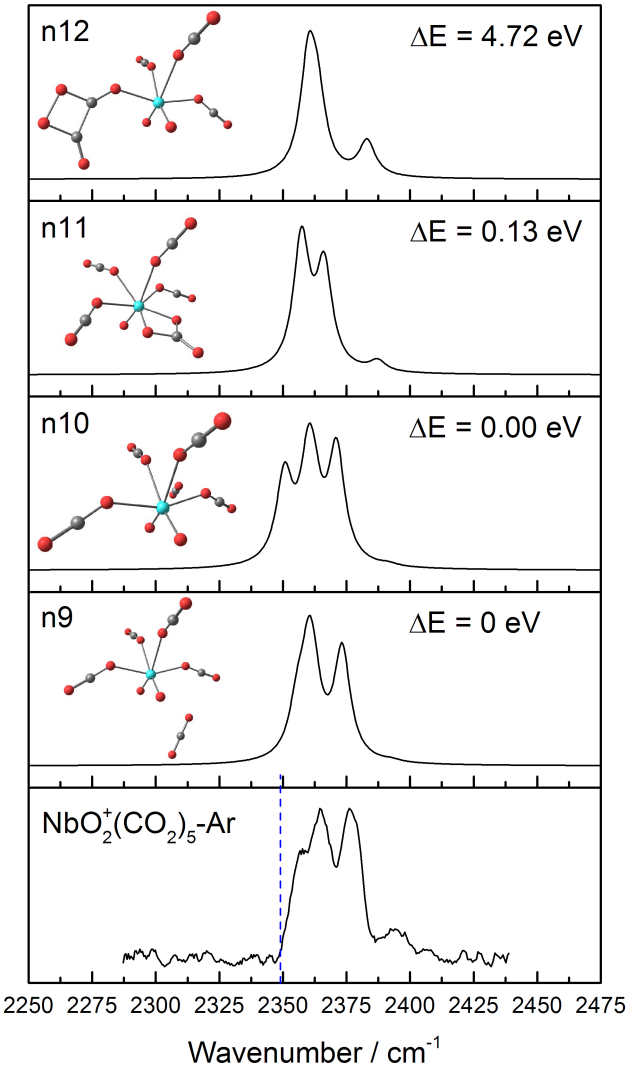

Figure 5.11: Experimental IR-REPD spectrum for $NbO_2^+(CO_2)_5$–Ar together with the simulated IR spectra for all candidate structures. All calculations are performed at the B3P86/Def2TZVP level of theory. The vertical dashed line marks the position of the asymmetric stretch ν_3 in an isolated CO_2.

In the IR-REPD spectrum for $NbO_2^+(CO_2)_5$–Ar presented in Figure 5.11, a shoulder peak at 2357 cm^{-1}, close to the energy of free CO_2, first appears. This suggest a weakly-bound, almost non-perturbed ligand residing in the

second coordination sphere. The remaining three features are observed at 2365 cm^{-1}, 2377 cm^{-1} and 2393 cm^{-1}. The DFT calculations suggest a core of the $NbO_2^+(CO_2)_4$ ion and a more weakly-bound "fifth" ligand (structure n9).

The $n = 4$ core itself is comprised of two pairs of two most inner and outer ligands with similar structural parameters, as in the $NbO_2^+(CO_2)_4$ complex. The intermolecular bond distance for the fifth ligand is then at 3.54 Å significantly longer than the comparable distances for the core ligands. An isoenergetic isomer n10 – with better resolved shoulder peak in the corresponding simulated IR spectrum – is also likely to be present in the molecular beam. Isomers n11 and n12 are unlikely to be contributing to the experimental IR spectrum.

5.6.7 $NbO_2^+(CO_2)_6$–Ar

The features for the $n = 6$ complex are observed at *ca.* 2353 cm^{-1}, 2363 cm^{-1}, 2380 cm^{-1} and 2397 cm^{-1} (Figure 5.12). The DFT-predicted global minimum structure consists of a core of four ligands with two additional weakly-perturbed ligands residing in the second coordination sphere (Figure 5.6, structure n13). Intermolecular bond distances confirm this: between 2.22 Å and 2.50 Å for the core ligands, and 3.59 Å and 4.05 Å for the second coordination sphere ligands (see Figure 5.6 f)).

An isoenergetic isomer, n14, is likely to be a competing structure as it involves only a repositioning of the second coordination sphere ligands. These structures may be sufficiently floppy to undergo rapid isomerisation. Ligands in the second coordination sphere are expected to be sufficiently weakly-bound with a low barrier for interconversion between different isomers (with no changes in the $n = 4$ core structure). The higher-lying isomers n15 and n16 are unlikely to be present in the molecular beam.

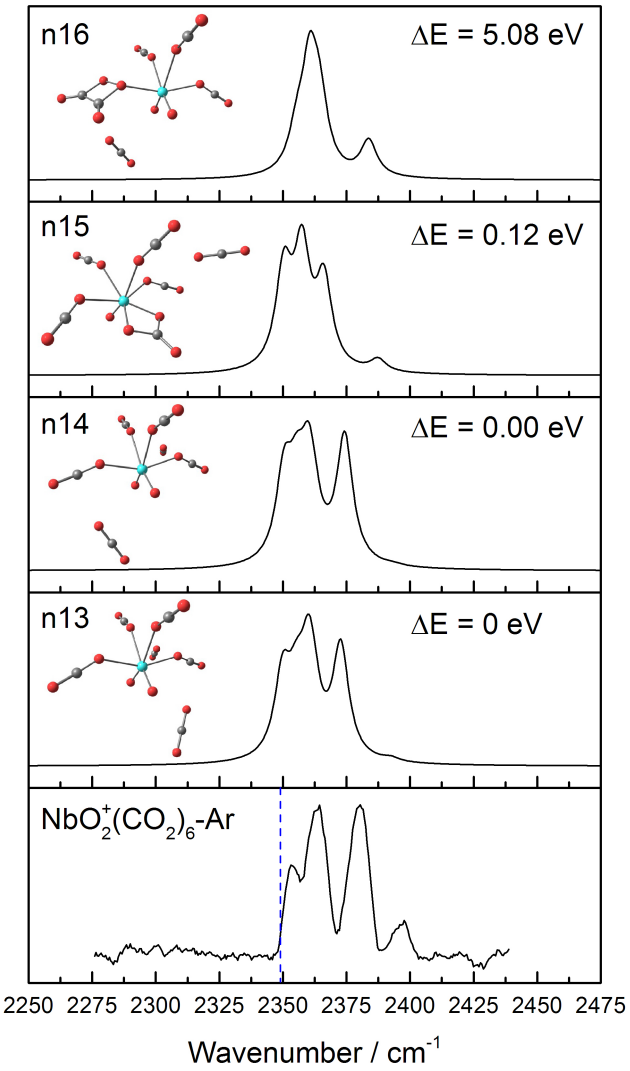

Figure 5.12: Experimental IR-REPD spectra for $NbO_2^+(CO_2)_6$–Ar together with the simulated IR spectra for all candidate structures. All calculations are performed at the B3P86/Def2TZVP level of theory. The vertical dashed line marks the position of the asymmetric stretch ν_3 in an isolated CO_2.

5.6.8 $NbO_2^+(CO_2)_7$–Ar

The IR-REPD spectrum for the $n = 7$ complex (Figure 5.13) is very similar to the spectra for $n = 5$ and 6. Four bands are observed at *ca.* 2353

cm^{-1}, 2363 cm^{-1}, 2381 cm^{-1} and 2398 cm^{-1}. The DFT calculations predict $[NbO_2^+(CO_2)_4]$ core and 3 weakly-bound ligands in the second coordination sphere. Again, the intermolecular bond distances at 3.59 Å, 3.95 Å and 4.13 Å are notably longer for the second coordination sphere ligands (see Figure 5.6 g)). An isoenergetic isomer, n18, is also likely to contribute to the observed structure. We are unable to find a converged structure containing the "CO_3" moiety. Isomer n19 is not expected to contribute to the overall structure.

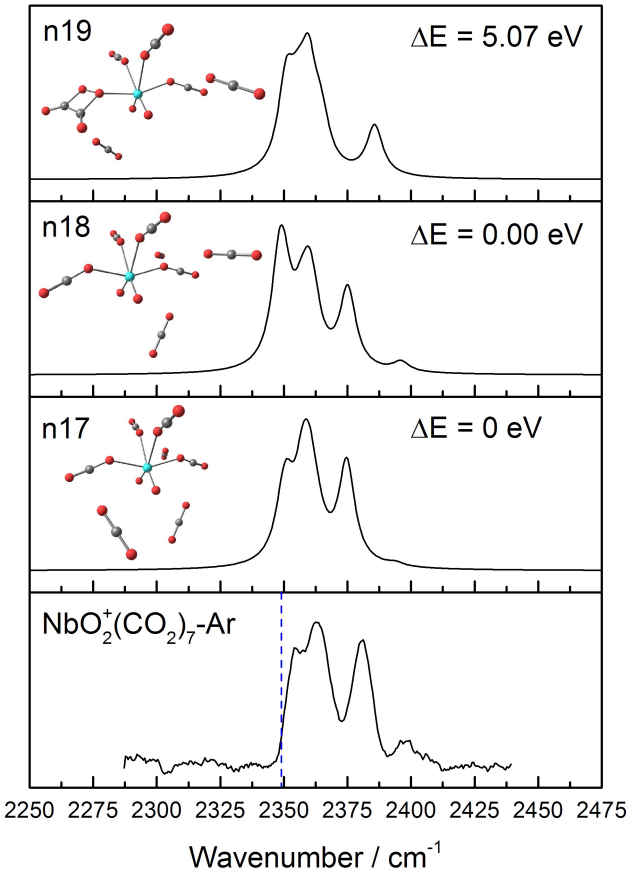

Figure 5.13: Experimental IR-REPD spectrum for $NbO_2^+(CO_2)_7$–Ar together with the simulated IR spectra for all candidate structures. All calculations are performed at the B3P86/Def2TZVP level of theory. The vertical dashed line marks the position of the asymmetric stretch ν_3 in an isolated CO_2.

5.7 Simulated IR Spectra for $TaO_2^+(CO_2)_n$

5.7.1 Structural Parameters and Theoretical Energies

Table 5.3: Theoretical energies for $TaO_2^+(CO_2)_n$ complexes calculated at the B3P86/Def2TZVP level of theory. The energies include zero point energy corrections.

Species	Multiplicity	Energy / eV	ΔE / eV	Structure
$TaO_2^+(CO_2)$	singlet	-10800.68513	0	t1
	triplet	-10798.64967	2.04	–
	quintet	-10794.97441	5.71	–
$TaO_2^+(CO_2)$–Ar	singlet	-25166.0323	–	t1*
$TaO_2^+(CO_2)_2$	singlet	-15946.07616	0	t2
	triplet	-15943.36322	2.71	–
	quintet	-15940.45406	5.62	–
$TaO_2^+(CO_2)_2$–Ar	singlet	-30310.96188	–	t2*
$TaO_2^+(CO_2)_3$	singlet	-21090.71375	0	t3
	singlet	-21090.35197	0.36	t4
	triplet	-21088.22681	2.49	–
	quintet	-21084.05341	6.65	–
$TaO_2^+(CO_2)_3$–Ar	singlet	-35455.42452	0	t3*
$TaO_2^+(CO_2)_3$–Ar	singlet	-35455.0954	0.33	t4*
$TaO_2^+(CO_2)_4$	singlet	-26235.06603	0	t5
	singlet	-26234.98773	0.08	t6
	singlet	-26234.83294	0.23	t7
	singlet	-26230.16857	4.90	t8
$TaO_2^+(CO_2)_5$	singlet	-31379.42593	0	t9
	singlet	-31379.17997	0.25	t10
	singlet	-31379.17397	0.25	t11
	singlet	-31374.49728	4.93	t12
$TaO_2^+(CO_2)_6$	singlet	-36523.52051	0	t13
	singlet	-36523.29095	0.23	t14
	singlet	-36523.29006	0.23	t15
	singlet	-36518.24252	5.28	t16
$TaO_2^+(CO_2)_7$	singlet	-41667.62758	0	t17
	singlet	-41667.30651	0.32	t18
	singlet	-41662.35269	5.27	t19

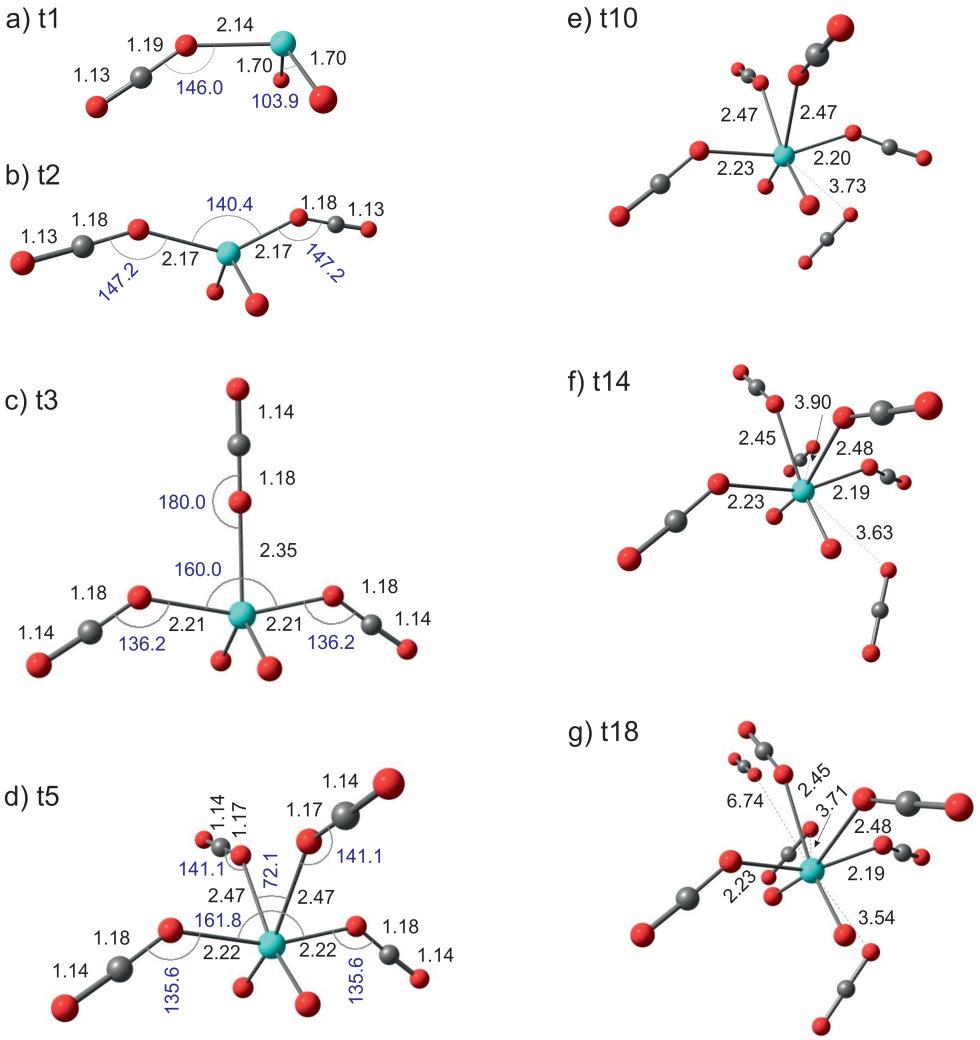

Figure 5.14: Structural parameters for the assigned structures: a) $TaO_2^+(CO_2)$ (structure t1), b) $TaO_2^+(CO_2)_2$ (structure t2), c) $TaO_2^+(CO_2)_3$ (structure t3), d) $TaO_2^+(CO_2)_4$ (structure t5), e) $TaO_2^+(CO_2)_5$ (structure t10), f) $TaO_2^+(CO_2)_6$ (structure t14) and g) $TaO_2^+(CO_2)_7$ (structure t18). Bond distances (black) are in Ångstroms (Å) and bond angles (blue) are in degrees (°). All calculations are performed at the B3P86/Def2TZVP level of theory. Colour scheme: tantalum (light green), oxygen (red) and carbon (grey).

Table 5.3 lists the theoretical energies for all $TaO_2^+(CO_2)_n$ calculated structures. Singlet, triplet and quintet multiplicities were considered for $n = 1$, 2 and 3. Similarly to the equivalent niobium complexes, the singlet multiplicities are consistently found to be the in lowest energy for $TaO_2^+(CO_2)_n$

complexes. Figure 5.14 displays structural parameters for all assigned structures that are thought to be the dominant contributors to each respective experimental IR spectrum.

5.7.2 $TaO_2^+(CO_2)$–Ar

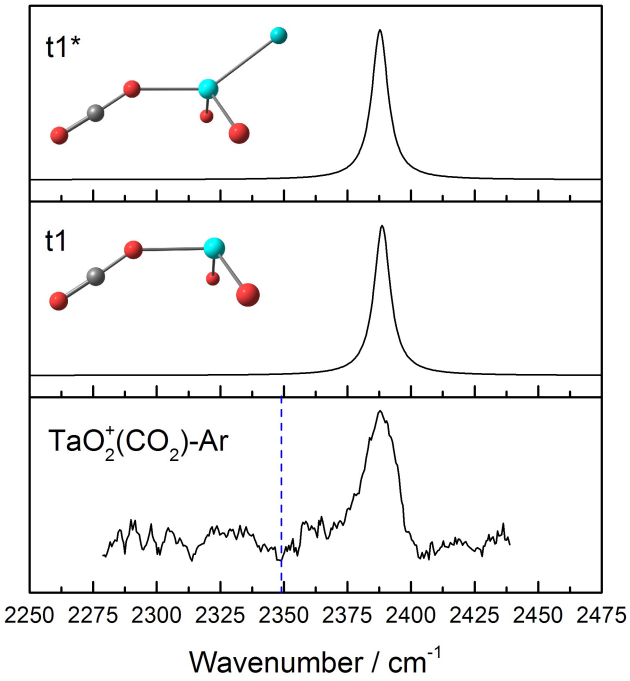

Figure 5.15: Comparison of the experimental IR-REPD spectrum for $TaO_2^+(CO_2)$–Ar with the simulated spectra for both the neat (structure t1), and argon-tagged complex (t1*). All calculation are performed at the B3P86/Def2TZVP level of theory. The vertical dashed line marks the position of the asymmetric stretch ν_3 in an isolated CO_2.

In the experimental IR spectrum for $n = 1$, a single strong feature centred at *ca.* 2387 cm^{-1} is observed (Figure 5.15). This feature is blue-shifted from the free CO_2 frequency by 38 cm^{-1}, which indicates a significantly-perturbed CO_2 molecule directly attached to the metal oxide ion. CO_2 is attached *via* the O-end to the previously identified TaO_2^+ ion. The simulated IR spectrum for structure t1 gives a single strong feature consistent with the

experimental IR-REPD spectrum. No additional features are observed when an argon atom is included (structure t1*). Similar to the equivalent NbO_2^+ ion structure, it appears that CO_2 attaches to a virtually unperturbed TaO_2^+ ion without disturbing the singlet multiplicity or the underlying geometry of the metal oxide ion, as evident from the structural parameters exhibited in Figure 5.14 a).

5.7.3 $TaO_2^+(CO_2)_2$–Ar

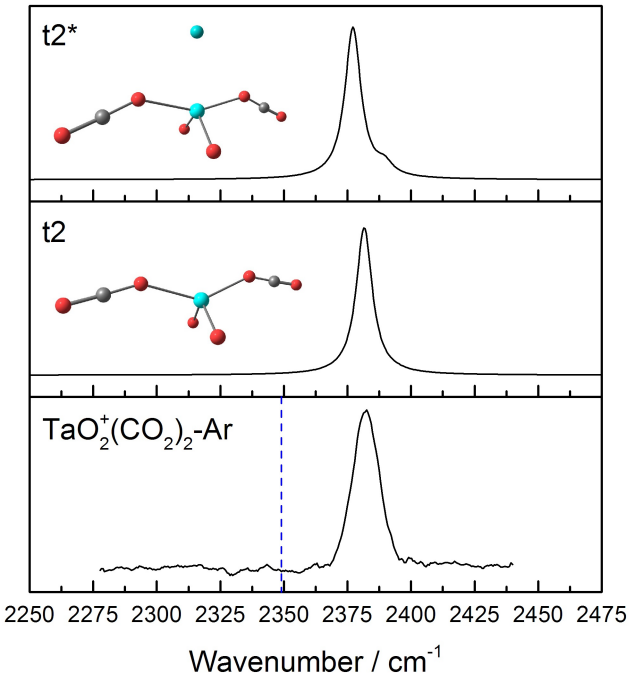

Figure 5.16: Experimental IR-REPD spectrum for $TaO_2^+(CO_2)_2$–Ar together with the simulated IR spectra for both neat structure (t2) and its argon tagged counterpart (structure t2*). All calculations are performed at the B3P86/Def2TZVP level of theory. The vertical dashed line marks the position of the asymmetric stretch ν_3 in an isolated CO_2.

The experimental IR-REPD spectrum for $TaO_2^+(CO_2)_2$-Ar gives a single strong feature centred at 2382 cm^{-1}, as shown in Figure 5.16 indicating a structure of high symmetry. This feature is blue-shifted by 33 cm^{-1} from

the asymmetric stretching frequency of free CO_2. The calculated global minimum structure is of C_{2v} geometry with two CO_2 molecules bound on opposite ends the TaO_2^+ ion (Figure 5.16 and 5.14, structure t2). This structure exhibits an obvious resemblance to the equivalent niobium structure. The angle defined by C–O–Ta^+ is found to be 147.2 ° for both ligands. Again, just as in the case of Nb^+, Rh^+ and Ir^+, the obtuse nature of this angle is expected to occur due to the rather large polarisability of $\alpha = 42.0\ a_0^3$ for Ta^+.[314]

The effect of an argon tag was also considered but there is no evidence in the experimental spectrum for the simulated additional small shoulder peak (Figure 5.16, structure t2*). In fact, argon may be sufficiently weakly-bound to be delocalised around the complex instead of occupying a specific site, as previously observed by Fielicke and co-workers in their calculations on Au_7Kr clusters.[325]

5.7.4 $TaO_2^+(CO_2)_3$–Ar

With obvious similarity to the $NbO_2^+(CO_2)_3$-Ar ion, the IR spectrum for $TaO_2^+(CO_2)_3$-Ar consists of a strong feature centred at *ca.* 2371 cm^{-1}, along with a noticeable shoulder peak at 2391 cm^{-1}. This is reproduced in the simulated IR spectrum for the global minimum structure of C_{2v} symmetry (Figure 5.17, structure t3), albeit with a slightly lower relative intensity for the shoulder band. This geometry is comprised of an additional, slightly more weakly-bound "third" ligand added to the previously determined structure for $n = 2$. The t3 structure is strongly reminiscent of the equivalent niobium structure (n3). In the simulated spectrum, the strong feature is a superposition of normal modes corresponding to: i) the asymmetric stretch predominantly centred on the third ligand, and ii) the out-of-phase combination of the asymmetric stretches of two inner CO_2 ligands. The shoulder peak is then due to the in-phase combination of all three ligands. Intermolecular bond distances reveal a longer bond for the third ligand (2.35 Å versus 2.22 Å), as displayed in Figure 5.14 c).

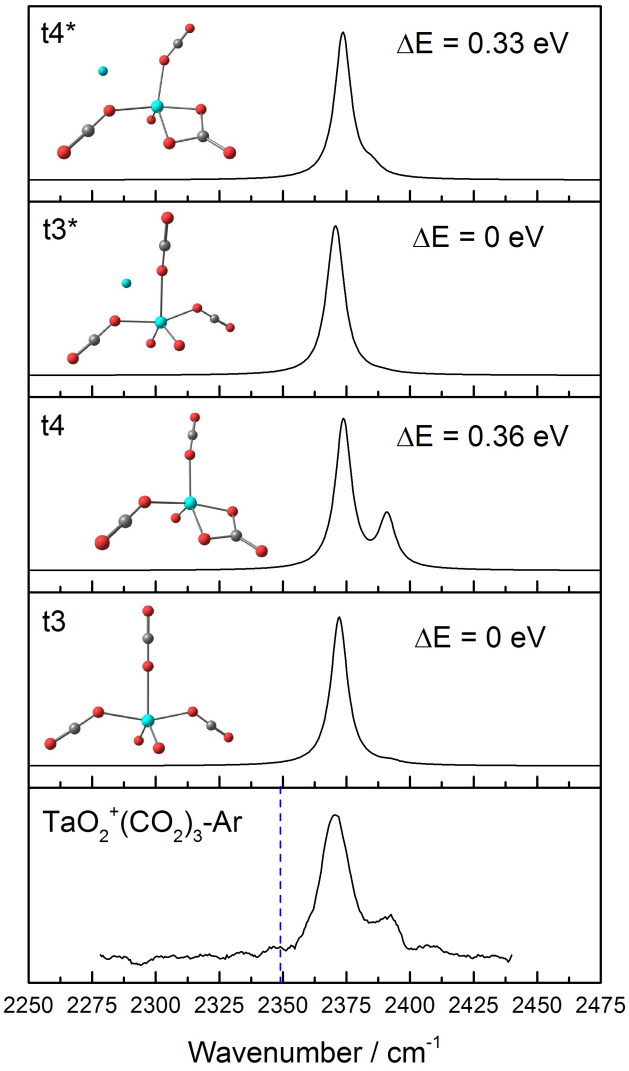

Figure 5.17: Experimental IR-REPD spectrum for $TaO_2^+(CO_2)_3$–Ar together with the simulated IR spectra for both neat structures (t3 and t4) and their argon tagged counterparts (structures t3* and t4*). All calculations are performed at the B3P86/Def2TZVP level of theory. The vertical dashed line marks the position of the asymmetric stretch ν_3 in an isolated CO_2.

A low-lying isomer (Figure 5.17, t4), 0.36 eV above the global minimum, is also found for the $n = 3$ complex. Here, a bent CO_2 ligand is observed to interact *via* a carbon atom with one of the oxygens of the TaO_2^+ ion. This structure is also predicted to have an additional feature (*i.e.* an activated C–

O stretch) at *ca.* 1897 cm^{-1}. This "CO_3" moiety is also encountered in larger complexes up to $n = 7$. However, after extensive experimental screening in the region around 1750 – 2100 cm^{-1}, no evidence of this isomer's presence in the molecular beam was found. The absence of any evidence for this structure is intriguing. While this moiety is an excited isomer for $n = 3$ and 4, it becomes a putative global minimum in larger complexes unlike for $NbO_2^+(CO_2)_n$ complexes, where isomers with all intact CO_2 ligands are found to be global minimum structures.

There might be a kinetic barrier to formation of isomer t4 in the conditions that exist in the ablation block, or this particular isomer might have an anomalously low photofragmentation yield. Furthermore, structures containing the "CO_3" moiety provide somewhat worse agreement with the experimental IR spectra for larger complexes (*vide infra* - Figure 5.18, 5.19 and 5.20 for $n = 4 - 7$). The relative energetic order is also unchanged when repeating the calculations using the B3LYP and TPSS density functionals.[258,326] Higher order derivatives of structure t4 might also be unfavourable to form as they first require the formation of t4 isomer, which itself is not a global minimum structure. With available results, we can nevertheless unequivocally support the presence of structure t3 and its higher order derivatives (t6, t10, t14, t19).

5.7.5 $TaO_2^+(CO_2)_4$–Ar

In the IR-REPD spectrum for $TaO_2^+(CO_2)_4$–Ar, three well-resolved features are observed at *ca.* 2360, 2371 and 2387 cm^{-1} (Figure 5.18). The calculated global minimum structure is of C_{2v} symmetry (structure t5) with three predicted features which compare well with the experimental IR-REPD spectrum. This structure is formed by binding two additional ligands to the structure identified for the $n = 2$ complex (Figure 5.18, structure t2). Intermolecular bond distances confirm this: 2.47 Å versus 2.22 Å for the inner two CO_2 (Figure 5.14 d)). The $TaO_2^+(CO_2)_4$ complex is thus formed of two

"inner" CO_2 and two slightly more "outer" CO_2 ligands.

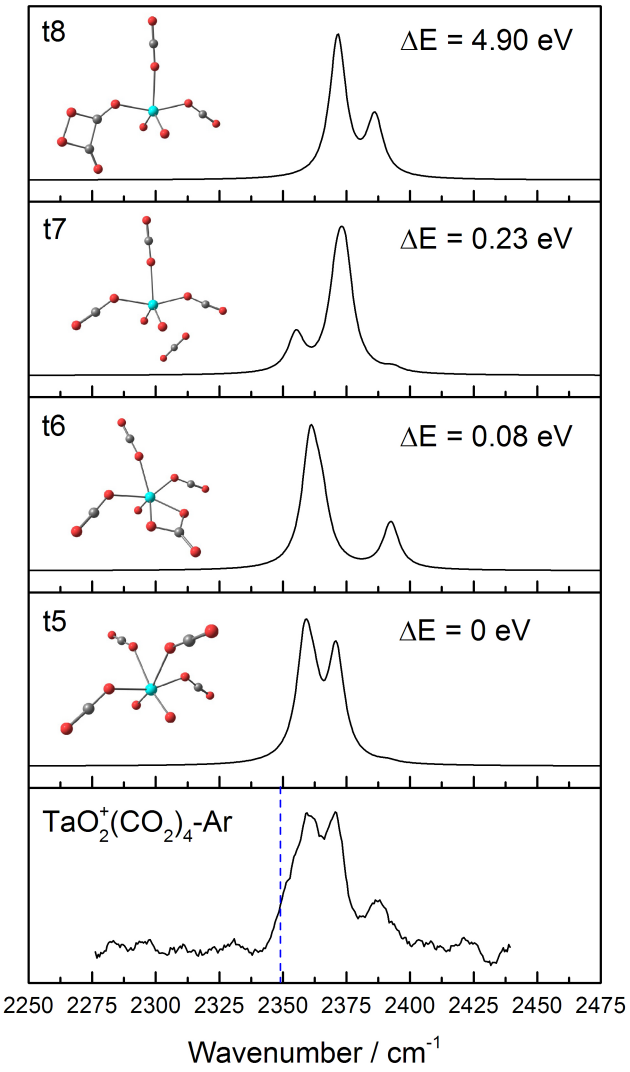

Figure 5.18: Experimental IR-REPD spectrum for $TaO_2^+(CO_2)_4$–Ar together with the simulated IR spectra for all candidate structures. All calculations are performed at the B3P86/Def2TZVP level of theory. The vertical dashed line marks the position of the asymmetric stretch ν_3 in an isolated CO_2.

DFT calculations characterised the three spectral features as (in the order of ascending energy): i) superposition of peaks due to out-of-phase and in-phase combinations of the asymmetric stretches of the "outer" two ligands,

ii) a feature corresponding to the out-of-phase combination of the asymmetric stretches of the two inner CO_2 ligands, and iii) a feature corresponding to the in-phase combination of the two inner CO_2 ligands. Equivalent vibrational modes were also observed for $NbO_2^+(CO_2)_4$.

A higher-lying isomer with a "CO_3" moiety provides a poorer agreement with the experimental data. Additionally, a higher-lying isomer (structure t7) consists of a significantly more weakly-bound CO_2 ligand attached to the $TaO_2^+(CO_2)_3$ complex. This structure (t7) may be contributing in some capacity to the overall IR spectrum.

Similarly with an equivalent niobium complex, no evidence for isomer t8 was found in the spectral region around *ca.* 1900 cm^{-1}. Furthermore, t8 is 4.90 eV above the global minimum structure so it is unlikely to be produced in the ablation block and survive sufficiently long to be probed by the IR-OPO/OPA laser.

5.7.6 $TaO_2^+(CO_2)_5$–Ar

Similarly to the $n = 4$ complex, the IR-REPD spectrum for $TaO_2^+(CO_2)_5$–Ar (Figure 5.19) exhibits features at 2360 cm^{-1}, 2376 cm^{-1} and 2394 cm^{-1}, and an additional shoulder peak at *ca.* 2351 cm^{-1}, which is virtually at the vibrational frequency of free CO_2. This latter peak is indicative of ligands which are not directly attached to the metal ion, as confirmed by the assigned structures of t10 and t11 (contrary to the equivalent niobium complexes, structure t10 is not the global minimum). Examination of intermolecular bonds reveals a $[TaO_2^+(CO_2)_4]$ core structure with a significantly more weakly-bound "fifth" CO_2 ligand. The intermolecular distance for the fifth ligand to TaO_2^+ is 3.73 Å. This is markedly longer than the comparable bond distances of 2.23 Å – 2.47 Å for the core ligands. A slight deviation of the underlying $n = 4$ core structure is expected due to presence of the fifth ligand.

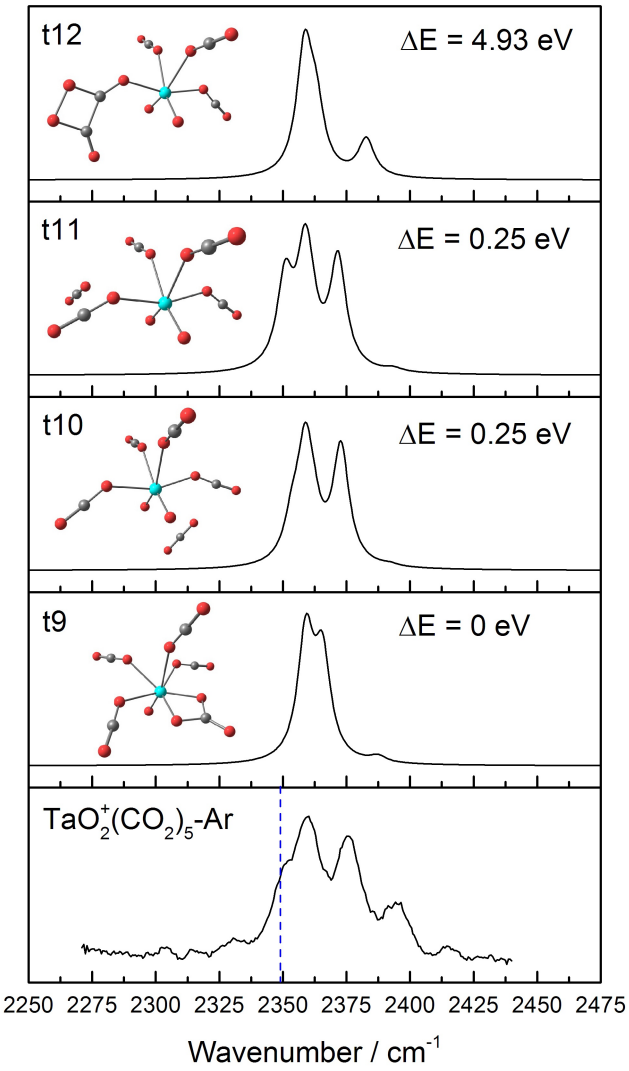

Figure 5.19: Experimental IR-REPD spectrum for $TaO_2^+(CO_2)_5$–Ar together with the simulated IR spectra for all candidate structures. All calculations are performed at the B3P86/Def2TZVP level of theory. The vertical dashed line marks the position of the asymmetric stretch ν_3 in an isolated CO_2.

The simulated IR spectrum is thus composed of the previously identified spectrum for the $n = 4$ core and an additional CO_2 with an asymmetric stretching frequency close to 2349 cm^{-1}. The $n = 4$ core is itself composed of two sets of two CO_2 molecules (*i.e.* inner and outer core). One could

thus describe the fifth ligand as residing in the second coordination sphere. Isomers t10 and t11 are *de facto* isoenergetic and are likely to be present in the molecular beam in comparable abundances.

Isomer t9 (a putative global minimum) gives a poorer agreement with the experimental IR-REPD spectrum and it does not predict the loosely-bound CO_2 ligand observed experimentally. Again, isomer t12 containing an oxalate-type moiety is too high in energy to be present in the molecular beam.

5.7.7 $TaO_2^+(CO_2)_6$–Ar

The experimental IR-REPD spectrum and the corresponding DFT simulated spectra for $TaO_2^+(CO_2)_6$–Ar are shown in Figure 5.20. The spectral features are observed at 2353 cm^{-1}, 2363 cm^{-1}, 2377 cm^{-1} and 2395 cm^{-1}. Again, we are unable to detect the contribution of the structure containing the "CO_3" moiety (structure t13) to experimental spectrum. Instead, structure t14, 0.23 eV above the putative global minimum, provides excellent agreement with the experimental data. This structure consists of a $TaO_2^+(CO_2)_4$ core and two loosely-bound CO_2 molecules occupying the second coordination sphere. This interpretation is reinforced by comparing the intermolecular bond distances of 3.63 Å and 3.90 Å versus 2.19 – 2.48 Å for the core ligands (Figure 5.14 f)). A competing isoenergetic structure t15 also gives a good agreement with the experimental data. Under our source conditions, there is unlikely to be any preference for formation of either the t14 or t15 isomers, and since these structures are essentially isoenergetic, one can expect the two competing isomers to be formed in comparable abundances.

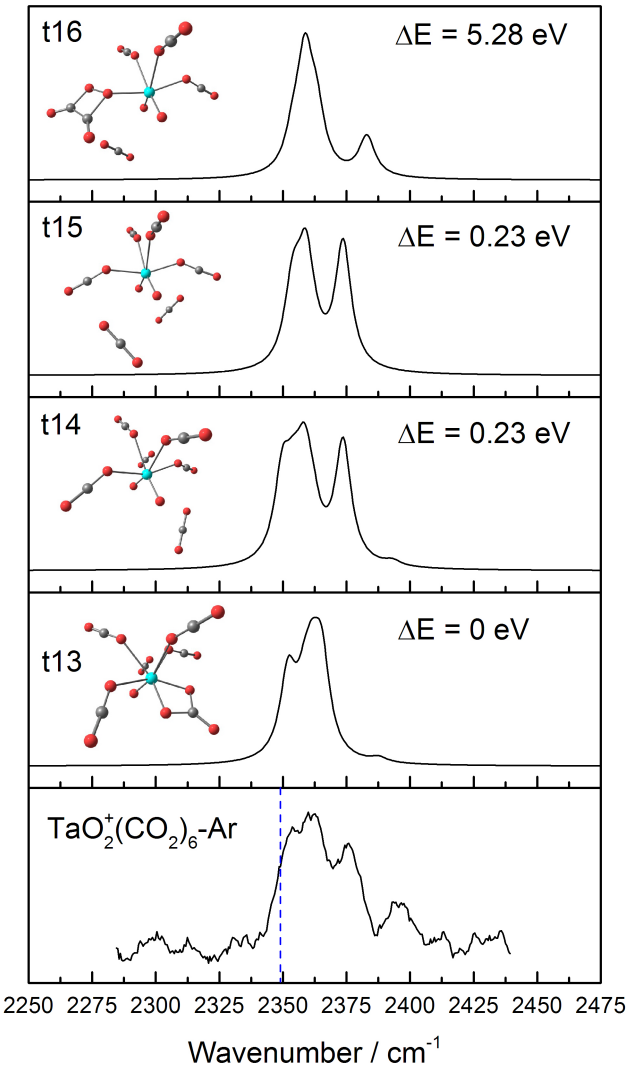

Figure 5.20: Experimental IR-REPD spectra for $TaO_2^+(CO_2)_6$–Ar together with the simulated IR spectra for all candidate structures. All calculations are performed at the B3P86/Def2TZVP level of theory. The vertical dashed line marks the position of the asymmetric stretch ν_3 in an isolated CO_2.

5.7.8 $TaO_2^+(CO_2)_7$

The IR spectrum for $TaO_2^+(CO_2)_7$ recorded in the channel corresponding to the depletion of the "untagged" parent ion is shown in Figure 5.21. Four

spectral features are observed at 2348 cm^{-1}, 2358 cm^{-1}, 2379 cm^{-1} and 2395 cm^{-1}. Structure t18 provides a good agreement with the experimental IR spectrum. Similarly to the hitherto discussed geometries, structure t18 consists of a $TaO_2^+(CO_2)_4$ core and three loosely-bound ligands, as evident from corresponding bond distances: 2.54 Å, 3.71 Å and 6.74 Å versus 2.19 – 2.48 Å for core ligands.

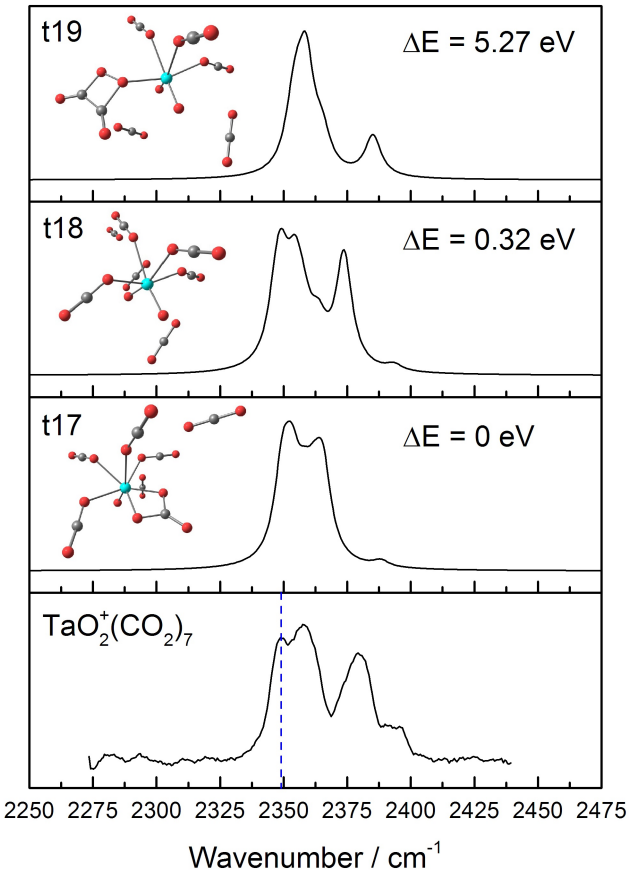

Figure 5.21: Experimental IR-REPD spectra for $TaO_2^+(CO_2)_7$ together with the simulated IR spectra for all candidate structures. All calculations are performed at the B3P86/Def2TZVP level of theory. The vertical dashed line marks the position of the asymmetric stretch ν_3 in an isolated CO_2.

5.8 Trends for $NbO_2^+(CO_2)_n$ and $TaO_2^+(CO_2)_n$ Complexes

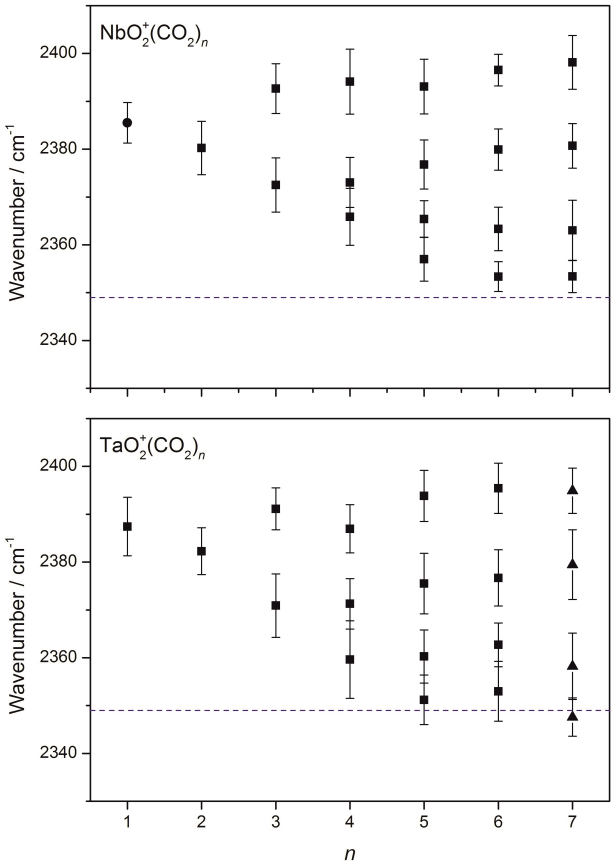

Figure 5.22: Peak positions plotted as a function of cluster size for the $NbO_2^+(CO_2)_n$ and $TaO_2^+(CO_2)_n$ complexes. The square markers correspond to singly Ar-tagged complexes, the circular markers to the doubly argon-tagged $NbO_2^+(CO_2)_n$–Ar_2 complex, and the triangular to the neat $TaO_2^+(CO_2)_7$ complex. The error bars correspond to the full-width-half-maximum (FWHM) of a fitted Gaussian function used to determine the position of each peak. Horizontal dashed line marks the energy of the asymmetric stretch in an isolated CO_2.

For completion, Figure 5.22 exhibits the observed peak positions plotted as a function of complex size. For both NbO_2^+- and TaO_2^+- based complexes, the

smallest two complexes $n = 1$ and 2 exhibit only a single feature due to out-of-phase combination of normal modes for $n = 2$. For $n = 3$, vibrations resulting from the in-phase combination of the normal modes of inner CO_2 molecules become apparent, as well. For $n = 4$, the vibrations due to both in and out-of-phase combinations of normal modes for the two inner-most ligands are observed. These two features then experience a gradual blue-shift with increasing n as the inner ligands experience additional rigidity as a result of outer coordination sphere. The features due to CO_2 molecules directly attached to the central metal ion continue to persist in larger complexes and these features then slowly reach plateau at $n = 7$ at 2381 cm^{-1} and 2398 cm^{-1} for $NbO_2^+(CO_2)_n$. Similarly for $TaO_2^+(CO_2)_n$ complexes, a plateau is reached at *ca.* 2379 cm^{-1} and 2395 cm^{-1} at $n = 7$. In all cases, the feature at *ca.* 2360 cm^{-1} remains a superposition of peaks corresponding to two outer ligands of the $[MO_2^+(CO_2)_4]$ core, where M = Nb and Ta.

Ligands vibrating close to the frequency of an isolated CO_2 first appear at $n = 5$, indicating an inner coordination sphere of four CO_2 ligands to which other ligands bind more loosely. The features due to the "surface" ligands become better resolved with an increasing n, where more ligands reside in the second coordination sphere. To illustrate this point further, $n = 7$ consists of four ligands in the inner coordination shell (with vibrational frequencies $>$ *ca.* 2360 cm^{-1}), and three ligands in the second coordination shell with their corresponding vibrational frequency close to 2349 cm^{-1}. Including the oxygen atoms one may even describe the coordination number around Nb^+ and Ta^+ to be six (four CO_2 ligands and two oxygen atoms).

A coordination number of six is commonly encountered for niobium and tantalum complexes in the condensed phase, especially in the coordination complexes involving alkynes or amide based ligands.[327–329] The Duncan group have observed an octahedral $n = 6$ core for gas-phase $Nb^+(N_2)_n$ complexes.[330] In the case of N_2 ligand, some incipient chemical bonding is present in accordance with the Dewar-Chatt-Duncanson complexation model,[166–168] which

also explains the propensity for the symmetric structure. In our case, the four CO_2 ligands and two oxygen atom around Nb^+ and Ta^+ ions are not in a perfect octahedral arrangement. The predominant interaction here is the charge-quadrupole interaction between the metal ion and CO_2.

Although this might not be a *bona fide* comparison with the complexes of NbO_2^+ and TaO_2^+ ions, the Duncan group has previously identified that four CO_2 ligands form the first coordination sphere in the case of $V^+(CO_2)_n$ complexes[324,331] (as discussed in Section 5.3, VO_2^+ ions are not formed upon the ablation of vanadium target in the presence of CO_2/Ar). In the case of $V^+(CO_2)_2$ and $V^+(CO_2)_3$, only a single feature with a blue-shifted shoulder peak was observed. Unlike in NbO_2^+- and TaO_2^+- based complexes, the shoulder peak was assigned to either structures of low symmetry, or high symmetry structures perturbed by argon. Only a single strong feature is observed for $V^+(CO_2)_4$, indicating a structure of high symmetry - DFT calculations at the B3LYP/Def2TZVP identified a planar structure of D_{4h} symmetry.[324] The experimental IR-REPD spectra and DFT calculations indicate that all four core ligands occupy equivalent positions, unlike for the NbO_2^+ and TaO_2^+ ions. In larger $V^+(CO_2)_n$ complexes (for $n \geq 9$), a feature due to ligands occupying intermediate coordination shells were observed. No such features were observed for near-equivalent NbO_2^+ and TaO_2^+ complexes, at least not in the size regimes considered in this work.

The final piece of the evidence that confirms the core of four ligands for $NbO_2^+(CO_2)_n$ and $TaO_2^+(CO_2)_n$ complexes comes from the trends in binding energies displayed in Figure 5.23. With the calculated binding energy of 1.34 (1.63 eV), the $n = 1$ complex exhibits the strongest attraction between NbO_2^+ (TaO_2^+) and CO_2. The obvious drop in the binding energy is noticed between $n = 2$ and $n = 3$ (from 1.2 eV (1.40 eV) to 0.57 eV (0.65 eV) for NbO_2^+ (TaO_2^+) ions, which correspond to the addition of the third ligand to the $[MO_2^+(CO_2)_2]$ structure, which contains the two most strongly-bound CO_2 ligands. A drop between $n = 3$ and $n = 4$ ligand is then less drastic.

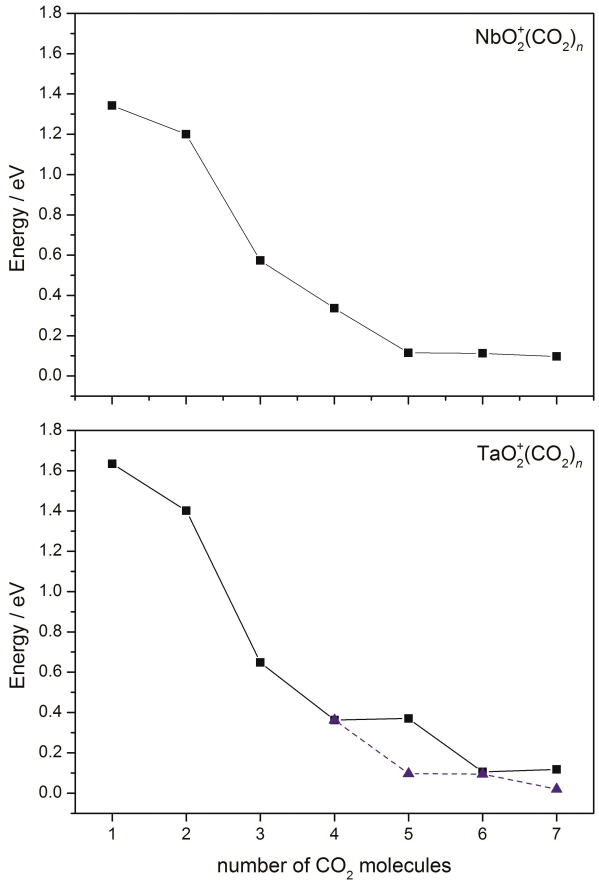

Figure 5.23: Binding energies of successive CO_2 molecules calculated at the B3P86/Def2TZVP of theory. The energies are calculated by considering the following dissociation process: $MO_2^+(CO_2)_n$ to $MO_2^+(CO_2)_{n-1}$ + CO_2 for M = Nb to Ta. Black squares correspond to the values calculated relative to the putative global minima structures. In the case of $TaO_2^+(CO_2)_n$, blue triangles mark the dissociation energies relative to structures t10, t14 and t18 that are assigned to be the major contributors to the experimental IR-REPD spectra.

In Figure 5.23 (bottom), blue triangles indicate the dissociation energies relative to the t10, t14 and t18 structures. These geometries are assigned to be the major contributors to the observed $TaO_2^+(CO_2)_{5-7}$ experimental IR-REPD spectra. Here, the binding energies of the terminal CO_2 is very close to zero for n = 5, 6 and 7 (*ca.* 0.10 eV, 0.09 eV and 0.02 eV, respectively). Likewise for NbO_2^+ complexes, the binding energies of the terminal ligand in

$n = 5$, 6 and 7 complexes is very close to zero (*ca.* 0.10 eV or less), which is consistent with weakly-bound ligands not directly attached to the metal ion. Ligands in the second coordination sphere predominantly interact with other CO_2 molecules. Hence their binding energy energies are similar to that of a neutral CO_2 dimer of *ca.* 0.06 eV (500 cm^{-1}).[277–279] This is in good agreement with the DFT calculated binding energies for the second coordination sphere ligands ($n \geq 5$) in $NbO_2^+(CO_2)_n$ and $TaO_2^+(CO_2)_n$ complexes.

For both metal oxide ions, low binding energies for the ligands in the second coordination sphere are further consistent with large intermolecular distance to Nb^+ or Ta^+, and with the onset of spectral features close to 2349 cm^{-1} at $n \geq 5$.

5.9 $(CO_2)_n^+$ Gaseous Complexes

As observed in the time-of-flight mass spectrum produced upon ablation of a tantalum target in presence of CO_2/Ar gas mix shown in Figure 5.3, $(CO_2)_n^+$ metal-free complexes are also present in the molecular beam, some with an argon atom attached. The IR-REPD spectra for $(CO_2)_{3,4}^+$–Ar and $(CO_2)_{5,6}^+$ are shown in Figure 5.24 and are in excellent agreement with previous work by Inokuchi *et al.*[320] Calculations by Inokuchi *et al.* suggest the $C_2O_4^+$ ion as the nucleation site, where the ion itself is thought to be of C_{2h} symmetry with CO_2 molecules interacting *via* their respective O-ends. The third and fourth CO_2 molecules are then added orthogonally to the plane defined by $C_2O_4^+$. All features in the IR-REPD spectra appear close to the asymmetric stretching frequency of free CO_2, which indicates modestly-perturbed CO_2 molecules. While Inokuchi *et al.* do not provide simulated IR spectra, they assigned two peaks in the spectrum for $n = 4$ to molecules that bind to different positions at the $C_2O_4^+$ ion.

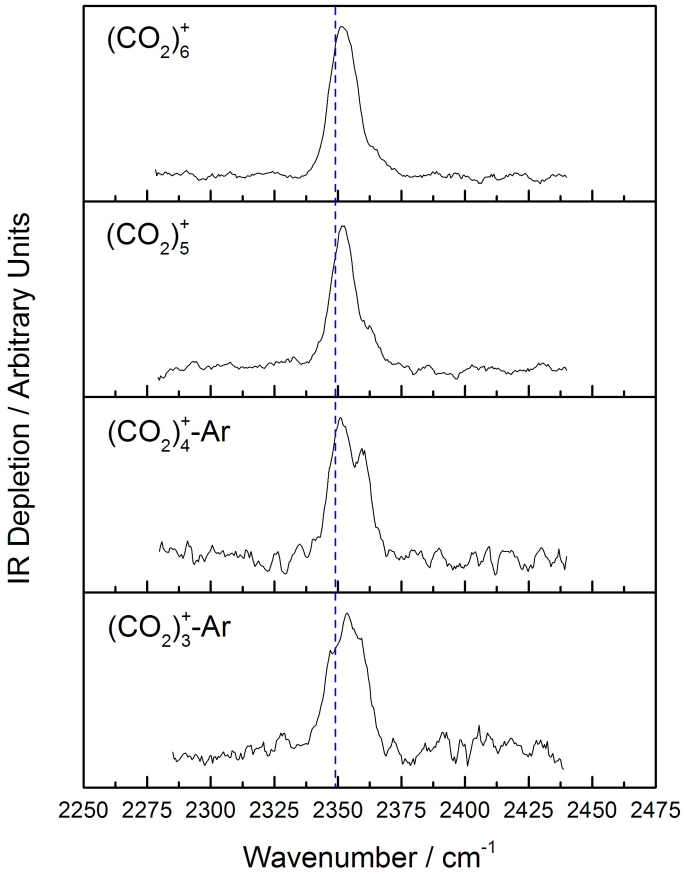

Figure 5.24: IR-REPD spectra for $(CO_2)_{3,4}^+$–Ar and $(CO_2)_{5,6}^+$ complexes recorded in the channel corresponding to the depletion of the parent ion. The vertical dashed line indicates the position of the asymmetric stretch in free CO_2.

5.10 Conclusions

IR-REPD spectra are recorded for $MO_2^+(CO_2)_n$ complexes (where M = Nb and Ta) in the $n = 1 - 7$ size regime *via* means of argon tagging. This study reveals a further insight into CO_2 complexation around transition metal dioxide cations. Strong similarities exist between the complexes of NbO_2^+ and TaO_2^+ ions. Experimental data, in conjunction with the DFT simulated IR spectra, allows for identification of a strongly-bound $[MO_2^+(CO_2)_4]$ core. The

$n = 4$ core itself consists of two pairs of most inner and outer CO_2 molecules. A notable increase in the intermolecular bond distances is observed for all ligands that are thought to occupy the second coordination sphere. This coincides with features arising at energies close to the asymmetric stretching frequency of free CO_2, providing additional evidence for the $n = 4$ core. Furthermore, binding energies close to zero were calculated for the weakly-bound molecules in the second coordination sphere (*i.e* from $n \geq 5$). This study also demonstrates a remarkable degree of agreement between the experimental and DFT simulated IR spectra even for the complexes up to $n = 7$. Despite the similarities between the complexes of NbO_2^+ and TaO_2^+ ions, these species are notably different when compared to $V^+(CO_2)_n$ complexes.

Chapter 6

A Velocity Map Imaging Study of Vanadium Oxide

This chapter presents a VMI study of VO photofragmentation in the visible region in the vicinity of $C^4\Sigma^-$ - $X^4\Sigma^-$(v',0) transitions in VO. The experimental setup employs a recently-modified Oxford VMI spectrometer equipped with a laser ablation source. The dynamics are interpreted in terms of three photon nature with the first photon loosely resonant with vibrational levels of the $C^4\Sigma^-$ state. The quantum state distribution of photofragments is strongly dependant on the intermediate vibrational state accessed in the vibronic progression of the $C^4\Sigma^-$ state. A refined value for the dissociation energy $D_0(\mathrm{VO}) = 53190 \pm 261$ cm^{-1} resulting from this work is in good agreement with available literature.

6.1 Previous Studies of VO

Vanadium oxides are of industrial importance as catalysts, semiconductors, and because of their use in optical devices.[332,333] VO is also an important molecule from an astrophysical perspective, where transitions corresponding

to its presence are commonly observed in the spectra of cool (2500-3000 K) M-class stars and serve as a means for their characterisation.[334,335] VO has recently (2017) been detected in the atmosphere of a super Neptune-like exoplanet (WASP-127b) discovered by Lam *et al.*[336,337]

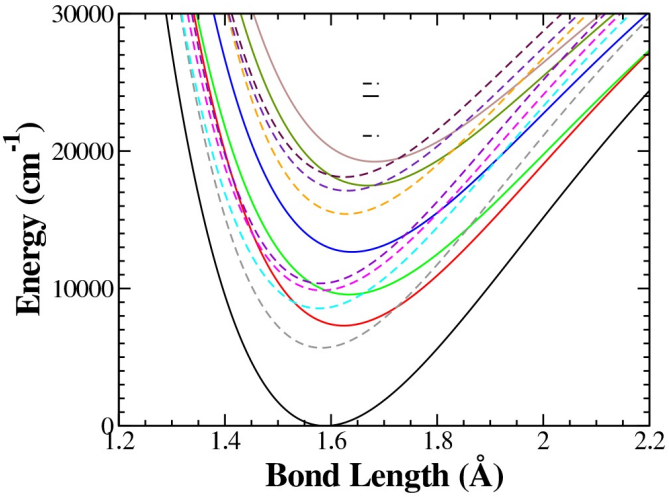

Figure 6.1: Potential energy curves for the known states of VO. Solid and dashed lines refer to quartet and doublet states, respectively. Colour scheme in the ascending order, solid: X $^4\Sigma^-$, A' $^4\Phi$, A $^4\Pi$, B $^4\Pi$, C $^4\Sigma^-$ and D $^4\Delta$; dashed: a $^2\Sigma^-$, b $^2\Gamma$, c $^2\Delta$, d $^2\Sigma^+$, e $^2\Phi$, f $^2\Pi$ and g $^2\Pi$. The potential energy surfaces are calculated using the extended Morse potential (EMO) by Lee *et al.* (that includes centrifugal correction functions expanded as a power series),[338] and fitting the empirical parameters: dissociation energy (by Balducci *et al.*[339]), empirical excitation energies and bond lengths. Reprinted from McKemmish, L.K.; Yurchenko S. N.; Tennyson, J. *Mon. Not. R. Astron. Soc.*, 2016, 463, 771–793 with permission from Oxford University Press on behlf of Royal Astronomical Society.[335]

Due to its astrophysical significance, the lower-lying states of VO have been characterised extensively. Merer *et al.* used Fourier transform spectroscopy to study the ground and the excited states of VO.[340–344] Figure 6.1 illustrates the potential energy curves of the lower lying states of VO with $X^4\Sigma^-$ as the ground state. Our group has previously studied the electronic spectrum of VO in the visible region and characterised a spin-forbidden transition from the ground state to the 3 $^2\Pi$ state.[345] Furthermore, monovanadium oxide

anions (VO_x^-, $x = 1 - 4$) were studied by Wang and co-workers using photoelectron spectroscopy.[346] A recent article by Tennyson provides an extensive overview of the spectral lines of VO, including the potential energy surfaces of the lower-lying states of VO presented in Figure 6.1.[335]

Bauschlicher and Langhoff have, in their theoretical study of the low-lying electronic states of VO using the complete active space-space self-consistent field (CASSCF) method, identified $X^4\Sigma^-$ as the ground state.[347] This confirms an earlier assignment by Carlson and Moser.[348] Vanadium has a ground state electronic configuration of [Ar]$3d^3 4s^2$; although, the [Ar]$3d^4 4s^1$ state is only *ca.* 0.25 eV higher in energy and greatly contributes to the covalent bonding. It is thought that there is a covalent, V($3d\sigma^1 3d\pi^1 3d\delta^2 4s^1$) O($2p\sigma^1 2p\pi^3$), and an ionic, V^+($3d\sigma^1 3d\delta^2 4s^1$) O^-($2p\sigma^1 2p\pi^4$), contribution to the bonding in VO. For the ground state of VO, a certain amount of triple bond character is presumed. The covalent bonding contributions arise from the overlap of $3d\sigma$ and $3d\pi$ orbitals of V with the $2p\sigma$ and $2p\pi$ orbitals of O, respectively. The sole $4s$ electron of V is polarised away from O. Additional contribution arises from the donation of the $2p\pi$ O electrons into the empty $3d\pi$ orbital of V. In the ionic component, the $4s$ electron of V is again polarised away from O and the bond is formed between the V $3d\sigma$ and O $2p\sigma$ orbitals, and with the electron donation from oxygen's $2p\pi$ orbitals into the empty $3d\pi$ orbitals on V.[347]

Bauschlicher and Langhoff have also calculated a dissociation energy of 5.68 eV (45812 cm^{-1}) for VO. This value is thought to be significantly lower than the experimentally measured values (see Table 6.1) due to limited consideration of the correlation energy in the CASSCF only method employed by Bauschlicher and Langhoff.[347] A more recent investigation by Miliordos and Mavridis using CASSCF and single plus double replacements (CASSCF+1+2=MRCI) obtained a value of $D_0 = 52464$ cm^{-1} (6.95 eV),[349] which is closer to the experimentally determined dissociation energies (*c.f.* Table 6.1).

Jones and Gole determined the lower-bound D_0 value of VO in their study of the gas-phase reaction of vanadium with nitrogen dioxide: V + N_2O → VO + NO.[350] Under single-collision conditions, the authors observed chemiluminescence from vibrational levels up to $v' = 11$ of the $C^4\Sigma^-$ - $X^4\Sigma^-$ system of VO. From a thermodynamic cycle and the knowledge of D_0(O–NO), Jones and Gole determined the lower limit for the dissociation energy of D_0(VO) as 6.034 eV (48677 cm^{-1}).

Using a combination of Knudsen cell and mass spectrometry, Balducci *et al.* studied the gas-phase equilibria between the following reactions: VO + Eu ⟺ EuO + V.[339] From the measurements of equilibrium constants at different temperatures, the heat of reaction was derived. As D_0(EuO) is well-known, the authors were able to determine the dissociation energy of D_0(VO) as 52345 ± 726 cm^{-1} (6.51 ± 0.09 eV). In the same work the authors measured the ionisation potential of VO to be 8.4 ± 0.5 eV (67751 ± 4033 cm^{-1}). Thus, in the visible range, at least three photons are required to ionise VO. Pedley and Marshall used the available thermochemical data from older Knudsen cell experiments[351] to determine the value of D_0(VO) as 51942 ± 1613 cm^{-1} (6.44 ± 0.20 eV).[352]

Table 6.1: Literature values of the experimental and theoretical value of D_0(VO).

Author	D_0 / cm^{-1}	Method	Year
Jones *et al.*[350]	> 48677	Chemiluminescence	1976
Pedley *et al.*[352]	51942 ± 1613	Knudsen cell	1983
Balducci *et al.*[339]	52345 ± 726	Knudsen cell	1983
Bauschlicher *et al.*[347]	45812	CASSCF	1986
Miliordos *et al.*[349]	52464	CASSCF+1+2=MRCI	2007

In their collision-induced dissociation study of VO^+, Aristov and Armentrout determined the dissociation energy of the vanadium monoxide cation to be D_0 = 48393 ± 2823 cm^{-1} (6.00 ± 0.35 eV).[353] Spectroscopy and structures of larger vanadium oxide cluster ions have also been extensively studied by

Asmis *et al.*[354–356] and were also the subject of a recent review by Asmis and Sauer.[357]

6.2 Experimental Methods

6.2.1 Experimental Apparatus

The schematic of the experimental setup is shown in Figure 6.2. Initially, the Oxford VMI spectrometer equipped with the laser ablation cluster source was designed to target only neutral molecules. With the first generation of the Oxford laser ablation - VMI spectrometer, our group studied the photodissociation dynamics of numerous neutral molecules: Au_2, Au-RG, Xe_2, Cu_2, CuO Ag-RG, AgO, CrO and MoO.[358–363] The spectrometer has now been modified so that in the future, it will also allow the study of charged species. The instrument consists of two differentially pumped regions: i) a source chamber, housing the laser ablation source and a Wiley-McLaren acceleration stage, and ii) a detection chamber housing an Einzel lens, VMI lenses assembly, and VMI detector. A Smalley/Bondybey-type ablation source[34,35] is used with focused 532 nm light generated from a pulsed Nd:YAG laser (Continuum Minilite) operated at 10 Hz (typical pulse width of 5-7 ns). The ablated metal plasma is entrained in a pulse of a backing gas delivered by a pulsed solenoid valve (Parker-Hannifin General valve, series 9). The molecular beam then passes through a 1 mm skimmer (Beam Dynamics) prior to entering the Wiley-McLaren acceleration stage consisting of grid-free repeller, extractor and ground electrode. Species with different mass-to-charge ratios can be mass-separated by the time they reach the VMI region by virtue of different arrival time; the arrival time is proportional to the square root of the mass-to-charge ratio (as discussed in Section 2.3). The potentials at the repeller and extractor electrodes are adjusted to allow for the time focus of the species in the VMI region. Prior to the VMI region an Einzel lens,

consisting of a positive electrode sandwiched between two ground electrodes, ensures that the expending trajectories of ions are tightly space focused in the VMI lens assembly. The Einzel lens does not affect kinetic energies of the particles. Just before the VMI lens assembly, a retractable MCP detector allows to monitor the ion signal of the mass-separated species, allowing the determination of the flight time taken to reach the VMI lens assembly.

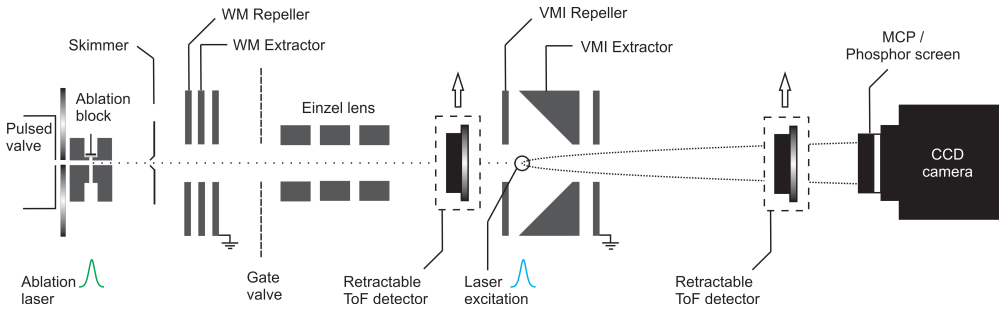

Figure 6.2: A diagram of the VMI spectrometer equipped with a laser ablation source. The instrument permits a study of both neutral and charged species. For the study of neutrals Wiley-McLaren (WM) acceleration stage and Einzel lens are grounded. Static voltages are applied to the VMI electrodes.

The VMI lens assembly consists of variation of the original Eppink/Parker VMI electrode design. As discussed in the previous publications,[358,361] the cone-shaped extractor design provides more homogeneous electric fields in the extraction region, which are more forgiving to the exact birth position of the ions; photofragmentation with an unfocused laser beam yields fragments over a relatively large volume.[364] Consequently, this also results in the instrument-specific magnification factor close to 1, whereas the original Eppink/Parker design generally has a magnification factor of 1.3 – 1.4.[212,358] Previously, a stepped-chain of electrodes coupled with resistors was coupled to the extractor electrode to bring the potential slowly to ground. In order to a allow for quick pulsing of the repeller and the extractor plate, as required for VMI of charged species, the resistor stack has been grounded as it does not allow for fast-pulsing of voltages. The new VMI assembly *de facto*

consists of a repeller, conical extractor and ground electrode. Neutral and charged species are photodissociated (and ionised in the case of neutrals) between the repeller and extractor electrodes by orthogonally crossing the molecular beam with the probe laser. Prior to the VMI detector, a second retractable MCP detector enables the recording of time-of-flight mass spectra and to perform spectroscopic measurements, *e.g.* REMPI, on the systems while using VMI lenses in time-of-flight mode. The signal from the MCP detector is displayed on a digital oscilloscope (LeCroy Wavesurfer 64MXs-A) connected to PC *via* ethernet cable and recorded with a custom-built LabVIEW program. In the VMI mode, the photofragments are detected using a conventional VMI detector setup (Photek) at the end of the field-free region. The detector consists of two imaging-quality MCP plates in a chevron arrangement coupled to a P46 phosphor screen. Any arrival of an ion at the MCP plates causes a cascade of electrons hitting the phosphor screen triggering fluorescence which is then captured by a position sensitive CCD camera (776 × 586 pixels). The detector allows time-gating ($\Delta t > 70$ ns) in order to mass-discriminate for the ion of the interest.

A gate valve separates the source and the detection region to protect MCP plates from any sudden rises in the pressure in the source region when the instrument is not operational. It permits necessary maintenance such as changing metal targets or aligning the ablation laser without exposing MCP plates to atmospheric pressures. Three turbomolecular pumps in turn backed by two rotary pumps and a scroll pump are used to keep the instrument at a high vacuum. Typical pressures in the source and detection regions are *ca.* 10^{-7} mbar. When the experiment is in operation, the pressure in the source (detection) region rises to *ca.* 5×10^{-5} (6×10^{-7}) mbar.

For the study of neutrals, the Wiley-McLaren acceleration stage and Einzel lens are kept at ground. Static fields are employed in the VMI regions – neutral molecules will not be perturbed by the electric field until they are ionised. VO is formed by laser ablation of a rotating vanadium disk target

(Goodfellow, 1mm thickness) and using 3 bar stagnation pressure of He buffer gas. The VO impurity is present on the surface of the target. No additional O_2 gas was added to the expansion gas. VO is photodissociated between the VMI repeller and extractor electrode using radiation generated from an OPO (Panther EX OPO, Continuum). The OPO itself is pumped by the third harmonic (355 nm) of a Nd:YAG laser (Continuum Surelite II) with a pulse width of *ca.* 8 ns. The polarisation of the photodissociation laser was set to be parallel to plane of the detector.

6.2.2 Polar Onion-Peeling Inversion Method

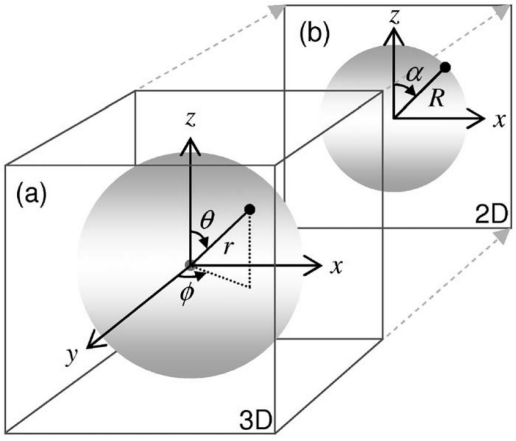

Figure 6.3: a) 3D initial distribution of fragments, $F(r, \theta, \phi)$, where r is the radial distance from the centre, θ is the polar angle and ϕ is the azimuthal angle. b) 2D distribution, $G(R, \alpha)$, obtained by velocity mapping of fragments onto a 2D detector, where R is the radius of the 2D image, and α is the angle between R and the z-axis. For photodissociation experiments involving a vertically-polarised laser parallel to the detector place (xz-plane), the distribution of photofragments will be cylindrically symmetric around the z-axis. Figure reprinted from Roberts, G. M.; Nixon, J. L.; Lecointre, J.; Wrede, E.; Verlet, J. R. R. *Rev. Sci. Instrum.* 2009, *80*, 053104-1–053104-7 with permission from AIP Publishing.[216]

All velocity map images presented in this thesis are reconstructed using the POP algorithm developed by Roberts *et al.*[216] Similarly to BASEX methods, the POP algorithm uses basis functions to generate a suitable fit for the 2D

image. Let us consider an initial 3D Newton sphere of fragments, $F(r, \theta, \phi)$, which in a VMI set-up, will be mapped onto a 2D detector as $G(R, \alpha)$, as shown in Figure 6.3.

The recorded velocity map image can be considered as the sum of individual images of different radii. The complete 2D projection, $G(R, \alpha)$, can be described as the integral of separate 2D projections $g(r; R, \alpha)$ at a particular radius, [i] which satisfies $(R \leq r)$. Hence:

$$G(R, \alpha) = \int_0^{r_{max}} g(r; R, \alpha) dr \tag{6.1}$$

At the maximum radius, where $r = r_{max}$, the 2D projection only has a contribution from the central slice of the full distribution with $\phi = 0$, so the 3D distribution becomes $F(r, \theta, \phi = 0)$. The central slice can thus be written as $h(r_{max}, \theta,)$. Hence:

$$g(r_{max}; R, \alpha) = h(r_{max}, \theta) \tag{6.2}$$

The algorithm now performs a linear least-squares fit of the $h(r_{max}, \theta)$ to the well-known photofragment angular distribution function:[365,366]

$$I(\theta) = N(r) \sum_n \beta_n(r) P_n[cos(\theta)] \tag{6.3}$$

here $N(r)$ are intensity factors, β_n are anisotropy parameters, and P_n is the n^{th} order Legendre polynomial.

Starting at r_{max}, the simulated distribution $g_{fit}(r; R, \alpha)$ can now be be removed from the observed 2D image:

$$G^*(R, \alpha) = G(R, \alpha) - g_{fit}(r; R, \alpha) \tag{6.4}$$

[i] 2D projections $g(r; R, \alpha)$ are considered at specific radii r of the original 3D Newton sphere, which will yield the corresponding R and α

where $G^*(R, \alpha)$ is the remainder of the original image after the subtraction of the outermost layer. This procedure is iteratively repeated for $r = r_{max} - dr$ until $r = 0$. The sum of $h(r, \theta)$ from each iteration then yields the required central 2D slice of the original Newton sphere of photofragments.

6.2.3 Determination of Kinetic Energy Release Spectra

Following the reconstruction of the central slice of the Newton sphere, kinetic energies of the fragments can be determined. The radius, r, of a particular ring on the detector is related to the magnification factor, N, velocity, v, and time-of-flight, t, *via*:[212]

$$r = N \times v \times t \tag{6.5}$$

The instrument specific magnification factor, N, takes into the account the inhomogeneous electric field in the extraction region. The magnitude of the magnification factor can be determined either by modelling, or by performing measurements on system with a well-known photofragment product distribution.

Let us consider a photodissociation of a vanadium containing molecule VX into fragments V and X:

$$\mathrm{VX} + n \times h\nu \rightarrow \mathrm{V}^* + \mathrm{X}^* \tag{6.6}$$

Photofragments V and X can often be produced in their excited electronic states, labelled as V^* and X^*, respectively. The photodissociation is considered to occur with n photons of energy $h\nu$, where h is the Planck's constant and ν is the frequency. A schematic of a photodissociation on an idealised potential energy surface (PES) is shown in Figure 6.4.

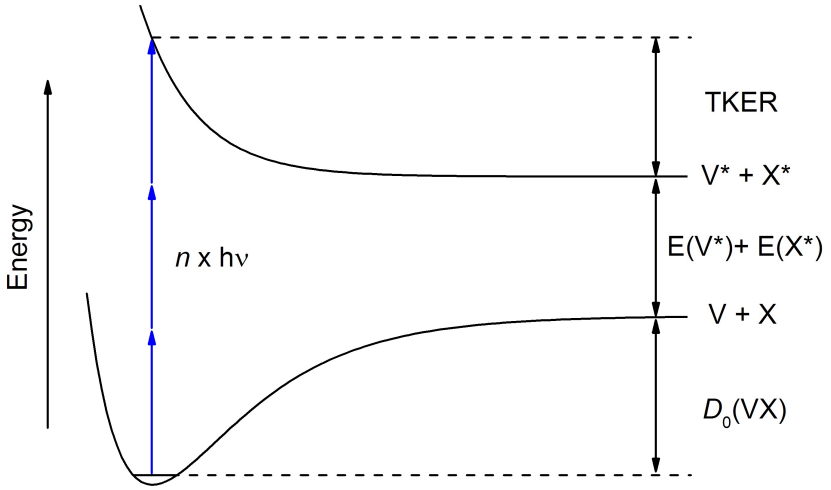

Figure 6.4: An idealised picture of a photodissociation process concerning the parent molecule VX. The atomic excitation energies of the resulting photofragments V^* and X^* are labelled as $E(V^*)$ and $E(X^*)$. The dissociation energy is marked as $D_0(VX)$ and TKER refers to the total kinetic energy release.

Following the reconstruction of the central slice of the Newton sphere, the kinetic energy release (KER) of each fragment can be determined. For the vanadium fragment, this would lead to the following expression:

$$KER_V = \tfrac{1}{2} m_V v_V^2. \tag{6.7}$$

In order to correctly describe the photodissociation energetics, *i.e* the sum of both fragment's KERs or better, the total kinetic energy release (TKER) is required. Considering the conservation of momentum, the KER of the co-fragment X can also be determined. The velocity of the co-fragment, v_X, can thus be derived from:

$$m_V v_V = m_X v_X \tag{6.8}$$

$$v_X = \frac{m_V v_V}{m_X} \tag{6.9}$$

where m_X is the mass of the co-fragment X. Thus, TKER can be expressed as:

$$TKER = KER_V \times \left(1 + \frac{m_V}{m_X}\right) \tag{6.10}$$

Now, TKER for a photodissociation process can be determined by measuring the recoil velocity of only one fragment.

Inferring from Figure 6.4, the energetics of a photodissociation process can be described as:

$$n \times h\nu = D_0(VX) + E(V^*) + E(X^*) - E(VX) + TKER, \tag{6.11}$$

where E(V^*) and E(X^*) are the internal energies of the fragments, E(VX) is the internal energy of the parent molecule, and D_0(VX) is the dissociation energy of the parent molecule VX. In some systems, the dissociation energy will be well-established; TKER spectra can then be used to identify the product quantum states. Similarly, employing a suitable REMPI scheme can state selectively-ionise a particular photofragment – dissociation energy of the parent species can then be inferred using Equation 6.11. In practice, as presented in Section 6.3.2, velocity map images will often be recorded over a large spectral range, which will provide clearer indications of the photodissociation channels.

6.2.4 Identification of the Molecular Carrier

Experiments on neutral species come with a particular experimental challenge. The laser ablation process produces various metal-containing species with no means of mass discrimination. Only in the post-analysis, one is able to determine the parent molecule by examining signatures in the photofragment quantum states.

As seen from the Equation 6.11, photodissociation of the parent species VX produces photofragments V and X. The V fragment is subsequently ionised and detected *via* VMI. The ionisation step does not affect the recoil velocity of V since any excess energy is carried away by the electron. The ionisation potential of V is 54412 cm^{-1} (6.746 eV);[367] ionisation from the ground electronic state requires a three-photon process in the energy range considered here. The parent species can be assumed to be in the electronic ground state (a reasonable assumption for species undergoing supersonic expansion), hence E(VX) = 0.

By inserting the expression for TKER (Equation 6.10) into Equation 6.11 one obtains:

$$n \times h\nu = D_0(VX) + E(V^*) + E(X^*) + KER_V \times \left(1 + \frac{m_V}{m_X}\right). \qquad (6.12)$$

For a particular photodissociation channel, a pair of photofragments V and X are produced in specific quantum states. Hence, one can write E(V^*) + E(X^*) + D_0(VX) = k, where k is simply a constant. Equation 6.12 can now be simplified:

$$n \times h\nu = k + KER_V \times \left(1 + \frac{m_V}{m_X}\right). \qquad (6.13)$$

Upon rearrangement this becomes:

$$KER(V) = h\nu \times \left(\frac{n}{1 + m_V/m_X}\right) - k', \qquad (6.14)$$

where $k' = \dfrac{k}{1 + m_V/m_X}$.

By plotting KER(V) against the photon energy ($h\nu$), the identity of co-fragment X and the number of photons involved in the photodissociation

process can be determined. Knowing that the number of photons is necessarily an integer limits the selection of possible candidates for X. This analysis is employed to confirm the co-fragment in Section 6.3.2.

6.3 Experimental Results

6.3.1 REMPI spectrum of VO

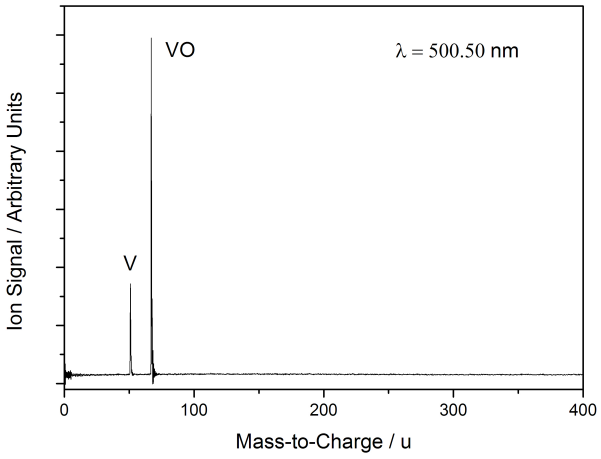

Figure 6.5: Time-of-flight REMPI mass spectrum recorded at 500.50 nm. The vanadium target was ablated in the presence of He buffer gas administered from 3 bar static pressure. Only V atom and VO were observed; no larger species were detected. The energy at 500.50 nm (19980 cm^{-1}) corresponds to the $C^4\Sigma^-$ - $X^4\Sigma^-$ (3,0) transition in VO.

The time-of-flight mass spectrum recorded with the laser wavelength set on the $C^4\Sigma^-$ - $X^4\Sigma^-$ (3,0) transition in VO at 500.50 nm (19980 cm^{-1}) is shown in Figure 6.5. Vanadium disk is used for ablation in the presence of helium carrier gas delivered from 3 bar static pressure. The mass spectrum is recorded at an energy of a REMPI transition in VO, so it is not unexpected that VO is the dominant species detected at this particular energy. Neutral

species require ionisation prior to the detection, however, no species other than V and VO were observed. The backing pressure of the expansion gas was also intentionally kept at a low static pressure of 3 bar, thus discouraging any clustering.

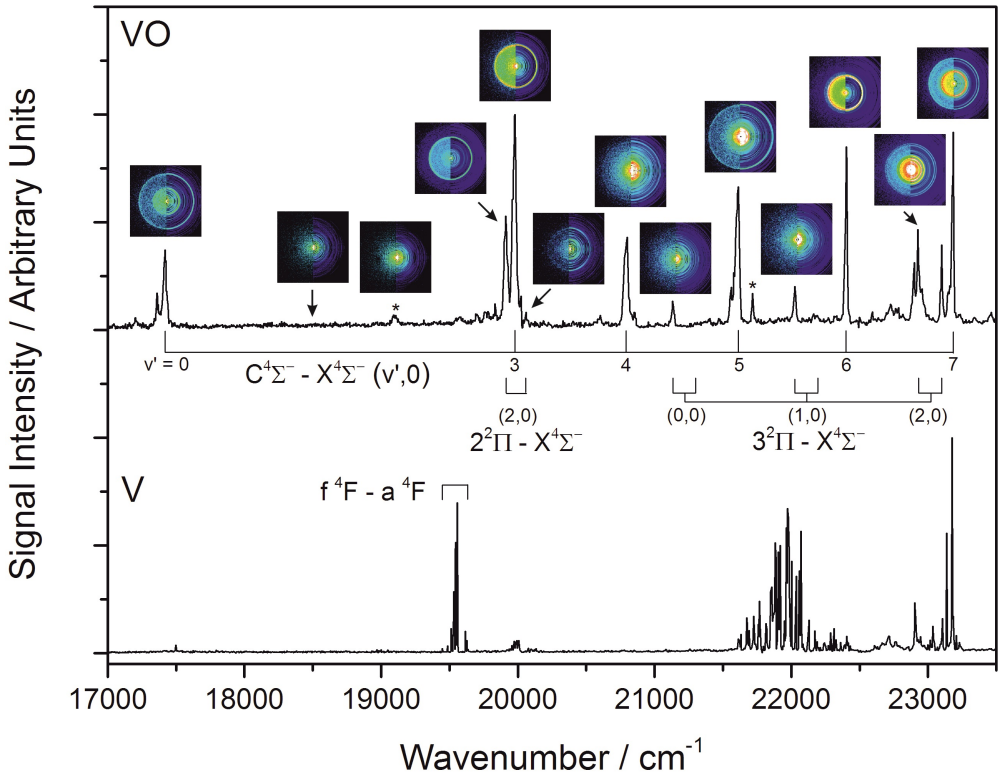

Figure 6.6: One colour (1 + n) REMPI spectrum of VO recorded in the range 17000 - 23500 cm^{-1}. Velocity map images of vanadium ion recorded at energies of vibrational transitions are included. The data includes the assignments by Hopkins *et al.*[345] The asterisk (*) indicates major bands that are unassigned. Transitions to v' = 1 and 2 require a (1 + 1') REMPI scheme not explored in this work. Bottom: The corresponding signal observed in the V channel. The considered species are neutrals, VO and V, and are ionised prior to the detection.

A (1+n) REMPI spectrum of VO in the region $C^4\Sigma^-$ - $X^4\Sigma^-$ (v',0) is shown in Figure 6.6. The REMPI spectrum reproduces transitions previously identified by our group.[345] As shown in Figure 6.6, velocity map images of the

vanadium ion recorded at the energies corresponding to different $C^4\Sigma^-$ - $X^4\Sigma^-(v',0)$ and $^2\Pi$ - $X^4\Sigma^-(v',0)$ transitions display dramatic changes in the observed photofragment distributions.

Notably, fragments with non-zero kinetic energy release are only observed on resonances that correspond to transitions in VO. Figure 6.6 also shows the detected signal intensities for vanadium atom in the considered spectral region. The only REMPI transitions we are able to assign are the two photon transitions to f ^{4}F spin-orbit states from the vanadium ground electronic state (f ^{4}F – a ^{4}F). The transitions around 22000 cm^{-1} do not match any known REMPI transitions in vanadium atom. As we are unable to mass discriminate in the ablation process, the vanadium atom signal could also be resulting from a fragmentation of a larger vanadium containing species. However, the signal in the vicinity of the $C^4\Sigma^-$ - $X^4\Sigma^-$ (v' = 1, 3 and 7, 0) vibronic transitions in VO is also clearly reproduced in the vanadium atom (and less obviously around v' = 4 and 5). This indicates that the detected vanadium atom is likely to be resulting from the photofragmentation of VO.

6.3.2 Images Around v' = 3

A velocity map image recorded in the V^+ channel at the position of the $C^4\Sigma^-$ - $X^4\Sigma^-$(3,0) transition is shown in Figure 6.7. A magnification factor of N = 1.055 is used throughout this work, which is consistent with our SIMION simulations and past experiments.[362,368] The image itself is rather simple - only one strong feature with a KER of 1190 cm^{-1} is observed.

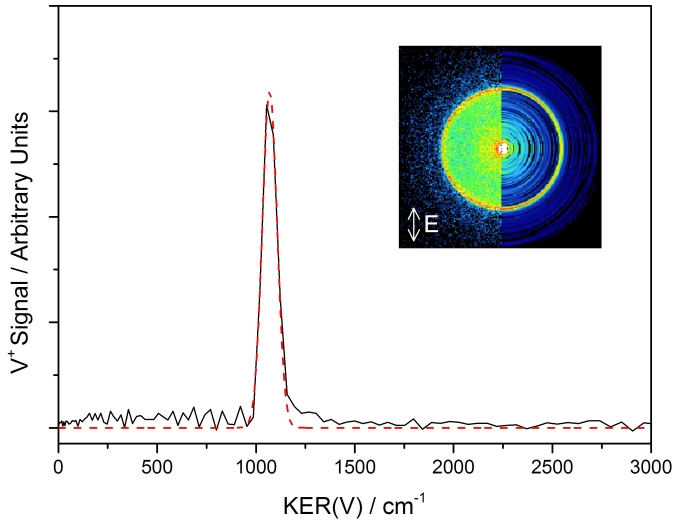

Figure 6.7: Vanadium fragment KER spectra recorded at the position of the $C^4\Sigma^-$ - $X^4\Sigma^-(3,0)$ transition (19980 cm^{-1}) with the corresponding velocity map image (inset). The double-headed arrows depict the laser polarisation plane. The left half depicts the raw image and the right half corresponds to the POP reconstructed central slice of the original Newton sphere. The dotted red line represents a Gaussian function fit to the peak centred at 1190 cm^{-1} with FWHM of 72 cm^{-1}.

In order to identify the parent species, velocity map images were recorded in the vicinity of the $C^4\Sigma^-$ - $X^4\Sigma^-(3,0)$ transition of VO as demonstrated in Figure 6.8. An increase in the KER upon increasing the probe laser energy is expected, since any additional energy above the dissociation threshold will be converted directly into the kinetic energy of the photofragments. Figure 6.8 also depicts typical KER spectra recorded in the V^+ channel around the region of v' = 3, together with the corresponding velocity map images.

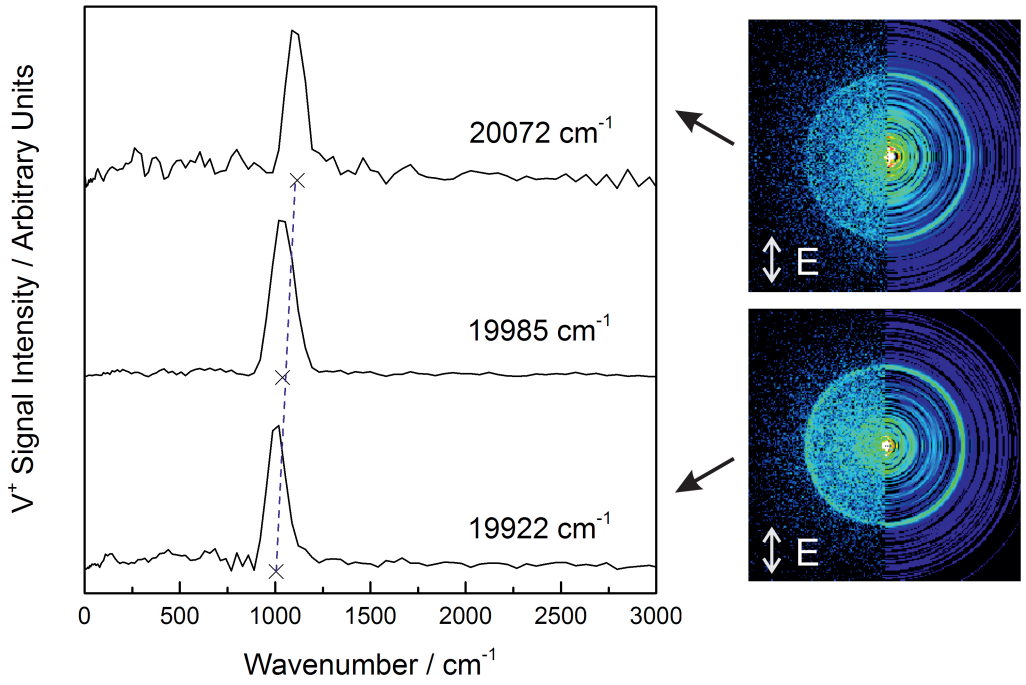

Figure 6.8: KER spectra recorded in the V^+ channel in the vicinity of the $C^4\Sigma^-$ - $X^4\Sigma^-$(3,0) transition of VO. The radius of the ring due to off-axis velocity component of the vanadium fragment increases with increasing energy, which is also replicated in the KER spectra.

As evaluated in Equation 6.17, a plot of KER(V) versus the photon energy will be in the form of a linear function with a gradient of $\frac{n}{1+m_V/m_X}$. From here, the number of photons involved in a photofragmentation process and the identity of the co-fragment X can be determined. A plot of all measured KER for the vanadium co-fragment, over the region between 19912 and 20072 cm^{-1}, is shown in Figure 6.9 (top).

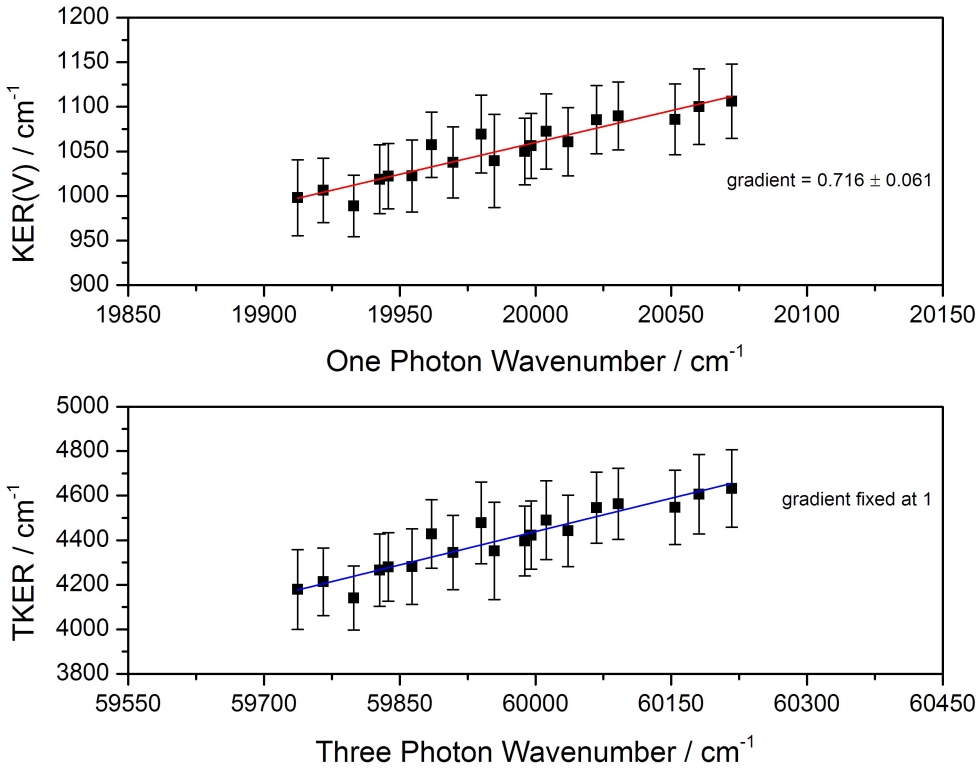

Figure 6.9: Top: KER plotted as a function of one photon energy between 19912 and 20072 cm^{-1} . A linear function fitted to the experimental data gives a gradient of 0.716 ± 0.061. Bottom: TKER plot against three-photon wavenumber. The photodissociation process is thought to produce vanadium and oxygen co-fragments. The gradient of the fitted linear function is fixed at 1, which gives the -y-intercept of 55561 ± 168 cm^{-1}. The error bars in both datasets correspond to the FWHM of each fitted Gaussian used to identify the centre of each peak.

A linear fit to the measured KER values gives a gradient of 0.716 ± 0.061. Table 6.2 lists possible co-fragment candidates with the corresponding number of photons required to photodissociate the parent molecule.

Table 6.2: List of potential co-fragment candidates; n refers to the number of photons needed to photodissociate the parent species. Oxygen co-fragment gives the required number of photons the closest to an integer. Errors in n arise from the uncertainty (standard deviation) in the gradient of the fitted line using linear regression.

Gradient	Co-fragment (X)	n
0.716 ± 0.061	V	1.432 ± 0.122
	V_2	1.074 ± 0.092
	C	3.759 ± 0.321
	N	3.324 ± 0.284
	O	2.998 ± 0.256
	He	18.975 ± 1.622

As shown in Table 6.2 the most likely co-fragment is oxygen. VO is also the only molecular species observed in the molecular beam (Figure 6.5). Based solely on the number of photons required for photodissociation, V_2 and C co-fragments would also give an integer value for n narrowly within the error limits. However, this is very unlikely as there is no evidence of V_3 or VC being present in the molecular beam. Additionally, our group has in the past measured the ionisation energy for V_3 of 44336 cm^{-1},[369] which is lower than the IP for V (the IP for V is 54411.7 cm^{-1}).[370] Hence, if the V_3 had been produced, it would have been expected to be detected, even non-resonantly with the focused laser. In order to produce carbon-containing clusters, the expansion gas is typically seeded with a low percentage of carbon-rich molecules such as methane or acetylene. This was not the case in this experiment - neat He was used as the buffer gas. An additional piece of evidence that points towards VO as the parent molecule is the presence of any off-axis velocity component in the V^+ images only at the energies that correspond to vibronic transitions in VO. Even at the excitation energies corresponding to the $2^2\Pi$ - $X^4\Sigma^-(2,0)$ vibronic transitions a single intense ring is observed in the velocity map images. Images recorded at energies between the vibronic transitions in VO yield only an intense central spot.

Having determined the identity of the co-fragment, the VMI data can now be employed to determine the dissociation energy of VO. As discussed earlier, the most recent (and exact) experimental value for the dissociation energy is that of Balducci *et al.* (D_0(VO) = 52345 ± 726 cm^{-1}).[339] Initially, this value for D_0 is used to identify the channels resulting from the photofragmentation of VO in the vicinity of the C$^4\Sigma^-$ - X$^4\Sigma^-$(3,0) transition.

Rearranging Equation 6.14, a plot of TKER versus $n \times h\nu$ will yield a straight line with the y-intercept of -(D_0(VO) + E(V*) + E(O*)):

$$TKER = n \times h\nu - (D_0(VO) + E(V^*) + E(O^*)). \tag{6.15}$$

With the number of photons, n, and the identity of the molecular carrier known, a linear function can be fitted to the dataset of TKER versus the energy of three photons, as shown in Figure 6.9 (bottom). The fit gives the -y-intercept of 55561 ± 168 cm^{-1}. Using the upper limit of the dissociation energy of Balducci *et al.* (53071 cm^{-1}) implies total fragment internal energy of 2490 cm^{-1}. Assuming the production of oxygen in its ground electronic state (^{3}P: 78 ± 119 cm^{-1}), gives the internal energy of vanadium co-fragment of 2412 ± 206 cm^{-1}. [ii] [iii]

This unequivocally points toward the production of vanadium in the first excited electronic state of ^{6}D: 2293 ± 128 cm^{-1} The third excited state of the V atom is significantly higher in energy (^{4}D: 8596 ± 131 cm^{-1}).

Applying this approach in reverse, assuming the quantum states of photofrag-

[ii] The resolution of VMI spectrometer is too low to resolve separate spin-orbit components of the electronic states of vanadium and oxygen. Instead, the weighted arithmetic mean energy of the spin-orbit components for a particular electronic state with the corresponding weighted standard deviation is considered. The energies of J levels for V ($3d^4(^5\mathrm{D})4\mathrm{s}$; a $^6\mathrm{D}_{\mathrm{J}=1/2-9/2}$)) are: 2112, 2153, 2220, 2311, 2425 cm^{-1}. This gives a weighted mean energy of V (a ^{6}D) = 2293 ± 128 cm^{-1}. Similarly for O($^3\mathrm{P}_{\mathrm{J}=2-0}$): 0, 158 and 227 cm^{-1}. Hence O($^3\mathrm{P}_{\mathrm{J}=2-0}$) = 78 ± 119 cm^{-1}.

[iii] All atomic energies are quoted from the NIST Atomic Spectral Database.[323]

ments allows us to refine the dissociation energy for VO. Using the value for the -y-intercept of 55561 ± 168 cm^{-1}, V(^{6}D: 2293 ± 128 cm^{-1}) and O(^{3}P: 78 ± 119 cm^{-1}) gives a refined value for the dissociation energy of D_0(VO) = 53190 ± 242 cm^{-1}.

6.3.3 Images Around v' = 7

Contrary to the images around v' = 3, the measured TKER spectra around v' = 7 show the production of vanadium atom in several different quantum states manifest in the presence of several rings in the VMI images. The TKER spectrum recorded at position of the $C^4\Sigma^-$ - $X^4\Sigma^-$(v' = 7, 0) vibronic band is shown in Figure 6.10.

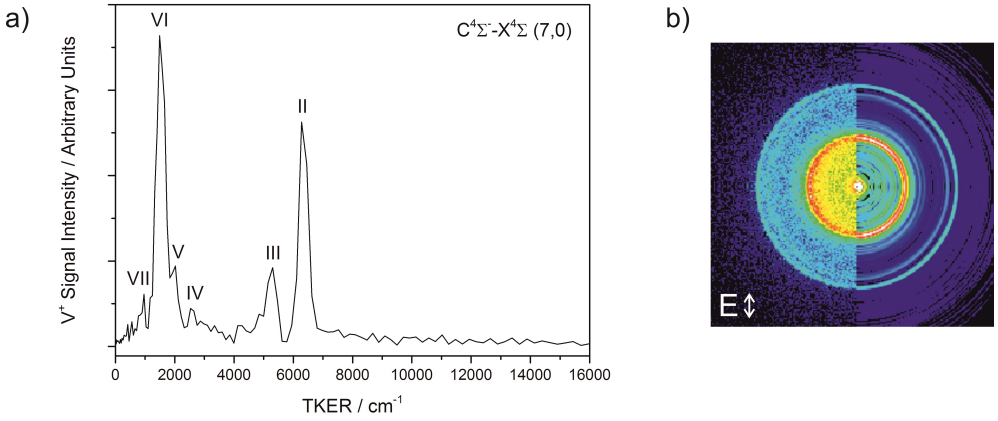

Figure 6.10: Black: Experimental TKER spectrum recorded at the $C^4\Sigma^-$ - $X^4\Sigma^-$(v' = 7, 0) vibronic band (23196 cm^{-1}). Six identified features II–VII belong to series identified in the vicinity of v' = 7 (*vide infra* Figure 6.11) b) The corresponding velocity map image. Left side: the raw image; right side: POP reconstructed central slice. The double-headed arrows mark the laser polarisation plane.

The plot of TKER versus three photon energy, along with relevant assignments is shown in Figure 6.11. The observed photodissociation channels compare well with the production of V in known electronic states from the

third excited state onwards up to the ninth excited state, *i.e.* between 8413 and 15572 cm^{-1} of excitation energy:

- V ($3d^4(^5D)4s$; a $^4D_{J=1/2-7/2}$): 8413, 8476, 8579, 8716 cm^{-1},
- V ($3d^34s^2$; a $^4P_{J=1/2-5/2}$): 9545, 9367, 9825 cm^{-1},
- V ($3d^34s^2$; a $^2G_{J=7/2-9/2}$): 10893, 11101 cm^{-1},
- V ($3d^34s^2$; a $^2P_{J=3/2-1/2}$): 13802, 13811 cm^{-1},
- V ($3d^34s^2$; a $^2D2_{J=3/2-5/2}$): 14515, 14549 cm^{-1},
- V ($3d^4(^3H)4s$; a $^4H_{J=7/2-13/2}$): 14910, 14949, 15001, 15063 cm^{-1},
- V ($3d^4(^3P2)4s$; b $^4P_{J=1/2-5/2}$): 15078, 15271, 15572 cm^{-1}.

The weighted mean energies of these states, together with the corresponding weighted standard deviations as the errors, are considered. This gives the following values: a ^4D = 8596 ± 131 cm^{-1}, a ^4P = 9717 ± 142 cm^{-1}, a ^2G 11017 ± 147 cm^{-1}, a ^2P = 13805 ± 7 cm^{-1}, a $^2D_2$ 14535 ± 24 cm^{-1}, a ^4H = 14992 ± 66 cm^{-1}, and b ^4P = 15389 ± 248 cm^{-1}. Figure 6.11 shows TKER plotted against the three-photon energy in the vicinity of the $C^4\Sigma^-$ - $X^4\Sigma^-(7,0)$ and $^2\Pi$ - $X^4\Sigma^-(2,0)$ transitions. The photodissociation fragments are assigned to the production of vanadium in the a ^4D, a ^4P, a ^2G, a ^2P, a $^2D_2$, a ^4H, and b ^4P states, and oxygen in the ground (^3P) state. The observed photodissociation channels thus match well with the production of vanadium in all electronic states between 8413 to 15572 cm^{-1} of excitation energy.

For completion, events that might lead to the production of oxygen in the first excited state (^1D) are also considered. However, even the peaks with the lowest detected TKER do not appear to correlate with a process forming oxygen in the ^1D state.

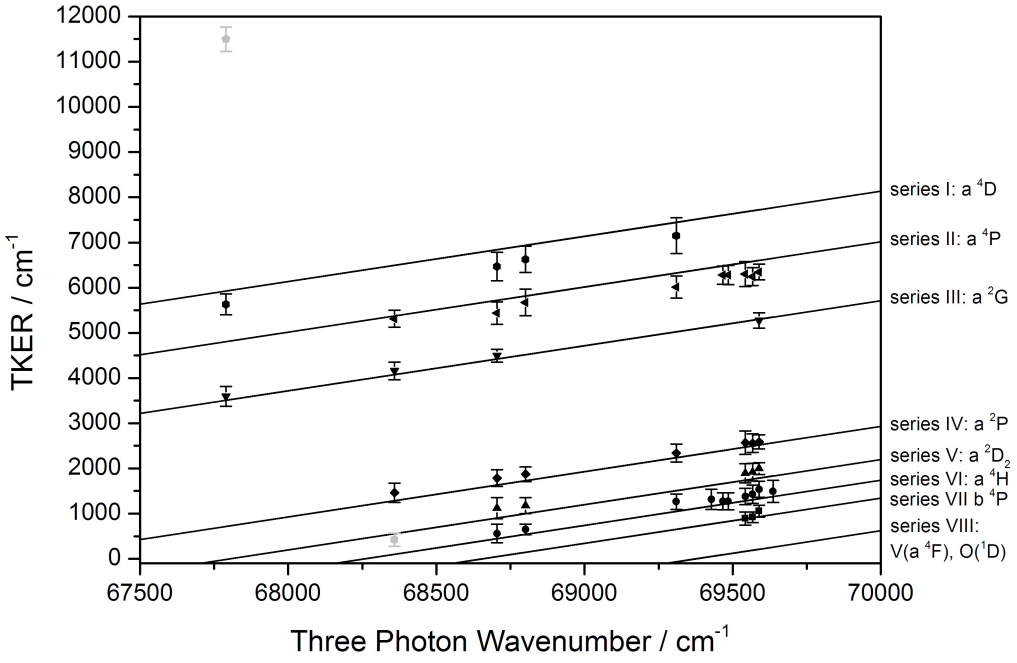

Figure 6.11: TKER spectra of the V and O co-fragments plotted as a function of three-photon energy. The error bars represent the FWHM of the peak in consideration. The solid lines represent the simulated TKER based on the D_0 determined in the v' = 3 region and the identified product quantum states of vanadium and oxygen. From series I to VII, oxygen is produced the in the ground state (^{3}P). For completion, in series VIII, oxygen is modelled to be produced in the first excited state (^{1}D). The data points in grey do not seem to correlate with any of the assigned series.

Off-axis energy components in the velocity map images of V^+ are only observed when sitting on the peaks in the REMPI spectrum of VO. At the energy corresponding to the $C^4\Sigma^-$ - $X^4\Sigma^-(7,0)$ transition, the photodissociation of VO produces the V atom in the b ^{4}P, a ^{4}H, a $^2D_2$, a ^{2}P, a ^{2}G and a ^{4}P electronic states. When using the probe laser energy corresponding to the $^2\Pi$ - $X^4\Sigma^-(2,0)$ transition, a path towards the formation of the a ^{4}D state opens up. However, at lower probe energies, the b ^{4}P state is then no longer produced.

As alluded to in previous subsections, the knowledge of the product quantum state distributions of photofragments together with the measured TKER allows for the determination of parent molecule dissociation energy. For the photodissociation channels identified in Figure 6.11, fixing the gradient at 1 and performing a linear fit gives the following values for the -y-intercepts:

- Series I: 62181 ± 309 cm^{-1},
- Series II: 63214 ± 227 cm^{-1},
- Series III: 64231 ± 181 cm^{-1},
- Series IV: 66958 ± 197 cm^{-1},
- Series V: 67620 ± 190 cm^{-1},
- Series VI: 68136 ± 190 cm^{-1},
- Series VII: 68610 ± 181 cm^{-1}.

Using the information contained in the value of the -y-intercept one can determine the dissociation energy of VO. The calculated values for D_0 from each of the identified series are presented in Table 6.3. The table includes the weighted average for the D_0(VO) calculated from the individual contributions of the dissociation energies determined around v' = 3, and from contributions from Series I-VII.

Table 6.3: Assigned photofragments resulting from the photodissociation of VO in the vicinity of $C^4\Sigma^-$ - $X^4\Sigma^-$(v' = 3 and 7, 0) transitions together with D_0(VO) determined from each series. The weighted average of the D_0(VO) is evaluated from the contributions from the data collected around v' = 3 and from Series I - VII.

		Photofragments	D_0(VO) / cm^{-1}
v' = 3		V(a ^{6}D) + O(^{3}P)	53190 ± 242
v' = 7	Series I	V(a ^{4}D) + O(^{3}P)	53507 ± 356
	Series II	V(a ^{4}P) + O(^{3}P)	53419 ± 293
	Series III	V(a ^{2}G) + O(^{3}P)	53136 ± 262
	Series IV	V(a ^{2}P) + O(^{3}P)	53075 ± 230
	Series V	V(a ^{2}D$_2$) + O(^{3}P)	53007 ± 225
	Series VI	V(a ^{4}H) + O(^{3}P)	53066 ± 234
	Series VII	V(b^{4}P) + O(^{3}P)	53143 ± 329
		Weighted average	53190 ± 261

The D_0(VO) values from Series I – VII are in good agreement with each other, and with the D_0 value evaluated with the data in the vicinity of the v' = 3 transition. The agreement of D_0(VO) values derived from different series also further supports the assignments of the identified exit channels. The weighted average value for D_0(VO) also compares well with the available literature values. The value for the dissociation energy from this work lies within the range for the D_0(VO) value determined by Pedley *et al.* (51942 ± 1613 cm^{-1}), but is slightly higher than the upper limit of the D_0(VO) value by Balducci *et al.* (52345 ± 726 cm^{-1}). The D_0 value from this work inclusive of the error limits nonetheless falls within the range given by Balducci *et al.* It should be pointed out that there is an intrinsic uncertainty in the measurements performed with Knudsen cell mass spectrometry, which can only determine dissociation energies relative to that of a reference sample. In our view, this VMI study provides a more accurate, direct measurement of D_0 for VO.

6.3.4 Images Around v' = 4, 5 and 6

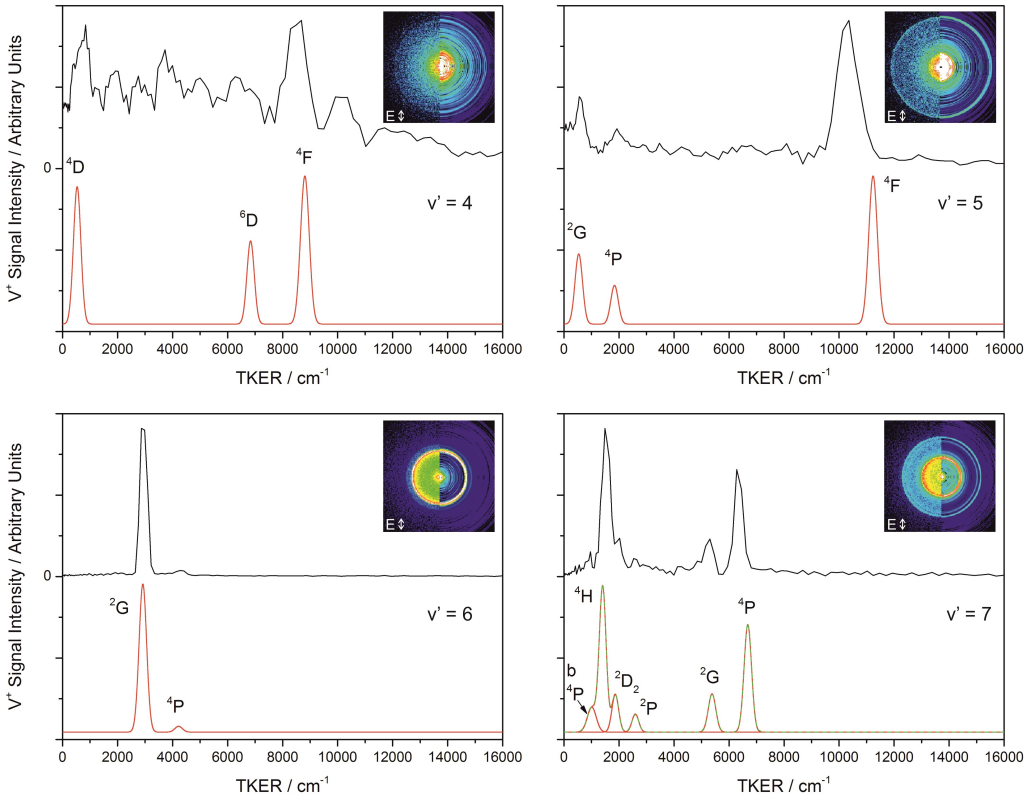

Figure 6.12: TKER spectra recorded at the positions of the vibronic bands of the $C^4\Sigma^-$ - $X^4\Sigma^-$(v' = 4 – 7, 0) system. Black: Experimental TKER spectra. Red: Simulated TKER spectra for different product quantum states of the vanadium co-fragment. In all instances, D_0(VO) = 53190 ± 261 cm^{-1} is used and photodissociation is thought to proceed at the three-photon level. FWHMs are based on the error contributions from the uncertainties in the D_0, and vanadium and oxygen quantum states. Relative amplitudes of the simulated features are fitted to the experimental data. Green: Cumulative fit for the simulated data for the photodissociation at v' = 7 (in all other instances, there are no overlapping features in the simulated TKER spectra). Inset: Velocity map image recorded at each vibronic band. The left side corresponds to the raw image and the right side corresponds to POP reconstructed central slice. If not stated otherwise, the labelled states refer to the "a" electronic states of vanadium. The oxygen co-fragment is assumed to be formed in the ground electronic state (^{3}P).

TKER spectra recorded at v' = 4 - 7 transitions of the $C^4\Sigma^-$ - $X^4\Sigma^-$ system are shown in Figure 6.12. Photodissociation at v' = 4 yields an image with surprisingly poor signal-to-noise resolution, which hints to an inefficient photodissociation process at this particular energy. Nevertheless, the simulated spectra allow for an identification of production of the vanadium atom in the a ^{4}D and a ^{4}F quantum states. Less convincing is the production of vanadium in the a ^{6}D state.

At the transition corresponding to the energy of v' = 5, three distinct features are observed in the TKER spectrum. These features match well with the formation of the vanadium atom in the a ^{2}G, a ^{4}P and a ^{4}F electronic states. The predicted TKER spectrum matches well for the three identified quantum states, albeit the position of the peak for the ^{4}F state in the simulated TKER spectrum is slightly higher than observed experimentally.

The TKER spectrum for the v' = 6 transition, shows a strong propensity for the production of the vanadium atom in the a ^{2}G state. Additionally, the less intense feature with slightly higher TKER forms vanadium in the a ^{4}P state. Both of the simulated features are in excellent agreement with the experimental data.

Lastly, the TKER spectrum recorded at the energy of the v' = 7 transition displays numerous features. The simulated peaks correspond to production of vanadium atom in the b ^{4}P, a ^{4}H, a $^2D_2$, a ^{2}P, a ^{2}G and a ^{4}P electronic states as identified previously (*c.f.* Figure 6.11). All six features in the simulated TKER spectrum for v' = 7 agree well with the experimental data.

The velocity map image at v' = 0 is inconclusive. At the energy of the $C^4\Sigma^-$ - $X^4\Sigma^-(0, 0)$ transition, three photons would not be sufficient to take VO over the dissociation threshold. Photodissociation might occur at a four-photon level, however, the data only at v' = 0 is insufficient to draw any indisputable conclusion.

The dynamics of VO photodissociation is intriguing. The intermediate vi-

brational state of VO appears to be of crucial importance in guiding the photodissociation. In the vicinity of the v' = 7 transition, some new features arise even when accessing either the $C^4\Sigma^-$ - $X^4\Sigma^-(7,0)$ and 3 $^2\Pi$ - $X^4\Sigma^-(2,0)$ vibronic transitions. The vibrational states appear to act as a "springboard" to the dissociation continuum. Different repulsive states may be accessed at different excitation energies. These repulsive states then lead to the production of photofragments in different product quantum states. However, no experimental or computational studies are available for any repulsive states that might be accessed at the excitation energies in this work.

6.4 Conclusions

This work represents the first complete investigation of photodissociation dynamics following the modification of the Oxford VMI spectrometer equipped with a laser ablation cluster source. The results demonstrate successful implementation of the new VMI electrostatic lenses setup and provide a new avenue to study neutral metal-based complexes using the instrument initially intended for charged species.

Velocity map images were recorded over the visible range in the vicinity of the $C^4\Sigma^-$ - $X^4\Sigma^-$(v',0) vibronic transitions. This work produced a refined value for the dissociation energy of $D_0(\mathrm{VO}) = 53190 \pm 261$ cm^{-1} from eight different sets of experimental data. All D_0(VO) values determined in this work are self-consistent. The value for D_0(VO) determined by VMI lies within the range given by Pedley *et al.* and Balducci *et al.*[339,352]

VMI investigation of the photodissociation dynamic of VO also revealed a strong dependence of vanadium product quantum states on the intermediate vibronic state of VO accessed in reaching the dissociation threshold. While the spectroscopy of VO is well-understood near the electronic ground state, higher-lying states are still poorly characterised. Additional spectroscopic and theoretical investigations would be required to fully understand

the potential energy surfaces accessed in reaching the photodissociation continuum. In the visible spectral range, the vanadium atom photofragment was produced in all electronic states between the ground ^{4}F and the ninth excited electronic state, b ^{4}P. No conclusive evidence was observed for the production of O atom in anything other than the ground ^{3}P state.

Chapter 7

Summary and Outlook

This work aimed to provide additional insight into the spectroscopy and binding motifs in metal ion-molecule complexes. A new purpose-built IR-REPD spectrometer equipped with a laser ablation source was employed to study the infrared spectroscopy of isolated metal-containing complexes. Metal ion-molecule complexes are produced in a cutaway ablation block specifically built to maximise the production of metal ion complexes with weakly-bound ligands.

The results in Chapter 3 demonstrate the efficient performance of the new ablation block with the production of $Rh^+(CO_2)_n$, $VO_2^+(N_2O)_n$ and $Au^+(CH_4)_n$ complexes. The ablation block thus allows production of intense atomic metal ion signals complexated with various ligands in sufficient abundances to be photodissociated by the IR-OPO/OPA laser and detected in a Wiley-McLaren time-of-flight mass spectrometer. Performance of the IR-REPD spectrometer was characterised by recording the infrared spectra for the well-studied $V^+(CO_2)_n$ complexes - the resulting spectra from this work are in good agreement with the literature.[272,273]

IR-REPD spectroscopy complemented by the density functional calculations is a powerful tool for elucidating the structures of small metal ion-molecule

complexes. The IR-REPD/DFT study of $M^+(CO_2)_n$ (M = Co, Rh, Ir) complexes presented in Chapter 4 reveals a common $[M^+(CO_2)_2]$ core for all three ions. Successive ligands bind less strongly as evident from the reduced blue-shift associated with these moieties. A linear structure for $Co^+(CO_2)_2$ was identified, whereas equivalent structures for the Rh^+ and Ir^+ ion are found to be bent. The trend in bond angles correlates well with the polarisability of the metal ion - the most bent structure being for $Rh^+(CO_2)_2$. Interestingly, for $Ir^+(CO_2)_2$ we have also observed a significant effect of an argon atom on the relative energy ordering of the identified isomers. Here argon is not a perfectly inert messenger.

In the IR-REPD/DFT study of $MO_2^+(CO_2)_n$ (M = Nb and Ta) complexes presented in Chapter 5, a remarkable similarity between the equivalent complexes of the NbO_2^+ and TaO_2^+ ions is observed. Complemented with the density functional calculations, it was shown that the common $[MO_2^+(CO_2)_4]$ core exists for both M = Nb and Ta, with other ligands binding significantly more weakly. A notable increase in the intermolecular bond distances for the minimally-perturb second coordination sphere ligands coincides with a decrease in the calculated binding energies. In order to compare accurately the properties of group 5 MO_2^+ cations, VO_2^+ ion could be formed by adding O_2 to the expansion gas mixture. We have, in the past, successfully formed $MO_m^+(CO_2)_n$ complexes by seeding a small percentage of CO_2 and O_2 in argon[371] - this is also the approach employed by the Duncan group.[287]

The legacy of this thesis will hopefully not only be the work presented herein but also a potential for the new avenues to be explored with the experimental setup and *modus operandi* outlined in Chapter 3. All complexes studied in this thesis were cations - with some initial success we have recently formed anionic complexes. Our group has also been extending the scope to the complexes of CO_2 with lanthanide ions. In addition, a study of interaction of N_2O ligands with Cu^+, Ag^+ and Au^+ has recently been submitted for publication.[268] This was the first IR-REPD study involving N_2O as a ligand

and it revealed different structural isomers for gas-phase $M^+(N_2O)$ (M = Cu, Ag, Au) complexes. N_2O can bind to the metal ion *via* the N-end or O-end, whose specific vibrational signatures can be detected with the IR-REPD spectroscopy and confirmed with DFT calculations. Furthermore, in $Au^+(CH_4)_n$ complexes we managed to observe vibrationally-enhanced dehydrogenation when exciting $\nu_3(t_2)$ stretch in methane before interactions with Au^+ ions.[372]

This brings us to one of the ultimate goals of the IR-REPD experiment. Besides performing spectroscopic measurements, the intention is to use the new instrument to detect infrared induced reactivity involving metal-ion complexes, too. Our group has previously observed infrared induced reactivity in N_2O adsorbed on a rhodium cluster.[373] While the aforementioned study is performed by exciting metal-metal modes using a free electron laser, it would be of a significant interest to try to guide chemical reactions mode-selectively by exciting ligand vibrational modes using the IR-OPO/OPA laser.

Interesting systems might involve mixed-chromophore complexes. For example, by co-adsorbing CO_2 and H_2 on a cluster one may drive chemical reaction by exciting one of the available vibrational modes. The behaviour of such system is mostly unknown and many questions arise. What happens upon the absorption of a photon in a mixed-chromophore complex? Is the more weakly-bound ligand always preferentially desorbed or can excitation of different vibrational modes lead to different branching ratios of products? Future IR-REPD experiments can shed a light on this fundamental process.

For the studies described herein, the Wiley-McLaren time-of-flight mass spectrometer was used in a linear mode. The instrument has a potential to be used in a reflectron mode and preliminary experiments have shown that this leads to the expected improvement in the mass resolution. Furthermore, in the current experimental setup we use no mass selectivity. In order to further improve the experiment, plans exist for a mass-selectivity stage involving a quadrupole ion guide that would permit for the recording of an

infrared spectrum of a particular complex at zero background. This would ensure that only complexes of interest reach the extraction stage, where they can be probed by the IR-OPO/OPA laser.

In this work, a VMI study of VO photodissociation in the vicinity of the $C^4\Sigma^-$ - $X^4\Sigma^-$(v',0) vibronic transitions reveals a strong dependence of the product quantum states on the intermediate vibrational state accessed in reaching the dissociation continuum. The photodissociation is rationalised to occur in a three-photon process with the first photon loosely resonant with a vibrational level in the $C^4\Sigma^-$ progression. This study also yields a refined value for the dissociation energy of $D_0(\mathrm{VO}) = 53190 \pm 261$ cm^{-1}, which is in good agreement with the literature experimental and theoretical values. The refined value for the dissociation energy will also find its place in astrophysical and astrochemical models.[335] This is expected to lead to a better understanding of exoplanet atmospheres.

The VMI experimental apparatus also has a capacity to study charged systems, developed during the course of the above studies. Apart from sparse quantum chemical calculations and CID experiments by the Armentrout group (see Section 1.6 and the references within), the binding energies of ligands, particularly those in the outer coordination shells, are mostly unknown. Also, due to its postulated use in hydrogen storage, the accurate determination of binding energies is particularly important for M^+H_2 complexes (see section 2.5.2).

The modified VMI spectrometer includes a Wiley-McLaren acceleration stage which allows for the mass selection of ions, ensuring that only species of interest are photodissociated. Each complex can thus be probed with zero background signal. Particularly for larger metal ion-molecule complexes, an absorption of a photon can lead to loss of several ligands. This process, yielding several photofragments, can then be detected with VMI. Recent developments of high-repetition rate detectors such as PImMS,[246] would even allow for a simultaneous detection of various photofragments.

Planned further modification of the VMI instrument will include a neutral molecular beam in a crossed-molecular beam setup in order to study ion–neutral reaction. This would allow the investigation of reactions such as an O-atom abstraction from CO_2 or N_2O by a metal ion. The kinetics of an O-atom abstraction from CO_2 by Nb^+ and Ta^+ are well understood.[297] However, the knowledge of particular potential energy surfaces accessed still poses a challenge for the theory and experiments. Other target systems include the FeO^+ mediated conversion of H_2 into H_2O (see section 1.3) which is believed to proceed on multiple potential energy surfaces. VMI would allow for accurate determination of the product quantum state distributions and together with quantum trajectory simulations be the final arbiter over the reaction profile of this reaction.

In addition to a VMI photofragmentation study of VO, the results presented herein demonstrate a powerful scope for a complementary use of the quantum chemical calculations and experiments in the elucidation of fundamental binding motifs between a metal ion and molecules. This thesis thus epitomises the conceptual framework isolated metal-containing species can provide in the quest to rationalise the fundamental chemical processes occurring at a molecular level.

In short, the instrument and technique development described in this thesis lay the foundations for exciting new areas of research in the Mackenzie group. The metal-ligand complexes which form the subject of much of this work represent a complementary development from the metal clusters the group has studied previously.

Appendix A

Supplementary Information for Chapter 4: Infrared Spectroscopy of $M^+(CO_2)_n$ (M = Co, Rh, Ir) Complexes

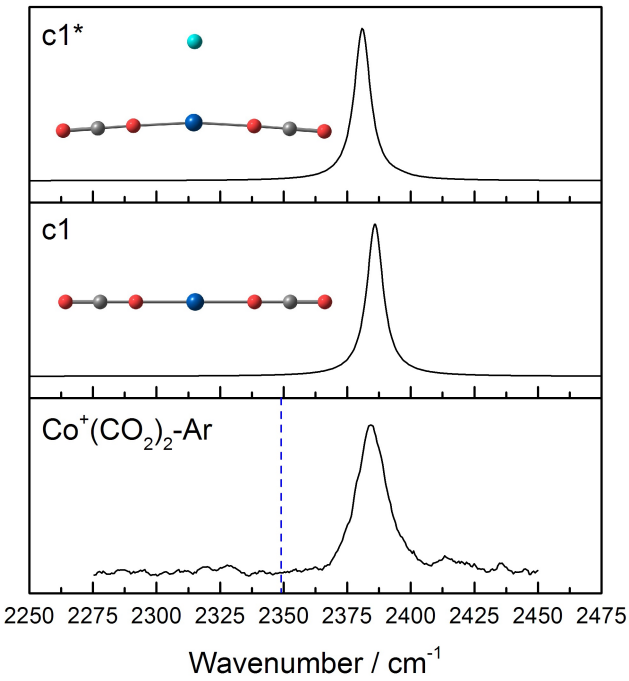

Figure A.1: Experimental IR-REPD spectrum for $Co^+(CO_2)_2$–Ar together with the simulated IR spectra for $Co^+(CO_2)_2$ (structure c1) and its Ar-tagged counterpart (structure c1*). All calculations are performed at the B3P86/Def2TZVP level of theory. The vertical dashed line marks the position of the asymmetric stretch ν_3 in an isolated CO_2.

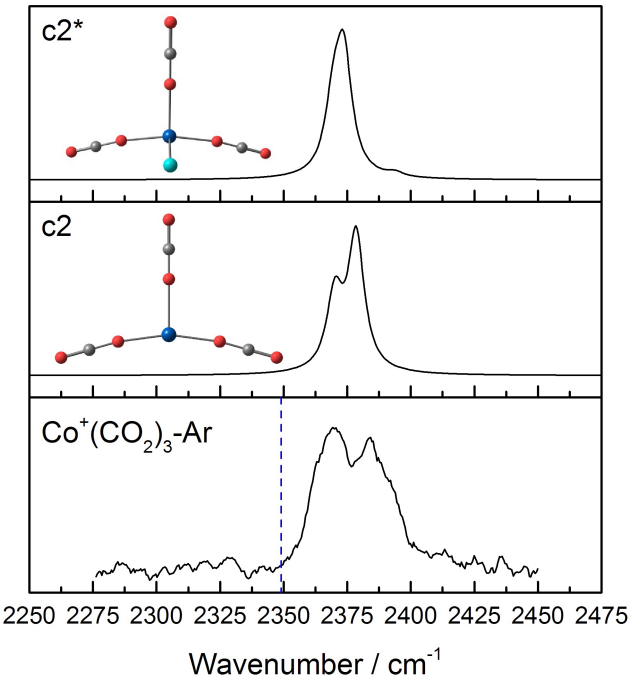

Figure A.2: Experimental IR-REPD spectrum for $Co^+(CO_2)_3$–Ar together with the simulated IR spectra for $Co^+(CO_2)_3$ (structure c2) and its Ar-tagged counterpart (structure c2*). All calculations are performed at the B3P86/Def2TZVP level of theory. The vertical dashed line marks the position of the asymmetric stretch ν_3 in an isolated CO_2.

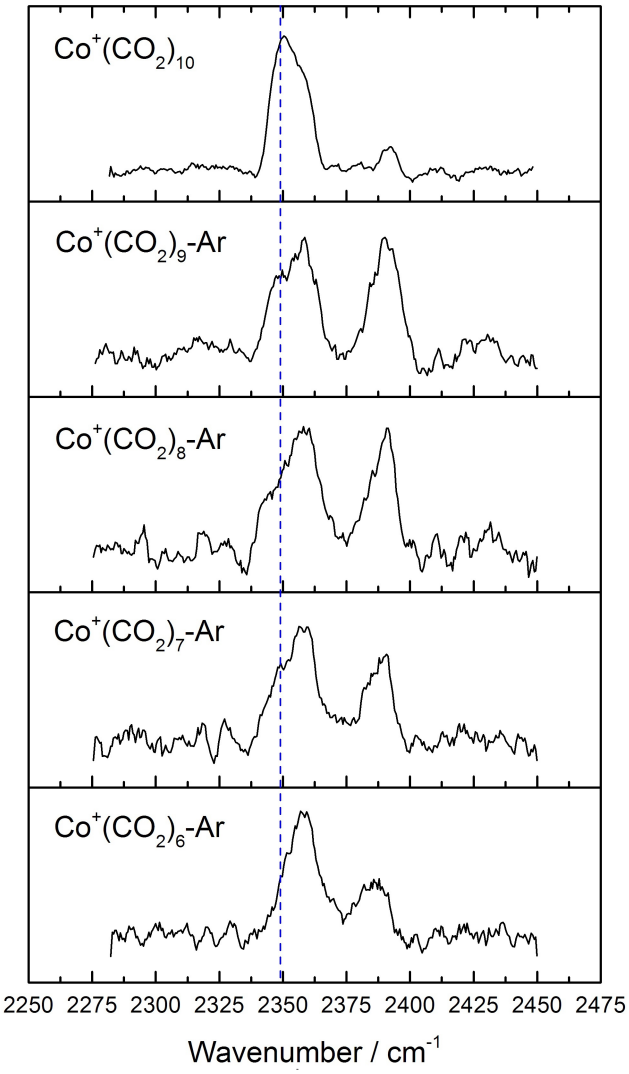

Figure A.3: Experimental IR-REPD spectra for $Co^+(CO_2)_{6-9}$–Ar and $Co^+(CO_2)_{10}$. The vertical dashed line marks the position of the asymmetric stretch ν_3 in an isolated CO_2.

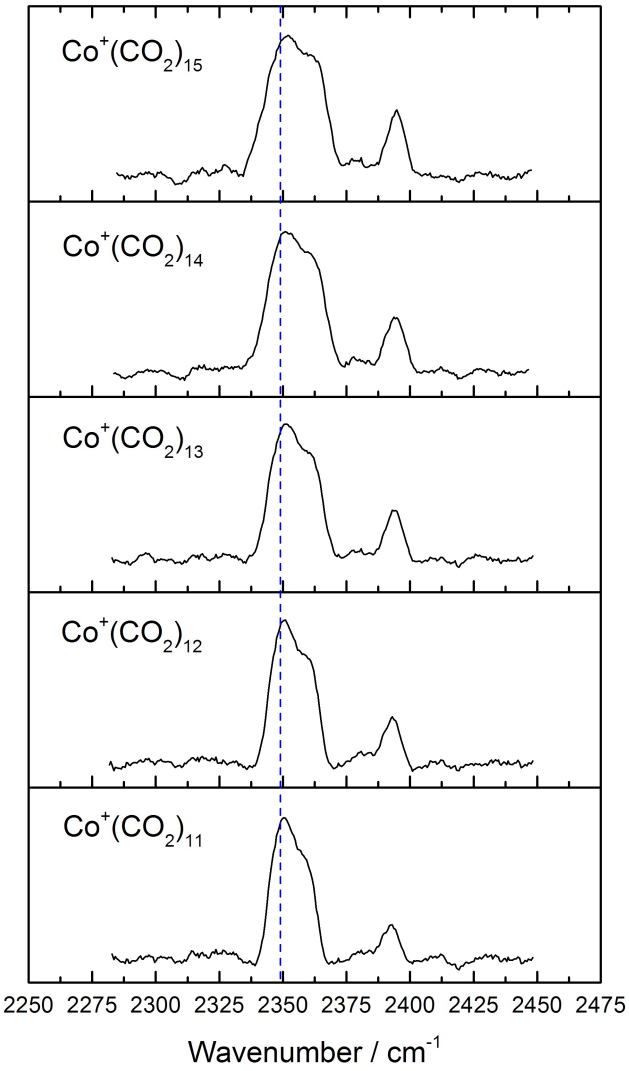

Figure A.4: Experimental IR-REPD spectra for $Co^+(CO_2)_{11-15}$. The vertical dashed line marks the position of the asymmetric stretch ν_3 in an isolated CO_2.

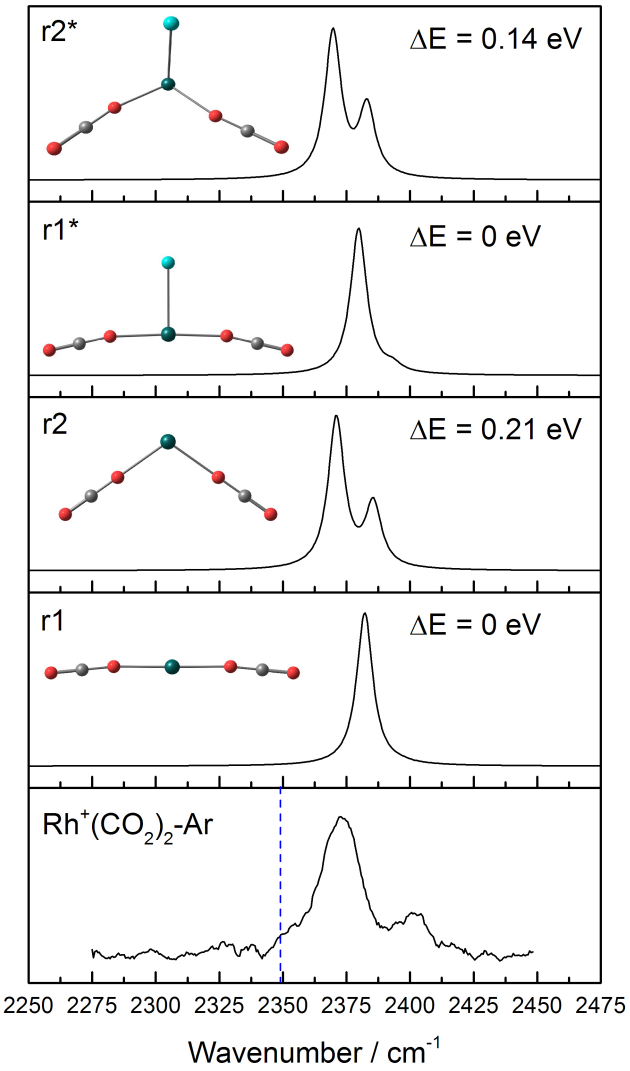

Figure A.5: Experimental IR-REPD spectrum for $Rh^+(CO_2)_2$–Ar together with the simulated IR spectra for $Rh^+(CO_2)_2$ (structures r1 and r2) and its Ar-tagged counterparts (structures r1* and r2*). All calculations are performed at the B3P86/Def2TZVP level of theory. The vertical dashed line marks the position of the asymmetric stretch ν_3 in an isolated CO_2.

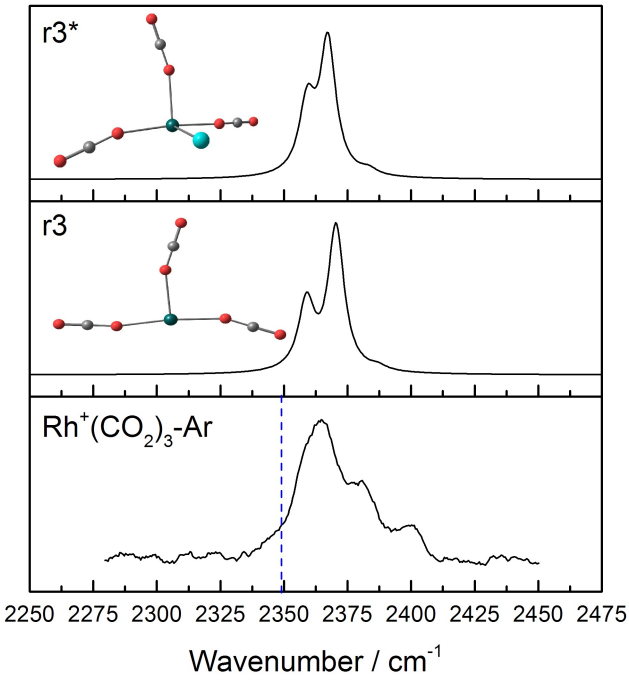

Figure A.6: Experimental IR-REPD spectrum for $Rh^+(CO_2)_3$–Ar together with the simulated IR spectra for $Rh^+(CO_2)_2$ (structure r3) and its Ar-tagged counterparts (structure r3*). All calculations are performed at the B3P86/Def2TZVP level of theory. The vertical dashed line marks the position of the asymmetric stretch ν_3 in an isolated CO_2.

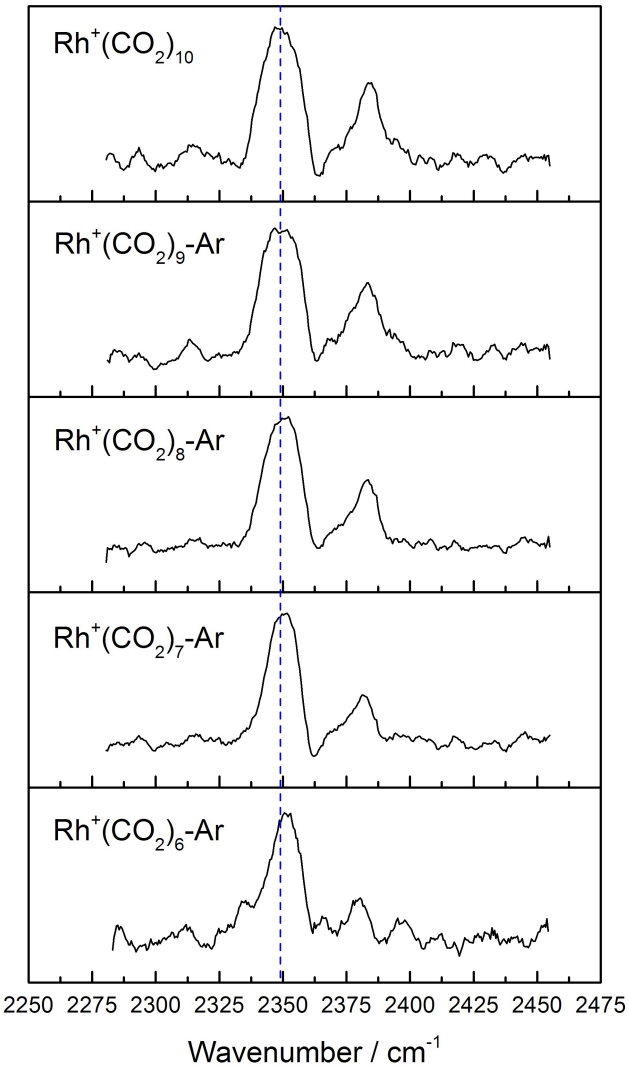

Figure A.7: Experimental IR-REPD spectra for $Rh^+(CO_2)_{6-9}$–Ar and $Rh^+(CO_2)_{10}$. The vertical dashed line marks the position of the asymmetric stretch ν_3 in an isolated CO_2.

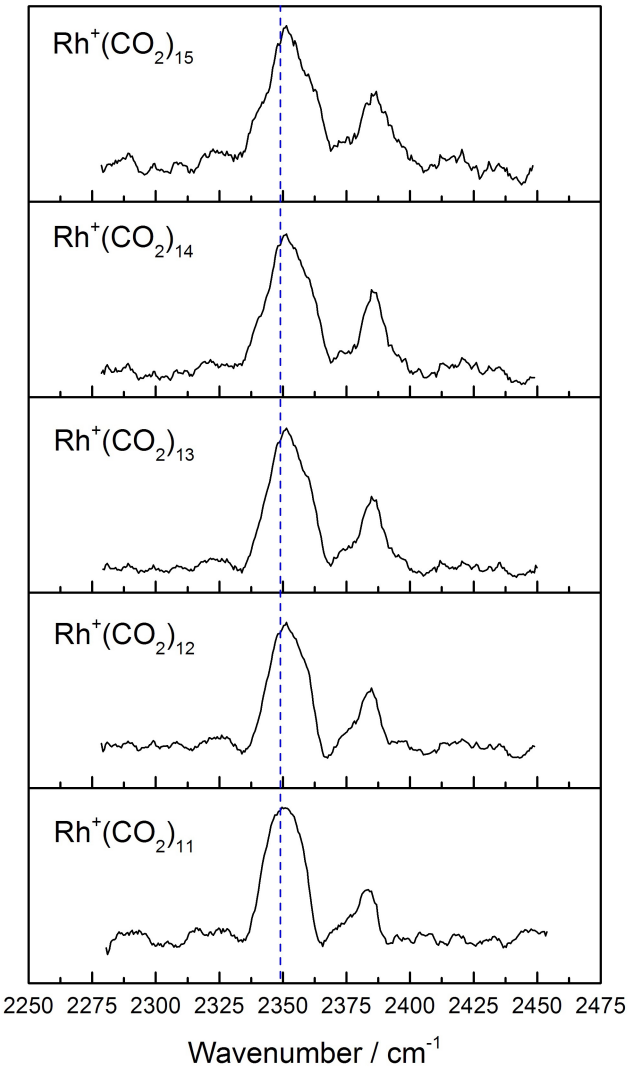

Figure A.8: Experimental IR-REPD spectra for $Rh^+(CO_2)_{11-15}$. The vertical dashed line marks the position of the asymmetric stretch ν_3 in an isolated CO_2.

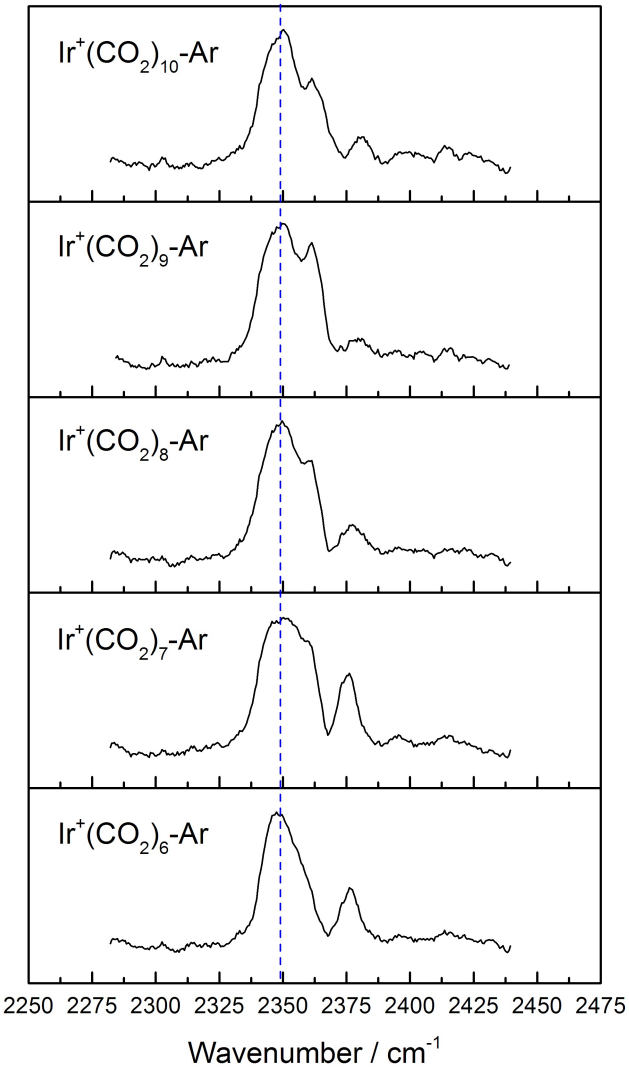

Figure A.9: Experimental IR-REPD spectra for $Ir^+(CO_2)_{6-10}$–Ar. The vertical dashed line marks the position of the asymmetric stretch ν_3 in an isolated CO_2.

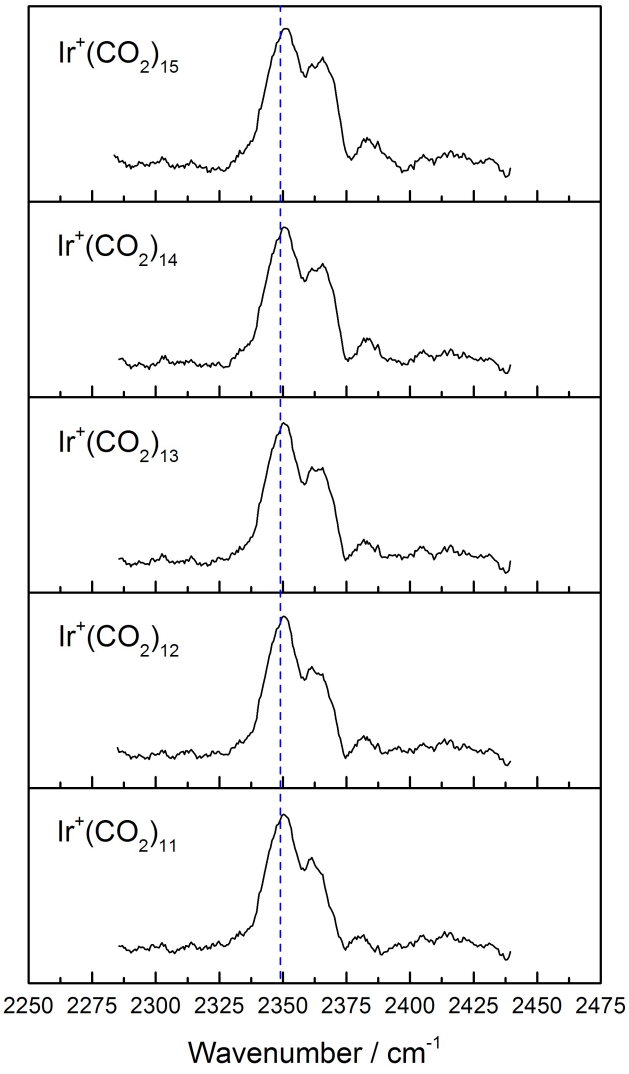

Figure A.10: Experimental IR-REPD spectra for $Ir^+(CO_2)_{11-15}$. The vertical dashed line marks the position of the asymmetric stretch ν_3 in an isolated CO_2.

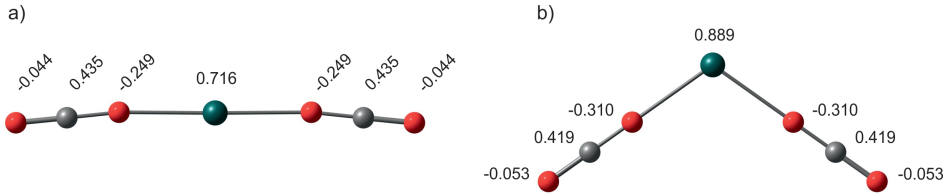

Figure A.11: DFT calculated structures for $Rh^+(CO_2)_2$. The partial charges derived from the Mulliken population analysis are included for a) structure r1 and b) structure r2.

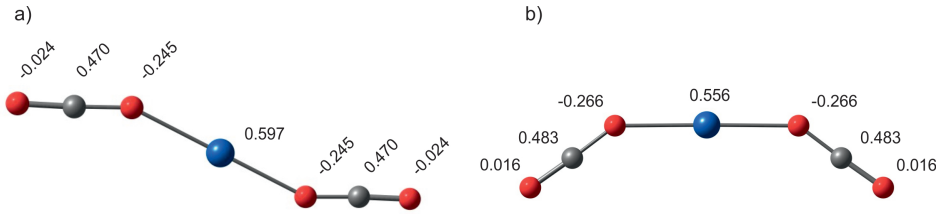

Figure A.12: DFT calculated structures for $Ir^+(CO_2)_2$. The partial charges derived from the Mulliken population analysis are included for a) structure i1 and b) structure i2.

Bibliography

(1) Holm, R. H.; Kennepohl, P.; Solomon, E. I. *Chem. Rev.* **1996**, *96*, 2239–2314.

(2) Kilpin, K. J.; Dyson, P. J. *Chem. Sci.* **2013**, *4*, 1410–1419.

(3) Andreini, C.; Bertini, I.; Cavallaro, G.; Holliday, G. L.; Thornton, J. M. *J. Biol. Inorg. Chem.* **2008**, *13*, 1205–1218.

(4) Pluth, M. D.; Bergman, R. G.; Raymond, K. N. *Science* **2007**, *316*, 85–88.

(5) Murphy, D. M.; Thompson, D. S.; Mahoney, M. J. *Science* **1998**, *382*, 1664–1669.

(6) Kopp, E. *J. Geophys. Res.* **1997**, *102*, 9667–9674.

(7) Pesnell, W. D.; Grebowsky, J. *J. Geophys. Res.* **2000**, *105*, 1695–1707.

(8) Grebowsky, J. M. *J. Geophys. Res.* **1981**, *86*, 1537–1543.

(9) Benna, M.; Mahaffy, P. R.; Grebowsky, J. M.; Plane, J. M. C.; Jakosky, B. M. *Geophys. Res. Lett.* **2015**, *42*, 4670–4675.

(10) Schwarz, H. *Angew. Chem. Inter. Ed.* **2015**, *54*, 10090–10100.

(11) Lang, S. M.; Bernhardt, T. M. *Chem. Phys. Phys. Chem.* **2012**, *14*, 9255–9269.

(12) Sauer, J.; Freund, H.-J. *Catal. Lett.* **2015**, *145*, 109–125.

(13) Luo, Z.; Castleman, A. W.; Khanna, S. N. *Chem. Rev.* **2016**, *116*, 14456–14492.

(14) Freund, H.-J.; Meijer, G.; Scheffler, M.; Schlogl, R.; Wolf, M. *Angew. Chem. Int. Ed.* **2011**, *50*, 10064–10094.

(15) Ertl, G.; Prigge, D.; Schloegl, R.; Weiss, M. *J. Catal.* **1983**, *79*, 359–377.

(16) Rayment, T.; Schlogl, R.; Thomas, J. M.; Ertl, G. *Nature* **1985**, *315*, 311–313.

(17) Gong, Y.; Zhou, M.; Andrews, L. *Chem. Rev.* **2009**, *109*, 6765–6808.

(18) Kieber-Emmons, M. T.; Riordan, C. G. *Acc. Chem. Res.* **2007**, *40*, 618–625.

(19) Hlavica, P. *Eur. J. Biochem.* **2004**, *271*, 4335–4360.

(20) Robbins, E. J.; Leckenby, R. E.; Willis, P. *Adv. Phys.* **1967**, *16*, 739–744.

(21) Larsen, R. S.; Neoh, S. K.; Herschbach, D. R. *Rev. Sci. Instrum* **1974**, *45*, 1511–16.

(22) Knight, W. D.; Clemenger, K.; de Heer, W. D.; Saunders, W. A.; Chou, M. Y.; Cohen, M. L. *Phys. Rev. Lett.* **1984**, *52*, 2141–2143.

(23) Riley, S. J.; Parks, E. K.; Mao, C.-R.; Pobo, L. G.; Wexler, S. *J. Phys. Chem.* **1982**, *86*, 3911–3913.

(24) Preuss, D. R.; Pace, S. A.; Gole, J. L. *J. Phys. Chem.* **1979**, *71*, 3553–3559.

(25) Ganteför, G.; Siekmann, H. R.; Lutz, H. O.; Meiwes-Broer, K. S. *Chem. Phys. Lett.* **1990**, *165*, 293–296.

(26) Cha, C.; Ganteför, G.; Eberhardt, W. *Rev. Sci. Instrum.* **1992**, *63*, 5661–5666.

(27) Koyanagi, G. K.; Baranov, V. I.; Tanner, S. D.; Bohme, D. K. *J. Anal. At. Spectrom.* **2000**, *15*, 1207–1210.

(28) Katakuse, I.; Ichihara, T.; Fujita, Y.; Matsuo, T.; Sakurai, T.; Matsuda, H. *Int. J. Mass Spectrom.* **1985**, *67*, 229–236.

(29) Fayet, P.; Wolf, J. P.; Wöste, L. *Phys. Rev. B* **1986**, *33*, 6792–6797.

(30) Ho, J.; Ervin, K. M.; Lineberger, W. C. *J. Chem. Phys.* **1990**, *93*, 6987–7002.

(31) Hahn, H; Averback, R. S. *J. Appl. Phys.* **1990**, *76*, 1113–1115.

(32) Pratontep, S.; Carroll, S. J.; Xiruchaki, C.; Streun, M.; Palmer, R. E. *Rev. Sci. Instrum.* **2005**, *76*, 045103–1–045103–9.

(33) Luo, Z; Woodward, W. H.; Smith, J. C.; Castleman, A. W. *Int. J. Mass. Spectrom.* **2012**, *309*, 176–181.

(34) Dietz, T. G.; Duncan, M. A.; Powers, D. E.; Smalley, R. E. *J. Chem. Phys.* **1981**, *74*, 6511–6512.

(35) Bondybey, V. E.; English, J. H. *J. Chem. Phys.* **1981**, *74*, 6978–6979.

(36) Duncan, M. A. *Rev. Sci. Instrum.* **2012**, *83*, 041101–1–0441101–19.

(37) Kroto, H. W.; Heath, J. S.; O'Brien, S. C.; Curl, R. F.; Smalley, R. E. *Nature* **1985**, *318*, 162–163.

(38) Walker, N. R.; Walters, R. S.; Duncan, M. A. *New J. Chem.* **2005**, *29*, 1495–1503.

(39) Ricks, A. M.; Reed, Z. E.; Duncan, M. A. *J. Molec. Spec.* **2011**, *266*, 63–74.

(40) Duncan, M. A. *J. Molec. Spec.* **2008**, *272*, 99–118.

(41) Knickelbein, M. B.; Yang, S.; Riley, S. J. *J. Chem. Phys.* **1990**, *93*, 94–104.

(42) Fielicke, A.; Kirilyuk, A.; Ratsch, C.; Behler, J.; Scheffler, M.; von Helden, G.; Meijer, G. *Phys. Rev. Lett.* **2004**, *92*, 023401–1–023401–4.

(43) Nonose, S.; Sone, Y.; Onodera, K.; Sudo, S.; Kaya, K. *J. Phys. Chem.* **1990**, *94*, 2744–2746.

(44) Kishi, R.; Iwata, S.; Nakajima, A.; Kaya, K. *J. Chem. Phys.* **1997**, *107*, 3056–3070.

(45) Pramann, A.; Nakajima, A.; Kaya, K. *J. Chem. Phys.* **2001**, *115*, 5404–5410.

(46) Koyasu, K.; Mitsui, M.; Nakajima, A.; Kaya, K. *Chem. Phys. Lett.* **2002**, *358*, 224–230.

(47) Yamashita, M.; Fenn, J. B. *J. Phys. Chem.* **1984**, *88*, 4451–4459.

(48) Fenn, J. B.; Mann, M.; Meng, C. K.; Wong, S. F.; Whitehouse, C. M. *Science* **1989**, *246*, 64–71.

(49) Lang, J.; Mohrbach, J.; Dillinger, S.; Hewer, J. M.; Niedner-Schatteburg, G. *Chem. Comm.* **2017**, *53*, 420–423.

(50) Nosenko, Y.; Riehn, C.; Niedner-Schatteburg, G. *Phys. Chem. Chem. Phys.* **2016**, *18*, 8491–8501.

(51) DePalma, J. W.; Kellehe, P. J.; Johnson, C. J.; Fournier, J. A.; Johnson, M. A. *J. Phys. Chem. A* **2015**, *119*, 8294–8302.

(52) DePalma, J. W.; Kellehe, P. J.; Tavares, L. C.; Johnson, M. A. *J. Phys. Chem. Lett.* **2017**, *8*, 484–488.

(53) Kappes, M. M.; Staley, R. H. *J. Am. Chem. Soc.* **1981**, *117*, 1286–1287.

(54) Blagojevic, V.; Salpin, J.-Y.; Bohme, D. K. *J. Am. Chem. Soc.* **2005**, *127*, 3345–3355.

(55) Fiedler, A.; Schroder, D.; Shaik, S.; Schwarz, H. *J. Am. Chem. Soc.* **1994**, *116*, 10734–10741.

(56) Baranov, V.; Javahery, G.; Hopkinson, A. C.; Bohme, D. K. *J. Am. Chem. Soc.* **1995**, *117*, 12801–12809.

(57) Clemmer, D. E.; Chen, Y.-M.; Khan, F. A.; Armentrout, P. B. *J. Chem. Phys.* **1994**, *98*, 6522–6529.

(58) Schroder, D.; Fiedler, A.; Ryan, M. F.; Schwarz, H. *J. Chem. Phys.* **1994**, *98*, 68–70.

(59) Danovich, D.; Shaik, S. *J. Am. Chem. Soc.* **1997**, *119*, 1773–1786.

(60) Harvey, J. N.; Tew, D. P. *Inter. J. Mass Spectros.* **2013**, *354–355*, 263–270.

(61) Essafi, S.; Tew, D. T.; Harvey, J. N. *Angew. Chem. Int. Ed.* **2017**, *56*, 5790–5794.

(62) Bohme, D. K.; Schwarz, H. *Angew. Chem. Int. Ed.* **2005**, *44*, 2336–2354.

(63) Schwarz, H. *Coord. Chem. Rev.* **2017**, *334*, 112–123.

(64) Roithova, J.; Schroder, D. *Coord. Chem. Rev.* **2009**, *253*, 666–677.

(65) Tyo, E. C.; Vajda, S. *Nat. Nanotechnol.* **2015**, *10*, 577–588.

(66) Shi, Y.; Ervin, K. M. *J. Chem. Phys.* **1998**, *108*, 1757–1760.

(67) Balaj, O. P.; Balteanu, I.; Rossteuscher, T. T. J.; Beyer, M. K.; Bondybey, V. E. *Angew. Chem. Int. Ed.* **2004**, *43*, 6519–6522.

(68) Socaciu, L. D.; Hagen, J.; Bernhardt, T. M.; Worste, L.; Heiz, U.; Hakkinen, H.; Landman, U. *J. Am. Chem. Soc.* **2003**, *125*, 10437–10445.

(69) Hakkinen, H.; Landman, U. *J. Am. Chem. Soc.* **2001**, *123*, 9704–9705.

(70) Koyanagi, G. K.; Bohme, D. K. *J. Phys. Chem. A* **2006**, *110*, 1232–1241.

(71) Raksit, A. B.; Bohme, D. K. *Int. J. Mass Spectrom. Ion Process.* **1989**, *55*, 69–82.

(72) Sodupe, M.; Branchadell, V.; Rosi, M.; Bauschlicher, C. W. *J. Phys. Chem. A* **1997**, *101*, 7854–7859.

(73) Cheng, P.; Koyanagi, G. K.; Bohme, D. K. *J. Phys. Chem. A* **2006**, *110*, 12832–12838.

(74) Lavrov, V. V.; Blagojevic, V.; Koyanagi, G. K.; Orlova, G.; Bohme, D. K. *J. Phys. Chem. A* **2006**, *110*, 1232–1241.

(75) Koyanagi, G. K.; Cheng, P.; Bohme, D. K. *J. Phys. Chem. A* **2010**, *114*, 241–246.

(76) Feil, S.; Koyanagi, G. K.; Viggiano, A. A.; Bohme, D. K. *J. Phys. Chem. A* **2007**, *111*, 13397–13402.

(77) Shayasteh, A.; Lavrov, V. V.; Koyanagi, G. K.; Bohme, D. K. *J. Phys. Chem. A* **2009**, *113*, 5602–5611.

(78) Rodgers, M. T.; Armentrout, P. B. *Mass Spectrom. Rev.* **2000**, *19*, 215–247.

(79) Ervin, K. M.; Armentrout, P. B. *J. Chem. Phys.* **1985**, *83*, 166–189.

(80) Schultz, R. H.; Armentrout, P. B. *J. Mass. Spectrom. Ion Process.* **1991**, *107*, 29–48.

(81) Dalleska, N. F.; Honma, K.; Armentrout, P. B. *J. Am. Chem. Soc.* **1994**, *116*, 3519–3528.

(82) Andersen, A.; Munteau, F.; Walter, D.; Rue, C.; Armentrout, P. B. *J. Phys. Chem. A* **2000**, *104*, 692–705.

(83) Brown, G. G.; Dian, B. C.; Douglass, K. O.; Geyer, S. M.; Shipman, S. T.; Pate, B. H. *Rev. Sci. Instrum.* **2008**, *79*, 053103–1–053103–13.

(84) Grubbs, G. S.; Dewberry, C. T.; Etchison, K. C.; Kerr, K. E.; Cooke, S. A. *Rev. Sci. Instrum.* **2007**, *78*, 096106–1–096106–3.

(85) Dewelerry, C. T.; Etchison, K. C.; Grubbs, G. S.; Powoski, R. A.; Serapin, M. M.; Peebles, S. A.; Cooke, S. A. *J. Molec. Spec.* **2008**, *248*, 20–25.

(86) Zaleski, D. P.; Stephens, S. L.; Walker, N. R. *Phys. Chem. Chem. Phys.* **2014**, *16*, 25221–25228.

(87) Stephens, S. L.; Zaleski, D. P.; Mizukami, W.; Tew, D. P.; Walker, N. R.; Legon, A. C. *J. Chem. Phys.* **2014**, *140*, 124310–1–124310–13.

(88) Bittner, D. M.; Zaleski, D. P.; Tew, D. P.; Walker, N. R.; Legon, A. C. *Angew. Chem. Int. Ed.* **2016**, *55*, 3768–3771.

(89) Medcraft, C.; Bittner, D. M.; Tew, D. P.; Walker, N. R.; Legon, A. C. *J. Chem. Phys.* **2016**, *145*, 194306–1–194306–10.

(90) Bittner, D. M.; Zaleski, D. P.; Stephens, S. L.; Tew, D. P.; Walker, N. R.; Legon, A. C. *J. Chem. Phys.* **2015**, *142*, 144302–1–144302–10.

(91) Centi, G.; Perathoner, S. *Catal. Today* **2009**, *148*, 191–205.

(92) Yang, L.; Wang, H. *ChemSusChem* **2014**, *7*, 962–998.

(93) Toda, Y.; Hirayama, H.; Kuganathan, N.; Torrisi, A.; Sushko, P. V.; Hosono, H. *Nat. Commun.* **2013**, *4*, 1–8.

(94) Benson, E. E.; Kubiak, C. P.; Sathrum, A. J.; Smieja, J. M. *Chem. Soc. Rev.* **2009**, *38*, 89–99.

(95) Sakakura, T.; Choi, J.-C.; Yasuda, H. *Chem. Rev.* **2007**, *107*, 2365–2387.

(96) Lie, Q.; Wu, L.; Jackstell, R.; Beller, M. *Nat. Commun.* **2015**, *6*, 1–15.

(97) Lunde, P. J.; Kester, F. L. *J. Catal.* **1973**, *30*, 423–429.

(98) Lunde, P. J. *Ind. Eng. Chem. Process. Des. Dev.* **1974**, *13*, 226–233.

(99) Fujita, S.; Terunuma, H.; Nakamura, M.; Takezawa, N. *Ind. Eng. Chem. Res.* **1991**, *30*, 1146–1151.

(100) Muller, K.; Stadter, M.; Rachow, F.; Hoffmannbeck, D.; Schmeisser, D. *Environ. Earth. Sci.* **2013**, *70*, 3771–3778.

(101) The Sabatier System: Producing Water on the Space Station., `https://www.nasa.gov/mission_pages/station/research/news/sabatier.html`.

(102) Adan-Plaza, S.; Carpenter, K.; Elias, L.; Grover, R.; Hilstad, M.; Hoffman, C.; Schneider, M.; Bruckner, A. In *HEDS-UP Mars Exploration Forum*, ed. by Budden, N. A.; Duke, M. B., 1998, pp 171–194.

(103) Dry, M. E. *Appl. Catal., A* **1996**, *138*, 319–344.

(104) Hollas, J. M., *High Resoltion Spectroscopy - 2nd ed.* John Wiley & Sons Ltd: Chichester, UK, 1998.

(105) Morse, P. M. *Phys. Rev.* **1929**, *34*, 57–64.

(106) Atkins, P.; Friedman, R., *Molecular Quantum Mechanics (Fifth edition)*; Oxford University Press Inc.: New York, USA, 2005.

(107) Banwell, C. N.; McCash, E. M., *Fundamental of Molecular Spectroscopy - 4th ed.* McGraw-Hill Publishing Company: Maidenhead, UK, 1994.

(108) Liu, X.; Atwater, M.; Wang, J.; Huo, Q. *Colloids Surf., B* **2007**, *58*, 3–7.

(109) Scherer, J. J.; Paul, J. B.; Collier, C. P.; O'Keefe, A.; Saykally, R. J. *J. Chem. Phys.* **1995**, *103*, 9187–9192.

(110) Kraus, D.; Saykally, R. J.; Bondybey, V. E. *Chem. Phys. Lett.* **1998**, *295*, 285–288.

(111) Rohlfing, E. A.; Velentini, J. J. *J. Chem. Phys.* **1986**, *84*, 6560–6566.

(112) Juvet, C.; Dedonder, C. L.; Martrenchard, S.; Solgadi, D. *J. Chem. Phys.* **1991**, *94*, 1759–1764.

(113) Cameron, A. E.; Eggers, D. F. *Rev. Sci. Instrum.* **1948**, *19*, 605–607.

(114) Wiley, W. C.; McLaren, I. H. *Rev. Sci. Instrum* **1955**, *26*, 1150–1157.

(115) Okumura, M.; Yea, L. I.; Lee, Y. T. *J. Chem. Phys.* **1985**, *83*, 3505–3506.

(116) Knickelbein, M. B.; Menzes, W. J. C. *J. Phys. Chem.* **1992**, *96*, 6611–6616.

(117) Menzes, W. J. C.; Knickelbein, M. B. *J. Chem. Phys.* **1993**, *98*, 1856–1866.

(118) Ayotte, P.; Weddle, G. H.; Kim, J.; Johnson, M. A. *Chem. Phys.* **1998**, *239*, 485–495.

(119) Ayotte, P.; Weddle, G. H.; Kim, J.; Johnson, M. A. *Chem. Phys.* **1998**, *120*, 12361–12362.

(120) Pinto, T.; Boudin, N.; Bréchignac, P. *J. Chem. Phys.* **1999**, *111*, 7337–7347.

(121) Roscioli, J. R.; McCunn, L. R.; Johnson, M. A. *Science* **2007**, *316*, 249–254.

(122) Kamrath, M. Z.; Ralph, R. A.; Johnson, M. A. *J. Am. Chem. Soc.* **2010**, *132*, 15508–15511.

(123) Cheung, T. C.; Bandyopadhyay, B.; Mosley, J. D.; Duncan, M. A. *J. Am. Chem. Soc.* **2012**, *134*, 13046–13055.

(124) Brümmer, M.; Kaposta, C.; Santambrogio, G.; Asmis, K. A. *J. Chem. Phys.* **2003**, *119*, 12700–12703.

(125) Jašik, J.; Žabka, J.; Rohitová, J.; Gerlich, D. *Int. J. Mass. Spectrom.* **2013**, *354*, 204–210.

(126) Johnson, C. J.; Fournier, A. A.; Sullivan, E. N.; Weddle, G. H.; Johnson, M. A. *J. Chem. Phys.* **2014**, *140*, 22110–221103.

(127) Gruene, P.; Rayner, D. M.; Redlich, B.; van der Meer, A. F. G.; Lyon, J. T.; Meijer, G.; Fielicke, A. *Science* **2008**, *321*, 674–676.

(128) Lyon, J. T.; Gruene, P.; Fielicke, A.; Meijer, G.; Janssens, E.; Claes, P.; Lievens, P. *J. Am. Chem. Soc.* **2009**, *131*, 1115–1121.

(129) Kamrath, M. Z.; Ralph, R. A.; Guasco, T. L.; Leavitt, C. M.; Johnson, M. A. *Int. J. Mass Spec.* **2011**, *300*, 91–98.

(130) Kamrath, M. Z.; Garand, E.; Jordan, P. A.; Leavitt, C. M.; Wolk, A. B.; van Stipdonk, M. J.; Miller, S. J.; Johnson, M. A. *J. Am. Chem. Soc.* **2011**, *133*, 6440–6448.

(131) Weinheimer, C. J.; Lisy, J. M. *J. Chem. Phys.* **1996**, *105*, 2938–2941.

(132) Lisy, J. M. *Int. Rev. Phys. Chem.* **1997**, *16*, 267–289.

(133) Weinheimer, C. J.; Lisy, J. M. *Int. J. Mass. Specrom.* **1996**, *159*, 197–208.

(134) Weinheimer, C. J.; Lisy, J. M. *J. Phys. Chem* **1996**, *100*, 15305–15308.

(135) Duncan, M. A. *Int. Rev. Phys. Chem.* **2003**, *22*, 407–435.

(136) Walker, N. R.; Walter, R. S.; Pillai, E. D.; Jordan, K. D.; Duncan, M. A. *J. Chem. Phys.* **2003**, *119*, 10471–1–10471–4.

(137) Walters, R. S.; Pillai, E. D.; Duncan, M. A. *J. Am. Chem. Soc.* **2005**, *127*, 16599–16610.

(138) Carnegie, P. D.; Bandyopadhyay, B.; Duncan, M. A. *J. Phys. Chem. A* **2008**, *112*, 6237–6243.

(139) Walker, N. R.; Walter, R. S.; Tsai, M.-K.; Jordan, K. D.; Duncan, M. A. *J. Phys. Chem. A* **2005**, *109*, 7057–7067.

(140) Carnegie, P. D.; McCoy, A. B.; Duncan, M. A. *J. Phys. Chem. A* **2009**, *113*, 4849–4854.

(141) Bandyopadhyay, B.; Reishus, K. N.; Duncan, M. A. *J. Phys. Chem. A* **2013**, *117*, 7794–7803.

(142) Ricks, A. M.; Reed, Z. E.; Duncan, M. A. *J. Mol. Spectrosc.* **2011**, *266*, 63–74.

(143) Walters, R. S.; Jaeger, T. D.; Duncan, M. A. *J. Phys. Chem. A* **2002**, *106*, 10482–10487.

(144) Walters, R. S.; Pillai, E. D.; va Ra Schleyer, P.; Duncan, M. A. *J. Am. Chem. Soc.* **2005**, *127*, 17030–17042.

(145) Velasquez, J.; Pillai, E. D.; Cernegie, P. D.; Duncan, M. A. *J. Phys. Chem. A* **2008**, *110*, 2325–2330.

(146) Jaeger, T. D.; Pillai, E. D.; Duncan, M. A. *J. Phys. Chem. A* **2004**, *108*, 6606–6610.

(147) Jaeger, J. B.; Pillai, E. D.; Jaeger, T. D.; Duncan, M. A. *J. Phys. Chem. A* **2005**, *109*, 2801–2808.

(148) Pillai, E. D.; Jaeger, T. D.; Duncan, M. A. *J. Phys. Chem. A* **2005**, *109*, 3521–3526.

(149) Pillai, E. D.; Jaeger, T. D.; Duncan, M. A. *J. Am. Chem. Soc.* **2007**, *129*, 2297–2307.

(150) Ohashi, K.; Teraboru, K.; Inokuchi, Y.; Mune, Y.; Machinaga, H.; Nishi, N.; Sekiya, H. *Phys. Chem. Lett.* **2004**, *393*, 264–270.

(151) Mune, Y.; Ohashi, K.; Iino, T.; Inokuchi, Y.; Nishi, K. J. N.; Sekiya, H. *Phys. Chem. Lett.* **2006**, *419*, 201–206.

(152) Koga, N.; Ohashi, K.; Furakawa, K.; Imamura, T.; Nishi, K. J. N.; Sekiya, H. *Phys. Chem. Lett.* **2012**, *539–540*, 1–6.

(153) Inoue, K.; Ohashi, K.; Iino, T.; Nishi, K. J. N.; Sekiya, H. *Phys. Chem. Chem. Phys.* **2007**, *9*, 4793–4802.

(154) Inoue, K.; Ohashi, K.; Iino, T.; Sasaki, J.; Nishi, K. J. N.; Sekiya, H. *Phys. Chem. Chem. Phys.* **2008**, *10*, 3052–3062.

(155) Wang, L.; Wang, G.; Qu, H.; Wang, C.; Zhou, M. *J. Phys. Chem. A* **2014**, *118*, 1841–1849.

(156) Wang, L.; Wang, G.; Qu, H.; Li, Z. H.; Zhou, M. *Phys. Chem. Chem. Phys.* **2014**, *16*, 3052–3062.

(157) Li, Y.; Wang, L.; Qu, H.; Wang, G.; Zhou, M. *J. Phys. Chem. A* **2015**, *119*, 3577–3586.

(158) Walker, N. R.; Walters, R. S.; Duncan, M. A. *New J. Chem.* **2005**, *29*, 1495–1503.

(159) Duncan, M. A. *Int. Rev. Phys. Chem.* **2003**, *22*, 407–435.

(160) Duncan, M. A. *Int. J. Mass Spectrom.* **2008**, *272*, 99–118.

(161) Lisy, J. M. *J. Chem. Phys.* **2006**, *125*, 132302–1–132302–16.

(162) Dryza, V.; Poad, B. L. J.; Bieske, E. J. *Phys. Chem. Chem. Phys.* **2012**, *14*, 14954–14965.

(163) Dryza, V.; Bieske, E. J. *Inter. Rev. Phys. Chem.* **2013**, *32*, 559–587.
(164) Langmuir, I. *Science* **1921**, *54*, 59–67.
(165) Mitchell, P. R.; Parish, R. V. *J. Chem. Educ.* **1969**, *46*, 811–814.
(166) Chatt, J.; Duncanson, L. A. *J. Chem. Soc.* **1953**, *0*, 2939–2947.
(167) Wrighton, M. *Chem. Rev.* **1974**, *74*, 401–430.
(168) Aubke, F.; Wang, C. *Coord. Chem. Rev.* **1994**, *137*, 483–524.
(169) Reed, Z. E.; Duncan, M. A. *J. Am. Soc. Mass Spectrom.* **2010**, *21*, 739–749.
(170) Shufler, S. L.; Sternber, H. W.; Friedel, R. A. *J. Am. Chem. Soc.* **1956**, *78*, 2687–2688.
(171) Ricks, A. M.; Bakker, J. M.; Duberly, G. E.; Duncan, M. A. *J. Phys. Chem. A* **2009**, *113*, 4701–4708.
(172) Bradwaite, A. D.; Duncan, M. A. *J. Phys. Chem. A* **2012**, *116*, 1375–1382.
(173) Bradwaite, A. D.; Maner, J. A.; Duncan, M. A. *Inorg. Chem.* **2014**, *53*, 1166–1169.
(174) Bradwaite, A. D.; Ricks, A. M.; Duncan, M. A. *J. Phys. Chem. A* **2013**, *117*, 1001–1010.
(175) Bradwaite, A. D.; Duncan, M. A. *J. Phys. Chem. A* **2013**, *117*, 11695–11703.
(176) Valesquez, J.; Duncan, M. A. *Phys. Chem. Lett.* **2008**, *461*, 28–32.
(177) Bradwaite, A. D.; Abbot-Lyon, H. L.; Duncan, M. A. *J. Phys. Chem. A* **2016**, *120*, 7659–7670.
(178) Bradwaite, A. D.; Ricks, A. M.; Duncan, M. A. *J. Phys. Chem. A* **2011**, *115*, 10461–10469.
(179) Valesquez, J.; Njegic, B.; Gordon, M. S.; Duncan, M. A. *J. Phys. Chem. A* **2008**, *112*, 1907–1913.
(180) Zhou, X.; Cui, J.; Li, Z. H.; Wang, G.; Liu, Z.; Zhou, M. *J. Phys. Chem. A* **2013**, *117*, 1514–1521.
(181) Cui, J.; Wang, G.; Zhou, Z.; Chi, C.; Li, Z. H.; Liu, Z.; Zhou, M. *Phys. Chem. Chem. Phys.* **2013**, *15*, 10224–10232.

(182) Wang, G.; Cui, J.; Chi, C.; Zhou, X.; Li, Z. H.; Xing, X.; Zhou, M. *Chem. Sci.* **2012**, *2*, 3272–3279.

(183) Chi, C.; Cui, J.; Li, Z. H.; Xing, X.; Wang, G.; Zhou, M. *Chem. Sci.* **2012**, *3*, 1698–1706.

(184) Zhang, N.; Luo, M.; Chi, C.; Wong, G.; Cui, J.; Zhou, M. *J. Phys. Chem. A* **2015**, *121*, 4142–4150.

(185) Qu, H.; Kong, F.; Wang, G.; Zhou, M. *J. Phys. Chem. A* **2015**, *121*, 1627–1632.

(186) Rosi, N. L.; Eckert, J.; Eddaouidi, M.; Vodak, D. T.; Kim, J.; O'Keeffee, M.; Yaghi, O. M. *Science* **2003**, *300*, 1127–1129.

(187) Dinca, M.; Long, J. R. *Angew. Chem. Inter. Ed.* **2008**, *47*, 6766–6779.

(188) Han, S. S.; Mendoza-Cortes, J. L.; III, W. A. G. *Chem. Soc. Rev.* **2009**, *38*, 1460–1476.

(189) Emmeluth, C.; Poad, B. L. J.; Thompson, C. D.; Weddle, G. H.; Bieske, E. J. *J. Chem. Phys.* **2007**, *126*, 204309–1–204309–9.

(190) Poad, B. L. J.; Wearne, P. J.; Bieske, E. J.; Buchachenko, A. A.; Bennet, D. I. G.; Klos, J.; Alexander, M. H. *J. Chem. Phys.* **2008**, *129*, 184306–1–184306–8.

(191) Dryza, V.; Poad, B. L. J.; Bieske, E. J. *J. Phys. Chem. A* **2009**, *113*, 199–204.

(192) Emmeluth, C.; Poad, B. L. J.; Thompson, C. D.; Weddle, G. H.; Bieske, E. J. *J. Chem. Phys.* **2007**, *127*, 164310–1–164310–8.

(193) Dryza, V.; Bieske, E. J. *J. Chem. Phys.* **2009**, *131*, 164303–1–164303–6.

(194) Dryza, V.; Poad, B. L. J.; Bieske, E. J. *J. Phys. Chem. A* **2009**, *113*, 6044–6048.

(195) Dryza, V.; Bieske, E. J. *J. Chem. Phys.* **2009**, *131*, 224304–1–224304–7.

(196) Dryza, V.; Bieske, E. J. *J. Phys. Chem. Lett.* **2011**, *2*, 719–724.

(197) Bragg, S. L.; Brault, J. W.; Smith, W. H. *Astrophys. J.* **1982**, *263*, 999–1004.

(198) Poad, B. L. J.; Thompson, C. D.; Bieske, E. J. *Chem. Phys.* **2008**, *346*, 176–181.

(199) Dryza, V.; Bieske, E. J. *Inter. J. Mass Spectrom.* **2010**, *297*, 46–54.

(200) Rodriguez, O.; Lisy, J. M. *J. Chem. Phys.* **2011**, *115*, 1228–1233.

(201) Citir, M.; Altimay, G.; Austen-Miller, G.; Metz, R. B. *J. Phys. Chem. A* **2010**, *114*, 11322–11329.

(202) Ashraf, M. A.; Copeland, C. W.; Kocak, A.; McEnroe, A. R.; Metz, R. B. *Phys. Chem. Chem. Phys.* **2015**, *17*, 25700–25704.

(203) Copeland, C. W.; Ashraf, M. A.; Boyle, E. M.; Metz, R. B. *J. Phys. Chem. A* **2017**, *121*, 2132–2137.

(204) Kocak, A; Sallese, Z.; Johnston, M. D.; Metz, R. B. *J. Phys. Chem. A* **2014**, *118*, 3253–3265.

(205) Kocak, A; Ashraf, M. A.; Metz, R. B. *J. Phys. Chem. A* **2015**, *119*, 9653–9665.

(206) Maitre, P.; Bauschlicher, C. W. *J. Phys. Chem.* **1993**, *97*, 11912–11920.

(207) Harding, D. J.; Walsh, T. R.; Hamilton, S. M.; Hopkins, W. S.; Mackenzie, S. R.; Gruene, P.; Haertelt, M.; Meijer, G.; Fielicke, A. *J. Chem. Phys.* **2010**, *132*, 0111010–0111014.

(208) Gruene, P.; Fielicke, A.; Meijer, G.; Rayner, D. M. *Phys. Chem. Chem. Phys.* **2008**, *10*, 6144–6149.

(209) Fielicke, A.; von Helden, G.; Meijer, G.; Pedersen, D. B.; Simard, B.; Rayner, D. M. *J. Chem. Phys.* **2006**, *124*, 194305–1–194305–8.

(210) Ashfold, M. N. R.; Howe, J. D. *Annu. Rev. Phys. Chem.* **1994**, *45*, 57–82.

(211) Chandler, D. W.; Houston, P. L. *J. Chem. Phys.* **1987**, *87*, 1445–1447.

(212) Eppink, A. T.J. B.; Parker, D. H. *Rev. Sci. Instrum.* **1997**, *68*, 3477–3484.

(213) Dribinski, V.; Ossadtschi, A.; Mandelshtam, V. A.; Reisler, H. *Rev. Sci. Instrum.* **2002**, *73*, 2634–2642.

(214) Garcia, G. A.; Nahon, L.; Powis, I. *Rev. Sci. Instrum.* **2004**, *75*, 4989–4996.

(215) Bordas, C.; Pauling, F.; Helm, H.; Huestis, D. L. *Rev. Sci. Instrum.* **1996**, *67*, 2257–2268.

(216) Roberts, G. M.; Nixon, J. L.; Lecointre, J.; Wrede, E.; Verlet, J. R. R. *Rev. Sci. Instrum.* **2009**, *80*, 053104–1–053104–7.

(217) Dick, B. *Phys. Chem. Chem. Phys.* **2014**, *16*, 570–580.

(218) Lin, J. J.; Zhou, J.; Shiu, W.; Liu, K. *Rev. Sci. Instrum.* **2003**, *74*, 2495–2500.

(219) Townsend, D.; Minitti, M. P.; Suits, A. G. *Rev. Sci. Instrum.* **2003**, *74*, 2530–2539.

(220) Chestakov, D. A.; Wu, S.-M.; Wu, G.; Parker, D. H.; Eppink, A. T.J. B.; Kitsopoulos, T. N. *J. Phys. Chem. A* **2004**, *108*, 8100–8105.

(221) Parker, D. H. *Acc. Chem. Res.* **2000**, *33*, 563–571.

(222) Leon, I.; Yang, Z.; Liu, H.-T.; Wang, L.-S. *Rev. Sci. Instrum.* **2014**, *85*, 083106–1–083106–12.

(223) Leon, I.; Yang, Z.; Wang, L.-S. *J. Chem. Phys.* **2013**, *139*, 194306–1–194306–8.

(224) Leon, I.; Yang, Z.; Wang, L.-S. *J. Chem. Phys.* **2014**, *140*, 084303–1–084303–13.

(225) Yang, Z.; Leon, I.; Wang, L.-S. *J. Chem. Phys.* **2013**, *139*, 021106–1–021106–4.

(226) Czekner, J.; Fun, L.; Wang, L.-S. *J. Phys. Chem. C* **2017**, *121*, 10752–10759.

(227) Kim, J. B.; Weichamn, M. L.; Neumark, D. M. *J. Chem. Phys.* **2012**, *141*, 174307–1–174307–11.

(228) Kim, J. B.; Weichamn, M. L.; Neumark, D. M. *J. Am. Chem. Soc.* **2014**, *136*, 7159–7168.

(229) Hock, C.; Kim, J. B.; Weichamn, M. L.; Yacovitch, T. I.; Neumark, D. M. *J. Chem. Phys.* **2012**, *137*, 244201–1–244201–16.

(230) Mooney, C. R. S.; Sanz, M. E.; McKay, A. R.; Fitzmaurice, R. J.; Aliev, A. E.; Caddick, S.; Fielding, H. H. *J. Phys. Chem. A* **2012**, *116*, 7943–7949.

(231) Horke, D. A.; Verlet, J. R. R. *Phys. Chem. Chem. Phys.* **2012**, *14*, 8511–8515.

(232) Mooney, C. R. S.; Parkes, M. A.; Iskra, A.; Fielding, H. H. *Angew. Chem. Inter. Ed.* **2015**, *54*, 5646–5649.

(233) Mooney, C. R. S.; Horke, D. A.; Chetterley, A. S.; Simprerler, A.; Fielding, H. H.; Verlet, J. R. R. *Chem. Sci.* **2013**, *4*, 921–927.

(234) Lin, J. J.; Zhou, J.; Shiu, W.; Liu, K. *Science* **2003**, *300*, 966–969.

(235) Zhou, J.; Lin, J. J.; Shiu, W.; Liu, K. *J Chem. Phys.* **2003**, *119*, 4997–5000.

(236) Zhou, J.; Lin, J. J.; Shiu, W.; Liu, K. *Phys. Chem. Chem. Phys.* **2006**, *8*, 3000–3006.

(237) Eyles, C. J.; Brouard, M.; Yang, C.-H.; Klos, J.; Aoiz, F. J.; Gijsbertsen, A.; Wiskerke, A. E.; Stolte, S. *Nat. Chem.* **2011**, *3*, 597–602.

(238) Brouard, M.; Chadwick, H.; Eyles, C. J.; Hornung, B.; Nichols, B.; Scott, J. M.; Aoiz, F. J.; Klos, J.; Stolte, S. *Mol. Phys.* **2013**, *111*, 1759–1771.

(239) Brouard, M.; Chadwick, H.; Eyles, C. J.; Hornung, B.; Nichols, B.; Aoiz, F. J.; Jambrina, P. G.; Stolte, S. *J. Chem. Phys.* **2013**, *138*, 1043101–1–104310–13.

(240) Chadwick, H.; Nichols, B.; Gordon, S. D. S.; Hornung, B.; Squires, E.; Brouard, M.; Klos, J.; Alexander, M. H.; Aoiz, F. J.; Stolte, S. *J. Phys. Chem. Lett.* **2014**, *5*, 3296–3301.

(241) Brouard, M.; Chadwick, H.; Gordon, S. D. S.; Hornung, B.; Nichols, B.; Klos, J.; Aoiz, F. J.; Stolte, S. *J. Chem. Phys.* **2014**, *141*, 164301–1–164306–14.

(242) Brouard, M.; Chadwick, H.; Gordon, S. D. S.; Hornung, B.; Nichols, B.; Aoiz, F. J.; Stolte, S. *J. Phys. Chem. A* **2015**, *119*, 12404–12416.

(243) Nichols, B.; Chadwick, H.; Gordon, S. D. S.; Eyles, C. J.; Hornung, B.; Brouard, M.; Alexander, M. H.; Aoiz, F. J.; Gijsbertsen, A.; Stolte, S. *Chem. Sci.* **2015**, *6*, 2202–2210.

(244) Brouard, M.; Chadwick, H.; Gordon, S. D. S.; Hornung, B.; Nichols, B.; Aoiz, F. J.; Stolte, S. *J. Chem. Phys.* **2016**, *144*, 224301–1–2243017.

(245) Aoiz, F. J.; Brouard, M.; Gordon, S. D. S.; Nichols, B.; Stolte, S. *Phys. Chem. Chem. Phys.* **2015**, *17*, 30210–30228.

(246) Nomerotski, A.; Brouard, M.; Campbell, E.; Clark, A.; Crooks, J.; John, J. J.; Johnsen, A. J.; Slater, C. S.; Turchetta, R.; Vallance, C.; Wilman, E.; Yuen, W. H. *JINST* **2011**, *5*, C07007.

(247) Slater, C. S.; Blake, S.; Brouard, M.; Lauer, A.; Vallance, C.; Bohun, C. S.; Christensen, L.; Nielsen, J. H.; Johansson, M. P.; Stapelfeldt, H. *Phys. Rev. A* **2015**, *91*, 053424–1–053424–14.

(248) Hohenberg, P.; Kohn, W. *Phys. Rev.* **1964**, *136*, 864–871.

(249) Kohn, W.; Sham, L. J. *Phys. Rev.* **1965**, *140*, 1133–1138.

(250) Parr, R.; Yang, W., *Density-functional Theory of Atoms and Molecules*; Oxford University Press: Oxford, UK, 1989.

(251) Cramer, C. J., *Essentials of Computational Chemistry*; Wiley: Chichester, UK, 2010.

(252) Becke, A. D. *J. Chem. Phys.* **2014**, *140*, 18A301–1–18A301–18.

(253) Becke, A. D. *Phys. Rev. A* **1988**, *38*, 3098–3100.

(254) Perdew, J. P.; Burke, K.; Ernzerhof, M. *Phys. Rev. Lett.* **1996**, *77*, 3865–3868.

(255) Perdew, J. P. *Phys. Rev. B: Condens. Matter Mater. Phys.* **1986**, *33*, 8822–8824.

(256) Perdew, J. P.; Burke, K.; Wang, Y. *Phys. Rev. B* **1996**, *54*, 16533–16539.

(257) Lee, C.; Yang, W.; Parr, R. G. *Phys. Rev. B* **1988**, *37*, 785–789.

(258) Berke, A. D. *J. Chem. Phys.* **1992**, *98*, 5648–5620.

(259) Burke, K. *J. Chem. Phys.* **2012**, *136*, 150901–1–150901–8.

(260) Buhl, M.; Reinmann, C.; Pantazis, D. A.; Bredow, T.; Neese, F. *J. Chem. Theory. Comput.* **2008**, *4*, 1449–1459.

(261) Guilhaus, M.; Selby, D.; Mlynski, V. *Mass Spectrom. Rev.* **2000**, *10*, 65–107.

(262) Bell, A. G. *Proc. Am. Assoc. Adv. Sci.* **1880**, *29*, 307–324.

(263) Kerr, E. L.; Atwood, J. G. *Appl. Opt.* **1968**, *7*, 915–922.

(264) Toth, R. A.; Brown, L. R.; Hunt, R. H.; Rothman, L. S. *Appl. Opt.* **1981**, *20*, 932–935.

(265) Hyber, K. P.; Herzberg, G., *Molecular Spectra and Molecular Structure IV, Constants of Diatomic Molecules*; Van Nostrand Reinhold Co: New York, USA, 1979.

(266) Kent, M. J., *Part II thesis: Spectroscopic Studies of Gas-phase Metal Hydrogen Complexes*, Department of Chemistry, University of Oxford, 2015.

(267) Lavrov, V. V.; Blagojevic, V.; Koyanagi, G. K.; Orlova, G.; Bohme, D. K. *J. Phys. Chem. A* **2004**, *108*, 5610–5624.

(268) Cunningham, E. M.; Gentleman, A. S.; Beardsmore, P. M.; Iskra, A.; Mackenzie, S. R. *J. Phys. Chem.* **2017**, *121*, 7565–7571.

(269) Höckendorf, R. F.; Balaj, O. P.; van der Linde, C.; Beyer, M. K. *Phys. Chem. Chem. Phys.* **2010**, *12*, 3772–3779.

(270) Price, D., *Part II thesis: A Combined Experimental and Computational Study of Infrared Photodissociation of Cationic Gas-Phase Metal-Methane Complexes*, Department of Chemistry, University of Oxford, 2017.

(271) Davies, P. R.; Orville-Thomas, W. J. *J. Molec. Struc.* **1969**, *4*, 163–177.

(272) Walker, N. R.; Walters, R. S.; Duncan, M. A. *J. Chem. Phys.* **2004**, *120*, 10037–10045.

(273) Ricks, A. M.; Brathwaite, A. D.; Duncan, M. A. *J. Phys. Chem. A* **2013**, *117*, 11490–11498.

(274) Siever, M. R.; Armentrout, P. B. *J. Chem. Phys.* **1995**, *102*, 754–762.

(275) Sharp, A. P., *Part II thesis: IR Depletion Studies of Gas-Phase Metal-Ligand Complexes*, Department of Chemistry, University of Oxford, 2015.

(276) Herzberg, G., *Molecular Spectra and Molecular Structure, Volume II: Infrared and Raman Spectra of Polyatomic Molecules*; Krieger Publishing Company: Malabar, FL, USA, 1991.

(277) Murthy, C. S.; Singer, K.; McDonald, I. R. *Mol. Phys.* **1981**, *44*, 135–143.

(278) Muenter, J. S. *J. Chem. Phys.* **1991**, *94*, 2781–2793.

(279) Bukowski, R.; Sadlej, J.; Jeziorski, B.; Jankowski, P.; Szalewicz, K.; Kuharski, S. A.; Williams, H. L.; Rice, B. M. *J. Chem. Phys.* **1999**, *110*, 3785–3803.

(280) Iskra, A.; Gentleman, A. S.; Kartouzian, A.; Kent, M. J.; Sharp, A. P.; Mackenzie, S. R. *J. Phys. Chem. A* **2017**, *121*, 133–140.

(281) Gregoire, G.; Brinkmann, N. R.; van Heijnsbergen, D.; Schaefer, H. F.; Duncan, M. A. *J. Phys. Chem. A* **2003**, *107*, 218–227.

(282) Walters, R. S.; Brinkmann, N. R.; Schaefer, H. F.; Duncan, M. A. *J. Phys. Chem. A* **2003**, *107*, 7396–7405.

(283) Jaeger, J. B.; Jaeger, T. D.; Brinkmann, N. R.; Schaefer, H. F.; Duncan, M. A. *Can. J. Chem.* **2004**, *82*, 934–946.

(284) Gregoire, G.; Velasquez, J.; Duncan, M. A. *Chem. Phys. Lett.* **2001**, *349*, 451–457.

(285) Gregoire, G.; Duncan, M. A. *J. Chem. Phys.* **2002**, *349*, 2120–2130.

(286) Walker, N. R.; Grieves, G. A.; Walters, R. S.; Duncan, M. A. *Chem. Phys. Lett.* **2003**, *380*, 230–236.

(287) Walker, N. R.; Walters, R. S.; Grieves, G. A.; Duncan, M. A. *J. Chem. Phys.* **2004**, *121*, 10498–10507.

(288) Xing, X. P.; Wang, G. J.; Wang, C. X.; Zhou, M. F. *Chin. J. Chem. Phys.* **2013**, *26*, 687–693.

(289) Zhao, Z.; Kong, X.; Yang, D.; Yuan, Q.; Xie, H.; Fan, H.; Zhao, J.; Jiang, L. *J. Phys. Chem. A* **2017**, *121*, 3220–3226.

(290) Griffin, J. B.; Armentrout, P. B. *J. Chem. Phys.* **1998**, *108*, 8075–8083.

(291) Sievers, M. R.; Armentrout, P. B. *J. Phys. Chem. A* **1998**, *102*, 10754–10762.

(292) Armentrout, P. B.; Koizumi, H.; Mackenna, M. *J. Phys. Chem. A* **2003**, *109*, 11365–11375.

(293) Zhang, X. G.; Armentrout, P. B. *J. Phys. Chem. A* **2003**, *107*, 8904–8914.

(294) Asher, R. L.; Bellert, D.; Butelezi, T.; Brucat, P. J. *Phys. Chem. Lett.* **1994**, *227*, 623–627.

(295) Asher, R. L.; Bellert, D; Buthelezi, T.; Weerasekara, G.; Brucat, P. J. *Phys. Chem. Lett.* **1994**, *228*, 390–392.

(296) Lessen, D. E.; Asher, R. L.; Brucat, P. J. *J. Chem. Phys.* **1991**, *95*, 1414–1416.

(297) Koyanagi, G. K.; Bohme, D. K. *J. Phys. Chem. A* **2006**, *110*, 1232–1241.

(298) Knurr, B. J.; Weber, J. M. *J. Phys. Chem. A* **2014**, *118*, 4056–4062.

(299) Knurr, B. J.; Weber, J. M. *J. Phys. Chem. A* **2014**, *118*, 8753–8757.

(300) Knurr, B. J.; Weber, J. M. *J. Phys. Chem. A* **2014**, *118*, 10246–10251.

(301) Knurr, B. J.; Weber, J. M. *J. Phys. Chem.* **2013**, *117*, 10764–10771.

(302) Boese, A. D.; Schneider, H.; Gloss, A. N.; Weber, J. M. *J. Chem. Phys.* **2005**, *122*, 1543011–1543017.

(303) Knurr, B. J.; Weber, J. M. *J. Am. Chem. Soc.* **2012**, *134*, 18804–18808.

(304) Thompson, M. C.; Ramsay, J.; Weber, J. M. *Angew. Chem. Inter. Ed.* **2016**, *155*, 15171–15714.

(305) Thompson, M. C.; Dodson, L. G.; Weber, J. M. *J. Phys. Chem. A* **2017**, *121*, 4132–4138.

(306) Ansari, M. B.; Park, S.-E. *Energy Environ. Sci.* **2012**, *5*, 9419–9437.

(307) Addicoat, M. A.; Metha, G. F. *J. Comput. Chem.* **2009**, *30*, 57–64.

(308) Weigend, F.; Ahlrichs, R. *Phys. Chem. Chem. Phys.* **2005**, *7*, 3297–3305.

(309) Frisch, J. M.; *et al.*, *Gaussian 09*; Gaussian, Inc.: Wallingford, CT, USA, 2009.

(310) Asher, R. L.; Bellert, D.; Butelezi, T.; Brucat, P. J. *Phys. Chem. Lett.* **1994**, *227*, 277–282.

(311) Radzig, A. A.; Smirnov, B. M., *Springer series in chemical physics, Vol. 31. Reference data on atoms, molecules and ions*; Springer: Berlin, Germany, 1995.

(312) Sodupe, M.; Bauschlicher, C. W.; Partridge, H. *Phys. Chem. Lett.* **1992**, *192*, 185–194.

(313) Garcia-Fernandez, P.; Bersuker, I. B.; Boggs, J. E. *J. Phys. Chem. A* **2007**, *111*, 10409–10415.

(314) Gould, T.; Bucko, T *J. Chem. Theory. Comput.* **2016**, *12*, 3603–3613.

(315) Sievers, M. R.; Chen, Y.-M.; Armentrout, P. B. *J. Chem. Phys.* **1996**, *105*, 6322–6333.

(316) Lias, S. G.; Bartmess, J. E.; Liebman, J. F.; Holmes, J. L.; Levin, R. D.; Mallard, W. G. *J. Phys. Chem. Ref. Data* **1998**, *17*, 1–861.

(317) Zhou, M.; Andrews, L. *J. Phys. Chem. A* **1998**, *102*, 8251–8260.

(318) Wesendrup, R.; Schwarz, H. *Angew. Chem. Int. Ed.* **1995**, *34*, 2033–2035.

(319) Deng, K.; Yang, J.; Zhu, Q. *J. Chem. Phys.* **2003**, *118*, 6868–6873.

(320) Ya Inokuchi Aa Muraoka, T. N.; Ebata, T. *J. Chem. Phys.* **2008**, *129*, 0443081–0443089.

(321) Freiser, B. S., *Organometallic Ion Chemistry*; Kluwer: Dordrecht, The Netherlands, 1996.

(322) Schroder, D.; Schwarz, H.; Shaik, H., *Structure and Bonding*; Springer-Verlag: Berlin, G, 2000.

(323) NIST Atomic Spectra Database Levels Data., `https://www.nist.gov/pml/atomic-spectra-database`.

(324) Ricks, A. M.; Brathwaite, A. D.; Duncan, M. A. *J. Phys. Chem. A* **2013**, *117*, 11490–11498.

(325) Ghiringhelli, L. M.; Gruene, P.; Lyon, J. T.; Rayner, D. M.; Meijer, G.; Fielicke, A.; Scheffner *New J. Phys.* **2013**, *15*, 083003–1–083003–22.

(326) Tao, J.; Perdew, J. H.; Staroverov, V. N.; Scuseria, G. E. *Phys. Rev. Rev.* **2003**, *91*, 146401–1–146401–4.

(327) Parker, K. D. J.; Fryzuk, M. D. *Organometallics* **2015**, *34*, 2037–2047.

(328) Hellwig, M.; Milanov, A.; Barrecia, D.; Deborde, J.-L.; Thomas, R.; Winter, M.; Kunze, U.; Fisher, R. A.; Devi, A. *Chem. Mater.* **2007**, *19*, 6077–6089.

(329) Maestre, M. C.; Paniagua, C.; Herdweck, E.; Mosquera, M. E. G.; Jimenez, G.; Cuenca, T. *Organometallics* **2007**, *26*, 4243–4251.

(330) Pillai, E. D.; Jaeger, T. D.; Duncan, M. A. *J. Am. Chem. Soc.* **2007**, *129*, 2297–2307.

(331) Walker, N. R.; Walker, R. S.; Duncan, M. A. *J. Chem. Phys.* **2004**, *120*, 10037–10045.

(332) Grzybowska-Swierkosz, B. *Appl. Catal. A* **1997**, *157*, 263–310.

(333) Becker, M. F.; Buckman, A. B.; Walser, R. M.; Lepine, T.; Georges, P.; Brun, A. *Appl. Phys. Lett.* **1994**, *65*, 1507–1509.

(334) White, N. M.; Wing, R. F. *Astrophys. J.* **1978**, *222*, 209–219.

(335) McKemmish, L. K.; Yurchenko, S. N.; Tennyson, J. *Mon. Not. R. Astron. Soc.* **2016**, *463*, 771–793.

(336) Lam, K. W. F.; Faedi, F.; Brown, D. J.; *et al. Astron. & Astrophys.* **2017**, *599*, A3–1–A3–10.

(337) Palle, E.; Chen, G.; Prieto-Arranz, J.; *et al. Astron. & Astrophys.* **2017**, *602*, L15–1–L15–5.

(338) Lee, E. G.; Sato, J. Y.; Hirao, R.; Bernath, P. F.; Roy, R. J. L. *J. Mol. Spectrosc.* **1999**, *194*, 197–202.

(339) Balducci, G.; Gigli, G.; Guido, M. *J. Chem. Phys.* **1983**, *79*, 5616–5622.

(340) Cheung, A. S.-C.; Taylor, A. W.; Merer, A. J. *J. Mol. Spectrosc.* **1982**, *92*, 391–409.

(341) Merer, A. J.; Huang, G.; Cheung, A. S.-C.; Taylor, A. W. *J. Mol. Spectrosc.* **1987**, *125*, 465–503.

(342) Huang, G.; Merer, A. J.; Clouthier, D. J. *J. Mol. Spectrosc.* **1992**, *153*, 32–40.

(343) Cheung, A. S.-C.; Hajigeorgiou, P. G.; Huang, G.; Huang, S. Z.; Merer, A. J. *J. Mol. Spectrosc.* **1994**, *163*, 443–458.

(344) Ram, R. S.; Bernath, P. F.; Davies, S. P.; Merer, A. J. *J. Mol. Spectrosc.* **2002**, *211*, 279–283.

(345) Hopkins, W. S.; Hamilton, S. H.; Mackenzie, S. R. *J. Chem. Phys.* **2009**, *130*, 144308–1–144308–8.

(346) Wu, H.; Wang, L.-S. *J. Chem. Phys.* **1998**, *108*, 5310–5318.

(347) Bauschlischer, C. W.; Langhoff, S. R. *J. Chem. Phys.* **1986**, *85*, 5936–5942.

(348) Carlson, K. D.; Moser, C. *J. Chem. Phys.* **1966**, *44*, 3259–3259.

(349) Miliordos, E.; Mavridis, A. *J. Phys. Chem. A* **2007**, *111*, 1953–1965.

(350) Jones, R. W.; Gole, J. L. *J. Chem. Phys.* **1976**, *65*, 3800–3802.

(351) Coppens, P.; Smoes, S.; Drowart, J. *Trans. Faraday Soc.* **1967**, *63*, 2410–2145.

(352) Pedley, J. B.; Marshall, E. M. *J. Phys. Chem. Ref. Data* **1983**, *12*, 967–1031.

(353) Ristov, N.; Armentrout, P. B. *J. Chem. Phys.* **1986**, *90*, 5135–5140.

(354) Asmis, K. R.; Brummer, M; Kaposta, C; Santambrogio, G.; von Helden, G.; Meijer, G.; Rademann, K.; Woste, L. *Phys. Chem. Chem. Phys.* **2002**, *4*, 1101–1104.

(355) Asmis, K. R.; Meijer, G.; Brummer, M; Kaposta, C; Santambrogio, G.; Woste, L.; Sauer, J. *J. Chem. Phys.* **2004**, *120*, 6461–6470.

(356) Asmis, K. R.; Santambrogio, G.; Brummer, M.; Sauer, J. *Angew. Chem. Int. Ed.* **2005**, *44*, 3122–3125.

(357) Asmis, K. R.; Sauer, J. *Mass Spectrom. Rev.* **2007**, *26*, 542–562.

(358) Hopkins, W. S.; Hamilton, S. M.; McNaughter, P. D.; Mackenzie, S. R. *Chem. Phys. Lett.* **2009**, *483*, 10–15.

(359) Hopkins, W. S.; Woodham, A. P.; Plowright, R. J.; Wright, T. G.; Mackenzie, S. R. *J. Chem. Phys.* **2010**, *132*, 214303–1–214303–9.

(360) Hopkins, W. S.; Mackenzie, S. R. *J. Chem. Phys.* **2011**, *135*, 081104–1–081104–4.

(361) Parry, I. S.; Hermes, A. C.; Kortouzian, A.; Mackenzie, S. R. *Phys. Chem. Chem. Phys.* **2014**, *16*, 458–466.

(362) Cooper, G. A.; Kartouzian, A.; Gentleman, A. S.; Iskra, A.; van Wijk, R.; Mackenzie, S. R. *J. Chem. Phys.* **2015**, *143*, 124302–1–124302–6.

(363) Cooper, G. A.; Gentleman, A. S.; Iskra, A.; Mackenzie, S. R. *J. Chem. Phys.* **2017**, *147*, 013921–1–013921–8.

(364) Wrede, E.; Laubach, S.; Schulenburg, S.; Brown, A.; Wouters, E. R.; Orr-Ewing, A. J.; Ashfold, M. N. R. *J. Chem. Phys.* **2001**, *114*, 2629–2646.

(365) Zare, R. N., *Angular momentum: understanding spatial aspects in chemistry and physics*; Wiley: Chicester, New York, USA, 1988.

(366) Reid, K. L. *Annu. Rev. Phys. Chem.* **2003**, *54*, 397–424.

(367) James, A. M.; Kowalczyk, P.; Langlois, E.; Campbell, M. D.; Ogawa, A.; Simard, B. *J. Chem. Phys.* **1994**, *101*, 4485–4495.

(368) *SIMION 8.0*; Scientific Instruments Services, Inc: USA.

(369) Ford, M. S.; Mackenzie, S. R. *J. Chem. Phys.* **2005**, *123*, 084308–1–084308–8.

(370) James, A. M.; Kowalczyk, P.; Langlois, E.; Campbell, M. D.; Ogawa, A.; Simard, B. *J. Chem. Phys.* **1994**, *101*, 4485–4495.

(371) Main, R., *Part II thesis: A Combined Experimental and Computational Study of Infrared Dissociation in Gas-Phase M^+–Ligand Com-*

plexes (M^+ = Pt, Au), Department of Chemistry, University of Oxford, 2017.

(372) Gentleman, A. S.; Green, A. E.; Price, D. R.; Cunningham, E. M.; Iskra, A.; Mackenzie, S. R. *Top. Catal.* accepted.

(373) Hamilton, S. M.; Hopkins, W. S.; Harding, D. J.; Walsh, T. R.; Gruene, P.; Haertelt, M.; Fielicke, A.; Meijer, G.; Mackenzie, S. R. *J. Am. Chem. Soc.* **2010**, *132*, 1448–1449.